

POSTGLACIAL CHRONOLOGY AND GEOHAZARDS OF POND INLET AND ECLIPSE
SOUND, NORTHEASTERN BAFFIN ISLAND, NUNAVUT

by

Laura-Ann Broom

Submitted in partial fulfilment of the requirements
for the degree of Masters of Science

at

Dalhousie University

Halifax, Nova Scotia

March 2019

© Copyright by Laura-Ann Broom, 2019

TABLE OF CONTENTS

LIST OF TABLES	viii
LIST OF FIGURES	ix
ABSTRACT	xi
LIST OF ABBREVIATIONS USED	xii
GLOSSARY	xiv
ACKNOWLEDGEMENTS	xv
CHAPTER 1: INTRODUCTION	1
1.1 General statement of problem	1
1.2 Objectives	2
1.3 Hypotheses	3
1.4 Motivation and impact	3
1.5 Organization of thesis	6
<i>1.5.1 Chapter 2 – Manuscript 1</i>	6
<i>1.5.2 Chapter 3 – Manuscript 2</i>	8
<i>1.5.3 Chapter 4 – Manuscript 3</i>	9
1.6 References cited in Chapter 1	11
CHAPTER 2: INVESTIGATION OF A HOLOCENE MARINE SEDIMENTARY RECORD FROM POND INLET, NORTHERN BAFFIN ISLAND, NUNAVUT	14
Abstract	14

2.1 Introduction	15
2.2 Background	17
2.2.1 <i>Setting and physiography</i>	17
2.2.2 <i>Glacial history</i>	18
2.2.3 <i>Regional seismicity of Baffin Bay</i>	18
2.3 Methods	21
2.3.1 <i>Hydroacoustic analysis</i>	21
2.3.2 <i>Core analysis</i>	21
2.3.3 <i>Geochronology</i>	22
2.4 Results	22
2.4.1 <i>Preliminary results from the hydroacoustic analysis</i>	22
2.4.2 <i>Lithofacies</i>	28
2.4.3 <i>Chronology</i>	32
2.5 Preliminary interpretations	32
2.5.1 <i>Mass transport deposits and turbidites</i>	32
2.5.2 <i>Sedimentation rates and frequency of gravity flows</i>	33
2.5.3 <i>Triggering mechanisms for mass transport deposits and turbidites</i>	34
2.5.4 <i>Ongoing and Future work</i>	34
2.6 Economic considerations	35
2.7 Conclusions	36

2.8 Acknowledgments	36
2.9 References cited in Chapter 2	37
CHAPTER 3: DEGLACIAL TO POSTGLACIAL SUBMARINE DEPOSITIONAL HISTORY OF ECLIPSE SOUND AND POND INLET, NUNAVUT, CANADA	40
Abstract	40
3.1 Introduction	41
3.2 Regional setting	42
3.2.1 <i>Physiography</i>	42
3.2.2 <i>Glacial history of Pond Inlet and vicinity</i>	43
3.3 Materials and Methods	45
3.3.1 <i>Multibeam Bathymetric Data</i>	45
3.3.2 <i>Sub-bottom Profiler Data</i>	45
3.3.3 <i>Sediment Core data</i>	46
3.3.4 <i>Synthetic Seismograms</i>	48
3.3.5 <i>Chronology</i>	49
3.4 Results	52
3.4.1 <i>Seafloor morphology</i>	52
3.4.2 <i>Lithostratigraphy</i>	56
3.4.3 <i>Acoustic Stratigraphy</i>	65
3.5 Discussion	75
3.5.1 <i>Interpretation of the Lower and Upper Stratigraphic Units</i>	75

3.5.2 <i>Deglacial to postglacial depositional history</i>	78
3.6 Conclusions	85
3.7 Acknowledgements	86
3.8 Supplementary Figures	87
3.10 References cited in Chapter 3	88
CHAPTER 4: GEOHAZARDS OF POND INLET AND ECLIPSE SOUND, BAFFIN BAY - OBSERVATIONS ON SUBMARINE SLOPE FAILURES AND POTENTIAL HAZARD ASSESSMENT	93
Abstract	93
4.1 Introduction	94
4.2 Background	96
4.2.1 <i>Physiography</i>	96
4.2.2 <i>Hamlet of Pond Inlet</i>	97
4.2.2 <i>Deglaciation of Baffin Island & Baffin Bay Seismicity</i>	98
4.3 Methods	100
4.3.1 <i>Geophysical imaging and core sedimentology analysis</i>	100
4.3.2 <i>Slope stability analysis</i>	105
4.3.3 <i>Calculation of displacement waves</i>	107
4.5 Results	109
4.5.1 <i>Seafloor instability features in acoustic data</i>	109
4.5.2 <i>Sub-sea-floor evidence for slope instability</i>	112

4.5.2 Seafloor instability features in core data	117
4.5.3 Slope stability analysis	124
4.6 Discussion	128
4.6.1 Slope instability in the postglacial record.....	128
4.6.2 Nature of MTD transport.....	130
4.6.3 Triggering mechanisms	132
4.6.3 Potential for a displacement wave at the Hamlet of Pond Inlet.....	134
4.7 Conclusions	135
4.8 References cited in Chapter 4	135
CHAPTER 5: CONCLUSIONS	140
5.1 Conclusions and significance	140
5.1.1 Interpretation of the bathymetric and depositional record	141
5.1.2 Extent of mass wasting	142
5.1.3 Chronology for depositional processes and key events	142
5.1.4 Potential landslide hazard for Pond Inlet and Eclipse Sound.....	143
5.2 Suggested future research	144
5.2.1 Triggering mechanisms	144
5.2.2 Nature of escarpment.....	145
5.2.3 Displacement wave risk at the Hamlet of Pond Inlet	146
5.3 References cited in Chapter 5	146

BIBLIOGRAPHY	148
APPENDICES	156
Appendix A: Core photography & x-radiographs	156
Appendix B: Thin sections	169
Appendix C: Physical properties	176
Appendix D: Grain size analysis	185
Appendix E: Synthetic seismograms	190
Appendix F: SPLASH analysis	191
Appendix G: Slope stability analysis	193
Appendix H: Age model results	207

LIST OF TABLES

Table 2.1: Characteristics of the major acoustic facies in Pond Inlet.	26
Table 2.2: Lithofacies characteristics for Pond Inlet, Baffin Bay.....	27
Table 3.1: Locations, water depth, and core length cores.....	47
Table 3.2: Information on radiocarbon dates	50
Table 3.3: Properties of lithofacies L1 to L6	59
Table 3.4: Sedimentation rates from cores in Pond Inlet Basin over the Holocene	60
Table 3.5: Sedimentation rates from cores in the Perched Basin over the Holocene.	60
Table 3.6: Examples and descriptions of acoustic facies.....	67
Table 4.1: Details on the piston cores and push cores taken from Pond Inlet.	103
Table 4.2: Details on the radiocarbon dates collected from piston cores.	104
Table 4.3: Information on the sites on Bylot Island used in the SPLASH calculations.	108
Table 4.4: Ages of the correlated turbidites penetrated by the piston cores.	114
Table 4.5: Turbidites correlated in Pond Inlet Basin in the sub-bottom profiler data	115
Table 4.6: MTDs correlated throughout Pond Inlet and Perched Basins	115
Table 4.7: Run-up heights at the Hamlet of Pond Inlet predicted by Equation 4.8	127
Table 4.8: Landslide volumes required to produce 10 and 60 m run-up heights.....	127

LIST OF FIGURES

Figure 1.1: Regional map showing Baffin Island, Greenland, and Baffin Bay	5
Figure 1.2: Thesis study area showing Eclipse Sound and Pond Inlet	6
Figure 2.1: A century of seismicity near Pond Inlet, Nunavut.	16
Figure 2.2: Data map of Pond Inlet.....	20
Figure 2.3: Interpretation of the submarine glacial landforms	24
Figure 2.4: Escarpment and slide scars shown in multibeam bathymetric data	25
Figure 2.5: Characteristics of acoustic facies	28
Figure 2.6: Lithofacies characteristics for Pond Inlet shown	29
Figure 2.7: Core logs showing lithofacies interpretations for piston cores	30
Figure 3.1: Regional map of northeastern Baffin Island, Bylot Island and Baffin Bay	43
Figure 3.2: Map of piston core locations and 3.5 kHz sub-bottom profiler lines	46
Figure 3.3: Synthetic seismogram for core 0067	49
Figure 3.4: Seafloor morphology map of Pond Inlet	52
Figure 3.5: Western region of Pond Inlet showing	54
Figure 3.6: Multibeam bathymetry of central Pond Inlet	55
Figure 3.7: Multibeam bathymetric map of the eastern region of Pond Inlet.....	56
Figure 3.8: Lithofacies photos, x-rays, and line drawings for the lithofacies.....	61
Figure 3.9: Thin section and line drawing from core 0065 and 0066.....	62
Figure 3.10: Stratigraphic columns of the five piston cores	63
Figure 3.11: Age models (Blaauw, 2010; version 2.2) for cores 0065, 0066 and 0067	64
Figure 3.12: Sub-bottom profiler lines showing the acoustic facies.....	68
Figure 3.13: Regional acoustic line	70

Figure 3.14: Sub-bottom profiler line for Pond Inlet Basin showing the acoustic facies	74
Figure 3.15: Piston core to sub-bottom profiler data tie	75
Figure 3.16: Depositional history of Pond Inlet Basin from LGM to present	84
Figure 3.17: Timeline of deglaciation of Pond Inlet.....	85
Figure 3.18: Physical properties measurements for cores 0067 and 0003	87
Figure 3.19: Examples of grain size plots from representative cores	88
Figure 4.1: Regional map of Baffin Bay showing earthquake locations and magnitudes	95
Figure 4.2: Regional physiography of the study region.....	97
Figure 4.3 Data map.....	105
Figure 4.4 Location of the seven sites used in the SPLASH calculations.	109
Figure 4.5: Mass wasting features at the seabed in Eclipse Sound.....	111
Figure 4.6: Escarpment observed at the seabed and in the sub-surface.....	112
Figure 4.7: Sub-bottom profiler lines showing the extents of turbidites and MTDs	116
Figure 4.8: Map showing extent of MTDs extrapolated from the sub-bottom profiler data.	117
Figure 4.9 Lithofacies interpretations for cores and correlations between turbidites.....	119
Figure 4.10: Piston core 0003 in sub-bottom and core data showing MTD-2.....	121
Figure 4.11: Piston core 0065 in sub-bottom and core data showing MTD-3.....	123
Figure 4.12: Slope stability analysis of core 0067	125
Figure 4.13 Map showing areas with a slope angle of $\geq 8.6^\circ$	126
Figure 4.14: Results of SPASH analysis showing run-up heights.....	128
Figure 4.15: Age models (Blaauw, 2010; version 2.2) for core 0066, 0067 and 0065.....	132

ABSTRACT

The fjords and inlets of Baffin Island contain a largely untapped postglacial sedimentary archive that records the timing and rates of important Arctic landscape, glacial, and geohazard responses to tectonic and climate change for more than ten thousand years. These are areas of high relief with the potential for submarine and subaerial slope failures. The majority of the population on Baffin Island lives along the coast of these fjords and inlets. Pond Inlet and Eclipse Sound make up a deglaciated seaway between Baffin and Bylot Islands, and the Hamlet of Pond Inlet (pop. 1,617) is located along the southern coast of Eclipse Sound. Interpreting the complex but valuable sedimentary records there will (1) improve our understanding of the timing and rate of deglaciation and sedimentation rates during postglacial warming in northeastern Baffin Island, and (2) will contribute to the geohazards assessment of northern Baffin Island. Recently acquired acoustic and core data provide the first opportunity to evaluate the depositional processes of this region in detail. High resolution multibeam bathymetric data and sub-bottom profiler data reveal depositional processes at a regional scale. Multiple cores penetrating the upper ten metres of sediment provide the first radiocarbon dates in Pond Inlet that establish rates and timing of key events, and sediment properties to assess slope stability and verify interpretations of the acoustic imagery.

Pond Inlet and Eclipse Sound archive depositional processes from the Last Glacial Maximum (LGM) to present. The multibeam bathymetry reveal the seabed is composed of glacial landforms deposited during the last glacial advance. The acoustic data resolve the upper ~65 m of sediment and reveal that it is composed of ice-contact till, glaciomarine, and postglacial sediments. The uppermost glacial till and overlying deposits are interpreted to be LGM and younger, and the moraine at the mouth of Pond Inlet is interpreted to represent a Younger Dryas re-advance, pinning the geometry and thickness of the Laurentide and regional glacier system at a time for which there is limited constraint. Radiocarbon dates reveal that postglacial sedimentation started after 10.7 ka BP. The postglacial record is vastly dominated by mass wasting events, including mass transport deposits (MTDs) and turbidites that interrupt hemipelagic sedimentation. Over the Late Pleistocene through mid-Holocene, there is a record of one mass wasting event every 1.6 ka, but the frequency increased to one event every 1.0 ka over the most recent 2.9 ka. The magnitudes and rates of mass wasting may be linked to permafrost thawing or the regional high seismic hazard. However, characteristics of the large MTDs and the bounding sediments suggest the MTDs are locally sourced and did not undergo significant transport. An assessment of submarine slope stability reveals that the postglacial sediments are stable under gravitational loading alone and sediments will require an external triggering mechanism to fail. A SPLASH model calculation showed that displacement waves large enough to affect infrastructure (>10 m run-up) at the Hamlet of Pond Inlet could be produced if a subaerial landslide entered the inlet from the southern mountain slopes of Bylot Island. This study addressed a dilemma regarding the position of the Laurentide Ice Sheet (LIS) during the Younger Dryas and reveals frequent slope failures have occurred over the Holocene. A displacement wave hazard does exist for the Hamlet of Pond Inlet, and a full risk analysis of the region is warranted.

LIST OF ABBREVIATIONS USED

ACD	Acoustically Chaotic Draping
ACW	Acoustically Chaotic Wedge
AI	Acoustic impedance
AMS	Accelerator mass spectrometry
ASL	Above sea level
BP	Before present – radiocarbon years before 1950 AD
BSL	Below sea level
Cal	Calibrated
CCGS	Canadian coast guard ship
CNGO	Canadian-Nunavut Geoscience Office
DEM	Digital Elevation Model
FS	Factor of safety
GRA	Gamma ray attenuation
GSC	Geological Survey of Canada
GSC-A	Geological Survey of Canada - Atlantic
IRD	Ice-rafted debris
LGM	Last Glacial Maximum
LIS	Laurentide Ice Sheet
LU	Lower Unit
MSCL	Multi-sensor core logger
MSGGL	Mega-scale glacial lineations
MTD	Mass transport deposit
OMG	Ocean Mapping Group
PC	Piston core
PGA	Peak ground acceleration
pXRF	portable X-ray fluorescence
ΔR	Reservoir correction

RC	Reflection coefficient
SRR	Strong Reflector Rough
SRS	Strong Reflector Smooth
TWC	Trigger weight core
TWT	Two way travel time
UU	Upper Unit
ULINNIQ	Underwater Listening Network for Novel Investigations of Quakes
WS	Well Stratified
XCT	X-ray computed tomography

GLOSSARY

- Cockburn end moraine system:** A system of end and lateral moraines, extending from near Frobisher, Baffin Island, to the west of the Penny Ice Cap, and roughly parallel to the fiord heads of the northeast coast to Bernier Bay (Andrew and Ives 1978).
- Cockburn substage:** A chronostratigraphic division of the Holocene Series based upon radiocarbon-dated sediments between 8000 and 9000 BP (Andrew and Ives 1978).
- Displacement wave:** waves generated by subaerial or submarine mass movements causing the sudden displacement of a large volume of water.
- Factor of Safety:** the ratio between the strength of the material and the maximum stress applied to the material.
- Global marine reservoir correction:** A correction of 400 years to account for the fact that radiocarbon ages of samples formed in the ocean appear several hundred years older than their terrestrial counterparts. The global average time it takes for present-day carbon dioxide in the atmosphere to be incorporated and distributed through the ocean water column.
- Mass transport deposit:** a deposit formed by submarine slope failure
- Last Glacial Maximum:** the most recent time during the last glaciation when ice sheets were at their greatest extent. The timing of the LGM varied locally.
- Local Reservoir Correction (ΔR):** The local difference from the average global marine reservoir correction is designated ΔR . This was determined in Baffin Bay by direct radiocarbon dating of pre-AD 1955 live-collected marine specimens of known historical age
- Radiocarbon age:** The uncalibrated apparent radiocarbon age of a sample. Radiocarbon ages are reported in terms of years 'before present' (BP) which refers to the year 1950.
- Run-up height:** the maximum vertical height onshore above sea level reached by a displacement wave.
- Turbidite:** a specific type of mass transport deposit that is transported and deposited by a turbidity current.
- Wisconsinan:** the most recent glacial period of the North American ice sheet complex.
- Younger Dryas:** A period of rapid cooling from 12.8-11.5 ka BP

ACKNOWLEDGEMENTS

I would like to thank my supervisors Calvin Campbell and John Gosse for their continued guidance and support throughout my MSc. I am thankful to my supervisor Calvin Campbell for all of his mentorship over the last few years. I would also like to thank Calvin for the opportunity to work as a casual employee at the GSC-A before my masters and for giving the chance to join the 2016 Hudson expeditions offshore Nova Scotia as a volunteer, which were both invaluable experiences. Equally, I would like to thank my other supervisor John Gosse for his guidance and thoughtful discussions over the course of my MSc. Throughout this experience John has helped me to continually to learn and grow as a scientist and has provided opportunities that pushed me out of my comfort zone. I would also like to thank both of my supervisors for the chance to present my research at national and international conferences throughout this process. I would also like to thank my committee members Lisel Currie and Stephanie Kienast for their thoughtful comments and discussions during our committee meetings and for the time they took to review my thesis.

I would like to thank the crew and staff onboard the CCGS Hudson and Amundsen who all helped with the collection of my MSc data. I thank many of the people at the GSC-A who have supported my thesis work. This includes Jenna Higgins, Makeala MacIntyre, and the co-op students who processed my core data, and Kate Jarrett who continually supported my many core sub-sampling requests. Also, Kimberley Jenner for her insights on interpreting marine sediment cores, and David Piper for running a directed studies course alongside Calvin Campbell, which provided a wealth of information on marine geology for me to complete this thesis. I thank Owen Brown for helping me collect grain size data and Alexandre Normandeau and Owen Brown for their help producing thin sections of my cores. I would also like thank Kevin MacKillop and his research assistant Danika Ouellette for teaching me about slope stability analysis.

Thank you to the Earth Science Department and the graduate students for their support and comradeship. The many morning coffee times with the graduate students were something I always looked forward too. Finally, I thank my friends and family. Without their unconditional love and support, I would not be where I am today.

CHAPTER 1: INTRODUCTION

1.1 General statement of problem

The basins of inlets and fjords are sediment sinks that can provide a high resolution sedimentary archive that records changes in depositional processes, environmental fluctuations, and geohazards (e.g. Syvitski et al. 1987; Syvitski 1989; Hjelstuen et al. 2009), yet relatively few fjords and inlets in the Canadian Arctic have been investigated in detail. Pond Inlet, Eclipse Sound and Navy Board Inlet comprise a deglaciaded seaway between Bylot and Baffin Islands in northeastern Canada (Figure 1.1; Figure 1.2). Little is known about the glacial and postglacial depositional processes and marine stratigraphy in this region, and the geohazards that could affect vulnerable communities such the Hamlet of Pond Inlet.

The northern Baffin Island region is in a strategic location to advance knowledge of glacial and postglacial processes. The region lies near the confluence of the former Laurentide and Innuitian Ice Sheets and their ice streams and numerous local alpine systems occupied the high relief mountains. Studies of the chronology of deglaciation of the region are relatively limited and are predominately based on terrestrial and shoreline records (Briner et al., 2007; Dyke, 2008; Dyke et al., 2001; Dyke and Hooper, 2001; McNeely and Atkinson, 1996). The marine record has been largely untapped owing to the cost of accessing and coring the typically sea-ice covered waters.

Mass wasting in fjord settings, whether submarine or subaerial, can lead to tsunamis (displacement waves) which are a significant hazard for coastal communities. All of the communities on Baffin Island and through the Arctic Archipelago are in coastal settings, mostly within 50 m of sea level. Mass wasting is common in steep-walled fjords and is often attributed to seismicity (e.g. Hampton et al. 1996; St-Onge et al. 2012; Bellwald et al. 2019) and

postglacial unloading, or permafrost thawing (e.g. Fischer et al., 2012, 2006; Hilger et al., 2018). Baffin Island and Baffin Bay are in a region of high seismicity with the potential for high magnitude earthquakes (1993 $M_s=7.3$) (Basham et al., 1977; Bent, 2002), however there is limited knowledge about the extent and frequency of mass wasting in the region and the seismic risk in the area. Thawing has been accelerating in recent decades in response to the amplified warming that occurs at high latitudes caused by global warming. Therefore, the region requires a thorough initial study of the evidence of postglacial mass wasting and submarine and subaerial slope stability to determine if there is a probability of seismically or climatically-triggered displacement waves in the vicinity of the Hamlet to cause concern.

In this study, recently collected geophysical and sediment core data enable the first investigation of the marine sedimentary record from Eclipse Sound and Pond Inlet (Figure 1.2). Utilizing multibeam bathymetric data, sub-bottom profiler data, and sediment cores, this study addresses a dilemma regarding the position of the LIS during the Younger Dryas, reveals a postglacial sedimentary record that is dominated by mass wasting, and shows a displacement wave hazard does exist for the Hamlet of Pond Inlet.

1.2 Objectives

The overall objective of this thesis is to analyse a sedimentary record in a high relief fjord with seismic activity in Arctic Canada to improve our understanding of marine geological hazards for northern Baffin Island. The short-term objectives of this thesis are to: (1) interpret the depositional record of Pond Inlet and Eclipse Sound, (2) determine the timing and rate of postglacial processes occurring in the seaway, (3) determine the source and extent of mass wasting deposits in the fjord, and (4) assess the potential displacement wave hazard for this region.

1.3 Hypotheses

This thesis aims to address two hypotheses:

Hypothesis 1 – The postglacial sedimentary succession in the deep basin in Pond Inlet is dominated by mass wasting deposits related to the region’s high seismicity. While deep basins in other Canadian fjords contain records of significant stream floods (St.-Onge et al., 2004) the proximity of Pond Inlet to the high seismicity in northern Baffin Bay and climatogenic changes related to glacial unloading of the fjord walls and thawing of permafrost provide three triggering mechanisms for submarine and coastal subaerial mass transport.

Hypothesis 2—There is a significant probability of displacement wave hazard to the Hamlet of Pond Inlet. The combination of the high relief of the seaway, steep fjord wall slopes, offshore seismic activity, and potential for thick and mobile submarine sediments provide multiple conditions and triggering mechanisms for displacement waves.

1.4 Motivation and impact

Slope failures in fjord and inlet systems in seismically active regions are commonly attributed to earthquakes. However, in Arctic regions, two other factors can trigger slope failures. Steep fjord walls experience unloading (relaxation) during and just after deglaciation, which may result in failure (Fischer et al., 2006). The accelerated rate of permafrost thawing has provided lubrication and changes in mass distribution that may contribute to a reduced effective shear strength, and refreezing of water in fractures can contribute a wedging effect (Fischer et al., 2006; Hilger et al., 2018). Regardless of their triggering mechanism, submarine and subaerial mass wasting along the coast have the potential to generate displacement waves (tsunamis that are caused by displacement of water by mass movements, not rapid sea-floor changes) that can impact coastal

communities (e.g. Bessette-Kirton et al., 2017; Fine et al., 2005; Hermanns et al., 2013). The communities of Baffin Island are located within tens of metres of the coast in regions of high relief (Figure 1.1), and displacement waves from submarine or subaerial slope failures could have devastating impacts on these population centres. In June of 2017, a subaerial landslide in Greenland, on the eastern side of Baffin Bay, triggered a displacement wave that resulted in four deaths and the loss of 11 homes in the nearby coastal community of Nuugaatsiaq (Bessette-Kirton et al., 2017). The potential landslide hazard for Baffin Island communities on the other side of Baffin Bay is unknown.

Fjord marine sedimentary records offer the potential to provide a robust archive of changes in depositional processes related to climate and tectonics. This thesis will establish (1) the first chronologies to determine the frequency of slope failures in northern Baffin Bay. These chronologies form the basis of the first displacement wave hazard assessment for Arctic Canada. In addition, they will improve our estimates on the timing of deglaciation of northeastern Baffin Island and the frequency of postglacial mass wasting in the fjord. (2) An assessment of the probability of displacement waves in Pond Inlet from sub-aerial slope failure will also be provided. While the source of displacement waves can also originate outside of fjords and inlets, this thesis will focus on the potential for displacement waves triggered within Pond Inlet and Eclipse Sound. This thesis contributes directly to the ongoing research goals of the Arctic ULINNIQ project (Underwater Listening Network for Novel Investigations of Quakes) at Dalhousie University in collaboration with McGill University (Canada), GSC-Atlantic (Canada), NGU (Norway), Uppsala University (Sweden), and C-NGO (Canada). This project aims to conduct a hazard assessment of coastal NE Baffin Island and the offshore region by determining

the location, magnitude, frequency, and cause of submarine earthquakes and submarine or coastal landslides.

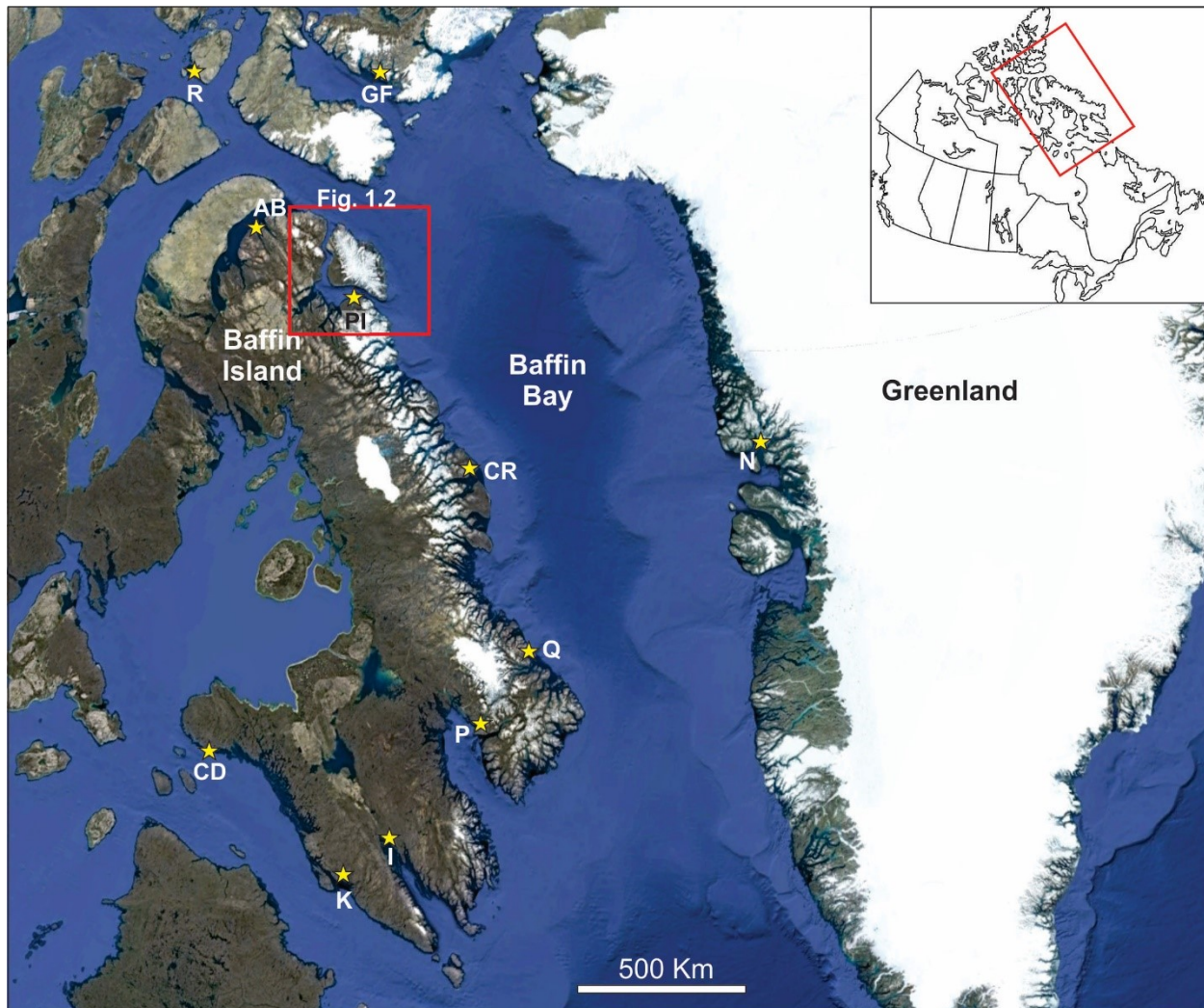


Figure 1.1: Regional map showing Baffin Island, Greenland, and Baffin Bay, and location of Figure 1.2. Stars denote communities. R = Resolute, GF = Grise Fiord, AB = Arctic Bay, PI = Pond Inlet, CR = Clyde River, Q = Qikiqtarjuaq, P = Pangnirtung, I = Iqaluit, K = Kimmirut, CD = Cape Dorset, N = Nuugaatsiaq.

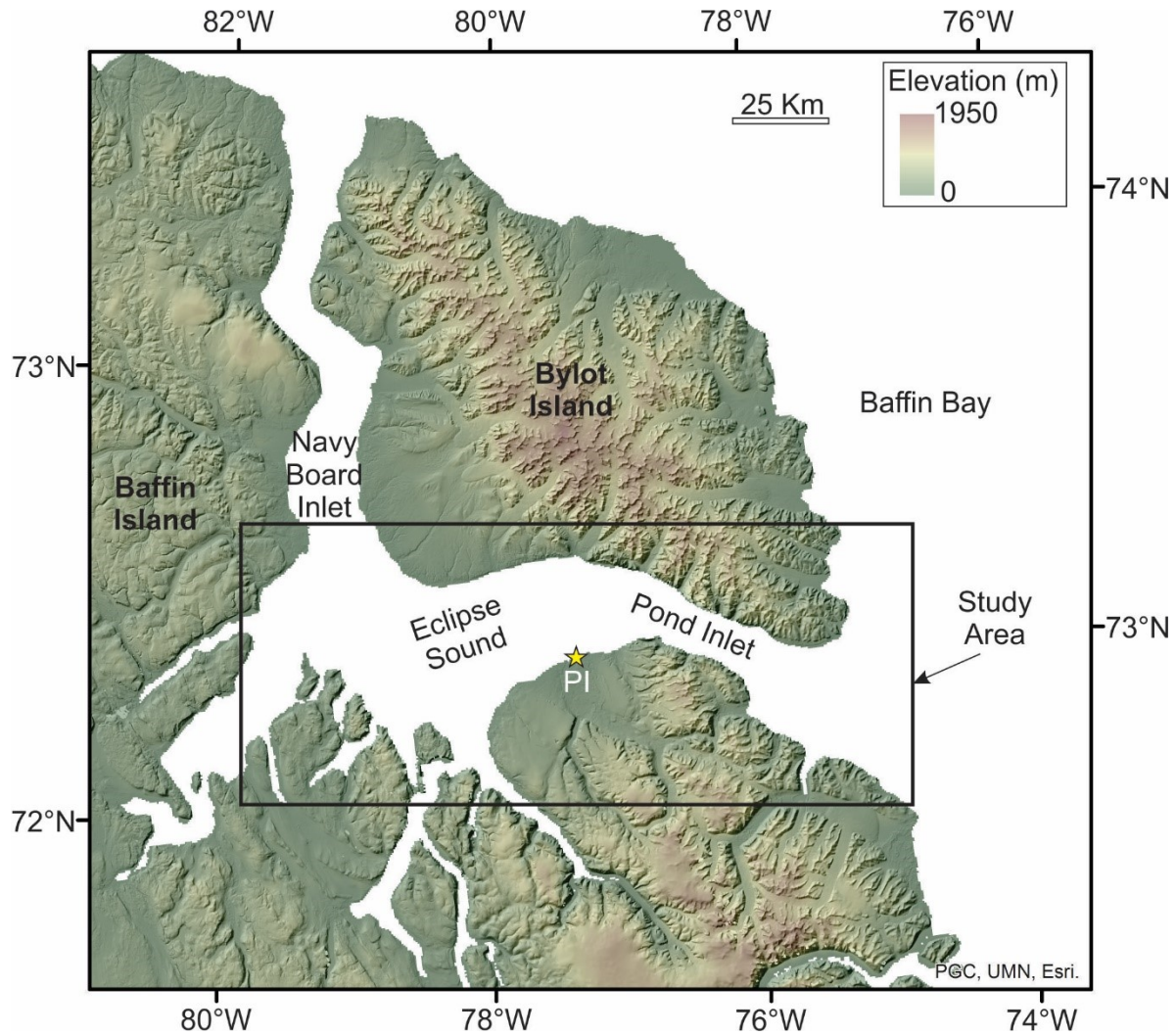


Figure 1.2: Thesis study area showing Eclipse Sound and Pond Inlet surrounded by Baffin and Bylot Islands. PI = Hamlet of Pond Inlet.

1.5 Organization of thesis

The first chapter of this thesis aims to introduce the research hypotheses and objectives, and the motivation of the research. This is followed by three manuscripts (Chapter 2-4) which address the research objectives. Chapter 5 summarizes the main conclusions derived from the thesis, their significance and suggestions for future work. Each chapter includes individual reference lists with a master bibliography included at the end of the thesis.

1.5.1 Chapter 2 – Manuscript 1

Title: Investigation of a Holocene marine sedimentary record from Pond Inlet, northern Baffin Island, Nunavut

Authors: L.M. Broom, D.C. Campbell and J.C. Gosse

Status: Published in the Canadian-Nunavut Geoscience Office Summary of Activities, 2017, pages 93-104.

Summary

Chapter 2 is a version of the article published in the Canadian-Nunavut Geoscience Office Summary of Activities in 2017, which summarizes preliminary research results. The purpose of this chapter is to summarize the initial interpretations of mass wasting in Pond Inlet and Eclipse Sound by presenting initial results from the acoustic and core data. The manuscript utilizes multibeam bathymetric data to identify landforms at the seabed and the high-resolution sub-bottom profiler data to determine initial interpretations of the acoustic facies. In addition, core data are used to determine lithofacies and the first radiocarbon dates are presented. The results show that the seafloor of Pond Inlet and Eclipse Sound is composed of glacial landforms, few slide scars, and a linear escarpment. Two acoustic facies are recognized including acoustically chaotic-to reflection-free facies interpreted to represent MTDs and an acoustically stratified facies representing hemipelagic deposition interrupted by turbidites. Six lithofacies are presented (L1-L6) representing hemipelagic and mass wasting deposits, and the first radiocarbon date from a sediment core in the centre of Pond Inlet is shown. Three major MTDs and recognized in the sub-bottom profiler data separated by five turbidite deposits, and turbidites are recognized as the most abundant gravity driven flow in the basin.

Contributions of Authors

Chapter 2 was led by Laura Broom (LB), who wrote the initial version of the chapter with major revisions and contributions to the writing by John Gosse (JG) and Calvin Campbell (CC). The interpretation of the seafloor morphology was completed by LB. The sub-bottom profiler data was interpreted by LB with guidance from CC on the interpretation of acoustic facies. The core data were interpreted by LB and the location of radiocarbon dates were selected by LB and discussed with CC. Calibration of radiocarbon dates was completed by LB under the guidance of JG. The production of the majority of the figures and tables were constructed by LB, with the exception of Figure 2.1, which was drafted by JG. The manuscript was reviewed and edited by CC and JG before submission.

1.5.2 Chapter 3 – Manuscript 2

Title: Deglacial to postglacial submarine depositional history of Eclipse Sound and Pond Inlet, Nunavut, Canada

Authors: L.M. Broom, D.C. Campbell and J.C. Gosse

Status: Ready for submission

Summary

Chapter 3 summarizes the description, interpretation and chronology of the marine sedimentary record in Eclipse Sound and Pond Inlet. The multibeam bathymetric data are used to interpret the seafloor morphology, with a focus on glacial landforms formed during the last glacial advance and retreat. The sub-bottom profiler data are used to interpret the depositional record below the subsurface including the description and interpretation of five acoustic facies representing ice-contact till and glaciomarine and postglacial deposits. The core data are used to describe and interpret six lithofacies in the study area representing hemipelagic sedimentation with or without IRD interrupted by MTDs and turbidites. Radiocarbon dates and an age model are used to

estimate the timing of various depositional processes within the study area. The paper shows that the sediments preserve a record from the last glacial advance to modern conditions. The moraine at the entrance of Pond Inlet is shown to be likely of Younger Dryas age. The end of IRD deposition at 9.8 ka BP has suggested that the ice sheet was west of central Pond Inlet by this time. The deposition of the first postglacial turbidite is shown to occur prior to 10.7 ka BP. Deposition during the Holocene was dominated by hemipelagic sedimentation, which was frequently interrupted by mass wasting.

Contributions of Authors

The initial concept for Chapter 3 was conceived as a collaboration between CC, JG and LB. The writing of this chapter was led by LB with the guidance of JG and CC. The description and interpretation of the multibeam bathymetric data was completed by LB, and the description and interpretation of the sub-bottom profiler data was completed by LB under the guidance of CC. LB conducted the lithofacies descriptions and interpretations, and radiocarbon dates were selected by LB with discussion with CC. Radiocarbon date calibrations and the age model were completed by LB under the guidance of JG. Synthetic seismograms were made by LB with the help of CC. Grain size analysis and thin section production were completed by LB with help from GSC staff. The figures and tables were produced by LB and incorporated edits from JG and CC. The paper was reviewed and edited by CC and JG who also made final contributions to the writing.

1.5.3 Chapter 4 – Manuscript 3

Title: Geohazards of Pond Inlet & Eclipse Sound, Baffin Bay: observations on submarine slope failures and potential hazard assessment

Authors: Laura M. Broom, D. Calvin Campbell and John C. Gosse

Status: Under review by co-authors

Summary

Chapter 4 summarizes the description and interpretation of mass wasting in Pond Inlet and Eclipse Sound and the potential for displacement waves generating by subaerial landslides affecting the Hamlet of Pond Inlet. The study uses the multibeam bathymetric data to recognize mass wasting at the seabed, and sub-bottom profiler and core data are used to recognize mass wasting in the sub-surface. An assessment of slope stability is completed for core 0067 to consider the stability of sediments under modern conditions. Radiocarbon dates are used to determine the timing and frequency of mass movement deposits preserved in Pond Inlet and Eclipse Sound. In addition, the empirically derived equation is used to determine if a subaerial landslide occurring on the steep mountain faces on Bylot Island could generate a displacement wave with a run-up height high enough to reach infrastructure at the Hamlet of Pond Inlet. The results show that there is a record of basin wide instability from the late Pleistocene to present. One mass wasting event has been recorded every 1.6 ka, and the frequency has increased to one event every 1.0 ka over the last 3 ka. Sedimentation rates from the age model along with sedimentary features in MTDs in cores show that some of the MTDs have likely undergone little transport and were likely mobilized in place. The slope is stable under current conditions and likely requires an external triggering mechanism to fail. It is also shown that a subaerial landslide along the coast of Bylot Island could generate a displacement wave run-up high enough to affect infrastructure at the Hamlet of Pond Inlet.

Contributions of Authors

The concept for Chapter 4 was conceived as a collaboration between the three authors. The writing was led by LB under the guidance of JG and CC. The extents of MTDs and turbidites were mapped by LB and the volumes of MTDs were computed by LB with help from CC.

Interpretations of the MTDs in core and sub-bottom profiler data were completed by LB. The age model was completed by LB with guidance from JG. The idea for conducting slope stability analysis was initiated by CC and completed by LB with support from JG and discussions with GSC staff. The idea for the displacement wave analysis was introduced by JG and was complete by LB under JG's guidance and support. All figures and tables were drafted by LB and incorporated edits from CC and JG. The paper was edited and reviewed by CC and JG who also made final contributions to the writing.

1.6 References cited in Chapter 1

- Basham, P.W., Forsyth, D.A., Wetmiller, R.J., 1977. The seismicity of northern Canada 14, 1646–1667. <https://doi.org/10.1139/e77-140>
- Bellwald, B., Hjelstuen, B.O., Sejrup, H.P., Stokowy, T., Kuvås, J., 2019. Holocene mass movements in west and mid-Norwegian fjords and lakes. *Mar. Geol.* 407, 192–212. <https://doi.org/10.1016/j.margeo.2018.11.007>
- Bent, A.L., 2002. The 1933 Ms= 7.3 Baffin Bay earthquake: strike-slip faulting along the northeastern Canadian passive margin. *Geophys. J. Int.* 150, 724–736.
- Bessette-Kirton, E., Allstadt, K., Pursley, J., Godt, J., 2017. Preliminary Analysis of Satellite Imagery and Seismic Observations of the Nuugaatsiaq Landslide and Tsunami, Greenland [WWW Document]. URL https://www.usgs.gov/natural-hazards/landslide-hazards/science/preliminary-analysis-satellite-imagery-and-seismic?qt-science_center_objects=0#qt-science_center_objects
- Briner, J.P., Overeem, I., Miller, G.H., Finkel, R., 2007. The deglaciation of Clyde Inlet, northeastern Baffin Island, Arctic Canada. *J. Quat. Sci.* 22, 223–232.
- Dyke, A.S., 2008. The Steensby Inlet Ice Stream in the context of the deglaciation of Northern Baffin Island, Eastern Arctic Canada. *Earth Surf. Process. Landforms J. Br. Geomorphol. Res. Gr.* 33, 573–592.
- Dyke, A.S., Clark, J.T.A.P.U., England, J.H., 2001. Geological Survey of Canada Open File 4120 Radiocarbon Dates pertinent to defining the last glacial maximum for the Laurentide and Innuitian ice sheets.
- Dyke, A.S., Hooper, J.M.G., 2001. Deglaciation of Northwest Baffin Island, Nunavut.

- Fine, I. V., Rabinovich, A.B., Bornhold, B.D., Thomson, R.E., Kulikov, E.A., 2005. The Grand Banks landslide-generated tsunami of November 18, 1929: Preliminary analysis and numerical modeling. *Mar. Geol.* 215, 45–57. <https://doi.org/10.1016/j.margeo.2004.11.007>
- Fischer, L., Käab, A., Huggel, C., Noetzli, J., 2006. Geology, glacier retreat and permafrost degradation as controlling factors of slope instabilities in a high-mountain rock wall: The Monte Rosa east face. *Nat. Hazards Earth Syst. Sci.* 6, 761–772. <https://doi.org/10.5194/nhess-6-761-2006>
- Fischer, L., Purves, R.S., Huggel, C., Noetzli, J., Haeberli, W., 2012. On the influence of topographic, geological and cryospheric factors on rock avalanches and rockfalls in high-mountain areas. *Nat. Hazards Earth Syst. Sci.* 12, 241–254. <https://doi.org/10.5194/nhess-12-241-2012>
- Hampton, M.A., Lee, H.J., Locat, J., 1996. Submarine landslides. *Rev. Geophys.* 34, 33–59.
- Hermanns, R.L., L'Heureux, J.S., Blikra, L.H., 2013. Landslide triggered tsunami, displacement wave, in: *Encyclopedia of Natural Hazards*. Springer, Dordrecht, pp. 611–615. <https://doi.org/10.1007/978-1-4020-4399-4>
- Hilger, P., Hermanns, R.L., Gosse, J.C., Jacobs, B., Etzelmüller, B., Krautblatter, M., 2018. Multiple rock-slope failures from Mannen in Romsdal Valley, western Norway, revealed from Quaternary geological mapping and ¹⁰Be exposure dating. <https://doi.org/10.1177/0959683618798165>
- Hjelstuen, B.O., Haflidason, H., Sejrup, H.P., Lyså, A., 2009. Sedimentary processes and depositional environments in glaciated fjord systems - Evidence from Nordfjord, Norway. *Mar. Geol.* 258, 88–99. <https://doi.org/10.1016/j.margeo.2008.11.010>
- McNeely, R., Atkinson, D.E., 1996. Geological Survey of Canada Radiocarbon dates XXXII, Geological Survey of Canada Paper 83-1A. <https://doi.org/10.1126/science.ns-6.149S.521-a>
- St-Onge, G., Chapron, E., Mulsow, S., Salas, M., Viel, M., Debret, M., Foucher, A., Mulder, T., Winiarski, T., Desmet, M., Costa, P.J.M., Ghaleb, B., Jaouen, A., Locat, J., 2012. Comparison of earthquake-triggered turbidites from the Saguenay (Eastern Canada) and Reloncavi (Chilean margin) Fjords: Implications for paleoseismicity and sedimentology. *Sediment. Geol.* 243–244, 89–107. <https://doi.org/10.1016/j.sedgeo.2011.11.003>
- St-Onge, G., Mulder, T., Piper, D.J.W., Hillaire-Marcel, C., Stoner, J.S., 2004. Earthquake and flood-induced turbidites in the Saguenay Fjord (Québec): A Holocene paleoseismicity record. *Quat. Sci. Rev.* 23, 283–294. <https://doi.org/10.1016/j.quascirev.2003.03.001>
- Syvitski, J.P.M., 1989. Glacier-Influenced Fjords: Oceanographic Controls. *Mar. Geol.* 85, 301–329.

Syvitski, J.P.M., Burrell, D.C., Skei, J.M., 1987. Subaqueous Slope Failure, in: Fjords. Springer, New York.

CHAPTER 2: INVESTIGATION OF A HOLOCENE MARINE SEDIMENTARY RECORD FROM POND INLET, NORTHERN BAFFIN ISLAND, NUNAVUT

Authors: L.M. Broom, D.C. Campbell and J.C. Gosse

Status: Published in the Canadian-Nunavut Geoscience Office Summary of Activities, 2017, pages 93-104.

Abstract

Newly acquired sediment cores and geophysical data from Pond Inlet, a fiord in northern Baffin Bay, provide the first opportunity for a thorough investigation of the Holocene sedimentary record in this region. Northern Baffin Bay is in a zone of high seismic hazard and earthquakes in this area have the potential to trigger slope failures. It is not known if the fiord preserves a record of seismogenic mass wasting and a detailed analysis of the marine sedimentary record is necessary to begin to investigate this issue. This study uses high-resolution multibeam bathymetric data, 3.5 kilohertz sub-bottom profiler data and piston cores to assess the sedimentary record in Pond Inlet. This is being accomplished through seabed mapping, analysis of cores, shallow lithological and acoustic stratigraphy, and geochronology.

Preliminary results indicate a record of gravity-driven sedimentary events in the fiord, including mass transport deposits (MTDs) and turbidites. Sub-bottom profiler data reveal acoustically chaotic to transparent reflection-free facies interpreted as MTDs, as well as continuous high-amplitude reflections interpreted as turbidites; both the MTDs and turbidites are correlatable over a large area. The piston cores show evidence of MTDs, including deformed mud and mudclast conglomerate deposits up to 5 m thick, as well as centimetre-thick sandy-silty turbidites. A radiocarbon date indicates that over the last 3 ka, a minimum of four turbidite deposits have reached the centre of Pond Inlet and work is ongoing to establish if these deposits were the result

of seismic activity. This research will contribute to an improved understanding of geohazards in the northern Baffin region.

2.1 Introduction

Northeastern Baffin Island is close to one of Canada's high risk, active, seismic zones. The seismic activity is related to tectonics in Baffin Bay and upper mantle adjustments associated with ongoing deglaciation (Figure 2.1; Stein et al. 1979). Several studies have demonstrated that marine sediments in fiords can preserve detailed records of climatic and geological hazards because of typically very high sedimentation rates (St-Onge et al., 2012). Until now, the marine sediments in Pond Inlet, Baffin Island, have not been evaluated in detail for their Holocene depositional record, including seismic mass wasting. Due to the lack of paleoseismology studies in northeastern Baffin Island, the potential for Holocene marine sediments to hold useful information for assessing paleoseismic frequency or magnitude is unknown. Over the next decade, there are plans to identify, correlate and date regionally extensive thick deposits of deformed marine sediments (mass transport deposits [MTDs]) in numerous fiords on the coast of Baffin Island. A MTD can be identified as an acoustically chaotic seismic facies that is associated with, and commonly overlain by turbidites (Posamentier and Kolla, 2003). In core, MTDs are recognized as folded mud, stratified mud exhibiting tilted beds, mudclast conglomerate and diamicton (Jenner et al., 2007). Using the results of the ongoing mapping and dating distribution of large MTDs around eastern Baffin Island, the long-term objective is to determine if spatial and temporal patterns of intraplate non-tectonic shaking can be predicted by considering the mantle stress fields related to regional deglaciation, a significant concern for countries that are experiencing rapid deglaciation. To do this, it is necessary to establish the magnitude, location and frequency of previous large earthquakes that possibly have variable

recurrence intervals of centuries or longer and are not likely to have been recorded by instruments. This report will outline the preliminary results of the ongoing proof-of-concept analysis of the postglacial stratigraphy in Pond Inlet, Baffin Island.

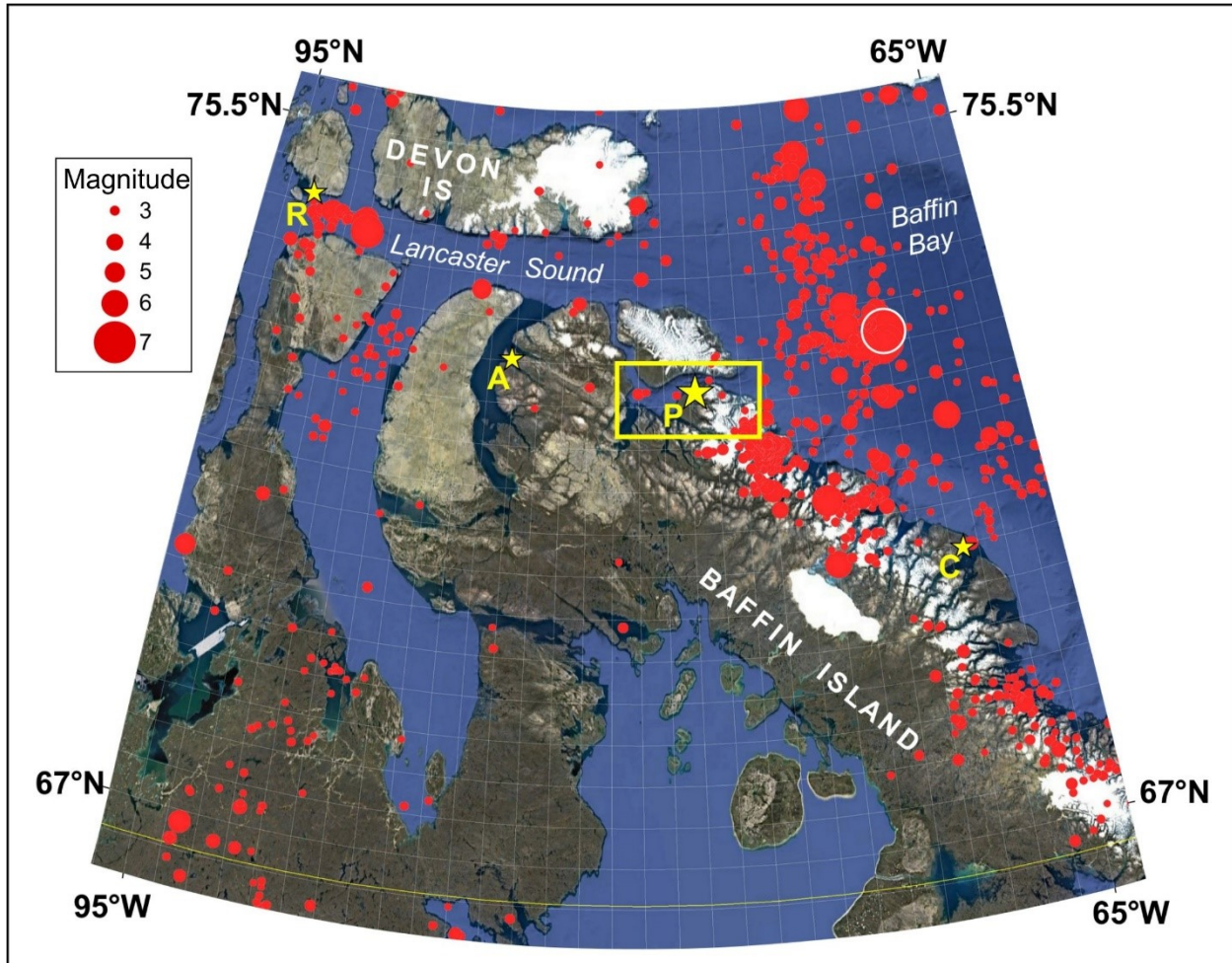


Figure 2.1: A century of seismicity near Pond Inlet, Nunavut. Data for the mapped area are ISC-Catalog Bulletin events with known magnitude ($M \geq 3$) and known depth, from October 1, 1917 to October 1, 2017 (Di Giacomo et al., 2014; International Seismological Centre, 2017). White circle shows the location of the 1933 surface-wave magnitude 7.3 earthquake. Stars are communities near seismically active regions: A, Arctic Bay; C, Clyde River; P, Pond Inlet; R, Resolute. Study area is outlined in yellow. Base map is from imagery ©2017 IBCAO, Landsat/Copernicus, U.S. Geological Survey; data SIO, NOAA, U.S. Navy, NGS, GEBCO; map data ©2017 Google. Google Earth (2017).

In 2013, the Geological Survey of Canada (GSC) conducted a scientific expedition to Baffin Bay aboard the Canadian Coast Guard Ship (CCGS) Hudson, affording the opportunity to collect 3.5 kilohertz (kHz) sub-bottom profiler data and piston cores from the seabed (Figure 2.2b;

Campbell, 2014). This data acquisition was guided by multibeam bathymetry previously collected in the region by ArcticNet, a Network of Centres of Excellence of Canada, aboard the CCGS Amundsen (OMG, 2005-2008). The Pond Inlet phase of this expedition revealed thick basal sediment packages. Subsequent to the 2013 expedition, additional piston cores in Pond Inlet were collected in 2015 on the CCGS Amundsen (Figure 2.2b).

The newly available sediment cores and geophysical data enable the first detailed analysis of the Holocene sedimentary record in Pond Inlet. The purpose of this study is to determine the extents of MTDs, turbidite, glaciomarine, and hemipelagic sediment deposits in the inlet, the timing of their deposition and what factors triggered their deposition, such as the high seismicity in the region. The first objective of this research is to characterize the MTDs and turbidite deposits within Pond Inlet, obtain radiocarbon dates to constrain their timing, and correlate these deposits throughout the inlet. This will lead to determining if these MTDs and turbidites can be indicative of significant Holocene ground-shaking events.

2.2 Background

2.2.1 Setting and physiography

The physiography of Baffin Bay is related to the tectonic, fluvial and glacial history of the region. Baffin Bay is a rifted basin that separates Baffin Island from Greenland, seafloor spreading and transform shearing from the Cretaceous to the Oligocene (MacLean et al., 1990). Pond Inlet is a fiord located in northeastern Baffin Bay and separates Baffin Island from Bylot Island to the north (Figure 2.2a). The surrounding mountain ranges on Bylot Island and Baffin Island are approximately 1900 m high and bathymetry indicates that the fiord exceeds 1000 m in depth to create a combined local relief of approximately 2900 m. The fiord is fed by active alpine glaciers and second-order streams from northeastern Baffin Island. The fiord walls appear to be

mostly barren of sediment owing to their steepness and the erosive nature of the Pond Inlet ice stream. The rectangular nature of the fiord and tributary valleys is partly a result of pre-rift– and rift–related structures in the dominantly Proterozoic crust exposed there. Faults associated with mid-Paleozoic arching and Mesozoic and early Cenozoic rifting may provide planes of weakness for subsequent faulting (L. Currie, pers. comm., 2016). On land, Eocene and potentially Pliocene sediments have been mapped, however, no evidence of Cenozoic offsets has been observed (Jackson and Davidson, 1975a; Jackson and Davidson, 1975b).

2.2.2 Glacial history

Relative to other regions of Baffin Island, the glacial history of Pond Inlet and Tasiujaq (formerly Eclipse Sound) and Pond Inlet are not well studied. There has been no report of pre-Wisconsinan stratigraphy on land. Owing to the polythermal nature of the regional ice (Hilchey, 2004; Willenbring Staiger et al., 2006) much of the region was covered by glaciers with limited capacity for erosion of the interfiord summits. During the early Holocene, the entire fiord of Pond Inlet was occupied by erosive wet-based ice (Dyke, 2004) and possibly an ice stream. Recent reconstructions utilizing marine geophysical data to determine the extent of the Laurentide Ice Sheet (LIS) during marine isotope stage 2 suggest that in western Baffin Bay, a fast-flowing ice stream occupied Pond Inlet and that the ice sheet extended to the edge of the continental shelf (Brouard and Lajeunesse, 2017). Since deglaciation, the fjord is surrounded by onshore cirque and valley glaciers on Bylot and Baffin islands.

2.2.3 Regional seismicity of Baffin Bay

Baffin Bay is one of the most seismically active regions in Canada and has experienced the largest instrumentally recorded earthquake north of the Arctic Circle (surface-wave magnitude of 7.3) in 1933 (northern Baffin Bay; Figure 1; Bent, 2002). Currently, seismicity along the Atlantic

margin is highest near Baffin Island and generally decreases southward (Stein et al., 1979). Despite the poor precision in determining the position and depth of the earthquake foci, many appear to be associated with thrust and strike-slip faults (Bent, 2002; Stein et al., 1979). However, it has been proposed that the high frequency and high magnitude seismicity in the region is related to the reactivation of faults by upper mantle dynamics related to the ongoing deglaciation (Stein et al., 1979). Alternatively, the relatively high intrafault seismicity in this region could be a result of recent active tectonic stresses between northern Baffin Island and Greenland; however, the earthquake foci positions are poorly resolved. There is a lack of paleoseismology studies in Canada's eastern Arctic, including Baffin Bay. The instrumental earthquake record from the Canadian National Seismograph Network was limited until its expansion in the 1960s. Until the expansion of seismograph stations into the Canadian Arctic, only large magnitude earthquakes could be recorded.

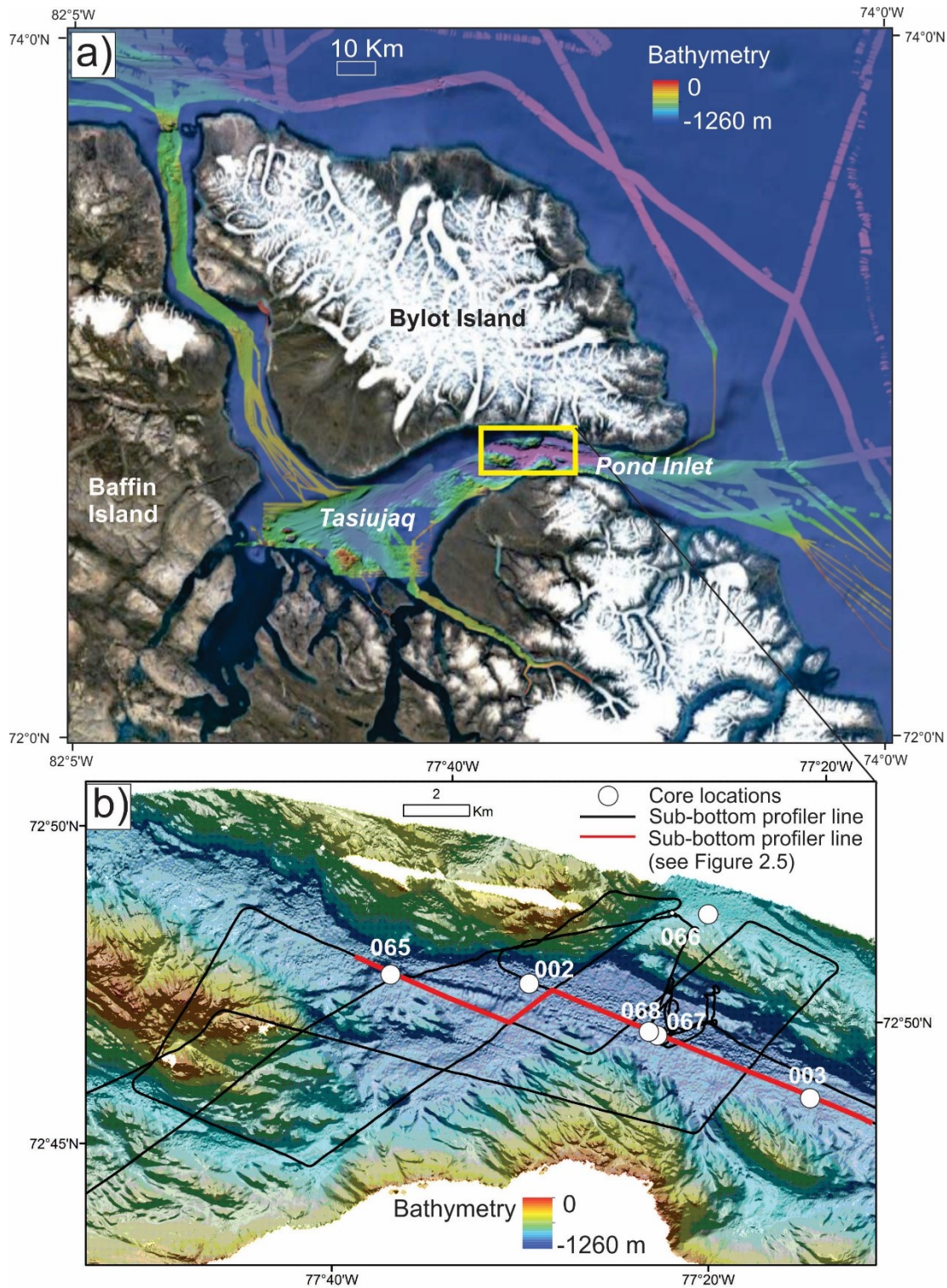


Figure 2.2: a) Pond Inlet, showing the multibeam bathymetric data of Pond Inlet and the area where the piston cores were collected is shown as a yellow polygon. Multibeam bathymetry collected by OMG as part of ArcticNet (2005-2008) and DEM(s) created by the Polar Geospatial Center from DigitalGlobe, Inc. imagery ©2017 IBCAO, Landsat/Copernicus, U.S. Geological Survey; data SIO, NOAA, U.S. Navy, NGS, GEBCO; map data ©2017 Google. b) Multibeam bathymetric data across the area where piston cores were collected with core locations and sub-bottom profiler lines.

2.3 Methods

2.3.1 *Hydroacoustic analysis*

High-resolution multibeam bathymetric data were collected using a Kongsberg Maritime EM 302 multibeam echosounder onboard the CCGS Amundsen. Multibeam bathymetry was utilized to identify landforms at the seabed including possible sediment sources, faults and evidence of unstable seabed (Figure 2.2a). The 3.5 kHz sub-bottom profiler (Knudsen Engineering Ltd. model 326006) data were collected in 2013 by the GSC Atlantic (GSC-A) on the CCGS Hudson and processed at the GSC-A facility (Figure 2.2b). Seismic facies were defined based on the amplitude, continuity and internal configuration of reflectors as described by Sangree and Widmier (1979) and major surfaces were defined by correlating continuous high-amplitude reflectors throughout the fiord.

2.3.2 *Core analysis*

Four piston cores were collected from Pond Inlet during the Hudson and Amundsen expeditions in 2013 and 2015 (Figure 2.2b). Piston core 065 (lat. 72.814891 °N, long. 77.676665°W) is 810 cm long and was collected at the base of an escarpment. Core 067 (lat. 72.815566°N, long. 77.426285°W) has a length of 1063 cm and was targeted to retrieve a high-resolution section of the sedimentary record. Core 002 (lat. 72.822°N, long. 77.553°W) is 299 cm long and targeted a condensed section of sediments. Core 003 (lat. 72.809333°N, long. 77.278166°W) has a total length of 520 cm and targeted a MTD close to the seabed.

Cores were split, photographed and X-radiographed using a Universal HE425 X-ray system at the GSC-A facility. Physical properties were measured along the cores using a Geotek Ltd. multi-sensor core logger (MSCL). Whole core sections were measured for compressional (p-wave) velocity, bulk density and magnetic susceptibility at 1 cm intervals. The split core sections

were then measured for magnetic susceptibility and colour at 1 cm intervals. Discrete measurements of shear strength (using a shear vane apparatus) and velocity (using transducer probes) were taken every 10 cm along the split core. Grain size was analyzed along core 067 using a Beckman Coulter LS 230 laser diffraction particle size analyzer. Grain size was measured every 20 cm within mud and every few centimetres within laminated sand.

2.3.3 Geochronology

The main purpose of determining the chronology of events is to guide correlations, particularly of deposits related to mass wasting, which are important for understanding the history of seabed stability and paleoseismology of Pond Inlet. A radiocarbon date was obtained from a fragmented benthic colus shell within core 067 at approximately 589–591 cm depth (dragged 2 cm when split) within hemipelagic mud. Sampling was completed at the GSC-A facility, and the shell was dated by accelerator mass spectrometry (AMS) at the Keck-Carbon Cycle Accelerator Mass Spectrometry Facility at the University of California (Irvine, California). The radiocarbon age was calibrated with Calib 7.1 using the Marine13 calibration curve (Stuiver et al., 2017). A marine reservoir correction of 220 years (Coulthard et al., 2010) was applied to account for regional air–sea reservoir difference in the benthic sample. Several additional radiocarbon analyses are underway.

2.4 Results

2.4.1 Preliminary results from the hydroacoustic analysis

Seabed geomorphology

The high-resolution multibeam bathymetric data show a seafloor composed of submarine glacial landforms, flat basinal floors and bedrock with varying amounts of sediment drape (Figure 2.3). The submarine glacial landforms include mega-scale glacial lineations, iceberg scours, drumlins,

crag-and-tail features and moraines (Figure 2.3). The cores and sub-bottom profiler data were collected in the middle of the fjord in an area with a relatively flat bottom surrounded by sediment-draped bedrock highs and steep fjord sides. The seafloor in this portion of the inlet reaches depths of approximately 1080 m and the bedrock highs can reach up to 900 m from the basin floor. The multibeam bathymetric data reveal no evidence of slide scars in the area surrounding the core sampling sites, though slide scars are observed along the north slope of the western part of the fjord (Figure 2.4b) and range in area from 2.9 to 13.3 km². A prominent escarpment is recognized adjacent to core 065 (Figure 2.4a). This escarpment appears to continue into the adjacent bedrock highs, though this is not imaged by the acoustic data owing to the steepness of the bedrock slopes. The escarpment has a vertical relief of approximately 20 m in sub-bottom profiler data and can be traced in the multibeam bathymetric data for a minimum of 3.5 km within the basinal sediments. It is not immediately obvious whether the escarpment is a fault scarp that cuts postglacial basinal sediments, an eroded fault-line scarp (associated with early Cenozoic or older faults mapped onshore (Currie et al., 2012)) that is draped by postglacial sediments, or simply a plucked or otherwise subglacially eroded wall not directly related to faulting.

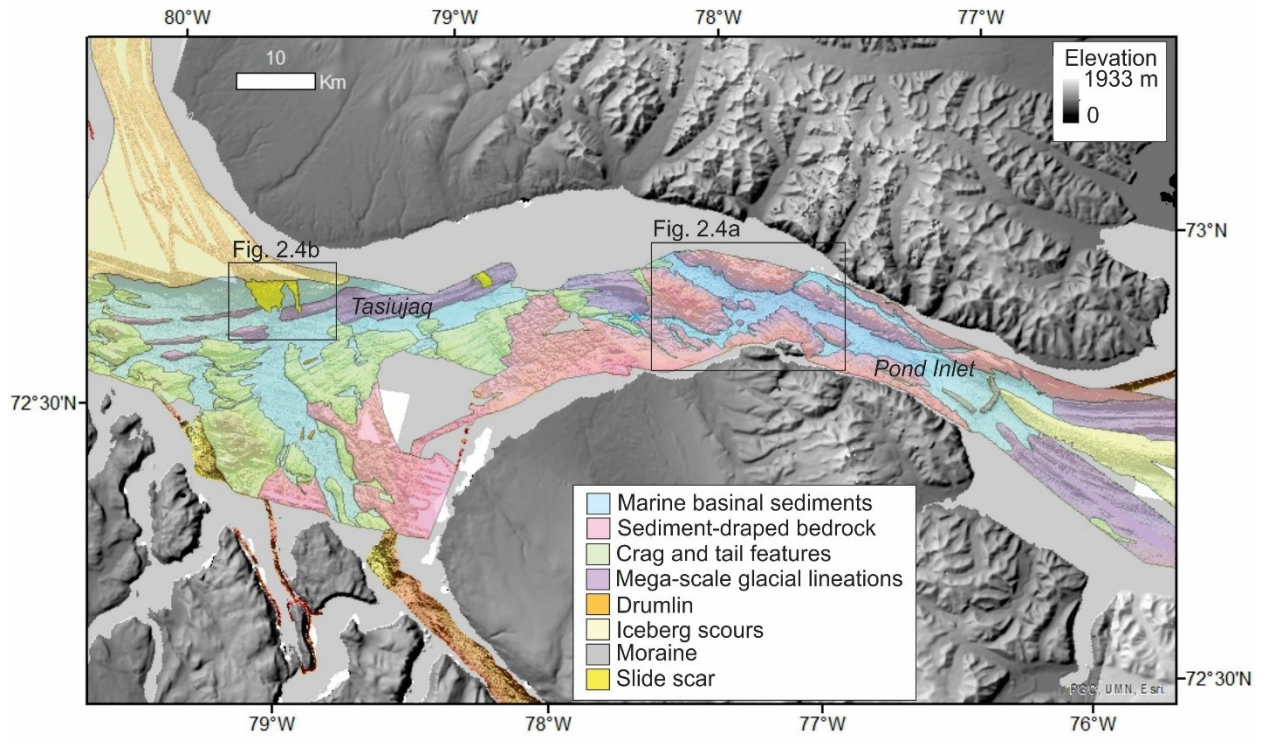


Figure 2.3: Interpretation of the submarine glacial landforms of Pond Inlet based on multibeam bathymetric data. Locations of Figure 2.4a and b outlined in black. Multibeam bathymetry collected by OMG as part of ArcticNet (2005-2008)

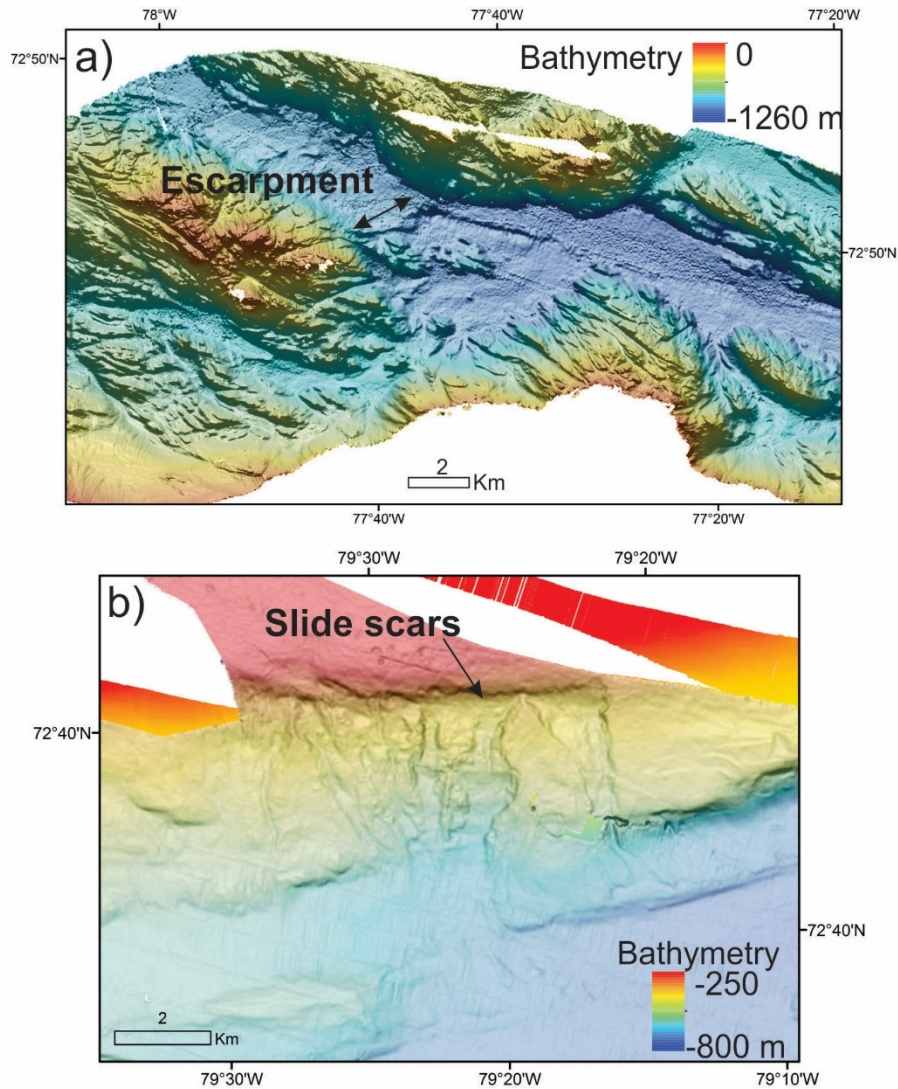


Figure 2.4: a) Escarpment shown in multibeam bathymetric data (OMG, 2005-2008) in the centre of Pond Inlet. b) Slide scars on the northwestern slope of Tasiuaq shown in multibeam bathymetric data collected by OMG as part of ArcticNet (2005-2008).

Acoustic facies

Sub-bottom profiler data reveal that the fjord is filled with a minimum of 50 m of basal sediments (Figure 2.5). Preliminary interpretations focus on the main sub-bottom profiler line, from the seafloor to the strong continuous basal reflector (Figure 2.2b). The two predominant acoustic facies in the Pond Inlet region are an acoustically chaotic to reflection-free facies (facies 1) and an acoustically stratified facies (facies 2; Table 2.1), similar to acoustic facies interpreted

in fjords in eastern Canada and Norway (Bellwald et al., 2016; St-Onge et al., 2012). Facies 1 is composed of discontinuous low to moderate strength reflections or is reflection free. It is defined by elongate wedges that pinch out and show erosional truncations with underlying units, and the upper surface of these deposits can be hummocky. Facies 1 deposits are often stacked and are separated by continuous high-amplitude reflectors. These wedge deposits reach up to 20 m in thickness and can be traced for 1550 m. Smaller deposits of facies 1 are lobe shaped and disrupt high-amplitude continuous reflections. These deposits reach thicknesses of 2.5 m and can be traced for <1000 m. Facies 2 (Figure 2.5, Table 2.1) comprises the majority of basinal sediments and is composed of parallel to divergent, moderate- to high-amplitude, continuous reflections. Facies 2 is often overlain by continuous high-amplitude reflectors and is locally interrupted by lobes and wedge-shaped bodies of facies 1, which intersect the moderate- to high-amplitude reflectors. This facies forms lens-shaped deposits that thicken toward the centre of the basin with a maximum thickness of 8 m and thin toward the east and west as accommodation in the basin decreases.

Table 2.1: Characteristics of the major acoustic facies in Pond Inlet.

Characteristics	Facies 1: acoustically chaotic to reflection free	Facies 2: acoustically stratified
Amplitude	Low to moderate or absent	Moderate to high
Continuity	Discontinuous	Continuous
Internal configuration	Chaotic	Parallel to divergent
Reflection geometry at boundaries	Downlap to erosional truncation	Onlap
External form	Wedge, lens	Lens
Thickness	2.5-20 m	2-8 m

Table 2.2: Lithofacies (L) characteristics for Pond Inlet, Baffin Bay.

Characteristics	L1	L2	L3	L4	L5	L6
Thickness (cm)	3-200	150	495	12-27	8-32	1-45
Sedimentary structures	Predominantly massive, with some parallel laminations	Inclined parallel laminations	Highly deformed, folding, inclined laminations	Clast supported, subrounded monomict mudclasts. Sandy mud to mud matrix	Mud matrix, with subrounded IRD clasts	Parallel/cross laminations, normally graded to massive.
Colour	Olive-grey to dark-grey	Olive-grey	Olive-grey to dark-grey	Olive-grey	Olive-grey	Dark-grey
Bioturbation	Low-high	Low	Moderate-high	Low	Low	Low-moderate
Bulk density (g/cm ³)	1.3-1.9	1.6	1.6-1.8	1.4-2.1	1.7-1.9	1.5-2.3
Magnetic Susceptibility (10 ⁻⁵ SI Units)	17-139	41-67	71-274	138-774	54-225	50-742

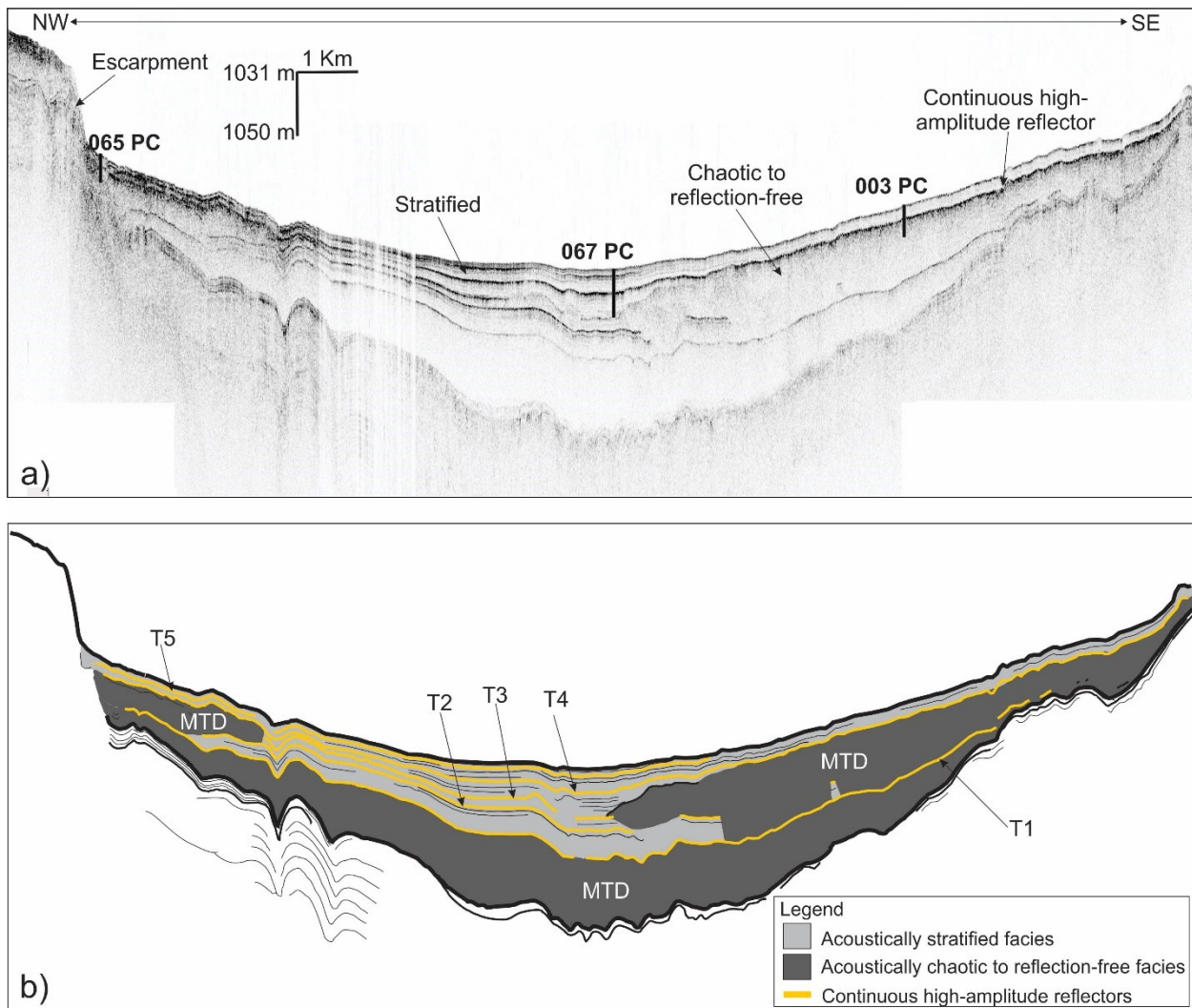


Figure 2.5: a) Sub-bottom profiler line (location shown in Figure 2.2b) showing characteristics of acoustic facies, the escarpment and the location of piston cores (PC) 065, 067 and 003 Pond Inlet. b) Line drawing showing stacks of acoustically stratified facies (facies 1) and acoustically chaotic to reflection-free facies (facies 2) and continuous high-amplitude reflectors in yellow. The mass transport deposits (MTDs) are shown in dark grey and five turbidites (T1–T5) are shown in yellow. Abbreviations: NW, northwest; SE, southeast.

2.4.2 Lithofacies

Analysis of four piston cores, including X-radiographs, core photographs and physical properties (bulk density, magnetic susceptibility, colour), suggest that the sediments in this part of Pond Inlet can be separated into six lithological facies (lithofacies L1–L6; Table 2.2). The background sedimentary infill is composed of olive-grey–dark grey massive to stratified mud (L1; Figure 2.6). Lithofacies 1 is the most abundant lithofacies, comprising the majority of the sediments in the cores (Figure 2.7). It is characterized by predominantly massive to occasionally parallel-

laminated mud and can have a high degree of bioturbation (Table 2.2). It ranges in thickness from 3 to 200 cm and is characterized by low to moderate bulk density and magnetic susceptibility.

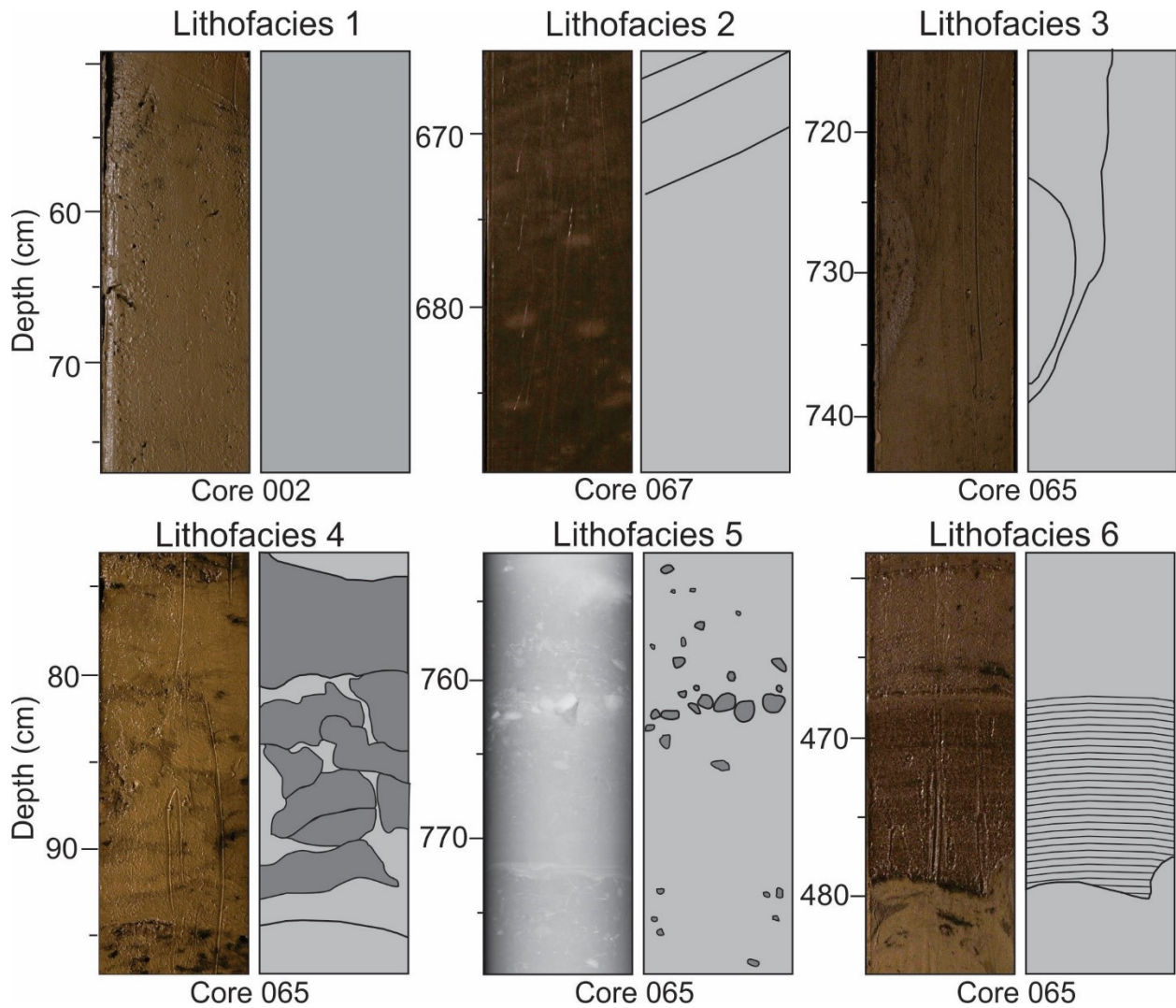


Figure 2.6: Lithofacies (L) characteristics for Pond Inlet shown in core photography (L1, L2, L3, L4, L6) and in X-radiographs (L5) onto the left side., and sedimentary structure interpretations are onto the right side.: L1 shows no structures; L2 shows inclined parallel laminations in black; L3 shows convolute layering in black; L4 shows mudclasts in dark grey; L5 shows ice-rafted debris (IRD) in dark grey; and L6 shows parallel laminations in black.

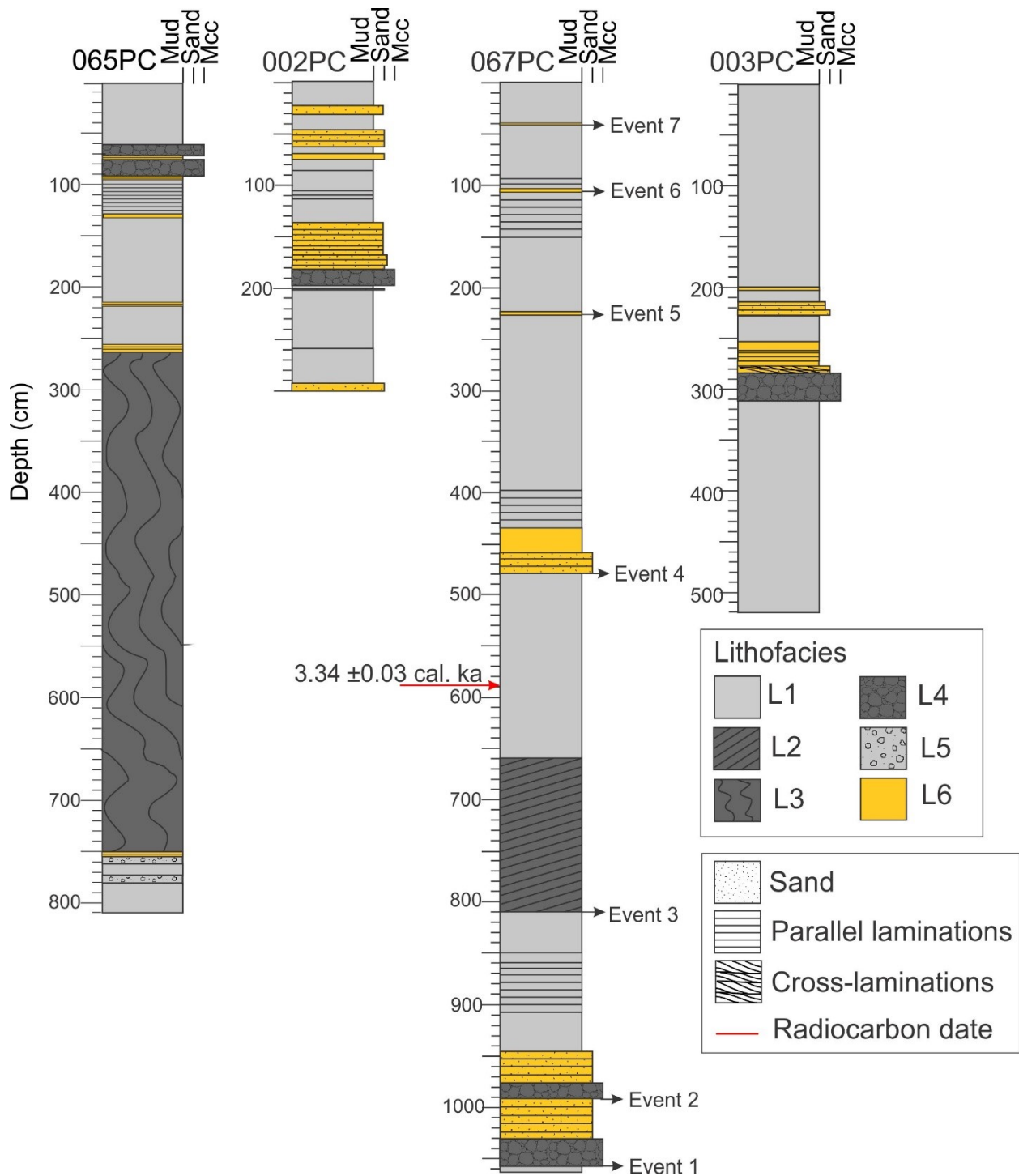


Figure 2.7: Core logs showing lithofacies interpretations for piston cores (PC) 065, 002, 067 and 003, Pond Inlet. Calibrated radiocarbon date shown in core 067 and the seven mass transport deposits (MTDs) and turbidite sequences labelled as events 1 to 7. Grain size shown as mud, sand and mudclast conglomerate (mcc).

Lithofacies 2 (L2) is composed of olive-grey inclined stratified mud (Figure 2.6). Lithofacies 2 is observed in core 067, is 150 cm thick, and deposited between units of L1 (Figure 2.7).

Lithofacies 2 is characterized by inclined parallel laminations, which have an inclination of approximately 25°, and has low bulk density and magnetic susceptibility (Table 2.2). Lithofacies 3 (L3) is composed of folded olive-grey–dark grey mud, makes up the majority of the sediments in core 065, and is 495 cm thick (Figure 2.7). Lithofacies 3 is characterized by highly deformed mud intervals with folded mud and convoluted layering, which can be vertical in the core (Figure 2.6), and has low to moderate bulk density and magnetic susceptibility (Table 2.2). Lithofacies 4 (L4) is composed of a monomict mudclast conglomerate (Figure 2.6), ranges in thickness from 12 to 27 cm, and is observed in all four cores (Figure 2.7). This lithofacies is often clast supported and occasionally matrix supported. Clasts are subrounded, the matrix ranges from silty mud to sandy mud, and this lithofacies is characterized by higher bulk density and magnetic susceptibility measurements (Table 2.2).

Lithofacies 5 (L5) is found near the base of core 065 (Figure 2.7) and consists of massive olive-grey mud with ice rafted debris (IRD; Figure 2.6). It has moderate bulk density and magnetic susceptibility (Table 2.2). Lithofacies 6 (L6) is located within all four piston cores and is composed of sorted sand and /silt deposits (Figure 2.7). This lithofacies is characterized by parallel-laminated or cross-laminated silt and sand beds that are normally graded and sometimes massive and often has an erosive base (Figure 2.6). Lithofacies 6 varies in thickness from <1 to 45 cm and is characterized by higher bulk density and magnetic susceptibility (Table 2.2).

The lithostratigraphic sequence preserved in Pond Inlet is as follows: discrete units of grey mud with some IRD (L5) are overlain by a succession of predominantly massive and occasionally laminated grey muds (L1). These grey muds are interrupted by intervals of deformed grey mud (L3 and L4) and mudclast conglomerate (L5), which are often overlain by sorted silt and /sand

deposits (L6). Thin layers of sorted silt (L6) also interrupt the background massive to laminated grey mud intervals.

2.4.3 Chronology

In core 067 at a depth of approximately 589–591 cm, a colus shell fragment was sampled from massive olive-grey mud (L1). A calibrate radiocarbon age of 3.34 ± 0.03 cal. ka was obtained from the shell and the age indicates that the deposition of the overlying sorted sand deposit (L6) occurred after 3.34 ka BP and that the underlying inclined stratified mud was deposited prior to the deposition of the shell at 3.34 ka BP. The shell may have redistributed so this provides a maximum age. Assuming the top of the trigger weight core was deposited during the 2013 cruise year, the mean sedimentation rate for this part of the fjord is 1.8 mm/yr. This also assumes that sedimentation rates did not change over the last 3.3 ka.

2.5 Preliminary interpretations

2.5.1 Mass transport deposits and turbidites

The sub-bottom profiler data and piston cores reveal that the basinal sediments of Pond Inlet are dominated by hemipelagic sediments interrupted by gravity flow deposits including MTDs and turbidites, which represent periods of environmental change or seabed instability. The massive olive-grey mud that comprises the majority of the cores (L1 and L5) is interpreted as hemipelagic sediment with occasional IRD. It is likely that local Holocene tidal-water glaciers calving into Pond Inlet from Bylot Island or Baffin Island could have sourced those IRD. The sub-bottom profiler section reveals three major MTDs separated by hemipelagic sediments and a minimum of five turbidite deposits (Figure 2.5). Mass transport deposits are the largest mass wasting deposits by volume, and are characterized in geophysical data by acoustically chaotic to reflection-free facies that form wedge deposits, similar to postglacial fiord mass wasting deposits

described by St-Onge et al. (2012) and Bellwald et al. (2016). These submarine MTDs are erosive and cut into underlying sediments. The smallest MTD in the study area is deposited adjacent to the 20 m escarpment (Figure 2.5). Lithofacies 2, 3 and 4 are interpreted to represent MTD lithofacies (Figure 2.7) and are similar to MTD lithofacies discussed by Tripsanas et al. (2008). The inclined and folded mud (L2, L3) represent a lower degree of deformation in comparison with the mudclast conglomerate (L4). The acoustically chaotic to reflection-free acoustic facies identified in the sub-bottom profiler data is intersected by cores 065 and 003, correlating with the MTD lithofacies L3 and L4 in the sediment cores.

Turbidites are the most abundant gravity flow deposit observed in the basin (Figure 2.5). They are interpreted as high-amplitude continuous reflectors in the sub-bottom profiler data and as the sorted silt and sand deposits (L6), in agreement with Tripsanas et al. (2008). A minimum of five major turbidite deposits can be recognized within the sub-bottom profiler section. These flows interrupt normal sedimentation in the basin and are interbedded with hemipelagic sediments (Figure 2.5). The turbidites often occur at the top of the MTD sequence, similar to the relationship reported by Jenner et al. (2007) along the central Scotian Slope. These deposits are the most laterally continuous gravity flows and can be correlated up to 2 km on sub-bottom profiler data, and range in thickness from <1 to 45 cm.

2.5.2 Sedimentation rates and frequency of gravity flows

The late Holocene sedimentation rate in Pond Inlet of 1.8 mm/yr. is higher than reported sedimentation rates for the Baffin Island Shelf and other Baffin Bay fiords, which are on the order of 0.3–0.6 mm/yr (Andrews et al., 1985). This gives Pond Inlet a greater potential to preserve a higher resolution sedimentary record. Core 067 represents the longest continuous record in Pond Inlet and reveals a total of seven MTDs and/or turbidites recorded in this portion

of the basin during the late Holocene (Figure 2.7). The geochronology results provide an initial estimate of the frequency of MTD and turbidite events in the basin of one every 800 years.

2.5.3 Triggering mechanisms for mass transport deposits and turbidites

Multiple Holocene MTDs and turbidites other gravity flows are preserved in Pond Inlet. It is possible that the sediment record contains a paleoseismological history of northern Baffin Bay. However, it is recognized that the record could be the result of a wide range of processes besides seismicity, such as local events including stream floods, subaerial landslides, jokulhaups and storm surges. However, the volume of the largest MTDs discovered in Pond Inlet and the paucity of thick sediment on the fjord walls above or below sea level may imply that the MTDs were reworked previously deposited basinal sediments. At this point, local events cannot yet be ruled out as possible triggering mechanisms, particularly for the voluminous MTDs. The recognition of synchronous events in multiple catchments has often been used to provide evidence for a paleoseismic origin (Goldfinger, 2011), and the areal extent of large multifjord seismic events would be proportional to earthquake magnitude.

2.5.4 Ongoing and Future work

Work is ongoing to characterize and correlate the MTDs and turbidites preserved in Pond Inlet to establish the first MTD/turbidite chronology for Baffin Bay. This work includes sedimentological analyses of thin sections, portable X-ray fluorescence (pXRF) and X-ray computed tomography (XCT) core imaging to improve understanding of depositional processes. Additional radiocarbon dates will be obtained in strategic positions to better constrain the timing of MTD and turbidite deposition in the fjord and to establish if deposits are correlative throughout and beyond the basin. If these deposits can be linked to seismicity, this will lead to

improved assessment of the seismic hazard and risk of displacement waves in northern Baffin Bay.

2.6 Economic considerations

Even though ground acceleration in this seismically active region may endanger community members and property, the greatest risk to the northeastern Baffin Island communities is displacement waves. Risks associated with displacement waves have been the focus of Norway and other Nordic countries, where fjords are common. Previous displacement waves in arctic settings have had run-up heights up to 12 m (Bondevik et al., 2003). Their disastrous effect was recently experienced in western Greenland on June 17, 2017, when a displacement wave killed four people in the village of Nuugaatsiaq and destroyed 11 homes (Schiermeier, 2017).

Nuugaatsiaq is situated across Baffin Bay from northeastern Baffin Island.

All of the communities on northeastern Baffin Island have infrastructure within 1 m of high tide, and many Hamlets are mostly within 50 m asl elevation. The Hamlet of Pond Inlet has a population of 1617 (Statistics Canada, 2017) and its economy is supported by government and tourism. Major infrastructure includes an airport at 55 m asl, two schools, one of the largest Arctic co-operatives in Nunavut (situated below 50 m asl) and a wharf system for tour cruises and sealifts. Activities in the area include mineral exploration in north-central Baffin Island and planned mining at Baffinland Iron Mines Corporation's Mary River site, located 160 km inland from the Hamlet.

This study is an initial attempt to examine marine geological hazards in Pond Inlet. This information will contribute to an improved understanding of the potential seismic submarine landslides in Pond Inlet and the vulnerability of existing and future infrastructure in this region.

2.7 Conclusions

Analysis of sediment cores and 3.5 kHz sub-bottom profiler data in Pond Inlet have revealed a record of late Holocene mass movement in the region. Two main acoustic facies were identified within the inner portion of the fiord, including an acoustically stratified facies representing normal hemipelagic sedimentation that is interrupted by MTDs of acoustically chaotic to transparent reflection-free facies. Packages of hemipelagic sediments and the tops of MTDs are overlain by five high-amplitude reflectors interpreted as turbidite deposits. The MTDs reach thicknesses up to 20 m in the basin and turbidites up to 45 cm thick can be traced over 2 km. One radiocarbon date reveal a basinal sedimentation rate of 1.8 mm/yr., and a preliminary estimate of gravity-flow frequency in this region is on the order of one event every 800 years. The region's high seismicity suggests that the gravity driven flows could be seismogenic, although locally derived triggering mechanisms, such as flooding, glacial outburst floods and onshore landslides, cannot be ruled out at this time. Analysis of the cores and acoustic data is ongoing and this investigation aims to establish the first MTD chronology for northern Baffin Bay, which will help improve the geohazard assessment for the region.

2.8 Acknowledgments

The authors thank the officers, crews and scientific staff on board the CCGS Hudson and Amundsen during the 2013 and 2015 field program. K. Jenner, A. Normandeau and D. Piper are thanked for guidance and discussion. Financial support for this study was provided by the Government of Canada's Program of Energy Research and Development (PERD), ArcticNet and Natural Sciences and Engineering Research Council of Canada (NSERC). DEMs provided by the Polar Geospatial Center under NSF OPP awards 1043681, 1559691 and 1542736.

Natural Resources Canada, Lands and Minerals Sector contribution 20170295

2.9 References cited in Chapter 2

- Andrews, J.T., Jull, A.J.T., Donahue, D.J., Short, S.K., Osterman, L.E., 1985. Sedimentation rates in Baffin Island fiord cores from comparative radiocarbon dates. *Can. J. Earth Sci.* 22, 1827–1834. <https://doi.org/10.1139/e85-194>
- Bellwald, B., Hjelstuen, B.O., Sejrup, H.P., Haflidason, H., 2016. Postglacial mass movements and depositional environments in a high-latitude fjord system – Hardangerfjorden, Western Norway. *Mar. Geol.* 379, 157–175. <https://doi.org/10.1016/j.margeo.2016.06.002>
- Bent, A.L., 2002. The 1933 Ms= 7.3 Baffin Bay earthquake: strike-slip faulting along the northeastern Canadian passive margin. *Geophys. J. Int.* 150, 724–736.
- Bondevik, S., Mangerud, J., Dawson, S., Dawson, A., Lohne, Ø., 2003. Record-breaking Height for 8000-Year-Old Tsunami in the North Atlantic. *Eos, Trans. Am. Geophys. Union* 84, 289–293. <https://doi.org/https://doi.org/10.1029/2003EO310001>
- Brouard, E., Lajeunesse, P., 2017. Maximum extent and decay of the Laurentide Ice Sheet in Western Baffin Bay during the Last glacial episode. *Sci. Rep.* 7, 1–8. <https://doi.org/10.1038/s41598-017-11010-9>
- Campbell, D.C., 2014. CCGS Hudson Expedition 2013-029. Geological Hazard Assessment of Baffin Bay and Biodiversity Assessment of Hatton Basin. August 14-September 16, 2013. 122.
- Coulthard, R.D., Furze, M.F.A., Pieńkowski, A.J., Chantel Nixon, F., England, J.H., 2010. New marine ΔR values for Arctic Canada. *Quat. Geochronol.* 5, 419–434. <https://doi.org/10.1016/j.quageo.2010.03.002>
- Currie, L.D., Coutand, I., Brent, T.A., Issler, D.R., Wielens, H., 2012. Structural style and thermal history of the eastern Lancaster Sound and Bylot Island area, NU. *Geol. Assoc. Canada–Mineralogical Assoc. Canada, Jt. Annu. Meet. St. John’s, Newfoundland, May 27–29, 2012, Abstr. p. 31.*
- Di Giacomo, D., Storchak, D.A., Safronova, N., Ozgo, P., Harris, J., Verney, R., Bondar, I., 2014. A New ISC Service: The Bibliography of Seismic Events. *Seismol. Res. Lett.* 85, 354–360. <https://doi.org/10.1785/0220130143>
- Dyke, A.S., 2004. An outline of North American deglaciation with emphasis on central and northern Canada. *Dev. Quat. Sci.* 2, 373–424. [https://doi.org/10.1016/S1571-0866\(04\)80209-4](https://doi.org/10.1016/S1571-0866(04)80209-4)
- Goldfinger, C., 2011. Submarine Paleoseismology Based on Turbidite Records. *Ann. Rev. Mar. Sci.* 3, 35–66. <https://doi.org/10.1146/annurev-marine-120709-142852>
- Hilchey, A., 2004. Deglacial geologic history of the Ravn River valley, northern Baffin Island, Nunavut. Dalhousie University.

- International Seismological Centre, 2017. International Seismological Centre 2017: Bulletin of the International Seismological Centre [WWW Document]. Int. Seismol. Centre, online Bull. URL <http://www.isc.ac.uk> (accessed 7.20.10).
- Jackson, G.D., Davidson, A., 1975. Geology, Pond Inlet and Nova Zembla Island, District of Franklin.
- Jackson, G.D., Davidson, A., 1975. Bylot Island map-area, District of Franklin.
- Jenner, K.A., Piper, D.J.W., Campbell, D.C., Mosher, D.C., 2007. Lithofacies and origin of late quaternary mass transport deposits in submarine canyons, central Scotian Slope, Canada. *Sedimentology* 54, 19–38. <https://doi.org/10.1111/j.1365-3091.2006.00819.x>
- MacLean, B., Williams, G.L., Srivastava, S. (Eds.), 1990. Geology of Baffin Bay and Davis Strait, in: *Geology of the Continental Margin of Eastern Canada*. Geological Survey of Canada, *Geology of Canada series no. 2*, pp. 293–348.
- OMG, 2005. Multibeam Sonar Data collected from the CCGS Amundsen: Ocean Mapping Group, University of New Brunswick, Fredericton, New Brunswick, Canada [WWW Document]. *Ocean Mapp. Gr.* URL <http://www.omg.unb.ca/Projects/Arctic/index.html>
- Posamentier, H.W., Kolla, V., 2003. Seismic Geomorphology and Stratigraphy of Depositional Elements in Deep-Water Settings. *J. Sediment. Res.* 73, 367–388. <https://doi.org/10.1306/111302730367>
- Sangree, J.B., Widmier, J.M., 1979. Interpretation of Depositional Facies from Seismic Data. *Geophysics* 44, 131–160. <https://doi.org/10.1190/1.1440957>
- Schiermeier, Q., 2017. Huge landslide triggered rare Greenland mega-tsunami. *Nat. News.* <https://doi.org/doi:10.1038/nature.2017.22374>
- St-Onge, G., Chapron, E., Mulsow, S., Salas, M., Viel, M., Debret, M., Foucher, A., Mulder, T., Winiarski, T., Desmet, M., Costa, P.J.M., Ghaleb, B., Jaouen, A., Locat, J., 2012. Comparison of earthquake-triggered turbidites from the Saguenay (Eastern Canada) and Reloncavi (Chilean margin) Fjords: Implications for paleoseismicity and sedimentology. *Sediment. Geol.* 243–244, 89–107. <https://doi.org/10.1016/j.sedgeo.2011.11.003>
- Statistics Canada, 2017. Pond Inlet, HAM [Census subdivision], Nunavut and Canada [Country] (table). *Census Profile. 2016 Census*. Statistics Canada Catalogue no. 98-316-X2016001. Ottawa. Released November 29, 2017. [WWW Document]. URL <https://www12.statcan.gc.ca/census-recensement/2016/dp-pd/prof/index.cfm?Lang=E> (accessed 11.8.18).
- Stein, S., Sleep, N.H., Geller, R.J., Wang, S., Kroeger, G.C., 1979. Earthquakes along the passive margin of eastern Canada 6, 537–540.
- Stuiver, M., Reimer, P.J., and Reimer, R., 2017. [WWW program] [WWW Document]. URL <http://calib.org>

Tripsanas, E.K., Piper, D.J.W., Jenner, K.A., Bryant, W.R., 2008. Submarine mass-transport facies: New perspectives on flow processes from cores on the eastern North American margin. *Sedimentology* 55, 97–136. <https://doi.org/10.1111/j.1365-3091.2007.00894.x>

Willenbring Staiger, J., Gosse, J., Little, E.C., Utting, D.J., Finkel, R., Johnson, J. V, Fastook, J., 2006. Glacial erosion and sediment dispersion from detrital cosmogenic nuclide analyses of till. *Quaternary Geochronology*. 1, 29–42. <https://doi.org/10.1016/j.quageo.2006.06.00>

CHAPTER 3: DEGLACIAL TO POSTGLACIAL SUBMARINE DEPOSITIONAL HISTORY OF ECLIPSE SOUND AND POND INLET, NUNAVUT, CANADA

Authors: L.M. Broom, D.C. Campbell and J.C. Gosse

Status: Ready for submission

Abstract

The sedimentary record of Canadian arctic inlets and fjords remains relatively underutilized due to their remoteness and persistent sea ice cover. These sediment sinks can provide an archive of tectonically and climatically driven processes that link terrestrial and marine sedimentary records. The depositional record and timing of deglaciation of Pond Inlet and Eclipse Sound can now be better constrained utilizing new multibeam bathymetric data, high-resolution sub-bottom profiler data and sediment cores. The geophysical and core data reveal a deglacial to postglacial sedimentary record including ice-contact till and glaciomarine deposits overlain by a postglacial hemipelagic deposits interrupted by mass-transport deposits and turbidites. The previously mapped Last Glacial Maximum (LGM) ice-sheet extent and the position of the Cockburn moraines suggest the moraine at the entrance of Pond Inlet was deposited during the Younger Dryas cold event (12.8-11.5 ka BP). The timing of ice-retreat recorded along the coastlines of Eclipse Sound and Navy Board Inlet corresponds with the end of IRD deposition at 9.8 ka BP, potentially indicating the shutoff of iceberg calving as the ice-sheet retreated landward. The first postglacial turbidite was deposited just prior to 10.7 ka BP. Once the region was ice free, sedimentation rates remained relatively stable with an average of 0.9 mm/yr. Postglacial hemipelagic deposition was frequently interrupted by mass movement events.

3.1 Introduction

Glacier-influenced inlets and fjords are important sediment traps that link terrestrial and submarine sedimentary processes. Their relatively rapid marine sedimentation rates provide the potential to preserve high-resolution records which can provide an archive of climate and tectonically driven sedimentary processes for a given region (Bellwald et al., 2016; Hjelstuen et al., 2009; St-Onge et al., 2012; Syvitski, 1989). Numerous fjords, inlets, bays, and sounds indent the coast of Baffin Island (Figure 3.1). The seabed morphology and sediments in these inlets contain useful constraints on ice sheet dynamics (e.g. Brouard and Lajeunesse, 2017; Dowdeswell et al., 2016), iceberg source and frequency, and yield proxy records for paleoclimate and paleo-sea ice cover. Relatively underutilized records in these basins are tectonic strain markers and history of mass movements—either subaerial or submarine, gravitational or seismogenic. Owing to their remoteness and a persistent sea ice cover for over eight months of the year, Baffin Island fjord sediments are less studied than their Norwegian and Greenland passive margin counterparts.

Eclipse Sound and Pond Inlet is a large fjord system located along the northeastern coast of Baffin Island between Baffin and Bylot Islands. During the Late Pleistocene, the system provided an outlet of the northeast Laurentide Ice Sheet (LIS) (Brouard and Lajeunesse, 2017). Today, the sound and inlet are fed by several rivers and alpine glaciers; the area also experiences frequent earthquakes (Basham et al., 1977; Bent, 2002). From 2005 to 2015, marine geological expeditions to the area collected multibeam bathymetric data, high-resolution sub-bottom profiler data, and sediment cores. These data show thick accumulations of deglacial and postglacial sediments in basinal settings (Campbell, 2014), however the depositional process responsible for the sedimentary succession is not known, which limits the utility of the

sedimentary record. For example, acoustically stratified sediment may represent monotonous hemipelagic sedimentation ideal for paleoenvironmental studies, or it could represent turbidite deposits, which may record a local or regional tectonic signal.

In this study, we interpret the seafloor morphology from the multibeam bathymetry, examine the late to postglacial stratigraphy using sub-bottom profiler data and piston cores, and obtain the first radiocarbon dates from the fjord bottom. Our results (1) constrain the history of deglaciation of the large fjord glacial system, and (2) determine the nature, timing, and extent of depositional processes preserved in the marine record in the study area. The results have implications for understanding the deglaciation and coastal geohazards in the eastern Canadian Arctic.

3.2 Regional setting

3.2.1 Physiography

Baffin Bay formed through rifting and seafloor spreading between Baffin Island and Greenland from the Cretaceous through the Eocene (Keen et al., 1972; Oakey and Chalmers, 2012). Pond Inlet, Eclipse Sound and Navy Board Inlet form a seaway between Baffin Island and Bylot Island. The seaway reaches a width of approximately 40 km across and 130 km in length (Figure 3.1). Water depths range from 1080 m in the centre of Pond Inlet to 15 m at bathymetric highs in Eclipse Sound. The topography around the fiord juxtaposes coastal lowlands with heavily dissected mountains. Peaks reach 1950 m asl on Bylot Island, where steep coastal cliffs ascend directly out of the water, and 1500 m near the Baffin Island coast of the fiord. Valley relief often exceeds 800 m. Resistant Archean and Proterozoic igneous and metamorphic rocks that dominate Bylot and northern Baffin Islands entirely comprise the mountainous regions and glacial and river source area (Jackson and Davidson, 1975; Skipton et al., 2018). However, the coastal lowlands of southern Bylot and northern Baffin Island are underlain by Cretaceous and

Cenozoic sedimentary rocks (Jackson and Davidson, 1975). The fjords, sounds and inlets along Baffin Island, including Pond Inlet and Eclipse Sound are the remnants of early Cenozoic drainage systems which formed through fluvial erosion and extensional faulting (Bornhold et al., 1976). These fjords have continued to be modified by glaciers through the late Quaternary (Briner et al., 2008).

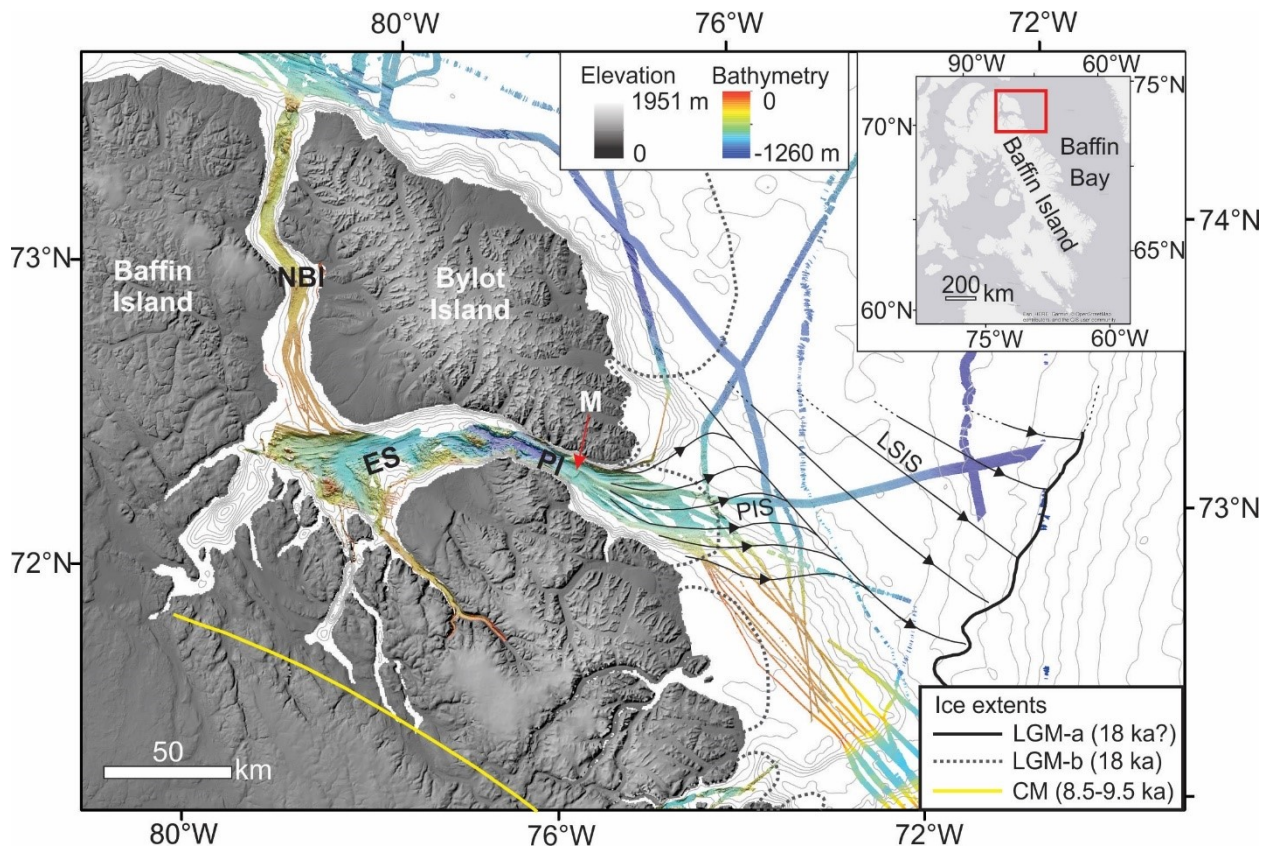


Figure 3.1: Regional map of northeastern Baffin Island, Bylot Island and Baffin Bay. Multibeam bathymetry collected by OMG as part of ArcticNet (2005-2008), 100 m contours, and ice extents are shown. Ice extents include LGM-a at approximately 18 ka from Brouard & Lajeunesse (2017), 18 ka (LGM-b) from Dyke (2004), and the Cockburn Moraine (CM) extent from (Falconer et al. 1965). PI = Pond Inlet, ES = Eclipse Sound, NBI = Navy Board Inlet, PIS = Pond Inlet Ice Stream, LSIS = Lancaster Sound Ice Stream. DEM(s) created from DigitalGlobe, Inc. imagery.

3.2.2 Glacial history of Pond Inlet and vicinity

Most of the knowledge of the glacial history of the region is based on mapping of glacial deposits onshore and dating of raised shoreline landforms (e.g. Dyke, 2008, 2004; Dyke et al., 2002; Dyke and Hooper, 2001; McNeely and Atkinson, 1996). Glacial ice that last occupied the

fjord system is considered to have been only partially fed by the LIS to the south (Miller and Dyke, 1974), and independent ice caps and alpine glaciers are thought to have fed the outlet lobe from the west and north during the LGM and also from the south during the deglacial phase (e.g. Margreth et al., 2017). The extent of glacial ice occupying Pond Inlet during the LGM has been redefined based on the recognition of submarine mega-scale glacial lineations (MSGs), which indicate glacial ice extended past the mouth of Pond Inlet towards the shelf break (Figure 3.1; LGM-a) (Brouard and Lajeunesse, 2017). The timing of the LGM, considered the most recent time when ice sheets were at their maximum extent, varied locally. While the maximum ice margin positions have been mapped or inferred for the region, denoted on Figure 3.1 as LGM-a (Brouard and Lajeunesse, 2017) and LGM-b (Dyke, 2004), no direct dating of the local deglacial and postglacial history of northeastern Baffin Island since the LGM has been obtained from the offshore marine sedimentary record. Radiocarbon dates from glacially transported marine shells indicate the maximum age of the advance around Pond Inlet and Eclipse Sound is approximately 33 ka BP (Dyke et al., 2001) and regionally the LIS advanced until approximately 24-21 ka (Dyke et al., 2002). The timing of deglaciation around Pond Inlet and northeastern Baffin Island is not established as well as in other regions west and south of the study area (Briner et al., 2007; Dyke, 2008; Dyke and Hooper, 2001). West of Pond Inlet, radiocarbon dates on marine shells (*Mya truncata* and *Hiatella arctica*) reveal ice re-advanced to the mouth of the Navy Board Inlet around 10 ka BP (Dyke and Hooper, 2001), based on a minimum limiting date ($9.8 \text{ ka} \pm 0.1 \text{ ka BP}$), and that the coastlines around Navy Board Inlet and Eclipse Sound were ice free between 9.3-6 ka BP (McNeely and Atkinson, 1996). The Cockburn Substage, marked by the Cockburn end moraine system (CM) on eastern Baffin Island (Figure 3.1), shows the ice sheet's position

around 8.5-9.5 ka BP, west of our study area (Andrews and Ives, 1978; Briner et al., 2009; Falconer et al., 1965) (Figure 3.1).

3.3 Materials and Methods

3.3.1 Multibeam Bathymetric Data

High resolution multibeam bathymetric data were collected during the 2005-2008 CCGS Amundsen ArcticNet Cruises under direction of the Ocean Mapping Group (OMG) at the University of New Brunswick (OMG, 2005-2008) (Figure 3.1). The data were collected in water depths of approximately 15-1000 m using a Kongsberg Simrad EM300 multibeam sonar system operating under standard collection settings using auto depth mode and an angular coverage of $\pm 60^\circ$ and equidistant beamforming. The multibeam data were gridded to resolution of 10 x 10 m² and visualized using ArcGIS version 10.2.2. Shaded relief and gradients of the bathymetry were computed over the majority of the Pond Inlet sea floor (ca. 300 km² area) using ArcGIS 10.2.2 software.

3.3.2 Sub-bottom Profiler Data

3.5 kHz sub-bottom profiler data were collected by the GSC Atlantic (GSC-A) onboard CCGS Hudson in August-September of 2013 (Figure 3.2) using a Knudsen 3260 Echo-Sounder (Campbell, 2014). These data are supplemented by additional data collected using a Knudsen K320R 3.5 KHz sub-bottom profiler coincident with multibeam bathymetric data acquired onboard CCGS Amundsen from 2005-2008. The sub-bottom data have a maximum theoretical vertical resolution of 11 cm and a maximum penetration depth of approximately 65 m. Interpretation of the sub-bottom profiler data was completed within Kingdom Suite Software 8.8. Envelope of the trace data were used for interpretation and presentation. Seismic facies were interpreted based on geometry and characteristics of reflections including their amplitude and

continuity (Sangree and Widmier, 1979). Sediment thicknesses and volumes were estimated by applying sediment velocities of 1500 m/s based on average sediment p-wave velocity measurements on core samples using a GEOTEK Multi-Sensor Core Logger (MSCL).

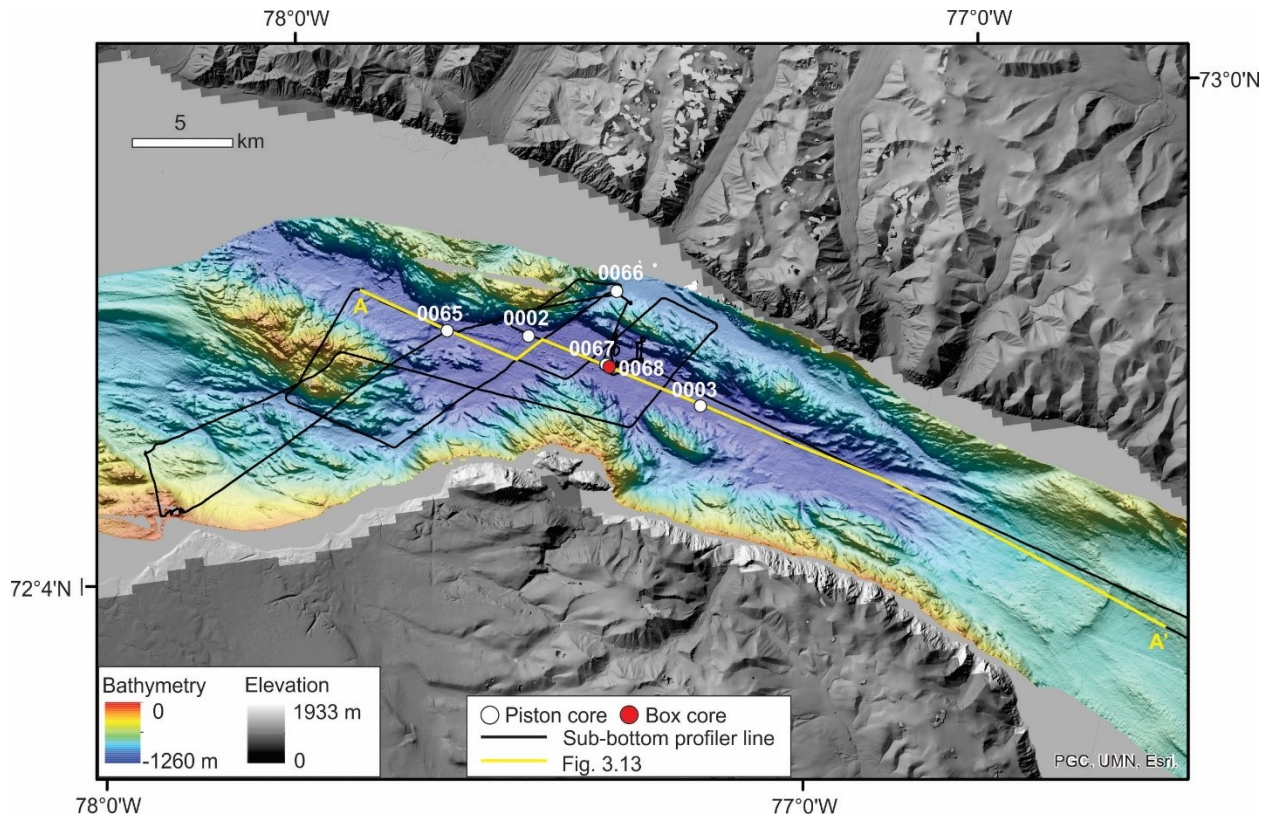


Figure 3.2: Map of piston core locations 0065, 0066, 0067, 0002 and 0003, and box core location 0068 and locations of 3.5 kHz sub-bottom profiler lines. Location of Figure 3.13 regional line is denoted in yellow. Multibeam bathymetry collected by OMG as part of ArcticNet (2005-2008). DEM(s) created from DigitalGlobe, Inc. imagery.

3.3.3 Sediment Core data

Six sediment cores ranging in lengths from 0.48 m to 10.63 m were collected from Pond Inlet in water depths of 880-1076 m (Figure 3.2; Table 3.1). Three piston cores (0065, 0066, 0067) and a box core (0068) were collected in 2013 onboard the CCGS Hudson during the 2013029 expedition (Campbell, 2014). Two push cores (0068B and 0068C) were collected from the box core. Two additional piston cores (0002 and 0003) were collected during the 2015805 expedition in 2015 onboard the CCGS Amundsen.

Table 3.1: Locations, water depth, and core length of piston cores and push cores collected during the 20130029 and 2015805 Hudson expeditions.

Expedition number	Core number	Core type	Latitude	Longitude	Water depth (m)	Core length (cm)
2013029	0065	Piston	72.814891	-77.676665	1035	810
	0066	Piston	72.849098	-77.441545	880	614
	0067	Piston	72.815556	-77.426285	1076	1063
	0068B	Push	72.816518	-77.428031	1074	49.5
	0068C	Push	72.816518	-77.428031	1074	47.5
2015805	0002	Piston	72.822051	-77.553080	1059	299
	0003	Piston	72.809268	-77.278225	1048	520

Sediment cores were assessed for physical properties and sedimentology in order to facilitate interpretation of depositional processes, core-to-core correlation, and core to sub-bottom profiler data correlation. A Geotek MSCL at the GSC-A laboratory was used to analyse core physical properties. Whole core sections were analysed for compressional (p-wave) velocity, bulk density and magnetic susceptibility at 1 cm intervals. Split core sections were then photographed and x-radiographed using a Universal HE425 X-ray system. The split cores were subsequently analysed for magnetic susceptibility and colour at a 1 cm intervals using the GEOTEK MSCL. Colour reflectance ($L^* a^* b^*$) (Robertson, 1977) was measured on split core sections using a Konica Minolta colour spectrophotometer every 5 cm. Discrete core measurements of shear strength and velocity were collected every 10 cm along the split cores.

The majority of grain size samples were measured using a Beckman Coulter LS230 Laser Diffraction Analyzer. Samples with a maximum grain size greater than 2000 microns were manually sieved at $\frac{1}{4}$ phi intervals and merged to normalize the data. Samples were taken at intervals between 1 to 330 cm depending on the frequency of change in lithofacies or sedimentological structures. Core 0067 was sub-sampled every 20 cm within homogeneous mud

sections and every few centimetres within silt/sands. Piston cores 0065, 0066, 0002 and 0003 were selectively sub-sampled for grain size at the base and top (every 1 to 10 cm) of sand deposits, once within cm thick sand deposits, and every 5 to 330 cm within homogeneous mud sections. Thin sections were collected from each piston cores to allow for high-resolution interpretation of sedimentary structures. The thin section aliquots were 18 cm long, dried and impregnated with resin, and separated into three 6-cm lengths in preparation for thin sectioning.

3.3.4 Synthetic Seismograms

Correlation of piston cores to the sub-bottom profiler data was achieved by generating synthetic seismograms with Kingdom Suite Software 8.8 (Figure 3.3). An initial time to depth relationship was generated for the core data utilizing discrete longitudinal velocity measurements taken at 10 cm intervals for each piston core. Down core velocity and bulk density measurements from the Geotek MSCL were cleaned to remove spikes and were then convolved with a Ricker wavelet to generate a synthetic trace. The generated wavelet was computed from the acoustic trace data adjacent to each piston core and both a high pass filter (2500 Hz) and low pass filter (4500 Hz) were applied to the acoustic data. A qualitative match between the sub-bottom and core data was determined by matching peaks and troughs of the acoustic data and the generated wavelet.

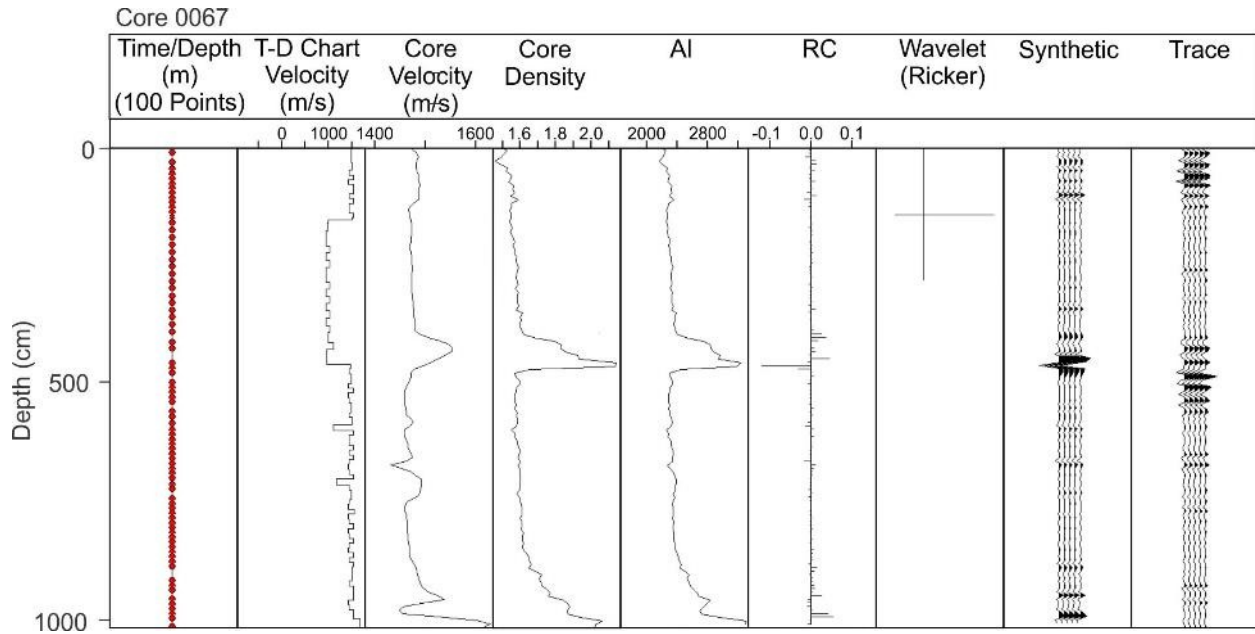


Figure 3.3: Synthetic seismogram for core 0067 showing core velocity (*p*-wave), density (g/cm^3), acoustic impedance (*AI*), reflection coefficient (*RC*), the Ricker wavelet, synthetic trace, and an acoustic trace adjacent to core 0067.

3.3.5 Chronology

To constrain the timing of late glacial and postglacial depositional processes, twelve radiocarbon ages were obtained from mixed benthic or planktonic foraminifera and shell fragments collected from the five piston cores. The dates were obtained using accelerator mass spectrometry (AMS) at the NOSAMS facility of the Woods Hole Oceanographic Institution and the Keck Carbon Cycle AMS Facility at the University of California (Irvine, California) (Table 3.2). The radiocarbon ages for the samples were calibrated using CLAM software (version 2.2; Blaauw, 2010). The Marine13 calibration curve was used and global reservoir correction of 400 years with a local marine reservoir correction (ΔR) of 220 years (Coulthard et al., 2010) was applied with a 1-sigma error of ± 100 years. This 1-sigma error was applied to account for uncertainty attributed to the fact that the *R* values available are not from Pond Inlet and that there is the potential for short-term variability in the reservoir effect when ocean circulation and reservoir mixing varied over the Holocene. Uncalibrated radiocarbon dates reported in McNeely and

Atkinson (1996) that define the deglaciation of the coast along Navy Board Inlet and Eclipse Sound were calibrated using the same methods outlined above.

Table 3.2: Information on radiocarbon dates from piston cores 0065, 0066, 0067, 0002 and 0003 including depth interval, sample media, uncalibrated radiocarbon age, analytical uncertainty, calibrated age, and total uncertainty.

Core	Depth (cm)	Sample media	Radiocarbon age (yrs BP)	Uncertainty (yrs BP)	Calibrated age (yrs BP) ($\Delta R = 220 \pm 100$)	Uncertainty (yrs BP)
0065	50-55	Mixed benthic foraminifera	1580	35	915	221
	120-125	Mixed benthic foraminifera	2630	40	2061	248
	208	Glacialis shell	3005	15	2520	219
	248-253	Mixed benthic foraminifera	3840	25	3557	252
	766-771	Mixed benthic & planktonic foraminifera	9450	30	9963	284
0066	14-19	Mixed benthic foraminifera	1580	50	917	229
	125-130	Mixed benthic & planktonic foraminifera	3970	20	3693	255
	531-534	Mixed benthic & planktonic foraminifera	8990	30	9421	250
0067	164-166	Colus shell	2250	15	1601	232
	589-591	Colus shell	3675	20	3318	253
0002	34-39	Mixed benthic & planktonic foraminifera	1350	45	710	187
0003	206-211	Mixed benthic & planktonic foraminifera	3350	20	2949	228

Classical Bayesian age-depth modelling was achieved with CLAM (version 2.2; Blaauw, 2010) for cores 0065, 0066, and 0067, where a minimum of two radiocarbon dates were obtained. To correct for any missing sediment from the top of the piston cores, the trigger weight cores (TWC) were correlated to their corresponding piston cores based on physical properties, and the top of the TWC was assumed to represent the year the core was collected. Deposits interpreted to be rapidly deposited with little to no erosion of the underlying sediment were incorporated into the age model as being instantaneous. Linear interpolation was used to determine ages between radiocarbon dates. In addition to the core chronology itself, radiocarbon dating provided sedimentation rates between dated intervals. These sedimentation rates are considered minimum rates because of the possibility of unrecognized hiatuses between dated layers (Table 3.4; Table 3.5). The age of the high-amplitude reflections could be constrained where dated cores overlapped the sub-bottom profiler data. The ages of the reflectors were determined at each core site that penetrated mapped reflectors and then averaged. Linear extrapolation was used to determine the age of reflections below the limit of core penetration. The basal sedimentation rate of core 0067, which directly overlies each of the mapped reflections, was used for the extrapolation. The depths of the reflectors below core 0067 were determined in Kingdom Suite using an assumed velocity of 1500 m/s. These ages potentially overestimate the age of these reflections, as sedimentation rates were likely significantly higher directly after the LGM with more sediments entering the seaway from the receding ice front (Andrews et al., 1985; Bellwald et al., 2019). Background sedimentation rates were determined by excluding deposits interpreted to be instantaneous.

3.4 Results

3.4.1 Seafloor morphology

Multibeam bathymetric data along with the available sub-bottom profiler data reveal diverse glacial and postglacial landforms, including glacially molded sediments and glacially sculpted bedrock outcrop, and relatively flat basin floors surrounded by steep flanks along the seaway walls (Figure 3.4). Based on the largest-scale bathymetric morphology, the seaway can be separated into *western*, *central*, and *eastern* regions that have a distinct distribution of seafloor landforms (Figure 3.4).

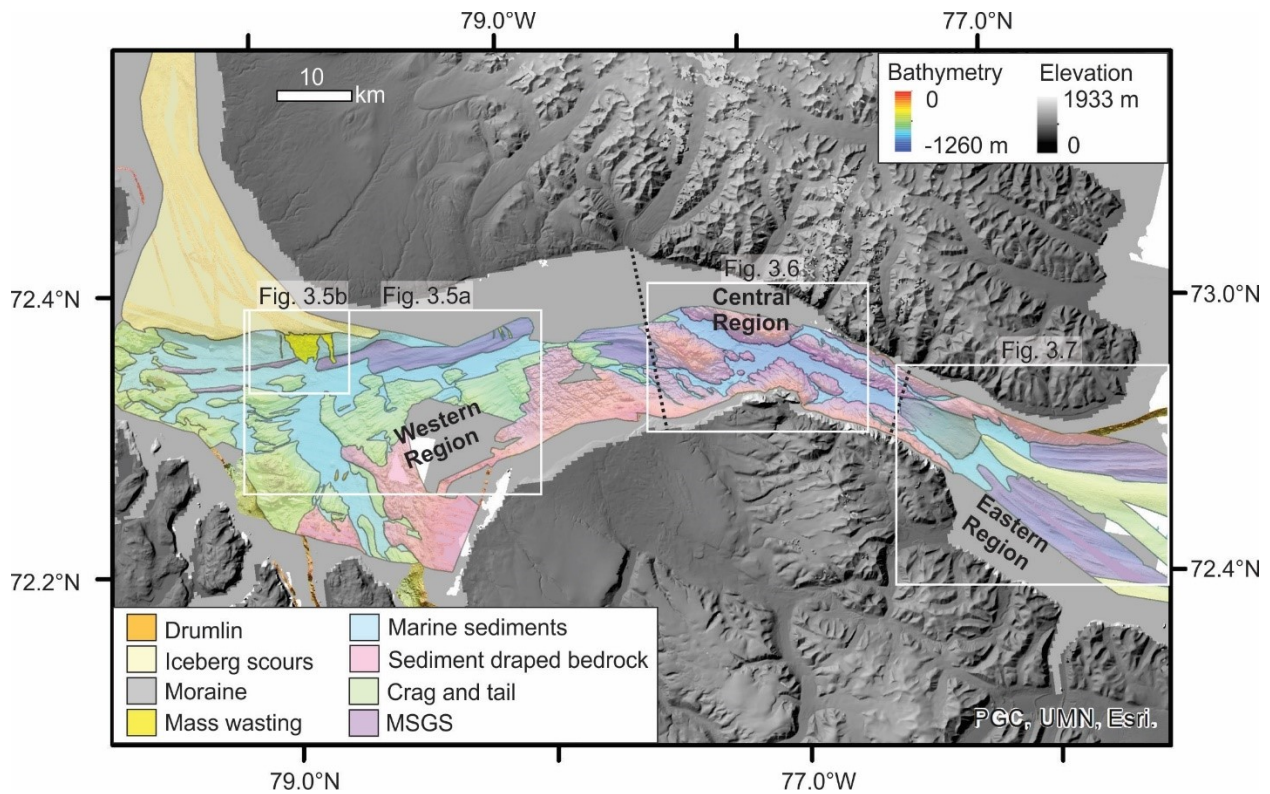


Figure 3.4: Seafloor morphology map of Pond Inlet showing glacial landforms, bedrock outcrop, and sedimentary basins. Pond Inlet and Eclipse Sound are divided into a Western Region, Central Region and Eastern Region based on the relative abundance of these landforms. Locations of Figure 3.5a, Figure 3.5b, Figure 3.6 and Figure 3.7 are denoted by white boxes. The dashed lines indicate separations of the regions. Multibeam bathymetry collected by OMG as part of ArcticNet (2005-2008). DEM(s) created from DigitalGlobe, Inc. imagery.

The *western region* includes Eclipse Sound (Figure 3.4) and is dominated by sediment draped bedrock and glacial landforms including crag and tail features and drumlins (Brouard and Lajeunesse, 2019; Dowdeswell et al., 2016) (Figure 3.5a) which are draped by up to 13 m of postglacial hemipelagic marine sediment (Figure 3.5c; Figure 3.5d). Including the postglacial sediment, the height of those landforms reaches up to 685 m. Zones of glacial landforms are separated by isolated sedimentary basins containing up to 45 m of stratified sediment overlying acoustic basement (Figure 3.5d). The floors of those basins range from 575-775 m below sea level (bsl). The slope entering Eclipse Sound from Navy Board Inlet contains gullies and mass movement scars caused by sediment eroding the seafloor and moving downslope (Figure 3.5b). The gullies to the east (Figure 3.5a) are aligned with glacier-fed rivers that flow southward on Bylot Island (Figure 3.4).

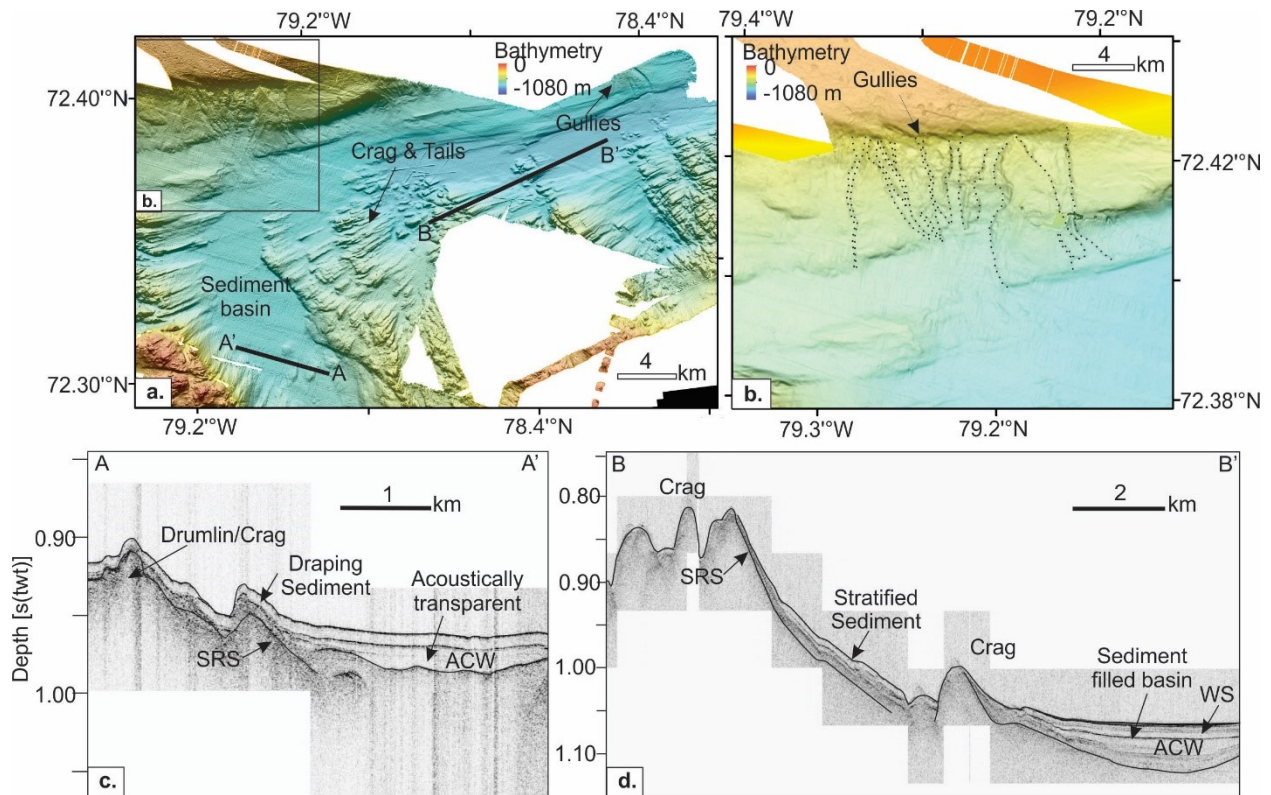


Figure 3.5: Western region of Pond Inlet showing (a.) multibeam bathymetry with crag and tail features, sediment basins, and slide scars and gullies, (b.) multibeam bathymetry with slide scars and gullies along the northwestern slope of Pond Inlet at its confluence with Navy Board Inlet, (c.) sub-bottom data with drumlins draped by sediment and an acoustically transparent ACW unit, and (d.) sub-bottom profiler data with crag and tail features draped with sediment and a sediment basin. Multibeam bathymetry collected by OMG as part of ArcticNet (2005-2008).

The *central region* of Pond Inlet has the greatest relief (up to 930 m from shoals to basin floors) and is composed of deep troughs surrounded by bedrock outcrops with steep flanks (Figure 3.6). The troughs are mostly flat-floored and the bedrock outcrops exhibit a rough surface in multibeam bathymetry; the rugose surface likely represents bedrock draped by a veneer of sediment with limited thickness, as it is not imaged by the sub-bottom profiler data. Within the central region, the largest sedimentary basin, informally referred to here as “Pond Inlet Basin” (Figure 3.6), covers an area of approximately 110 km² and is filled by at least 75 m of deglacial and postglacial sediment, distinguished by the acoustic facies from the sub-bottom profiler data discussed in section 4.3. Another smaller perched sedimentary basin, referred to as “Perched Basin”, occurs NE of Pond Inlet Basin between a bedrock outcrop and the steep flanks of Bylot

Island (Figure 3.6). Perched Basin covers an area of 17 km² and is filled by at least 65 m of deglacial to postglacial sediment. Within Pond Inlet Basin there is a 3.5 km-long escarpment that crosses almost the entire basin floor at a normal angle with a southeastward 7° slope (Figure 3.6). It has a relief of approximately 20 m in sub-bottom profiler data. This escarpment appears to continue as a lineament through the adjacent bedrock outcrop in Pond Inlet for approximately 7 km to the NE and for approximately 4.5 km to the SW.

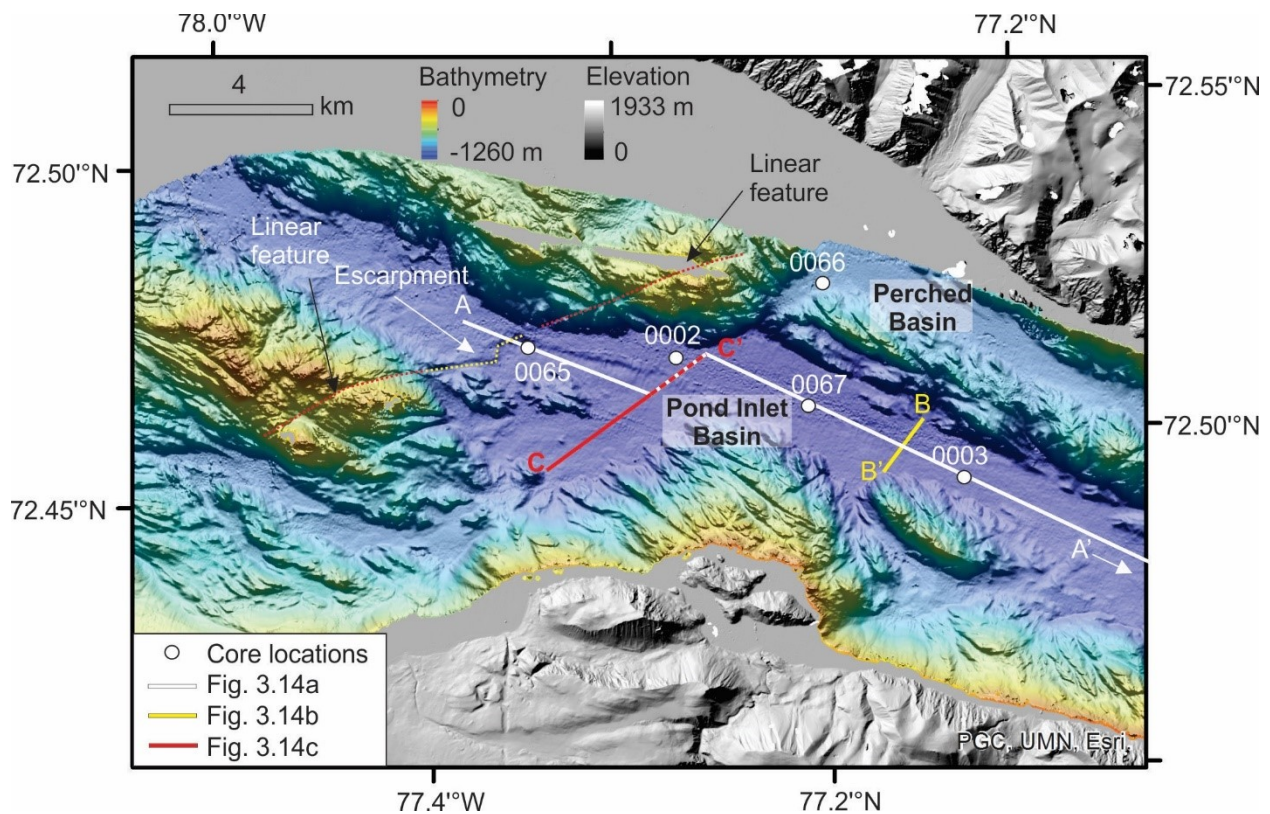


Figure 3.6: Multibeam bathymetry of central Pond Inlet showing the location of Pond Inlet Basin and Perched Basin. The surface expression of the escarpment west of core 0065 is denoted by a dashed line. Core locations and locations of sub-bottom profiler lines from Figure 3.14a, Figure 3.14b, and Figure 3.14c are denoted. Multibeam bathymetry collected by OMG as part of ArcticNet (2005-2008). DEM(s) created from DigitalGlobe, Inc. imagery.

The seafloor in the eastern portion of Pond Inlet is dominated by mega-scale (>30 km long) glacial lineations (MSGSL) and iceberg scours (Figure 3.7a). A prominent 5 km-long crescent-shaped ridge, interpreted as a moraine, and also recognized by Brouard and Lajeunesse (2019), is apparent at the eastern entrance of Pond Inlet (Figure 3.7a). In sub-bottom profiler data, the

observable relief ranges from 45-60 m on either side of the ridge; it is draped by postglacial sediment which ranges from 1 to 18 m thick (Figure 3.7b). East of this ridge, up to 11 m of postglacial sediment drapes the elongated ridges of the MSGs and up to 33 m of sediment infills their troughs (Figure 3.7c).

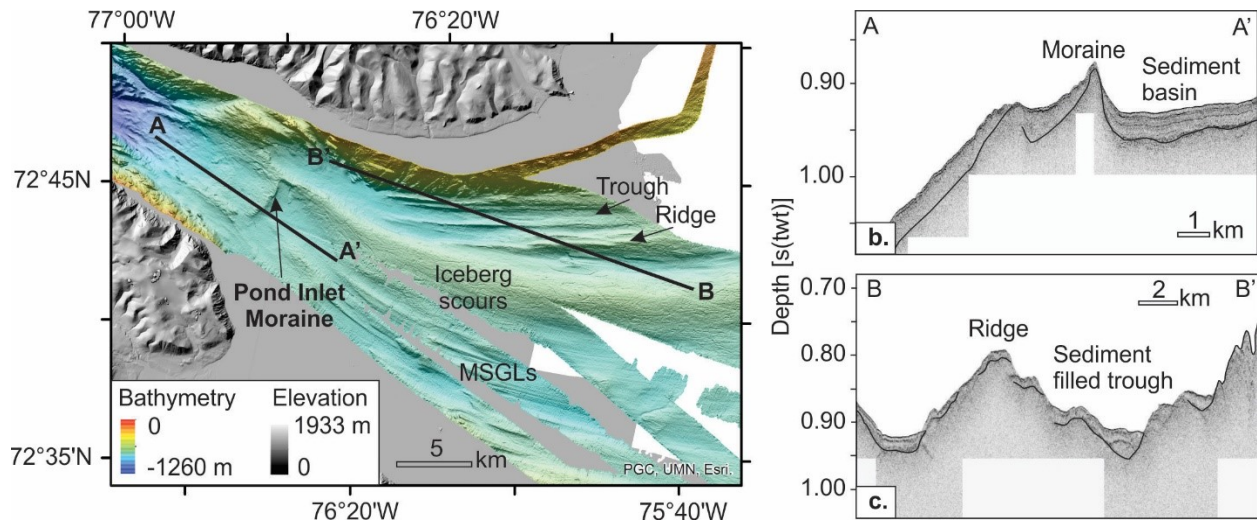


Figure 3.7: (a.) Multibeam bathymetric map of the eastern region of Pond Inlet showing the glacial landforms including the Pond Inlet moraine, MSGs and iceberg scours. (b.) Sub-bottom profiler line showing the moraine and sediment filled basin to the East from A to A'. (c.) Sub-bottom profiler line showing ridge and troughs associated with MSGs from B to B'. Multibeam bathymetry collected by OMG as part of ArcticNet (2005-2008). DEM(s) created from DigitalGlobe, Inc. imagery.

3.4.2 Lithostratigraphy

Six lithofacies are identified based on sedimentary structures, physical properties, colour and grain size (Table 3.3; Figure 3.8). Lithofacies 1 (L1) is the most abundant lithofacies, comprising 68% of thickness of the total length of all cores. L1 is composed of massive to weakly stratified, bioturbated, olive-grey to dark grey silty mud (Figure 3.8). L1 is interpreted to represent hemipelagic deposition. Lithofacies 2 (L2), contributing 2% of core sediments, is similar to L1 except it contains ice rafted debris (IRD) (Figure 3.8; Figure 3.9). IRD makes up 1-12% of the total sediment in L2 and ranges in size from sand to gravel.

Lithofacies 3-6 are interpreted to be the product of non-glacial gravity flow processes.

Lithofacies 3 (L3) is only observed in core 0067, comprising 15% of that core and 4% of the total recovered core material, and is composed of olive-grey inclined stratified mud with inclined parallel laminations up to 25° (Figure 3.8). Lithofacies 4 (L4) comprises the majority of core 0065 and makes up 12% of all cored sediments. L4 is composed of olive-grey to dark-grey folded silty-mud and displays convoluted silt/sand laminations, and sharp, angled contacts (Figure 3.8). Lithofacies 5 (L5) makes up approximately 4% of the cored sediments and is composed of olive-grey clast-supported monomict mudclast conglomerate with a mud-silt matrix and subrounded to rounded mudclasts (Figure 3.8). Lithofacies 6 (L6) comprises 9% of the core sediments and consists of laminated silt/sand deposits. L6 deposits are dominated by sand or silty-mud, show an erosive base with sharp basal contact, and are normally graded. L6 facies are parallel and cross-laminated, with some wavy discontinuous laminations (Figure 3.8; Figure 3.9).

The typical lithofacies succession within Pond Inlet Basin consists of the following: the lowermost units consist of massive units of olive-grey to dark grey mud with IRD (L2), which is overlain by units of massive to laminated olive-grey to dark grey mud (L1). L1 is interrupted by units of inclined stratified mud (L3), folded mud (L4) or clast-supported mudclast conglomerates (L5) which are overlain by sorted sand/silt deposits with sharp to erosive bases (L6) (Figure 3.10). L1 is also interrupted by <1 cm to 47 cm thick L6 deposits. The top of the piston cores and the entire interval of the box core consists of massive olive-grey bioturbated mud (L1).

The twelve radiocarbon ages indicate the cored sediments are Holocene in age with the oldest calibrated radiocarbon date of 10.0 ± 0.3 ka cal BP from forams within an L1 deposit near the base of core 0065 (Figure 3.10; Table 3.2). However, the sediments that fill the basin extend well

beyond the oldest radiocarbon date and are discussed further in the Acoustic Stratigraphy section Chapter 3.4.3. The only lithofacies with a distinct age range are L2 deposits, which occurs at the base of core 0065 and 0066 from 10.7-9.8 ka BP. From the age model derived here (chp.3.3.5), the average background sedimentation rate, which excluded instantaneous events (L5 & L6 deposits), is approximately 0.9 mm/yr for cores 0065, 0067, 0002 and 0003 in Pond Inlet Basin and 0.6 mm/yr for core 0066 in Perched Basin (Figure 3.11; Table 3.4; Table 3.5). Sedimentation rates reach a maximum of 2.2 mm/yr from 3.3-1.6 ka BP in the centre of Pond Inlet Basin at core site 0067 (Figure 3.11; Table 3.4).

Table 3.3: Properties of lithofacies L1 to L6 observed in cores from Pond Inlet including thickness, sedimentary structures, colour, bioturbation, magnetic susceptibility, bulk density, and their interpretation.

Lithofacies	Thickness (cm)	Sedimentary structures	Colour	Bioturbation	Average magnetic susceptibility (10^{-5} SI Units)	Average bulk density (g/cm^3)	Interpretation
L1: massive to parallel-laminated mud	4-224	Predominantly massive, with some parallel laminations	Olive-grey to dark-grey	Low-high	214 ± 92	1.59 ± 0.12	Hemipelagic
L2: massive mud with ice rafted detritus	3-24	Mud matrix, with subrounded IRD clasts	Olive-grey	Moderate	151 ± 28	$1.83 \pm .06$	Hemipelagic with IRD
L3: Inclined stratified mud	151	Inclined parallel laminations	Olive-grey	Low	98 ± 6	$1.60 \pm .02$	MTD (Slump)
59 L4: folded mud	486	Highly deformed, folding, inclined laminations	Olive-grey to dark-grey	Moderate	164 ± 24	1.69 ± 0.4	MTD (slide)
L5: monomict mudclast conglomerate	11-26	Clast supported, subrounded monomict mudclasts. Sandy mud to mud matrix	Olive-grey	Low	331 ± 82	1.77 ± 0.18	MTD (Flow/avalanche)
L6: sorted sand and silt deposits	1-47	Parallel/cross laminations, normally graded to massive. Occasional climbing ripples and fluid escape structures.	Olive-grey	Low-moderate	405 ± 179	1.88 ± 0.18	Turbidite

Table 3.4: Sedimentation rates from cores in Pond Inlet Basin over the Holocene for the dated intervals of the five piston cores (0065, 0067, 0002 and 0003) produced from the age model including their depth range and calibrated radiocarbon dates for each interval. Instantaneous deposits that occur over the depth range are not included in sedimentation rate calculation. Sedimentation rates for each interval in these cores are averaged to produce an average sedimentation rate for Pond Inlet Basin.

Core	Depth range (cm)	Calibrated age range (ka cal BP)	Sedimentation rate (mm/yr)	Instantaneous deposit intervals (cm)
0065	0-49	0-0.9	0.62	
0065	50-119	0.9-2.1	0.32	61-95
0065	120-207	2.1-2.5	1.83	130-132
0065	208-247	2.5-3.6	0.37	216-219
0065	248-766	3.6-10.0	0.78	255-263, 750-754
0067	0-163	0-1.6	1.12	104-106
0067	164-589	1.6-3.3	2.17	225-228, 433-481
0002	0-34	0-0.7	0.48	23-32
0003	0-206	0-2.9	0.69	
Average sedimentation rate (mm/yr)			0.9	

Table 3.5: Sedimentation rates from cores in the Perched Basin over the Holocene for the dated intervals of piston cores 0066 produced from the age model including their depth range and calibrated radiocarbon dates for each interval. Instantaneous deposits that occur over the depth range are not included in sedimentation rate calculation. Sedimentation rates for each interval in core 0066 are averaged to produce an average sedimentation rate for Perched Basin.

Core	Depth range (cm)	Calibrated age range (ka cal BP)	Sedimentation rate (mm/yr)	Instantaneous deposit intervals (cm)
0066	0-13	0-0.9	0.69	
0066	14-124	0.9-3.7	0.38	21-24, 104-107
0066	125-531	3.7-9.4	0.67	132-139, 242-244, 332-333, 422-425, 463-466, 516-519, 529-530
Average sedimentation rate (mm/yr)			0.6	

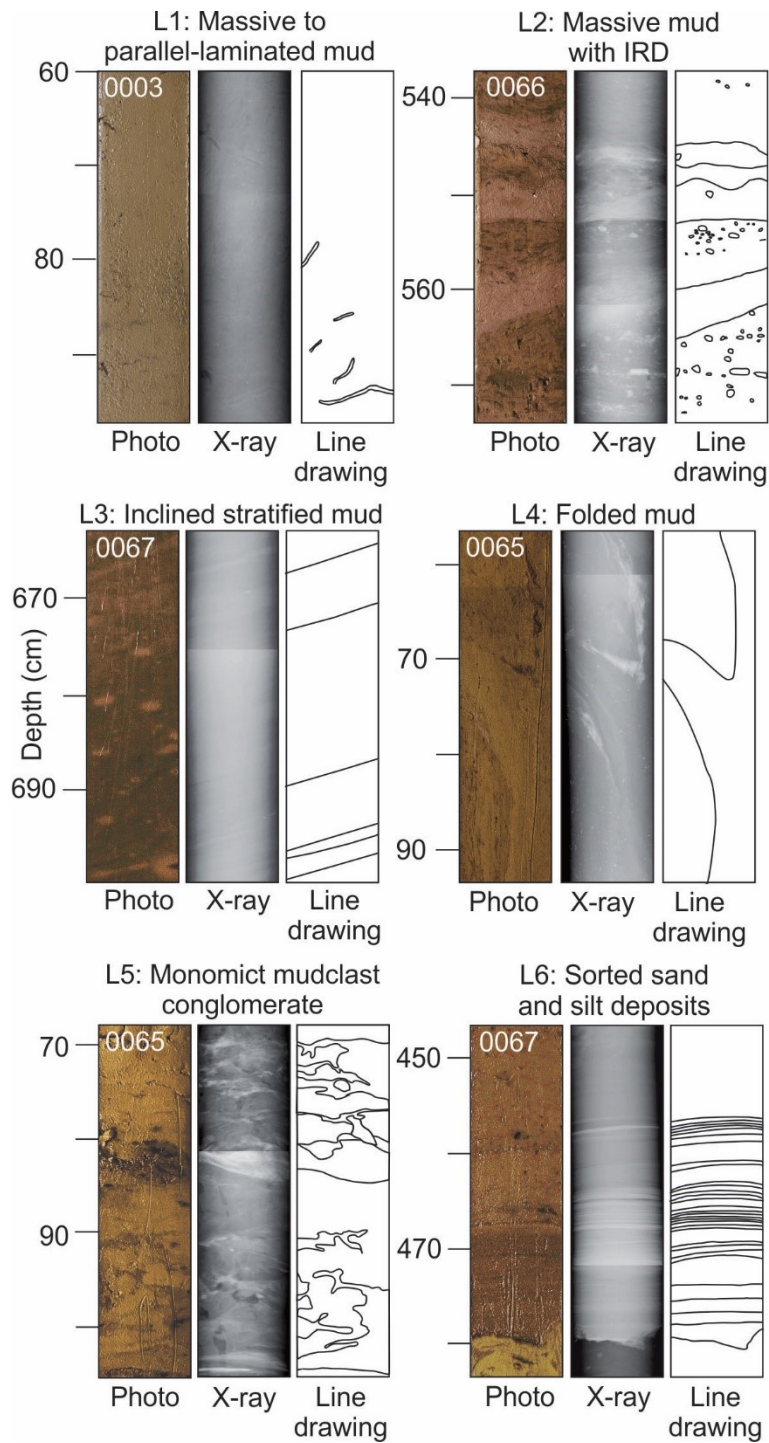


Figure 3.8: Lithofacies photos, x-rays, and line drawings for the 6 lithofacies (L1 through L6) from core 0003, 0066, 0067, and 0065.

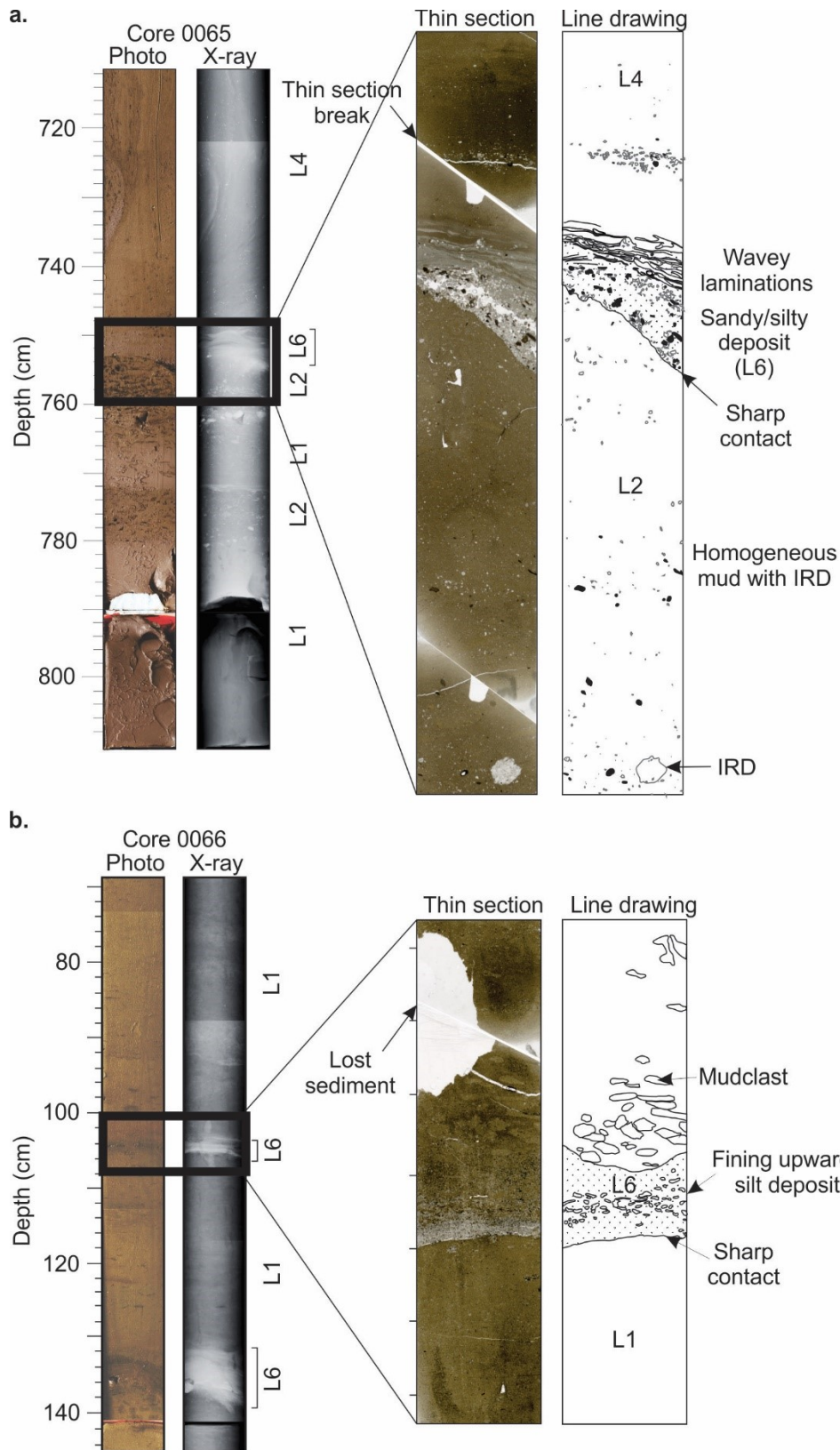


Figure 3.9: Thin section and line drawing from core 0065 and 0066 showing thin (cm thick) L6 deposits, mudclasts, and IRD. Artifacts from producing thin sections include thin section breaks and lost sediments.

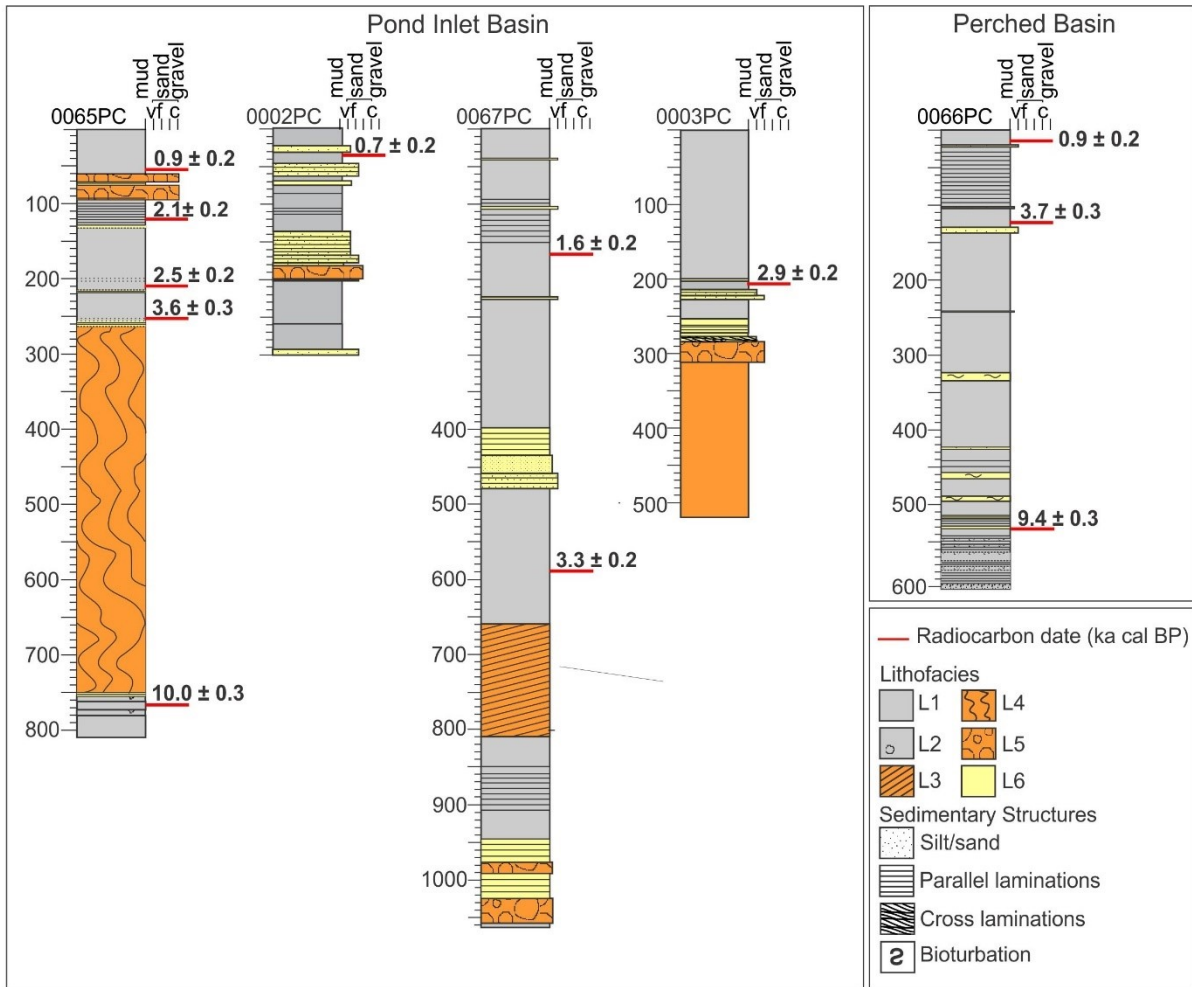


Figure 3.10: Stratigraphic columns of the five piston cores from Pond Inlet Basin and Perched Basin showing the six lithofacies (L1 through L6), sedimentary structures, and calibrated radiocarbon dates (in ka cal BP).

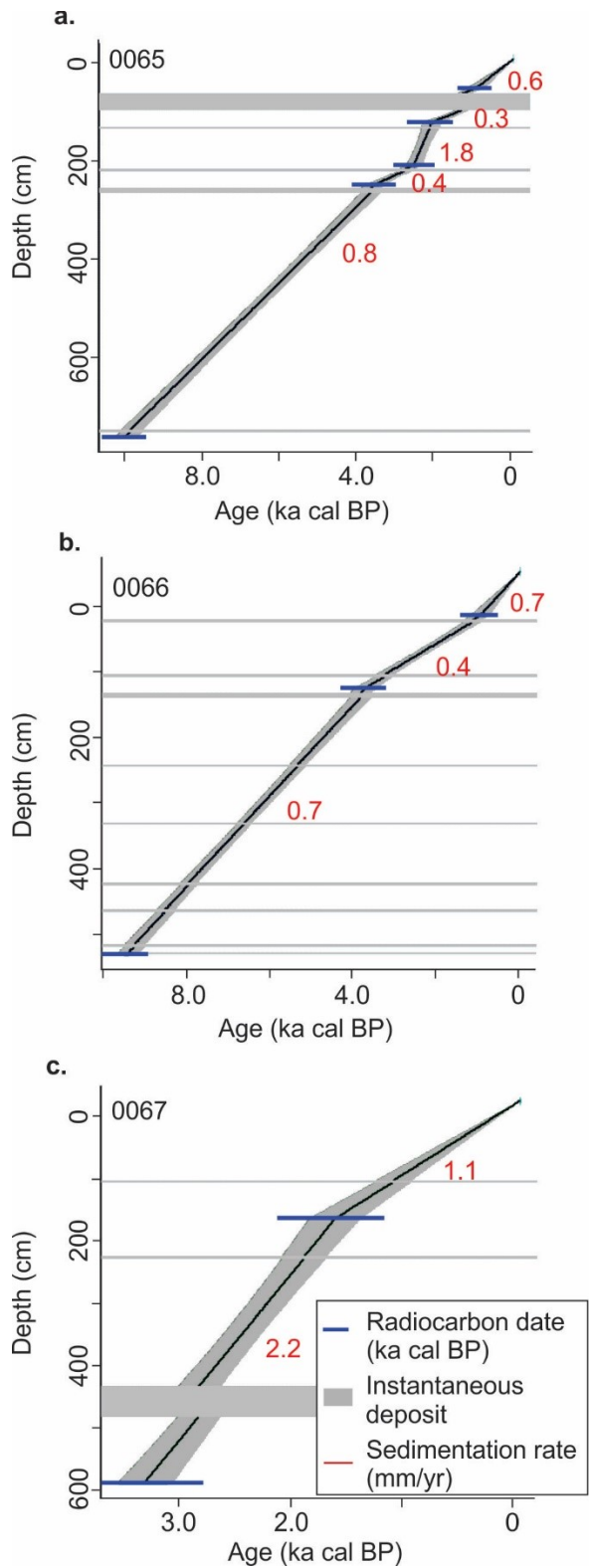


Figure 3.11: Age models (derived using Blaauw, 2010; version 2.2) for (a.) core 0065 with five radiocarbon dates and four instantaneous deposits. (b.) core 0066 with three radiocarbon dates and nine instantaneous deposits. (c.) core 0067 with two radiocarbon dates and three instantaneous deposits. Radiocarbon dates are plotted with 2-sigma error.

3.4.3 Acoustic Stratigraphy

Acoustic Facies

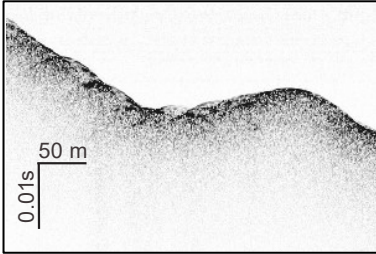
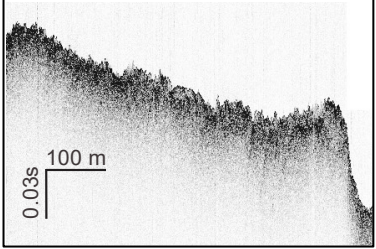
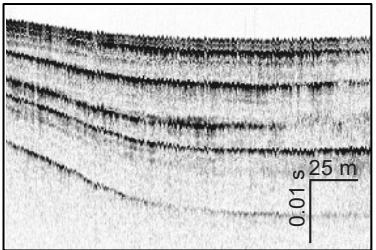
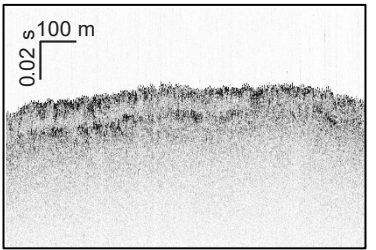
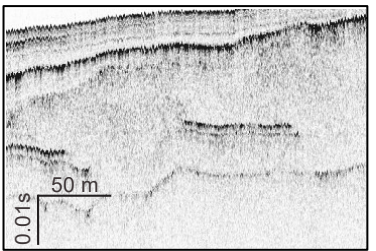
Three acoustic facies are identified from the sub-bottom profiler data in Pond Inlet based on the geometry, amplitude, continuity, and termination of reflections (Sangree and Widmier, 1979) (Table 3.6). These include a prolonged strong reflection facies, acoustically well stratified facies, and acoustically chaotic to reflection-free facies.

The prolonged strong reflection facies is composed of a single moderate to high-amplitude reflection that is laterally continuous over tens of kilometres and shows variable relief and lack of acoustic penetration. This facies is subdivided into a Strong Reflection Smooth (SRS) and a Strong Reflection Rough (SRR) subfacies. Within SRS, the reflection shows smooth to hyperbolic reflection geometries, while in SRR the reflection has a rough morphology (Table 3.6). The prolonged strong reflection facies is not penetrated by core samples, however it is interpreted to represent bedrock, indurated sediment (exhumed sediments or till), or poorly sorted or massive coarse-grained sediments (Damuth, 1980).

The Well Stratified facies (WS) is acoustically well stratified with moderate to strong continuous internal reflections that are parallel or diverging (Table 3.6). The lower extent of WS in some locations is beyond the penetration depth of the sub-bottom profiler data, restricting observations of its geometry. Where geometries can be observed, WS forms lens-shaped bodies and draping units that onlap or pinch out (Figure 3.12a; Figure 3.12b). WS is penetrated by all five piston cores (Figure 3.12a; Figure 3.12b; Figure 3.13) and the box core. In cores, the facies corresponds to undisturbed, stratified sediments punctuated by sand/silt deposits (L1, L2 & L6).

The third acoustic facies is an acoustically chaotic to transparent facies, which consists of discontinuous, chaotic, or transparent internal reflections (Table 3.6). Based on distinct changes in geometry, this facies is subdivided in an Acoustically Chaotic Draping subfacies (ACD) that drapes underlying units and is not penetrated by piston cores (Fig 12c), and an Acoustically Chaotic Wedge subfacies (ACW) unit which forms wedge and lens shaped bodies (Figure 3.13). ACD is interpreted to represent undisturbed sediment due to its draping geometry. ACW is penetrated by piston cores 0003 and 0065 (Figure 3.13) and corresponds to disturbed sediments (L4 and L5). Given these sedimentological characteristics and reflection geometry, ACW is interpreted as mass transport deposits (MTDs).

Table 3.6: Examples and descriptions of acoustic facies for Pond Inlet (SRS, SRR, WS, ACW and ACW) and their occurrence and interpretation.

Acoustic facies	Example	Description	Occurrence & Interpretation
Strong Reflector Smooth (SRS)		Prolonged strong reflection with a smooth or hyperbolic reflection geometry	Occurs below WS and ACD units in basinal settings and outcrops at surface. Interpreted as bedrock.
Strong Reflector Rough (SRR)		Prolonged strong reflection with rough reflection geometry	Occurs as a shallowly buried reflection underlying ACD to the NE and appears at the surface. Interpreted as till.
Well Stratified (WS)		Acoustically well stratified with continuous, medium-high amplitude reflections that are parallel to diverging. Some show lens shaped geometries that onlap or pinch out	Occurs in basinal settings within the LU and UU. Interpreted as ice-proximal and postglacial sediments.
Acoustically Chaotic Draping (ACD)		Thin acoustically chaotic unit with low to moderate amplitude, discontinuous, chaotic reflections. Drapes underlying units.	Occurs to the NE over iceberg turbated seabed. Interpreted as postglacial sediments.
Acoustically Chaotic Wedge (ACW)		Acoustically chaotic to reflection-free facies with low to moderate amplitude, discontinuous or absent reflections. Lens and wedge-shaped bodies	Occurs in basinal settings interrupting units of WS. Interpreted as MTDs.

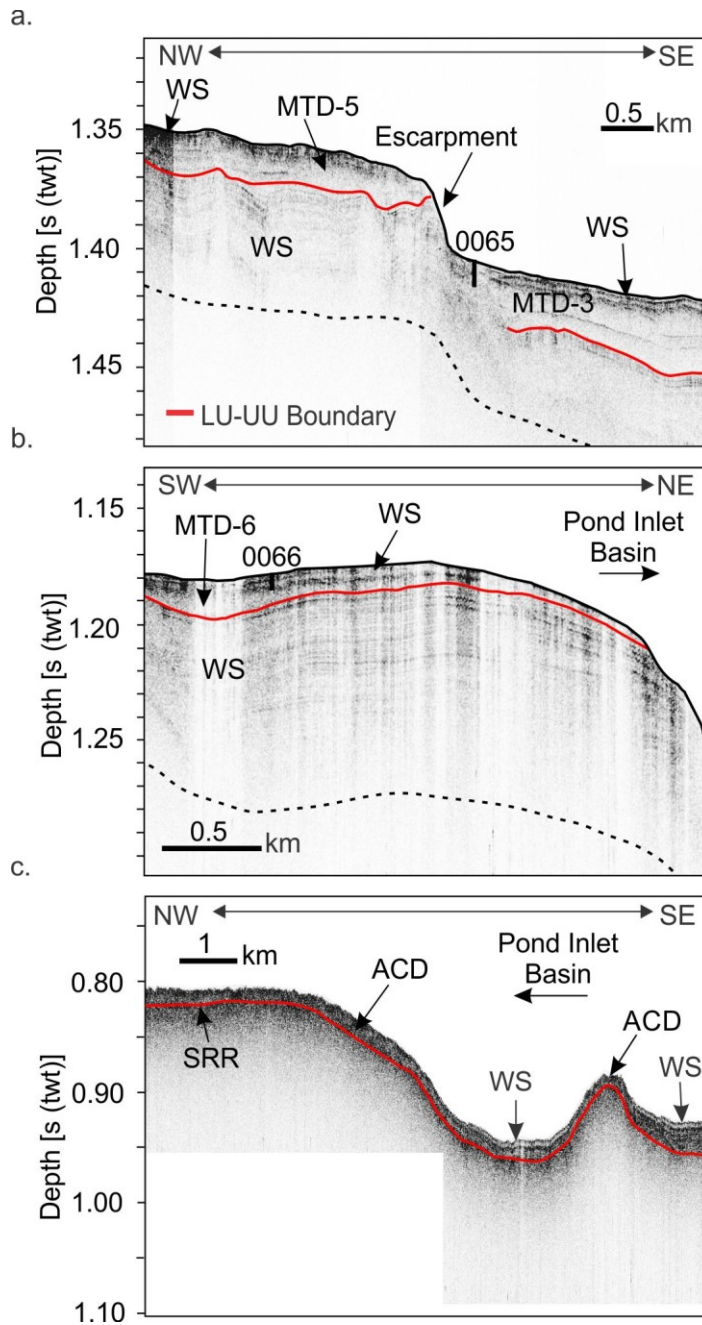


Figure 3.12: Sub-bottom profiler lines showing (a.) the acoustic facies above the escarpment including WS, ACW, MTDs and core site 0065 and the Lower Unit-Upper Unit (LU-UU) Boundary, (b.) acoustic facies WS, ACW, MTDs and the LU-UU Boundary at core site 0066 in Perched Basin, and (c.) acoustic facies to the SE of the moraine including SRR, ACD transitioning laterally in WS in bathymetric lows, and the LU-UU Boundary. Dashed line demarks depth of acoustic penetration.

Acoustic Stratigraphy Units

The acoustic stratigraphy was developed through lateral correlation of acoustic facies with guidance from lithofacies revealed in core. The sedimentary succession in the basins is divided into two distinct stratigraphic units. The type section for the acoustic stratigraphy is shown in the regional sub-bottom line from the escarpment in the centre of Pond Inlet to the moraine to the southeast (Figure 3.7a; Figure 3.13). Enlarged profiles provided in Figure 3.14 show these units in more detail.

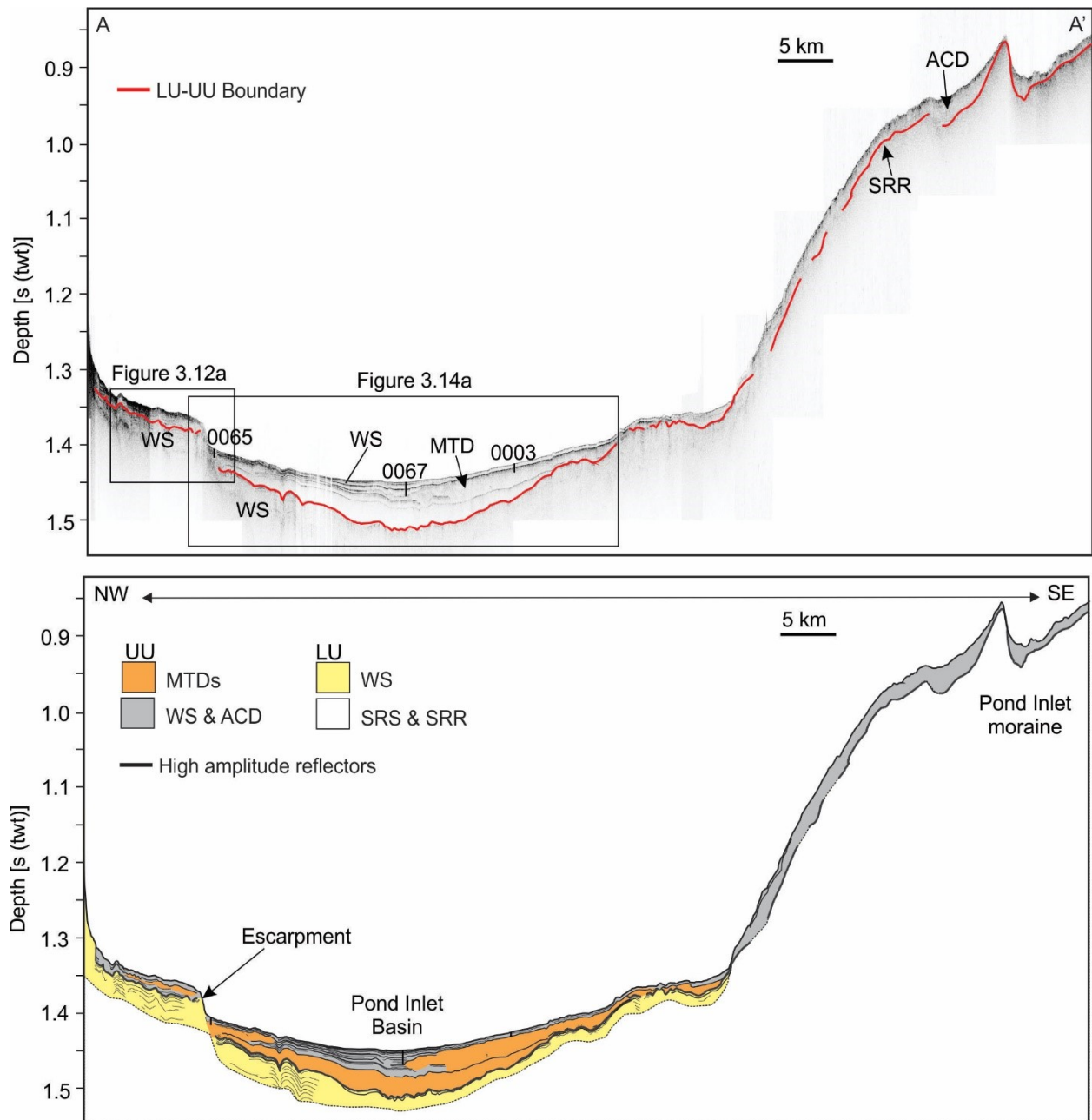


Figure 3.13: Regional acoustic line from Pond Inlet Basin from the Central Basin to the moraine towards the Southeast showing the acoustic facies, LU-UU boundary and escarpment. Locations of Figs. 12a and 14a are denoted.

Lower Stratigraphic Unit

The lower stratigraphic unit (Lower Unit) varies laterally between acoustic basement (SRR) and acoustically well stratified sediments (WS), which extend below the limit of acoustic penetration (Figure 3.13; Figure 3.14a). The maximum resolvable thickness of the Lower Unit is approximately 45 m. In general, the upper part of Lower Unit consists of WS and transitions gradually below into an acoustically chaotic facies. WS is observed within Pond Inlet Basin and Perched Basin, but is absent towards the SE of Pond Inlet (Figure 3.13). The internal reflections of WS taper off laterally in Pond Inlet Basin (Figure 3.14a), and in Perched Basin the reflections converge and terminate downslope towards Pond Inlet Basin (Figure 3.12a). Towards the SE, SRR is the predominant facies of the Lower Unit. The boundary between Lower Unit-Upper Unit is characterised by a strong continuous reflection, and the internal reflections of WS of the Lower Unit are conformable with this boundary (Figure 3.14a).

Upper Stratigraphic Unit

The upper stratigraphic unit (Upper Unit) is composed of WS subfacies draping acoustically chaotic deposits (ACD), and acoustically chaotic wedge and lens shaped deposits (ACW) that are interpreted to represent MTDs (Figure 3.13). The sediments of the Upper Unit smooth the irregular surface of the Lower Unit-Upper Unit boundary (Figure 3.14). Sediments of the Upper Unit have a maximum resolvable thickness of approximately 47 m. In Pond Inlet and Perched Basin, the Upper Unit consists of WS interrupted by the MTD facies. To the SE, the acoustically chaotic draping facies (ACD) dominates.

In Pond Inlet and Perched Basin (Figure 3.10a), WS occurs within bathymetric lows where basinal sediments can accumulate. In Pond Inlet Basin, this facies can be traced for at least 26

km, limited by the extent of sub-bottom profiler data, and reaches a maximum thickness of 47 m in the centre of the basin. Above the escarpment, thicknesses of the WS reach approximately 17 m (Figure 3.12a), and in Perched Basin, this facies reaches a thickness of 46 m (Figure 3.12b). Deposition of WS in the Upper Unit is bounded below by the Lower Unit-Upper Unit boundary and above by the seafloor.

Within the WS interval, prominent moderate to high amplitude internal reflections correspond to sand beds (L6 deposits) where they are intersected by core (Figure 3.15). These reflections onlap or pinch out against the Lower Unit-Upper Unit boundary or the acoustic basement (Figure 3.14). In Pond Inlet Basin, these reflections can be traced for up to 22 km and the sand beds reach thicknesses up to 47 cm in core 0067. Like other laterally extensive marker units, its almost ubiquitous distribution provides an important constraint on the relative timing of sediment deposits throughout the inlet. Approximate ages were extrapolated from sedimentation rates from core 0067. The lowermost high-amplitude reflection can be traced from its termination below the escarpment in the NW to the Lower Unit-Upper Unit boundary in the SE where it onlaps onto the boundary in the sub-surface. This reflection is interpreted to have a maximum age of 12.7 ka BP (Figure 3.14a). Eight more high amplitude reflections can be traced above the lowermost reflection. Within Perched Basin, three internal reflections were traced for up to 2 km, limited by the sub-bottom profiler data extent. The majority of the L6 deposits in core 0066 are 1-6 cm thick and could not be resolved by the sub-bottom data. The lowermost high-amplitude reflector can be followed for 2 km. Core 0066 penetrates sediments just above this lowermost reflector (Figure 3.12b). From the age model, the base of the core has a maximum age of 10.7 ka BP, which provides a maximum age estimate for this lowermost reflector.

In Pond Inlet and Perched Basin, WS is interrupted by wedge and lens shaped bodies of the ACW facies interpreted to be MTDs (Figure 3.12b; Figure 3.14). These deposits can be traced for 16 km and reach thicknesses of 21 m. They pinch out against acoustic basement and pinch out against or truncate reflections of WS. The MTDs are bound above by onlapping or conformable moderate to high-amplitude reflections of WS (Figure 3.14). In Pond Inlet Basin, five MTDs are recognized (MTD-1 to MTD-5) and they reach 21 m in thickness and can be traced for 16 km (Figure 3.14). Within Perched Basin, the WS interval is underlain by a 10 m thick MTD (MTD-6) that can be traced for at least 2 km, limited by the extent of sub-bottom profiler data (Figure 3.12b). Outside of Pond Inlet and Perched Basin, other MTDs are recognized at the base of the Upper Unit within sediment-filled basins in the western region. Those MTDs are also overlain by WS (Figure 3.5b).

Towards the moraines in the SE, ACD is observed draping the acoustic basement (Figure 3.12c; Figure 3.13). The draping unit of ACD facies ranges in thickness from 8-25 m and can be traced from the moraine in eastern Pond Inlet into Baffin Bay. This draping facies conformably follows the underlying relief of the acoustic basement, thickens in depressions, and is bounded below by SRR. The upper reflection of ACD is rough and this facies gradually transitions laterally into WS where thicker sedimentary fill is present. Based on this geometry, ACD is interpreted to represent postglacial hemipelagic mud.

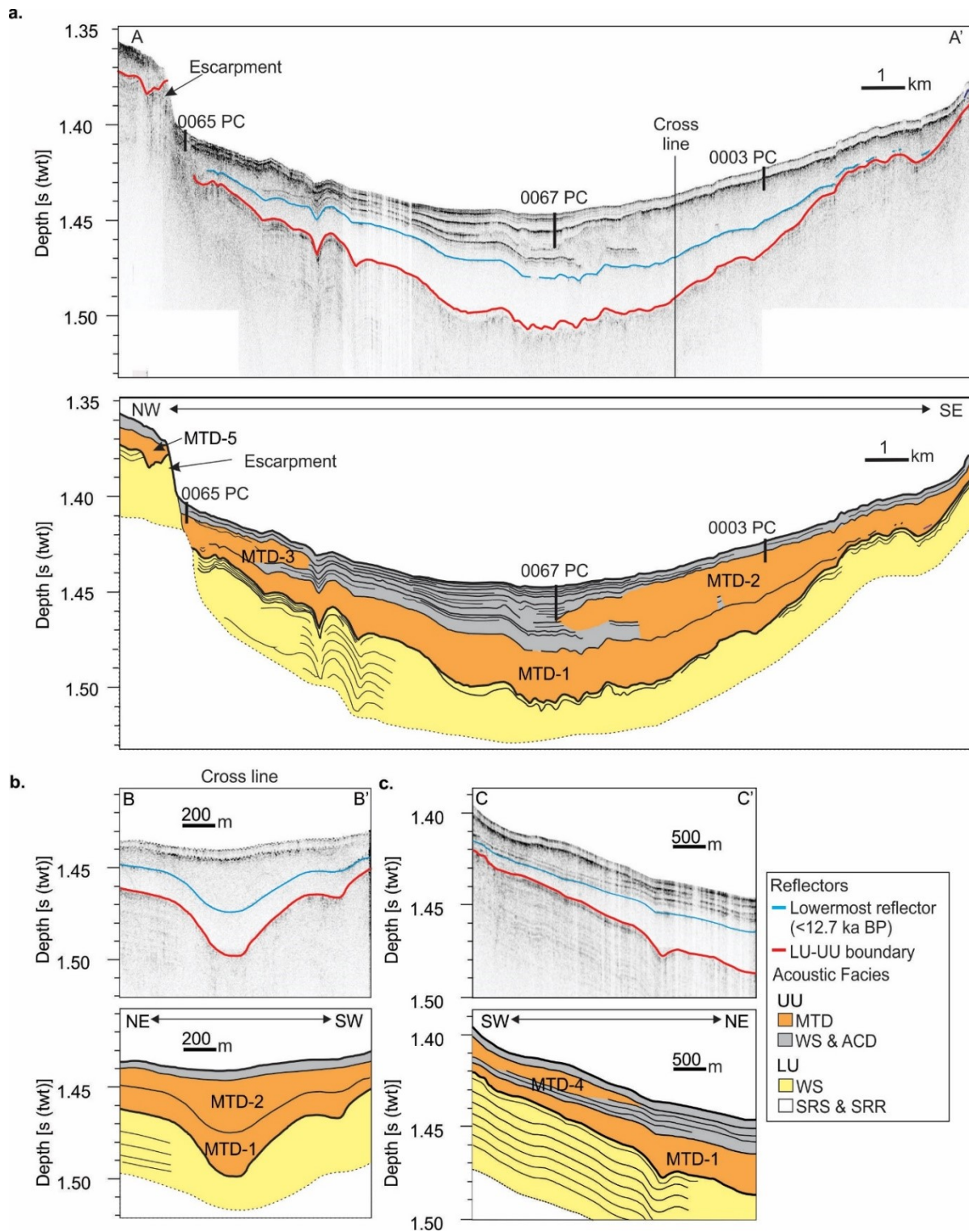


Figure 3.14: (a.) Sub-bottom profiler line for Pond Inlet Basin showing the acoustic facies including WS, ACD, MTDs, SRS and SRR of the lower unit (LU) and upper unit (UU), along with the lower most moderate-high amplitude reflection of the UU and the LU-UU boundary reflection. (b.) Sub-bottom line that crosses Figure 3.14a showing the high amplitude reflections acoustic facies (WS, MTDs), lowermost moderate-high amplitude reflection and the LU-UU boundary reflection (c.) Sub-bottom line showing the acoustic facies SE of Figure 3.14a showing the lowermost high amplitude reflection, the LU-UU boundary reflection and the acoustic facies (WS and MTDs).

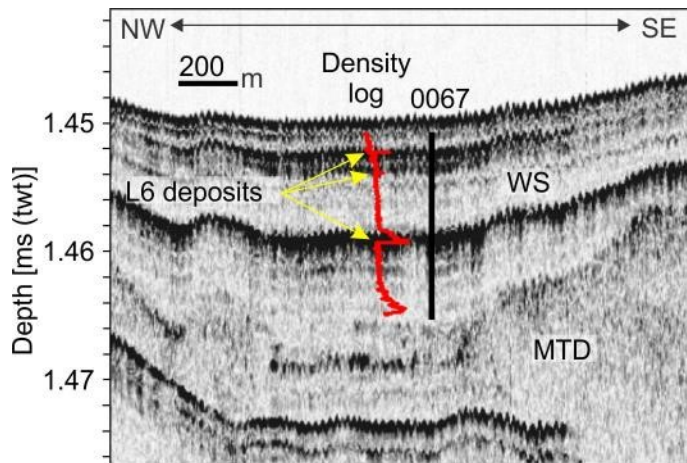


Figure 3.15: Piston core to sub-bottom profiler data tie showing the density log beside the core location highlighting the L6 deposits that correlate with the high amplitude reflections.

3.5 Discussion

3.5.1 Interpretation of the Lower and Upper Stratigraphic Units

Upper Stratigraphic Unit: Glacial to Paraglacial sedimentation

Where acoustic penetration allows, the base of the Lower Unit is defined by smooth to rugose strong reflections, which are interpreted to be bedrock, glacial till, and, in some places, glacial marine sediment. Distinctions between the types of basement is limited by the power and resolution of the sub-bottom profiler data. Where acoustic basement becomes chaotic to reflection free, reflections of glaciomarine sediments may become weak or absent due to a loss of energy of the seismic source. The sub-bottom profiler character where bedrock outcrops at the seabed in multibeam bathymetry data (Figure 3.6) shows prolonged strong reflections and large, irregularly spaced reflection hyperbolae (SRS) (Table 3.6). Therefore, it is reasonable to interpret that this acoustic facies, recognized in the sub-surface, represents bedrock. Based on regional mapping, the bedrock of the *western region* is likely a continuation of the Cretaceous to Tertiary sedimentary basin on western Bylot Island, and the bedrock of the *central* and *eastern regions* are likely Proterozoic and Archean bedrock (Jackson and Davidson, 1975; Oakey and

Chalmers, 2012). Towards the moraine in the SE, the acoustic character of outcropping basement changes to a rugose strong continuous reflection (SRR) interpreted as glacial till (Table 3.6). The till unit may represent multiple glacial advances which cannot be resolved with the available acoustic data; however, considering the new chronology presented here and previous research on glacial dynamics in the region (Brouard and Lajeunesse, 2017; Dyke, 2004), the uppermost portion of this till unit is potentially LGM and younger.

Above acoustic basement, the Lower Unit is thickest in Pond Inlet Basin. The superposition of well stratified sediments directly above bedrock and till suggest that these are glaciomarine sediments; the well stratified character suggests these deposits represent a transition from ice-proximal to ice-distal sedimentation (Syvitski and Praeg, 1989). This seismic reflection character has been observed in glacier-influenced regions including the St. Lawrence Estuary (Duchesne et al., 2010; Syvitski and Praeg, 1989) and Nordford, Norway (Hjelstuen et al., 2009) where strong, closely spaced reflections were indicative of alternating sand and muds beds. The acoustic data resolution and coverage is insufficient to determine if the sediments are ice-contact stratified drift or proglacial subaqueous fans; however, based on the modern water depth (1080 m), it is likely that the glaciogenic sediments were submarine. Areas where this unit is weakly stratified or massive could represent clay-dominated distal glaciomarine sedimentation (Syvitski and Praeg, 1989) or may indicate glacial till.

Upper Stratigraphic Unit: Postglacial sediments

The chronology of the uppermost stratigraphic unit is constrained by the extrapolated ages of the first high amplitude reflectors in the Central and Perched Basins. These provide maximum ages of the Upper Unit of 12.7 and 10.7 ka BP, following rapid retreat of the ice-sheet on northern Baffin Island according to Dyke and Hooper, (2001). The stratigraphic position above ice-

proximal sediments and the maximum age of 12.7-10.7 ka BP suggests the sediments of the Upper-Unit are postglacial. The entire Upper Unit within the Pond Inlet Basin and Perched Basin shows consistent acoustic character of the WS facies interrupted by the MTD facies and draping ACD deposits. WS is interpreted to represent hemipelagic deposits interbedded with turbidites. Core data shows the hemipelagic deposits include horizontally stratified and bioturbated L1 and L2 deposits with IRD. These sediments are interrupted by L6 silt/sand deposits, which correspond to the moderate-high amplitude internal reflections of WS. These reflections are characteristic of turbidites in postglacial sediments (e.g. Hjelstuen et al., 2009; St-Onge et al., 2012). Their associated L6 sand deposits in core correspond to the B through E divisions in the Bouma sequence (Bouma, 1962) and the centimetre thick silty-mud (L6) deposits are typical of fine grained turbidites (Piper and Stow, 1991). The ACD facies is interpreted to be basal muds of postglacial hemipelagic deposits. This is suggested by the draping geometry of this facies and the lateral transition of ACD into well stratified hemipelagic sediments (Figure 3.12c) (Syvitski and Praeg, 1989). The acoustically transparent nature of the facies may be due to iceberg turbation of the seabed, which could have homogenized any heterogeneity in the sediment, or they may be simply mud-dominated homogeneous sediments lacking impedance contrasts.

Damuth (1980) recognized mass transport deposits in 3.5 kHz echograms as convex lens and wedge shaped bodies that are transparent to chaotic and often overlie undisturbed acoustically stratified sediments. These characteristics are typical of the MTD facies deposits observed in the Upper Unit. A total of six MTDs are recognized in the acoustic stratigraphy of the Upper Unit within Pond Inlet Basin and Perched Basin. The erosive nature observed in some of these deposits indicates some have undergone transport. The transparent to chaotic acoustic character

suggests that most of the heterogeneity in sediment composition has been homogenized by sediment disturbance or mass movement.

A variety of MTD lithofacies are recognized in core, consisting of inclined stratified mud, folded mud, mudclast conglomerates, and massive mud. These lithofacies provide insight into the style of deposition. The inclined beds in core 0067 are interbedded with horizontally laminated hemipelagic muds of the same composition and colour and the inclination does not exceed 25° (Figure 3.8). This suggests that these sediments likely experienced a low degree of post-depositional deformation and could represent a small slump deposit (Tripsanas et al., 2008). In contrast, the folded mud deposit that makes up the majority of Core 0065 appears to have undergone a larger degree of post-depositional deformation. The deposit forms part of the wedge shaped MTD adjacent to the escarpment and comprises highly deformed dark to olive-grey mud with contacts of various inclinations. These sedimentological features and the supporting sub-bottom profiler data indicate that this deposit could be part of a high deformation slide (Tripsanas et al., 2008). The mudclast conglomerates (L5) indicate extensive break up of muddy sediment (Tripsanas et al., 2008). They are often found in association with overlying turbidites and could be part of a debris flow or debris avalanche deposit (Jenner et al., 2007). The widespread MTD penetrated by piston core 0003 appears as a massive mud deposit, indicating that either the disturbed material was composed of homogeneous mud, or any heterogeneity in the remobilized sediment was homogenized from mass movement or sediment disturbance.

3.5.2 Deglacial to postglacial depositional history

Glacial Maximum

Our investigation of the sedimentary record of Pond Inlet reveals a history from the Late Wisconsinan to present day. During the last glaciation, glacial ice occupying Pond Inlet and

Eclipse Sound was likely sourced from the LIS and local alpine and valley glaciers on Bylot and Baffin Islands (Klassen, 1993; Margreth et al., 2017). Radiocarbon ages from marine shells within glacially deposited sediment have indicated that the glacial ice reached its maximum extent along the outer coast of Pond Inlet by no later than 33 ka BP (Dyke and Hooper, 2001). At this time, MSGs extending out of Pond Inlet and into northern Baffin Bay indicate that Pond Inlet was occupied by a fast-flowing ice-stream (Brouard and Lajeunesse, 2017; Dyke, 2004; Ottesen et al., 2005). This is also suggested by the crag and tail and drumlinoid bathymetric features within Pond Inlet and Eclipse Sound, which are suggestive of rapidly flowing, thick, grounded glacier ice. The distal extent and southward deflection of the MSGs indicates that the Pond Inlet Ice Stream likely converged with the Lancaster Sound Ice Stream and grounded on the Lancaster trough-mouth fan (Brouard and Lajeunesse, 2017). Based on the maximum age of the postglacial sediments (<12.7-10.7 ka) extrapolated from the age model, it is reasonable to interpret that the uppermost portion of the till unit interpreted in the SE region of Pond Inlet would have been deposited during the late Wisconsin glaciation (Figure 3.16).

Deglaciation

The timing of deglaciation along northern Baffin Island is broadly constrained by radiocarbon and cosmogenic exposure dating (Briner et al., 2007; Dyke, 2008; Dyke and Hooper, 2001). While the timing of deglaciation along northern Baffin Island is generally known, the timing of deglaciation around Pond Inlet is not well constrained. Our acoustic data record the transition from full glacial to deglacial conditions in the Lower Unit. As the Pond Inlet Ice Stream receded from its termination at the Lancaster Ice Stream and its margin retreated towards Eclipse Sound, deposition of (probably ice-contact) stratified glaciomarine sediments occurred in the central region of Pond Inlet which were deposited by subglacial, englacial or proglacial processes

(Syvitski and Praeg, 1989). The strong indication of stratification in the acoustic record, indicating alternating stratified lithologies, suggests that much of this unit may have been a transition from ice-proximal to ice-distal glaciomarine sedimentation. Unfortunately, piston cores do not penetrate these deposits, which limits our determination of the precise timing and style of ice marginal retreat in Pond Inlet.

The elongated crag and tail features in Ellipse Sound are interpreted to have formed during late stage breakdown of glacial ice, and their preservation on the modern seabed suggests rapid retreat and that basal ice was somewhat raised above the seafloor (Dowdeswell et al., 2016). Rapid retreat and basal ice lift off is also indicated by the absence of recessional moraines in our multibeam bathymetric data west of the moraines at the entrance of Pond Inlet. Our data indicate that the ice-front was west of Central Pond Inlet by 10.7 ka BP, marked by the deposition of the first postglacial turbidites. In the Perched basin, the timing of the 10.7 ka BP turbidite occurring directly below the base of core 0066 is relatively well constrained by the age model. In the central Basin, the extrapolated age of the 12.7 ka BP turbidite occurring 20 m below core 0067, assumes that sedimentation rates did not change below the core. Sedimentation rates were likely higher following deglaciation in the early Holocene, indicating that the age estimate of 12.7 ka BP using the basal sedimentation rate from core 0067 at 3.3 ka cal BP is a maximum age, and this turbidite is likely significantly younger (Figure 3.16). The deposition of these turbidites indicate that the Pond Inlet Ice Stream had retreated a minimum of 184 km from the location of its convergence with the Lancaster Ice-Stream (Brouard and Lajeunesse, 2017) to the centre of Pond Inlet by this time, and likely had retreated further west towards the coast of Baffin Island. There is evidence of a small ice re-advance at around 10 ka BP marked by minimum limiting date ($9.8 \text{ ka} \pm 0.1 \text{ ka BP}$) at the mouth of Navy Board Inlet (Dyke and Hooper, 2001), likely a

result of Younger Dryas cooling. No cores have been obtained from the moraine at the entrance of Pond Inlet (informally termed Pond Inlet moraine); however, we propose a re-advance of glacial ice to this position during the Younger Dryas cold event from 12.8-11.5 ka (Taylor et al., 1993) (Figure 3.16; Figure 3.17). Ice then continued to retreat towards Eclipse Sound.

Radiocarbon dated marine shells (*Mya truncata* and *Hiatella arctica*) indicate the coastline around Navy Board Inlet and Eclipse Sound deglaciated from approximately 9.8 ± 0.6 ka cal BP though 6.0 ± 0.6 ka cal BP (Dyke and Hooper, 2001; McNeely and Atkinson, 1996). The position of the Pond Inlet moraine east of the Cockburn moraines (8.5-9.5 ka) further suggest this moraine was deposited during the Younger Dryas.

We interpret the IRD observed at the base of cores 0065 and 0066 prior to 9.8 ka BP was deposited from icebergs calving off the ice-front as it was receding towards the coastline west of Eclipse Sound and not from icebergs supplied from elsewhere. The majority of modern icebergs in Baffin Bay are produced by glaciers on the west coast of Greenland (Valeur et al., 1996). Some of these icebergs travel northward with the West Greenland Current and cross northern Baffin Bay to move south in the Baffin Island Current. These icebergs flow along the continental slope (Marko et al., 1986) and relatively few would be deflected into Pond Inlet. Another source of postglacial icebergs would be from those calved further up Lancaster Sound via Navy Board Inlet; however, the strongest current flows southeastward from Lancaster Sound. The absence of IRD in our cores after 9.8 ka BP (Figure 3.16; Figure 3.17) agrees with the timing of deglaciation of Navy Board Inlet and Eclipse Sound and further suggests the ice-stream along with the marine-terminating valley glaciers of Bylot and Baffin Island had retreated to the coast, shutting off the calving of icebergs into the central region of Pond Inlet.

Post-glaciation to present

Following LIS retreat, Holocene raised marine sediments in the area indicate that the land emerged up to 60 m near the Hamlet of Pond Inlet owing to glacial isostatic adjustments (Klassen, 1993). The seaway of Pond Inlet and Eclipse Sound, now free of glacial ice, was occupied by sea ice, including summer pack ice until approximately 6-5 ka BP, when it became ice-free in the summers based on the appearance of radiocarbon dated bowhead whale remains (Dyke et al., 1996). After the ice stream had left Pond Inlet and Eclipse Sound, it wasn't until the Neoglacial maximum approximately 120 years ago that the majority of the valley glaciers on Bylot Island reached their maximum extent (Dowdeswell et al., 2007; Klassen, 1993).

Our records indicate that postglacial marine sedimentation commenced prior to the deposition of the first turbidites at 10.7 ka BP (Figure 3.16; Figure 3.17). Our acoustic data and piston cores reveal that the postglacial depositional record in the deep basins of Pond Inlet is not exclusively filled by postglacial hemipelagic sediments, but is frequently interrupted by gravity flow deposition including turbidites, and punctuated by larger mass wasting or mass remobilization deposits (MTDs) (Figure 3.16). The relative contribution of different depositional processes varies laterally within the basin. For example, in the centre of Pond Inlet Basin, at core site 0067, hemipelagic deposition combined with turbidite deposition makes up approximately 55% of the sediments, while MTDs in this region account for 45% of the sediments. At core site 0003, MTD deposition dominates, making up approximately 90% of the sedimentary infill, with only 10% of the deposits made up of hemipelagic sediments. The thickest successions of postglacial sediment are confined to the deep inner basins of the seaway including Pond Inlet and Perched Basin where there was the most accommodation for sediments. The onlapping acoustic character indicates the hemipelagic sediments filled an underlying bedrock or till depression; once this was

filled, they began draping the underlying strata, similar to processes described by Hjelstuen et al., (2009). Over the late Holocene, there is no substantial trend in sedimentation rate fluctuations between the piston cores. Background sedimentation rates were relatively stable, reaching a maximum of 2.2 mm/yr from 3.3-1.6 ka BP in the middle of Pond Inlet Basin where there was the most accommodation for sediments, implying some gravitational process component is at play. Bulk sedimentation rates, which include instantaneous deposits, reached 2.5 mm/year in the centre of Pond Inlet Basin.

A range of sediment sources are considered to supply the postglacial marine sediments including tributary discharge along the coastal lowlands of Baffin and Bylot Island, outwash from valley glaciers, IRD, and sediment washed onto sea ice (Gilbert, 1983). There are bathymetric barriers for sediment from tributary discharge to reach central Pond Inlet. The majority of tributaries entering Pond Inlet and Eclipse Sound would have a tortuous route around bedrock highs to reach Pond Inlet Basin and Perched Basin (Figure 3.2). The tributaries that enter Pond Inlet and Eclipse Sound run through vegetated wetlands with an abundance of grasses (Gauthier et al., 1996). The remobilized sediment deposited in turbidites consisted of clean sands and silts absent of organic material (e.g. Figure 3.9). The absence of organic material could be further indication that that these turbidites were not hyperpycnal flows from tributary floods. The turbidites were more likely sourced from glacial fluvial outwash along unvegetated glacial outlets entering central Pond Inlet (Figure 3.1) or were sourced from remobilized marine sediments from bedrock highs. Remobilization could occur during postglacial relative sea level fall, when till and glaciomarine sediment deposited on bedrock highs could be redistributed, or by earthquake triggered ground shaking.

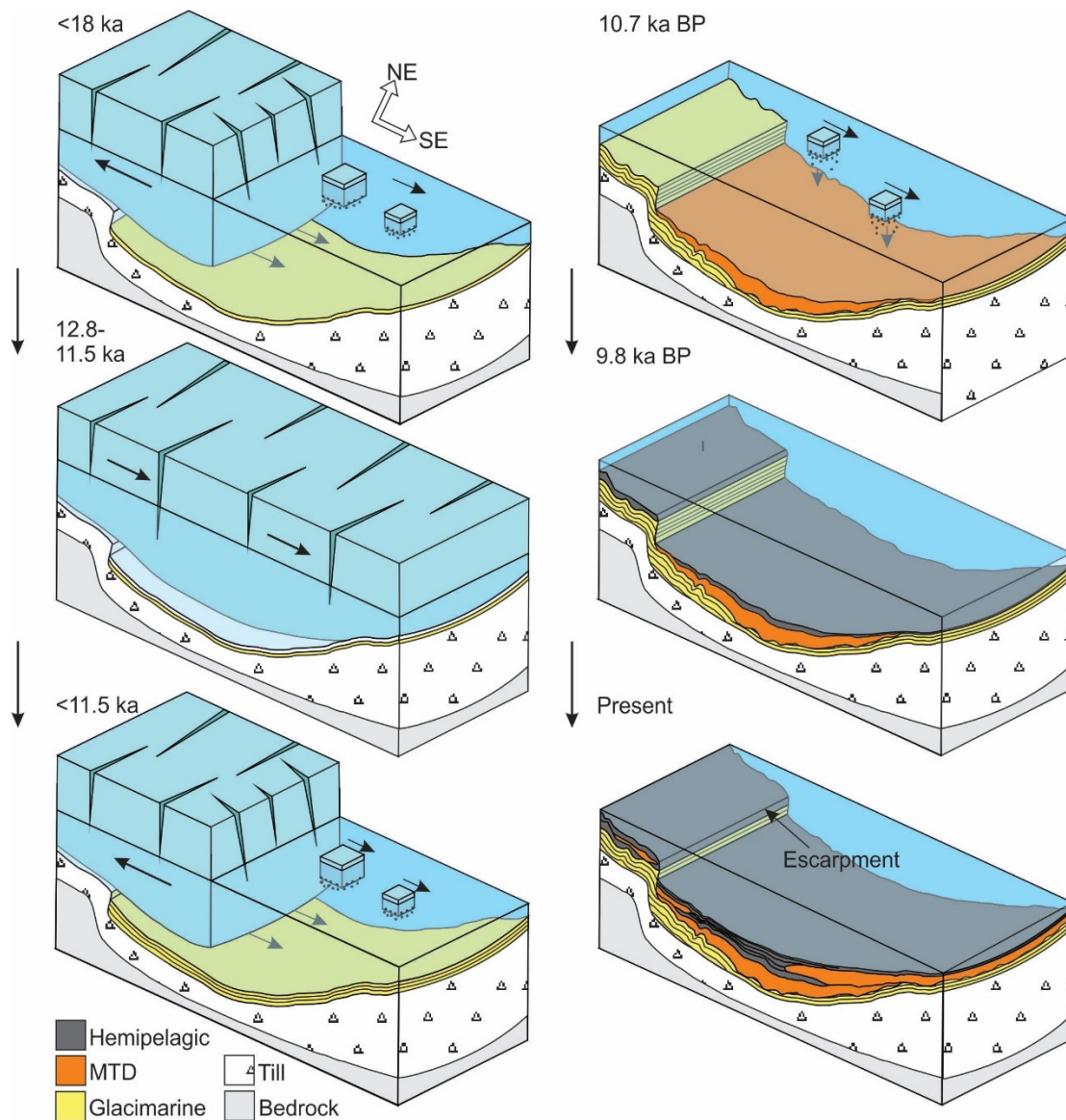


Figure 3.16: Depositional history of Pond Inlet Basin from LGM to present. <18 ka shows the receding ice front from its LGM position, calving of glaciers and deposition of IRD, and the deposition of glacial marine sediments above glacial till. 12.8-11.5 shows the Younger Dryas re-advance of the ice front. <11.5 ka shows ice-retreat after the Younger Dryas. 10.7 ka denotes the deposition of the first MTD and turbidite and continuing influence of icebergs and deposition of IRD. 9.8 ka shows the deposition of hemipelagic sediments above the MTD and glaciomarine sediments. Present shows the modern depositional environment with the deposition of hemipelagic sediments and the escarpment above Pond Inlet Basin.

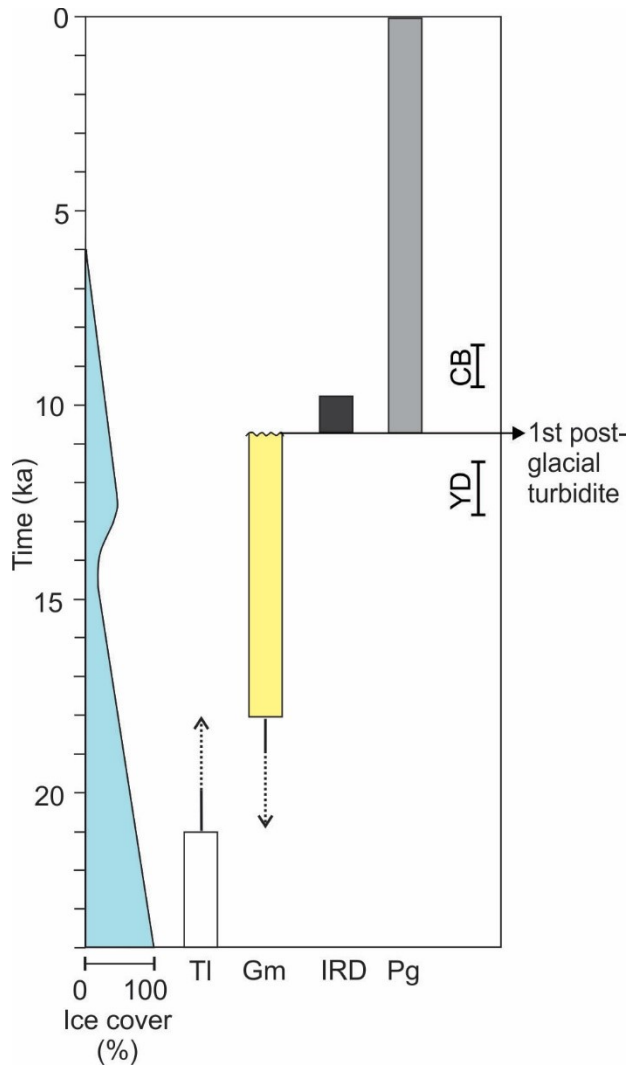


Figure 3.17: Timeline of deglaciation of Pond Inlet showing from left to right: ice cover, deposition of glacial till (TI), glaciomarine sediments (GM), IRD, and postglacial sediments (Pg). The timing of the first MTD in Pond Inlet, the Younger Dryas (YD) cold event and Cockburn Substage (CB) are also denoted.

3.6 Conclusions

The marine sedimentary record from Eclipse Sound and Pond Inlet, a glacially influenced seaway in northern Baffin Bay, reveals the deglacial to postglacial history of this region. The acoustic and core data reveal the deglacial to postglacial sedimentary processes occurring in Eclipse Sound and Pond Inlet since the last glaciation and provide the first dated marine record of the timing of deglaciation of northeastern Baffin Island.

The seafloor of Pond Inlet is composed of glacial landforms, bedrock outcrop, and a relatively flat basin floor. Central Pond Inlet is composed of two main sediment basins which are filled by two depositional units. The lower stratigraphic unit represents ice contact glacial till and ice-proximal glaciomarine sediment. The upper stratigraphic unit represents the postglacial record which is dominated by hemipelagic deposition interrupted by gravity driven flows, including turbidites and MTDs.

Pond Inlet preserves a geological history from the LGM to present day. Our chronologies indicate that: (1) By 10.7 ka BP, the deposition of postglacial sediments had commenced in central Pond Inlet; (2) The Pond Inlet moraine likely formed during a Younger Dryas re-advance; (3) Background sedimentation rates averaged 0.9 mm/yr in Pond Inlet Basin and 0.5 mm/yr in Perched Basin, with no apparent trend in sedimentation rate fluctuations over the Holocene; (4) Depositional processes varied laterally and through time within the basin.

3.7 Acknowledgements

The authors thank the officers, crews and scientific staff on board the CCGS Hudson and Amundsen during the 2013 and 2015 field program. K. Jenner, A. Normandeau and D. Piper are thanked for guidance and discussion. Multibeam bathymetric data was provided by the Ocean Mapping Group (OMG), University of New Brunswick, Fredericton, New Brunswick, Canada. DEMs provided by the Polar Geospatial Center under NSF-OPP awards 1043681, 1559691, and 1542736.

3.8 Supplementary Figures

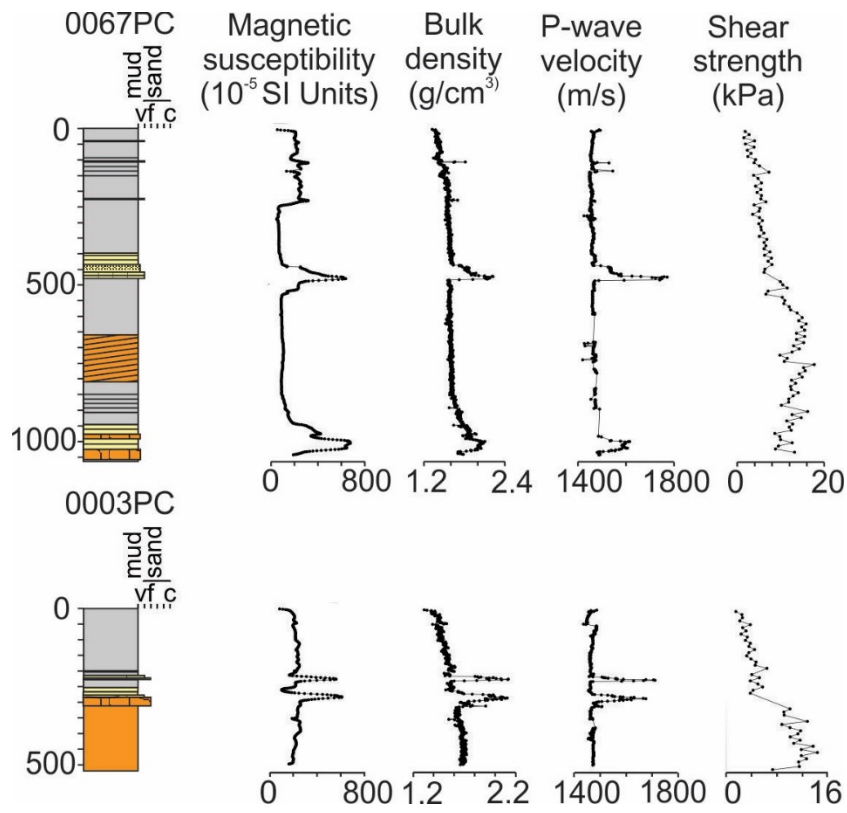


Figure 3.18: Physical properties measurements for cores 0067 and 0003 including magnetic susceptibility, bulk density, p-wave velocity and shear strength.

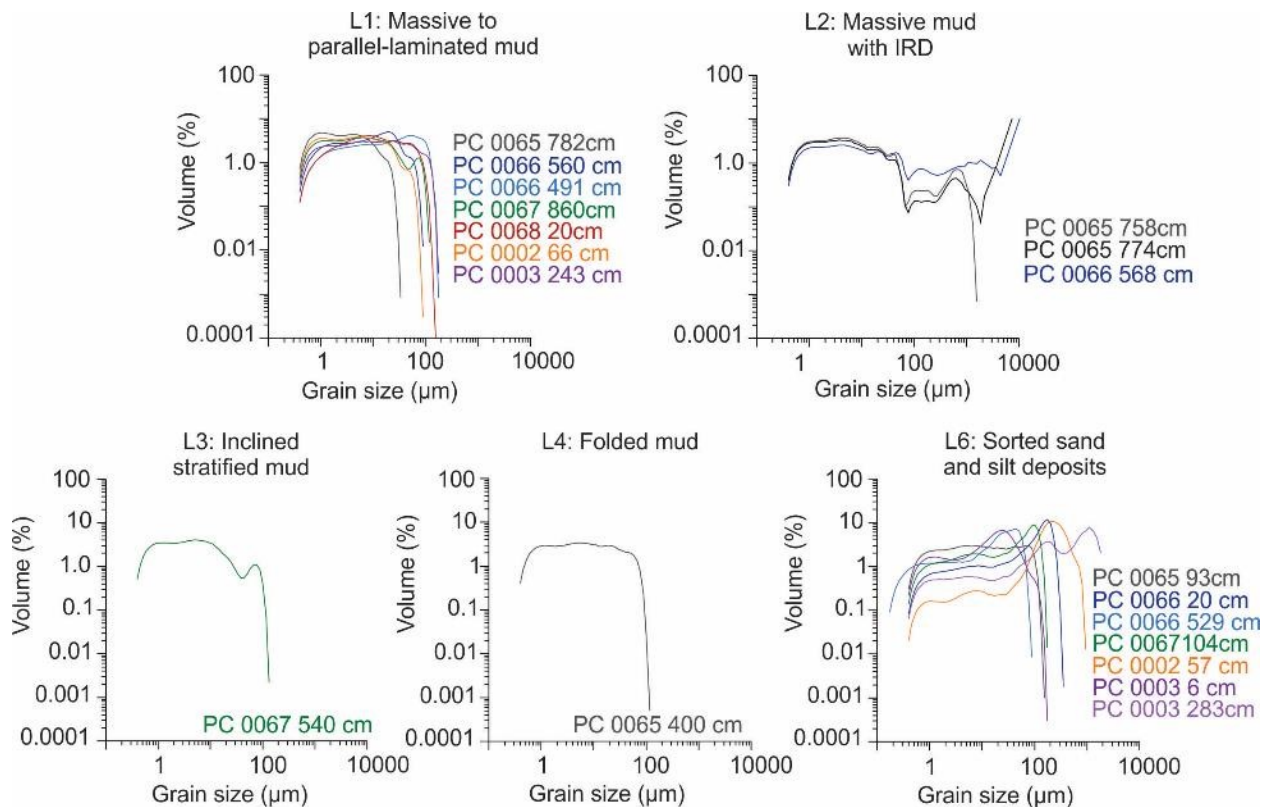


Figure 3.19: Examples of grain size plots from representative cores for each of the six lithofacies (L1 through L6).

3.10 References cited in Chapter 3

- Andrews, J.T., Ives, J.D., 1978. “Cockburn” Nomenclature and the Late Quaternary History of the Eastern Canadian Arctic. *Arct. Alp. Res.* 10, 617. <https://doi.org/10.2307/1550683>
- Andrews, J.T., Jull, A.J.T., Donahue, D.J., Short, S.K., Osterman, L.E., 1985. Sedimentation rates in Baffin Island fiord cores from comparative radiocarbon dates. *Can. J. Earth Sci.* 22, 1827–1834. <https://doi.org/10.1139/e85-194>
- Basham, P.W., Forsyth, D.A., Wetmiller, R.J., 1977. The seismicity of northern Canada 14, 1646–1667. <https://doi.org/10.1139/e77-140>
- Bellwald, B., Hjelstuen, B.O., Sejrup, H.P., Haflidason, H., 2016. Postglacial mass movements and depositional environments in a high-latitude fjord system – Hardangerfjorden, Western Norway. *Mar. Geol.* 379, 157–175. <https://doi.org/10.1016/j.margeo.2016.06.002>
- Bellwald, B., Hjelstuen, B.O., Sejrup, H.P., Stokowy, T., Kuvås, J., 2019. Holocene mass movements in west and mid-Norwegian fjords and lakes. *Mar. Geol.* 407, 192–212. <https://doi.org/10.1016/j.margeo.2018.11.007>

- Bent, A.L., 2002. The 1933 Ms= 7.3 Baffin Bay earthquake: strike-slip faulting along the northeastern Canadian passive margin. *Geophys. J. Int.* 150, 724–736.
- Blaauw, M., 2010. Methods and code for “classical” age-modelling of radiocarbon sequences. *Quat. Geochronol.* 5, 512–518. <https://doi.org/10.1016/j.quageo.2010.01.002>
- Bornhold, B.D., Finlayson, N.M., Monahan, D., 1976. Submerged drainage patterns in Barrow Strait, Canadian Arctic. *Can. J. Earth Sci.* 13, 305–311.
- Bouma, A.H., 1962. *Sedimentology of some Flysch deposits; a graphic approach to facies interpretation.* Elsevier Pub. Co, Amsterdam, New York.
- Briner, J.P., Davis, P.T., Miller, G.H., 2009. Latest Pleistocene and Holocene glaciation of Baffin Island, Arctic Canada: key patterns and chronologies. *Quat. Sci. Rev.* 28, 2075–2087. <https://doi.org/10.1016/j.quascirev.2008.09.017>
- Briner, J.P., Miller, G.H., Finkel, R., Hess, D.P., 2008. Glacial erosion at the fjord onset zone and implications for the organization of ice flow on Baffin Island, Arctic Canada. *Geomorphology* 97, 126–134. <https://doi.org/10.1016/j.geomorph.2007.02.039>
- Briner, J.P., Overeem, I., Miller, G.H., Finkel, R., 2007. The deglaciation of Clyde Inlet, northeastern Baffin Island, Arctic Canada. *J. Quat. Sci.* 22, 223–232.
- Brouard, E., Lajeunesse, P., 2019. Geomorphology Glacial to postglacial submarine landform assemblages in fiords of northeastern Baffin Island. *Geomorphology* 330, 40–56. <https://doi.org/10.1016/j.geomorph.2019.01.007>
- Brouard, E., Lajeunesse, P., 2017. Maximum extent and decay of the Laurentide Ice Sheet in Western Baffin Bay during the Last glacial episode. *Sci. Rep.* 7, 1–8. <https://doi.org/10.1038/s41598-017-11010-9>
- Campbell, D.C., 2014. CCGS Hudson Expedition 2013-029. Geological Hazard Assessment of Baffin Bay and Biodiversity Assessment of Hatton Basin. August 14–September 16, 2013. 122.
- Coulthard, R.D., Furze, M.F.A., Pieńkowski, A.J., Chantel Nixon, F., England, J.H., 2010. New marine ΔR values for Arctic Canada. *Quat. Geochronol.* 5, 419–434. <https://doi.org/10.1016/j.quageo.2010.03.002>
- Damuth, J.E., 1980. Use of high-frequency (3.5–12 kHz) echograms in the study of near-bottom sedimentation processes in the deep-sea: a review. *Mar. Geol.* 38, 51–75.
- Dowdeswell, E.K., Dowdeswell, J.A., Cawkwell, F., 2007. On the Glaciers of Bylot Island, Nunavut, Arctic Canada. *Arctic, Antarct. Alp. Res.* 39, 402–411. [https://doi.org/10.1657/1523-0430\(07-069\)](https://doi.org/10.1657/1523-0430(07-069))

- Dowdeswell, E.K., Todd, B.J., Dowdeswell, J.A., 2016. Crag-and-tail features: convergent ice flow through Eclipse Sound, Baffin Island, Arctic Canada. *Geol. Soc. London, Mem.* 46, 55–56. <https://doi.org/10.1144/M46.106>
- Duchesne, M.J., Pinet, N., Bédard, K., St-Onge, G., Lajeunesse, P., Campbell, D.C., Bolduc, A., 2010. Role of the bedrock topography in the Quaternary filling of a giant estuarine basin: The Lower St. Lawrence Estuary, Eastern Canada. *Basin Res.* 22, 933–951. <https://doi.org/10.1111/j.1365-2117.2009.00457.x>
- Dyke, A.S., 2008. The Steensby Inlet Ice Stream in the context of the deglaciation of Northern Baffin Island, Eastern Arctic Canada. *Earth Surf. Process. Landforms J. Br. Geomorphol. Res. Gr.* 33, 573–592.
- Dyke, A.S., 2004. An outline of North American deglaciation with emphasis on central and northern Canada. *Dev. Quat. Sci.* 2, 373–424. [https://doi.org/10.1016/S1571-0866\(04\)80209-4](https://doi.org/10.1016/S1571-0866(04)80209-4)
- Dyke, A.S., Andrews, J.T., Clark, P.U., England, J.H., Miller, G.H., Shaw, J., Veillette, J.J., 2002. The Laurentide and Innuitian ice sheets during the Last Glacial Maximum. *Quat. Sci. Rev.* 21, 9–31.
- Dyke, A.S., Clark, J.T.A.P.U., England, J.H., 2001. Geological Survey of Canada Open File 4120 Radiocarbon Dates pertinent to defining the last glacial maximum for the Laurentide and Innuitian ice sheets.
- Dyke, A.S., Hooper, J., Savelle, J.M., 1996. A history of sea ice in the Canadian Arctic archipelago based on postglacial remains of the bowhead whale (*Balaena mysticetus*). *Arctic* 49, 235–255. <https://doi.org/10.14430/arctic1200>
- Dyke, A.S., Hooper, J.M.G., 2001. Deglaciation of Northwest Baffin Island, Nunavut.
- Falconer, G., Andrews, J.T., Ives, J.D., 1965. Late-Wisconsin End Moraines in Northern Canada. *Science* (80-.). 147, 608–610.
- Gauthier, G., Rochefort, L., Reed, A., 1996. Exploitation of wetland ecosystems by herbivores on Bylot Island. *Geosci. Canada* 23.
- Gilbert, R., 1983. Sedimentary processes of Canadian Arctic fjords. *Sediment. Geol.* 36, 147–175.
- Hjelstuen, B.O., Haflidason, H., Sejrup, H.P., Lyså, A., 2009. Sedimentary processes and depositional environments in glaciated fjord systems - Evidence from Nordfjord, Norway. *Mar. Geol.* 258, 88–99. <https://doi.org/10.1016/j.margeo.2008.11.010>
- Jackson, G.D., Davidson, A., 1975. *Geology, Pond Inlet and Nova Zembla Island, District of Franklin.*

- Jenner, K.A., Piper, D.J.W., Campbell, D.C., Mosher, D.C., 2007. Lithofacies and origin of late quaternary mass transport deposits in submarine canyons, central Scotian Slope, Canada. *Sedimentology* 54, 19–38. <https://doi.org/10.1111/j.1365-3091.2006.00819.x>
- Keen, M.J., Johnson, J., Park, I., 1972. Geophysical and Geological Studies in Eastern and Northern Baffin Bay and Lancaster Sound. *Can. J. Earth Sci.* 9, 689–708.
- Klassen, R.A., 1993. Quaternary geology and glacial history of Bylot Island, Northwest Territories.
- Li, G., Piper, D.J.W., Calvin Campbell, D., 2011. The Quaternary Lancaster Sound trough-mouth fan, NW Baffin Bay. *J. Quat. Sci.* 26, 511–522. <https://doi.org/10.1002/jqs.1479>
- Margreth, A., Gosse, J.C., Dyke, A.S., 2017. Wisconsinan and early Holocene glacial dynamics of Cumberland Peninsula, Baffin Island, Arctic Canada. *Quat. Sci. Rev.* 168, 79–100. <https://doi.org/10.1016/j.quascirev.2017.04.033>
- Marko, J.R., Birch, J.R., Wilson, M.A., 1986. A Study of Long-Term Satellite-Tracked Iceberg Drifts in Baffin Bay. *Arctic* 35, 234–240.
- McNeely, R., Atkinson, D.E., 1996. Geological Survey of Canada Radiocarbon dates XXXII, Geological Survey of Canada Paper 83-1A. <https://doi.org/10.1126/science.ns-6.149S.521-a>
- Miller, G.H., Dyke, A.S., 1974. Proposed Extent of Late Wisconsin Laurentide Ice on Eastern Baffin Island. *Geology* 2, 125–130.
- Oakey, G.N., Chalmers, J.A., 2012. A new model for the Paleogene motion of Greenland relative to North America: Plate reconstructions of the Davis Strait and Nares Strait regions between Canada and Greenland. *J. Geophys. Res. Solid Earth* 117.
- OMG, 2005. Multibeam Sonar Data collected from the CCGS Amundsen: Ocean Mapping Group, University of New Brunswick, Fredericton, New Brunswick, Canada [WWW Document]. *Ocean Mapp. Gr.* URL <http://www.omg.unb.ca/Projects/Arctic/index.html>
- Ottesen, D., Dowdeswell, J.A., Rise, L., 2005. Submarine landforms and the reconstruction of fast-flowing ice streams within a large Quaternary ice sheet: The 2500-km-long Norwegian-Svalbard margin (57°-80°N). *Bull. Geol. Soc. Am.* 117, 1033–1050. <https://doi.org/10.1130/B25577.1>
- Piper, D.J.W., Stow, D.A.W., 1991. Fine-grained turbidites, in: Einsele, G., Seilacher, A. (Eds.), *Cyclic and Event Stratification*. Springer Verlag, New York, pp. 360–376.
- Sangree, J.B., Widmier, J.M., 1979. Interpretation of Depositional Facies from Seismic Data. *Geophysics* 44, 131–160. <https://doi.org/10.1190/1.1440957>

- Skipton, D.R., Saumur, B.M., St-Onge, M.R., Wodicka, N., Bros, E.R., Currie, L.D., Weller, O.M., Haggart, J.W., 2018. Bedrock geology, Pond Inlet, Nunavut, part of NTS 38-B; Geological Survey of Canada, Canadian Geoscience Map 347, scale 1:100 000. <https://doi.org/https://doi.org/10.4095/306578>
- St-Onge, G., Chapron, E., Mulsow, S., Salas, M., Viel, M., Debret, M., Foucher, A., Mulder, T., Winiarski, T., Desmet, M., Costa, P.J.M., Ghaleb, B., Jaouen, A., Locat, J., 2012. Comparison of earthquake-triggered turbidites from the Saguenay (Eastern Canada) and Reloncavi (Chilean margin) Fjords: Implications for paleoseismicity and sedimentology. *Sediment. Geol.* 243–244, 89–107. <https://doi.org/10.1016/j.sedgeo.2011.11.003>
- Syvitski, J.P.M., 1989. Glacier-Influenced Fjords : Oceanographic Controls. *Mar. Geol.* 85, 301–329.
- Syvitski, J.P.M., Praeg, D.B., 1989. Quaternary Sedimentation in the St. Lawrence Estuary and Adjoining Areas, Eastern Canada: An Overview Based on High-Resolution Seismo-Stratigraphy. *Géographie Phys. Quat.* 43, 291. <https://doi.org/10.7202/032784ar>
- Taylor, K.C., Lamoreyt, G.W., Doylet, G.A., Mayewskill, P.A., White, W.C., Barlow, L.K., 1993. The “flickering switch” of late Pleistocene climate change. *Nature* 361, 432–436.
- Tripsanas, E.K., Piper, D.J.W., Jenner, K.A., Bryant, W.R., 2008. Submarine mass-transport facies: New perspectives on flow processes from cores on the eastern North American margin. *Sedimentology* 55, 97–136. <https://doi.org/10.1111/j.1365-3091.2007.00894.x>
- Valeur, H.H., Hansen, C., Hansen, K.Q., Rasmussen, L., Thingvad, N., 1996. Weather, sea and ice conditions in eastern Baffin Bay, offshore northwest Greenland: A review. *Miner. Resour. Adm. Greenl.* 96–12, 37 pp.,.

CHAPTER 4: GEOHAZARDS OF POND INLET AND ECLIPSE SOUND, BAFFIN BAY - OBSERVATIONS ON SUBMARINE SLOPE FAILURES AND POTENTIAL HAZARD ASSESSEMENT

Authors: Laura M. Broom, D. Calvin Campbell and John C. Gosse

Status: Under review by co-authors

Abstract

The coastal communities of northern Baffin Island are located along fjords and inlets in regions of high relief, yet the potential for submarine and subaerial slope has not been evaluated in detail. Evaluating the potential for these events and determining their size and frequency in the recent sedimentary record is the first step to improving the hazard assessment of the region. Newly acquired multibeam bathymetric, sub-bottom profiler data, and sediment cores collected from Pond Inlet and Eclipse Sound allow for first the opportunity to evaluate the nature, extent and frequency of submarine slope failures in this region. The sedimentary record in Pond Inlet and Eclipse Sound reveals that since 12.7 ka BP, the region has experienced mass wasting in the form of mass transport deposits (MTDs) and turbidites. MTDs have occurred on average once every 1.6 ka over the late Pleistocene and early Holocene, and the frequency has increased to one event every 1.0 ka over the last 3 ka. The majority of these deposits appear to be locally sourced and have travelled relatively short distances. Slope stability analysis reveals that sediments are stable under current conditions and require an external triggering mechanism to fail, which could include seismicity, permafrost thaw, glacial unloading, and floods. Preliminary analysis of subaerial slope failures impacting the Hamlet of Pond Inlet predict that a subaerial landslide, with a similar volume to the 2017 Nuugaatsiaq landslide that entered Karrat Fiord, occurring on the steep slopes of Bylot Island, could produce displacement wave run-up heights of 11 to 22 m,

which would impact the coastal community. These results indicate the need for further investigations of the geohazards of northern Baffin Island.

4.1 Introduction

Submarine and subaerial slope failures are commonly recognized features in glacially influenced inlets and fjords (e.g. Hermanns et al., 2012; Syvitski, 1989). These events can be destructive to infrastructure and have the potential to generate displacement waves (tsunamis) that can have devastating impacts on coastal communities (e.g. Bessette-Kirton et al., 2017; Fine et al., 2005; Hermanns et al., 2013). Along the eastern coast of Baffin Island, most of the population lives along the coasts of these inlets and fjords (Figure 4.1). On the opposite side of Baffin Bay, on 17 June 2017, a large subaerial landslide, informally termed the “Nuugaatsiaq landslide”, entered Karrat Fiord on the west coast of Greenland. This generated a displacement wave that resulted in the loss of four lives and 11 homes in the nearby community of Nuugaatsiaq (Bessette-Kirton et al., 2017) (Figure 4.1). The Baffin Bay region also experiences high seismicity (Bent, 2002; Stein et al., 1979), which is recognized as a common triggering mechanism for slope failure deposits (Hampton et al., 1996). In the marine record, mass transport deposits have been recognized offshore along the continental slopes of Baffin Bay (Aksu, 1984; Aksu and Hiscott, 1989) and in fjords along eastern Baffin Island (Syvitski et al., 1987); however, the extent and frequency of slope failures in the glacially influenced fjords and inlets, which lie close to population centres, has not been evaluated in detail. Determining the size and frequency of these events is a crucial step toward future hazard assessments for nearby communities.

Recently collected acoustic and core data from Eclipse Sound and Pond Inlet, Baffin Bay, provide an opportunity to evaluate the geohazards of northwestern Baffin Bay. Eclipse Sound and Pond Inlet comprise a glacially influenced seaway that has experienced slope failures

throughout the Holocene. In this study, our results show the timing and extent of mass movement deposits in Pond Inlet, an evaluation of current slope stability, and the potential for displacement waves affecting the Hamlet of Pond Inlet from subaerial slope failures. These results suggest a further need for detailed investigation of displacement wave risks for the region.

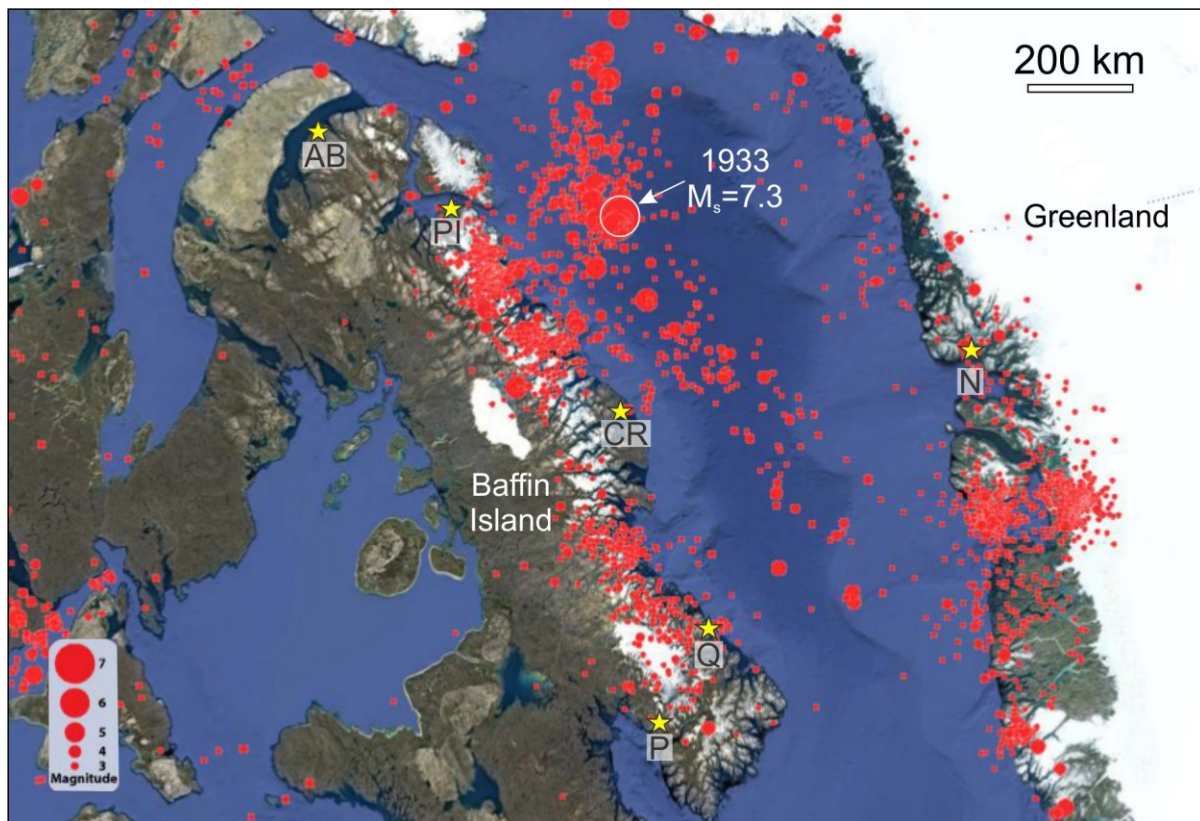


Figure 4.1: Regional map of Baffin Bay showing earthquake locations and magnitudes from 1921-2016 (ISC 2016) and the locations of coastal communities (AB = Arctic Bay, PI = Pond Inlet, CR = Clyde River, Q = Qikiqtarjuaq, P = Pangnirtung, N = Nuugaatsiaq). Base map imagery U.S. Geological Survey, Landsat/Copernicus, IIBCAO. Base map data SIO, NOAA, U.S. Navy, NGA, GEOBO; ©2018 Google.

4.2 Background

4.2.1 Physiography

Baffin Bay is a rifted margin that formed through seafloor spreading from the Cretaceous through the Eocene (Keen et al., 1972; Oakey and Chalmers, 2012). Pond Inlet and Eclipse Sound form a previously glaciated seaway along the northeastern coast of Baffin Island. This seaway is up to 40 km wide, 130 km long, and is bounded by Bylot Island to the north and Baffin Island to the west and south (Figure 4.2). The northern Baffin Island landscape that surrounds Pond Inlet and Eclipse Sound consists of peaks reaching 1950 m asl on rugged highlands dissected by steep-walled glacial valleys with underfit consequent streams that flow onto broad vegetated lowlands. The coastline of southern Bylot Island increases in peak height and steepness eastward and has low relief westward towards Eclipse Sound. The seafloor of Pond Inlet and Eclipse Sound is relatively flat and in places preserves glacial landforms under thin postglacial hemipelagic sediment (Broom et al., submitted). Water depths in Pond Inlet and Eclipse Sound reach up to 1080 m, and submarine bedrock ridges as shallow as 15 m occur in Eclipse Sound. Sediments entering the inlet and sound from Bylot and Baffin Islands are sourced by glacio-fluvial first-order streams.

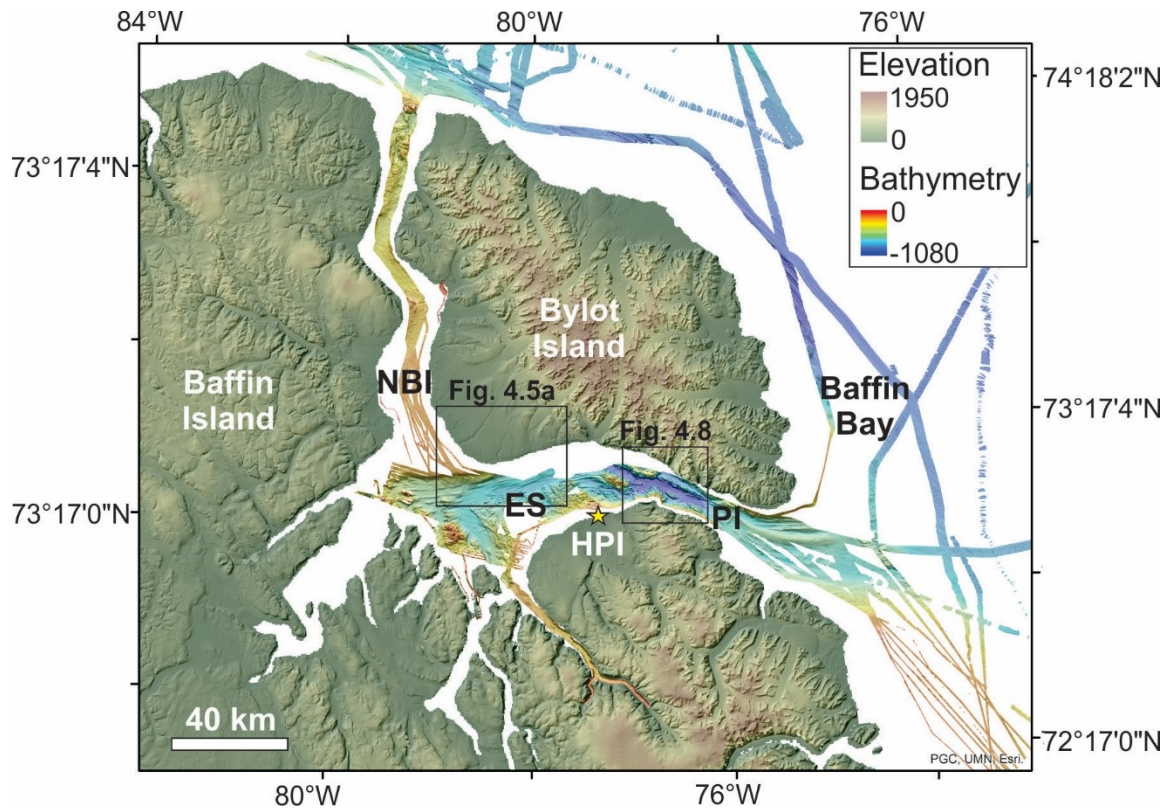


Figure 4.2: Regional physiography of the study region including northeastern Baffin Island, Bylot Island. Multibeam bathymetry collected by OMG as part of ArcticNet (2005-2008) collected within Pond Inlet, Eclipse Sound, and Navy Board Inlet. NBI = Navy Board Inlet, ES = Eclipse Sound, HPI = Hamlet of Pond Inlet. DEM(s) created from DigitalGlobe, Inc. imagery.

4.2.2 Hamlet of Pond Inlet

The Hamlet of Pond Inlet (pop. 1,617- (Statistics Canada, 2017)) is a coastal community located on the south coast of Eclipse Sound (Figure 4.2). The population of Pond Inlet is currently growing in part due to the expansion of the mining industry in the region. There are over 350 private dwellings in the Hamlet (Statistics Canada, 2017), all of which are located within two kilometres of the coastline at elevations from 5-100 asl, with most being at elevations less than 60 m. Transportation services include gravel roads, a floating dock, and an airport. Pond Inlet has also experienced an increase in cruise ship tourism, which is likely to increase infrastructure development, and a proposal for the development of a small craft harbour for the community has been made (Government of Nunavut, 2015).

4.2.2 Deglaciation of Baffin Island & Baffin Bay Seismicity

On northern Baffin Island, three geological processes are active and may contribute to the displacement wave risk: (i) The ongoing regional deglaciation has led to isostatic uplift and unloading of fjord walls; (ii) regional seismicity in Baffin Bay, which can trigger subaerial and submarine mass wasting; and (iii) ongoing rapid thawing of continuous permafrost, which decreases the shear strength of bedrock slopes (Hilger et al., 2018). Despite the active nature of these processes, and evidence that recently deglaciated steep-walled fjord regions elsewhere have unstable slopes (e.g. Hermanns et al. 2014), there has been no systematic study of the landslide inventory or slope stability around Pond Inlet.

The ice sheet, ice caps, and alpine glaciers that covered all but the highest coastal peaks of Baffin Island remained close to their maximum extent until 18 ka BP and later in some locations (Dyke, 2004). Outlet glaciers began retreating inland from the coast along eastern and northern Baffin Island between 10-8.5 ka BP, and final break-up of the Laurentide Ice Sheet occurred from 7-6 ka BP (Dyke, 2004). Since deglaciation, Baffin Island has been experiencing postglacial rebound (Andrews, 1970). For example, raised marine sediments near the Hamlet of Pond Inlet have risen 60 m over the course of the Holocene (Klassen, 1993).

Baffin Bay is a seismically active region with the potential for high magnitude earthquakes, yet the understanding of the seismicity of the region has been limited by the short (60 yr) instrumental record. Most of the recent seismicity occurs in northwestern Baffin Bay (Basham et al., 1977), including the 1933 7.3 M_s strike slip earthquake which was followed by two thrust sub-events (Bent, 2002). This is the largest recorded intraplate earthquake in eastern North America and the largest north of the Arctic Circle. The greatest occurrence of seismicity is in close proximity to linear features on the Baffin Bay seafloor which appear to be normal and

transform faults (Stein et al., 1979). However, there is also intraplate seismicity, with several seismically active areas on Baffin Island, which may be attributed to the regional deglaciation of Baffin Island (Basham et al. 1977). Postglacial rebound following deglaciation can produce the earthquakes recorded in northern Baffin Bay (Quinlan, 1984), and it has been shown that high differential uplift rates in the Baffin Bay region after deglaciation could reactivate pre-existing faults from the original rifting and produce the seismicity observed in Baffin Bay (Basham et al., 1977; Stein et al., 1979). More recently, several studies (Lund, 2015; Steffen et al., 2014a, 2014b) have demonstrated with glacio-isostatic adjustment models that the re-arrangement and weakening of horizontal stress fields parallel to ice flow can reduce the shear strength of pre-existing but tectonically inactive faults, leading to intraplate seismicity in deglaciating regions.

Subaerial landslides in deglaciating regions have often been associated with isostatic uplift and seismicity (Hewitt et al., 2008); however these slope failures have also been connected to climatic changes including increased precipitation and permafrost thaw (Hilger et al., 2018). Hilger et al. (2018) show that postglacial late Holocene catastrophic failures in Norway seem to be concurrent with wetter and warmer conditions at the end of the Holocene thermal optimum (~6 ka), and the associated thawing of permafrost on exposed rock slopes. Bylot Island occurs within the zone of continuous permafrost, and on southwestern Bylot Island, permafrost is estimated to be up to 400 m thick (Moorman and Michel, 1999). Permafrost is also likely present within bedrock in the high-mountain environment, and degradation of this ice in a warming climate could contribute to slope instability along the steep mountain faces of southern Bylot Island.

4.3 Methods

4.3.1 Geophysical imaging and core sedimentology analysis

Multibeam bathymetric data were collected throughout Pond Inlet and Eclipse Sound from 2005 to 2008 by the Ocean Mapping Group (OMG) (OMG 2005-2008) onboard the CCGS Amundsen (Figure 4.2). The data were collected using a Kongsberg Maritime Simrad EM300 multibeam sonar system in water depths of 10-1000 m. Standard collection settings were used including auto depth mode, an angular coverage of ± 60 degrees and equidistant beamforming.

Bathymetric data were input into ArcGIS version 10.2.2 where shaded relief and slope images were created to visualize instability features at the seabed.

In 2013 and 2015, sub-bottom profiler data and five piston cores were collected from Pond Inlet onboard the CCGS Hudson and CCGS Amundsen, in part for evaluating the geohazards in this region (Campbell, 2014) (Figure 4.3). High resolution 3.5 kHz sub-bottom profiler data were collected using a Knudsen 3260 Echo-Sounder in 2013 and 2015 by the Geological Survey of Canada Atlantic (GSC-A) onboard the CCGS Hudson. The sub-bottom data were visualized utilizing Kingdom Suite Software 8.8. The sub-bottom profiler data have a theoretical resolution of 11 cm and a maximum penetration of 65 m in the centre of Pond Inlet. Sediment thickness was estimated using sediment velocities of 1500 m/s, similar to the average p-wave velocity measurements from the Multi-Sensor Core Logger (MSCL). Minimum volume estimates were determined for MTDs using constraints from at least two sub-bottom profiler lines in Kingdom Suite by gridding the overlying and underlying reflections and producing an isochron map between the two grids.

Synthetic seismograms were created in Kingdom Suite to correlate the piston cores with the sub-bottom profiler data. A time to depth relationship was determined using the longitudinal velocity

measured at 10 cm intervals in the piston cores. The synthetic trace was produced by convolving the core velocity and bulk density measurements with a Ricker wavelet. A wavelet was computed from acoustic data adjacent to the core site and a high and low pass filter was applied to the acoustic data (2500-4500 Hz). The generated wavelet was then qualitatively matched to the sub-bottom data by matching peaks and troughs.

Five piston cores (0065, 0066, 0067, 0002 and 0003) and a box core (0068) were collected from the basin floor in the centre of Pond Inlet in water depths of 880-1076 (Table 4.1). The cores had lengths of 47.5-1063 cm. The five piston cores underwent processing at the GSC-A. Split core sections were photographed and x-radiographed using a Universal HE425 X-ray system.

Physical properties were measured using a Geotek MSCL. Whole core sections were measured for compressional (p-wave) velocity, bulk density, and magnetic susceptibility at 1 cm intervals.

Split core sections were then measured by the MSCL for magnetic susceptibility and colour using a Konica Minolta colour spectrophotometer measuring colour reflectance in $L^* a^*$ and b^* values. In core 0067, grain size sub-samples were taken every 20 cm in massive mud deposits and every few cm within turbidites. The other four piston cores were sub-sampled every 1-330 cm for grain size depending on the frequency of lithofacies changes. Grain size was measured using a Beckman Coulter LS230 Laser Diffraction Analyzer, except when grain size was greater than 2000 microns, in which case sub-samples were sieved at $\frac{1}{4}$ phi intervals.

Twelve radiocarbon dates were obtained from the five piston cores (Table 4.2) (Broom et al., submitted). Benthic and planktonic foraminifera were collected from bulk sediment samples and sent to accelerator mass spectrometer (AMS) facilities at NOSAMS (Woods Hole Oceanographic Institution) and the Keck Carbon Cycle (University of California, Irvine,) for radiocarbon dating. The dates were calibrated using the CLAM software (version 2.2; Blaauw,

2010) using the Marine13 calibration curve with a global marine reservoir correction of 400 years. A local marine reservoir correction (ΔR) of 220 ± 100 years (Coulthard et al., 2010) was also applied. Potential short-lived changes in the reservoir effect in Pond Inlet and Eclipse Sound due to the melting of the ice-sheet and changes in sea-ice cover over the Holocene are considered (Lochte et al., 2019), however since this is unknown for northern Baffin Bay, it is not accounted for in the marine reservoir correction. Bayesian age-depth modelling was completed using the CLAM software for cores where more than one radiocarbon date was obtained (0065, 0066 and 0067). The trigger weight cores (TWC) were correlated to the piston cores and the top of each TWC was assumed to represent the year the core was collected. The rapid deposition of turbidites was accounted for by incorporating them into the age model as instantaneous deposits. Linear interpolation was used to determine ages between radiocarbon dates. The age model was used to determine ages of turbidite and MTD deposits between radiocarbon dates and below the depth of radiocarbon dates. The basal sedimentation rate from core 0067 at 3.3 ka cal BP was used to extrapolate ages to the depth of the underlying high amplitude reflections to obtain ages of these reflections. These extrapolated ages are likely maximum ages because they assume sedimentation rates stay stable below the basal sedimentation rate, while sedimentation rates were likely higher in the early Holocene following deglaciation (Andrews et al., 1985; Bellwald et al., 2019). Core 0067 was used because it overlies each of the mapped high amplitude reflections.

Table 4.1: Details on the piston cores and push cores taken from Pond Inlet including their locations (latitude and longitude) water depth, and total core length.

Expedition number	Core number	Core type	Latitude	Longitude	Water depth (m)	Core length (cm)
2013029	0065	Piston	72.814891	-77.676665	1035	810
	0066	Piston	72.849098	-77.441545	880	614
	0067	Piston	72.815556	-77.426285	1076	1063
	0068B	Push	72.816518	-77.428031	1074	49.5
	0068C	Push	72.816518	-77.428031	1074	47.5
2015805	0002	Piston	72.822051	-77.553080	1059	299
	0003	Piston	72.809268	-77.278225	1048	520

Table 4.2: Details on the radiocarbon dates collected from piston cores (0065, 0066, 0067, 0002 and 0003) in Pond Inlet, including the depth interval bulk sediment samples were taken from, the type of material dated, the uncalibrated age and uncertainty, and the calibrated age and total uncertainty. The radiocarbon ages were calibrated using the Marine13 calibration curve and a local reservoir correction (ΔR) of 220 ± 100 .

Core	Depth (cm)	Sample media	Radiocarbon age (yrs BP)	Uncertainty (yrs BP)	Calibrated age (yrs BP) ($\Delta R = 220 \pm 100$)	Uncertainty (yrs BP)
0065	50-55	Mixed benthic foraminifera	1580	35	915	221
	120-125	Mixed benthic foraminifera	2630	40	2061	248
	208	Glacialis shell	3005	15	2520	219
	248-253	Mixed benthic foraminifera	3840	25	3557	252
	766-771	Mixed benthic & planktonic foraminifera	9450	30	9963	284
0066	14-19	Mixed benthic foraminifera	1580	50	917	229
	125-130	Mixed benthic & planktonic foraminifera	3970	20	3693	255
	531-534	Mixed benthic & planktonic foraminifera	8990	30	9421	250
0067	164-166	Colus shell	2250	15	1601	232
	589-591	Colus shell	3675	20	3318	253
0002	34-39	Mixed benthic & planktonic foraminifera	1350	45	710	187
0003	206-211	Mixed benthic & planktonic foraminifera	3350	20	2949	228

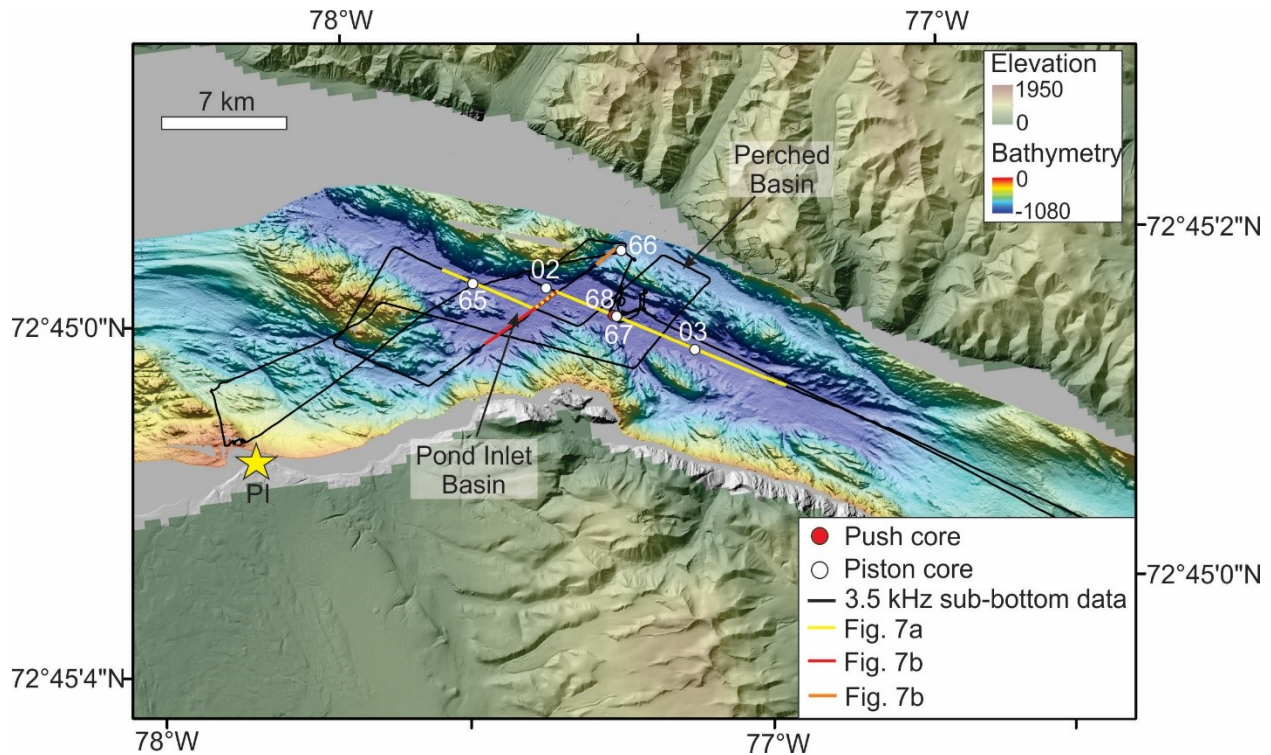


Figure 4.3 Data map showing the location of the sub-bottom profiler lines and piston and push core locations. Locations of Figure 9 sub-bottom profiler lines are shown in yellow. Multibeam bathymetry collected by OMG as part of ArcticNet (2005-2008). DEM(s) created from DigitalGlobe, Inc. imagery.

4.3.2 Slope stability analysis

To evaluate slope stability in Pond Inlet, it is assumed that slope failures occur when the shear stress on a slope surface (τ) exceeds the undrained shear strength of the sediment (S_u) (Morgenstern, 1967). The ratio of sediment shear strength (S_u) to shear stress (τ) is used to determine the factor of safety (FS). When $FS \leq 1$ the slope is unstable and there is the potential for a slope failure. The infinite slope method was used for slope stability analysis. It assumes the slope is planar and of infinite length.

$$\text{Equation 4.1: } FS = \frac{S_u}{\tau}$$

The effect of gravitational loading on sediment stability was evaluated, and from this the effect of slope angle and height of overburden was determined. FS was calculated using the basic infinite slope analysis equation of Morgenstern (1967), where S_u is the undrained shear strength,

γ' is the effective unit weight of the sediment (product of acceleration due to gravity, thickness of overburden, and sediment density), β is the slope angle, and h is the height of overlying sediment. The slope angle was obtained from the multibeam bathymetric data at the core site of interest.

$$\text{Equation 4. 2: } FS = \frac{2}{\sin 2\beta} \frac{S_u}{\gamma' h}$$

The equation can be rearranged to evaluate the critical slope angle (β_c), and the critical height (H_c), where $FS = 1$ (Equation 4.3 and Equation 4.4).

$$\text{Equation 4.3: } \beta_c = \left[\frac{1}{2} \left\{ \sin^{-1} \left(\frac{2S_u}{\gamma' h} \right) \right\} \right]$$

$$\text{Equation 4.4: } H_c = \frac{2S_u}{\gamma' \sin 2\beta}$$

The effect of horizontal acceleration due to earthquakes was also evaluated. The pseudostatic method was used to simulate the inertial forces of an earthquake including static horizontal and vertical forces in limit equilibrium (Newmark, 1965). A FS was calculated, which includes an additional static constant force applied to the slope during an earthquake. The effect of the vertical force on a sliding mass was ignored as it has very little effect on its slope stability. The pseudostatic horizontal force (F_h) was calculated using Equation 4.5, where m is the mass of slide material, γ is the weight of the slide mass, a is the ground acceleration due to the earthquake, g is the acceleration due to gravity, and k_h is the horizontal seismic coefficient.

$$\text{Equation 4.5 } F_h = ma = \frac{\gamma a}{g} = k_h \gamma$$

The FS was determined using Equation 4.6, which was rearranged to Equation 4.7 to determine the minimum acceleration (k_{min}) needed to cause slope failure by setting FS to 1.

$$\text{Equation 4.6 } FS = \frac{S_u}{\gamma' h} \left(\frac{1}{\frac{1}{2} \sin 2\beta + k_h \cos^2 \beta \frac{\gamma}{\gamma'}} \right)$$

$$\text{Equation 4.7 } k_{min} = \frac{S_u}{\gamma' h \cos^2 \beta} - \frac{\gamma}{\gamma'} \tan \beta$$

4.3.3 Calculation of displacement waves

An estimate of the maximum possible run-up height at the Hamlet of Pond Inlet from a displacement wave (tsunami) generated by an onshore landslide entering Pond Inlet from the steep mountain faces along Bylot Island was determined using the SPLASH equation (Equation 4.8) by Oppikofer et al. (2018), where R is the run-up height in metres, V is the landslide volume millions of cubic metres, and x is the distance from the landslide in kilometres. This equation was developed using a catalog of landslide-generated displacement waves to develop semi-empirical relationships between these parameters. This catalog helped develop the best-fitted parameters $a = 18.093$, $b = 0.57110$ and $c = -0.74189$ for the following equation:

$$\text{Equation 4.8 } R = a V^b x^c$$

The steepest and longest slopes that have the potential of triggering a > 5 m displacement wave occur along the southeastern coast of Bylot Island, directly across from the Hamlet of Pond Inlet. Seven sites were selected along that coast to evaluate the potential for displacement wave run-up heights at the Hamlet (Table 4.3; Figure 4.4). These sites were selected because they have steep ($>45^\circ$) and long (>600 m) slopes and are positioned directly across from the Hamlet (bends around coastal protrusions will reduce run-up heights). There has been no landslide assessment conducted in this location, so these sites are only used to determine the potential for significant run-up. Residential property elevations are as low as 5 to 10 m asl so 10 m asl was used as the minimum run-up height. Since no volumes of subaerial landslides along Baffin Island are

published in the literature, volumes input into the Equation 4.8 were compared to known volumes of subaerial coastal landslides (Oppikofer et al., 2018; Roberts et al., 2014). Primarily, the volume of the June 2017 Nuugaatsiaq landslide (Bessette-Kirton et al., 2017; Chao et al., 2018) was used for comparison. Three volume estimates have been made for the Nuugaatsiaq landslide. The most conservative volume estimate by Bessette-Kirton et al. (2017) is 33.4 Mm³, Fritz et al. (2017) provide an estimate of 45 Mm³, and the largest volume estimate is 74.4 Mm³ by Chao et al. (2018).

Table 4.3: Location, average slope and maximum elevation of the seven sites on the southern coast of Bylot Island used in the SPLASH calculations.

Site	Latitude	Longitude	Distance to Hamlet of Pond Inlet (km)	Average slope (°)	Max elevation (m)
1	72°54'5.00"N	78° 6'38.73"W	21.7	51	727
2	72°54'19.23"N	78° 0'9.54"W	21.5	44	602
3	72°54'25.79"N	77°54'42.46"W	21.8	57	811
4	72°54'11.92"N	77°45'51.87"W	22.5	51	599
5	72°54'31.56"N	77°31'18.14"W	25.3	51	1259
6	72°52'16.00"N	77°17'37.01"W	28.3	54	758
7	72°51'52.52"N	77°10'9.63"W	31.0	55	943

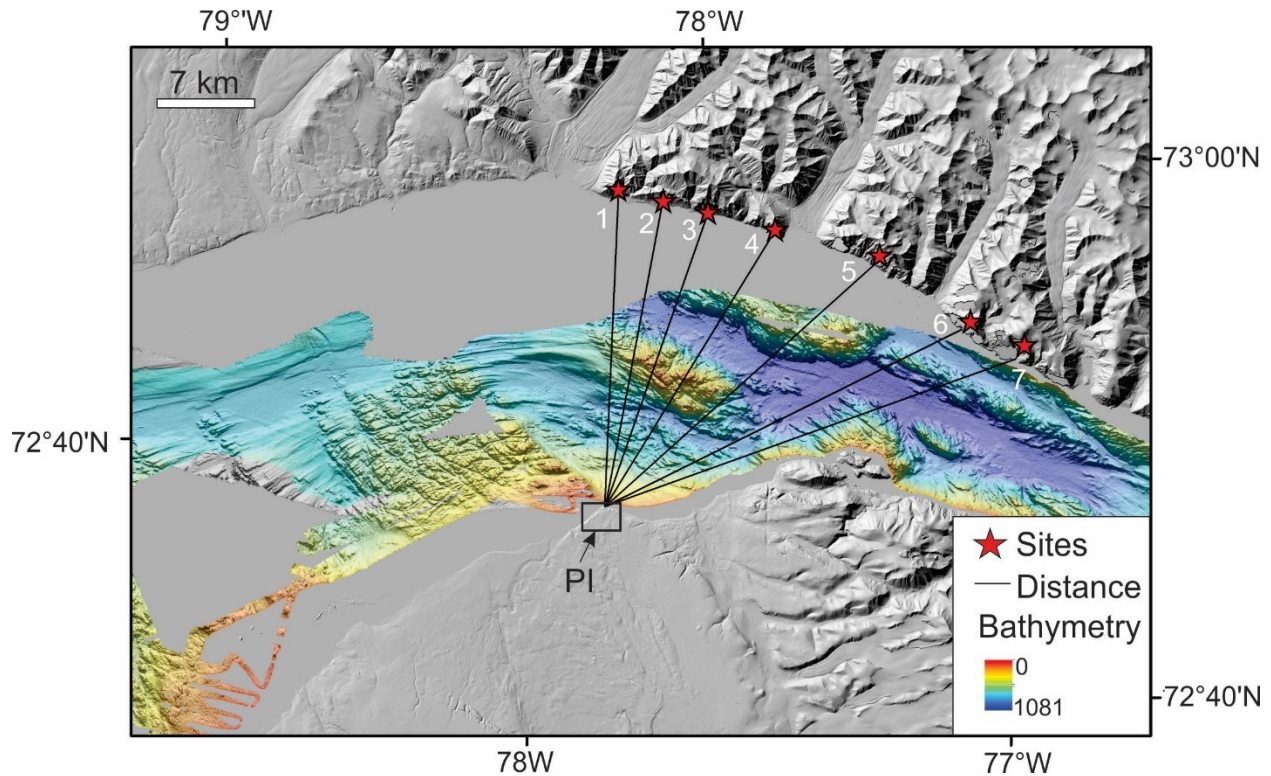


Figure 4.4 Location of the seven sites on the southern coast of Bylot Island used in the SPLASH calculations. The Hamlet of Pond Inlet (PI) is denoted by the black box, and the distances of the seven potential landslide sites from the Hamlet are shown as black lines. Multibeam bathymetry collected by OMG as part of ArcticNet (2005-2008). DEM(s) created from DigitalGlobe, Inc. imagery.

4.5 Results

4.5.1 Seafloor instability features in acoustic data

Broom et al. (submitted) and Brouard and Lajeunesse (2019) present a detailed account of the morphology of the seabed in the study area based on multibeam bathymetry. Several landforms on the seabed could indicate slope instability or mass movement. The largest mass wasting scar in the study area is observed along the slope where Navy Board Inlet enters Eclipse Sound (Figure 4.5). The mass wasting scar covers an area of approximately 17 km² and consists of gullies that are 2-5 km long and 10-150 m wide (Figure 4.5b). The slope in this region reaches 20° along the escarpment entering Eclipse Sound and averages 5° on the open slope adjacent to the gullies. Gullies are also observed along the north fjord wall of the central region of Pond Inlet south of Bylot Island (Figure 4.5c), where the slope is shallower than 3°. These gullies cover an

area of approximately 18 km² and are 1-2 km long and 10-20 m wide. The gullies towards central Pond Inlet (Figure 4.5c), and those directly south of Navy Board Inlet (Figure 4.5b), occur south of outlet glaciers on southern Bylot Island and appear related to glacial-fluvial drainage pathways (Figure 4.5a). This indicates they could have formed gradually, over a long period since deglaciation. Another possible instability feature observed in the multibeam bathymetry and sub-bottom profiler data is a linear escarpment in the centre of Pond Inlet (Figure 4.6; Figure 4.7). It has a relief of 20 m in sub-bottom profiler data and can be followed for 3.5 km along the basin floor. It appears to continue into the adjacent bedrock outcrops on the seafloor for 7 km to the NE and 4.5 km to the SE.

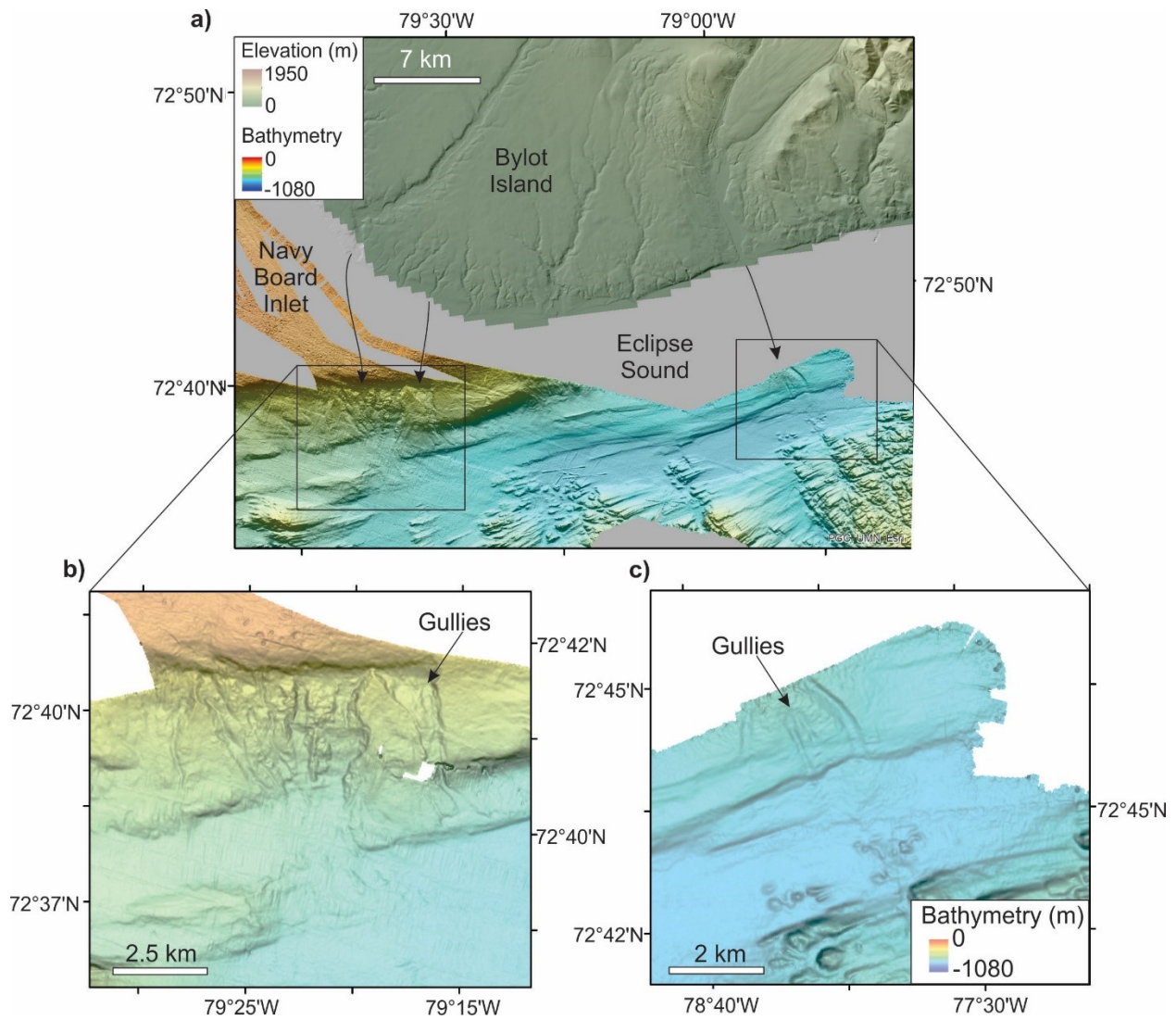


Figure 4.5: Mass wasting features at the seabed in Eclipse Sound. Drainage features of valley glaciers on Bylot Island are shown north of the gullies. Zoomed images of the gullies and slide scars showing the slope and the multibeam bathymetry collected by OMG as part of ArcticNet (2005-2008). DEM(s) created from DigitalGlobe, Inc. imagery.

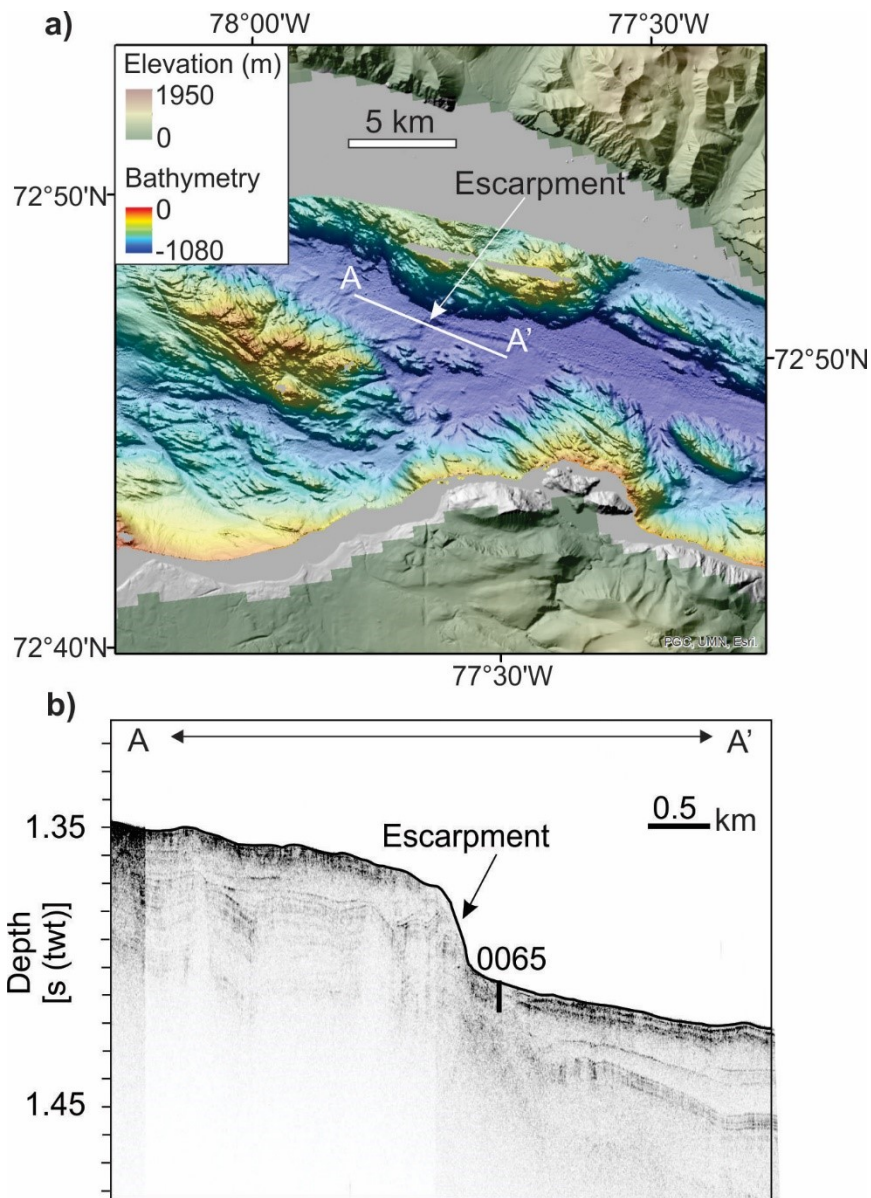


Figure 4.6: Escarpment observed at the seabed and in the sub-surface in the centre of Pond Inlet. Multibeam bathymetry collected by OMG as part of ArcticNet (2005-2008) and sub-bottom profiler line A-A' below. DEM(s) created from DigitalGlobe, Inc. imagery.

4.5.2 Sub-sea-floor evidence for slope instability

In the postglacial record, the majority of seabed instability features observed in Pond Inlet and Eclipse Sound are submarine. In the central region of Pond Inlet, where the sub-bottom profiler data and cores are concentrated, the inlet is separated into two distinct basins informally termed Pond Inlet Basin and Perched Basin by Broom et al. (submitted) (Figure 4.3). In the sub-bottom

profiler data, the postglacial record occurs above a distinct high-amplitude reflector (LU-UU Boundary, Broom et al., submitted) separating ice-contact and glaciomarine sediments from postglacial deposits. Analysis of the 3.5 kHz sub-bottom profiler data reveal postglacial sediments are composed of a well stratified acoustic facies and an acoustically chaotic to reflection-free facies. In Pond Inlet Basin, this well stratified facies consists of eight prominent moderate-high amplitude reflections, which have been interpreted as postglacial turbidites (Broom et al., submitted). These reflections are termed Turbidites A through H, and can be traced for 2-22 km and range in age from 1.1-12.7 ka BP. The upper three turbidites (Turbidite A-C) are penetrated by piston cores that were dated with foraminiferal and colus shell fragment radiocarbon dates, and the extrapolated ages of each of the turbidites are averaged (Table 4.4; Table 4.5). The five lower turbidites (Turbidite D-H) occur below the piston cores, and ages were extrapolated to their depth in sub-bottom profiler data using the basal sedimentation rate from core 0067 (Table 4.5). In Perched Basin, three moderate-high amplitude reflections are traced for up to 2 km, limited by the extent of sub-bottom profiler data. The age of deepest reflection in Perched Basin was interpolated from the oldest date in core 0066 to the depth of the reflection using the basal sedimentation rate in core 0066.

The sub-bottom profiler data also reveal six mass transport deposits (MTDs) preserved in the subsurface of Pond Inlet and Perched Basins. These were first recognized by Broom et al. (submitted). The MTDs occur in the subsurface below the relatively flat basin floors at a present day water depth of ~1060 m. The MTDs are acoustically chaotic-to transparent, lens to wedge shaped bodies that cover areas of approximately 4-34 km² and have maximum thicknesses from 9-22 m (Table 4.6; Figure 4.7; Figure 4.8). These MTDs are similar to those described by Damuth (1980). Their mapped area is a minimum estimate limited by the extent of the sub-

bottom profiler data. The turbidite chronology provides approximate ages for the MTDs from 12.7 to 2.9 ka BP (Table 4.6). MTDs 1 through 4 occur in Pond Inlet Basin. The lowermost MTD (MTD-1) is the largest MTD deposit and covers a minimum area of 34 km², a minimum volume of 320 Mm³, and is directly overlain by Turbidite H. The wedge shaped MTDs (MTD-2, MTD-3 and MTD-4) thin towards the centre of the basin (Figure 4.7). MTD-2 covers an area of 15 km², has a minimum volume of 100 Mm³, and is directly overlain by Turbidite D. MTD-3 and MTD-4 cover areas of 4-7 km², and are overlain by the same high-amplitude reflection (Turbidite C). They appear to represent two separate but possibly synchronous MTDs. MTD-5 occurs west of (above) the escarpment and terminates at the escarpment edge. It covers a minimum area of 7 km², limited by the extent of sub-bottom profiler data. No core has been taken above the escarpment so there is no direct age control for this MTD. MTD-6 occurs in Perched Basin between two bedrock highs and lies directly under core 0066. MTD-6 covers a minimum area of 6 km², limited by the sub-bottom profiler data.

Table 4.4: Ages of the correlated turbidites penetrated by the piston cores (Turbidites A-C). Ages were determined using linear interpolation between or below radiocarbon dates in the age model (Blaauw, 2010).

Core	Depth (cm)	Age (ka BP)	Turbidite
0065	61	1.26	Turbidite A
0067	104	1.09	Turbidite A
0002	47	0.97	Turbidite A
0065	130	2.11	Turbidite B
0067	225	1.89	Turbidite B
0065	216	2.74	Turbidite C
0067	433	2.83	Turbidite C
0002	138	2.87	Turbidite C
0003	213	3.04	Turbidite C

Table 4.5: Turbidites correlated in Pond Inlet Basin in the sub-bottom profiler data including their lateral extents, depth in TWT and m in the subsurface below core 0067, and ages. Ages for turbidite A-C (*) are average ages from Table 4.4. Turbidites D-H occur below core 0067 and ages were extrapolated using the basal sedimentation rate from core 0067 and depth of the reflector.

Turbidite	Lateral Extent (km)	TWT at core site 0067 (s)	Depth (m)	Maximum age (ka BP)	Standard deviation
Turbidite A	13	0.00241	2	1.1*	0.1
Turbidite B	12	0.00497	4	2.0*	0.1
Turbidite C	22	0.00895	7	2.9*	0.1
Turbidite D	2	0.01606	12	4.6	-
Turbidite E	5.5	0.01898	14	7.2	-
Turbidite F	7	0.02372	18	8.8	-
Turbidite G	7	0.02599	19	9.6	-
Turbidite H	17	0.03486	26	12.7	-

Table 4.6: MTDs correlated throughout Pond Inlet and Perched Basins including their geometry, area, maximum resolvable thickness in sub-bottom profiler data, volume, and age of the overlying reflectors described in Table 4.5. *represents the age of the high amplitude reflector above MTD-6 extrapolated using the basal sedimentation rate from core 0066 and depth of the reflector.

MTD	Geometry	Minimum area (km ²)	Max resolvable thickness (m)	Volume (Mm ³)	Approximate age (ka BP)
MTD-6	lens	6	10	-	10.7*
MTD-5	wedge	7	9	-	-
MTD-4	wedge	7	10	-	2.9
MTD-3	wedge	4	9	-	2.9
MTD-2	wedge	15	22	103	4.6
MTD-1	lens	34	21	322	12.7

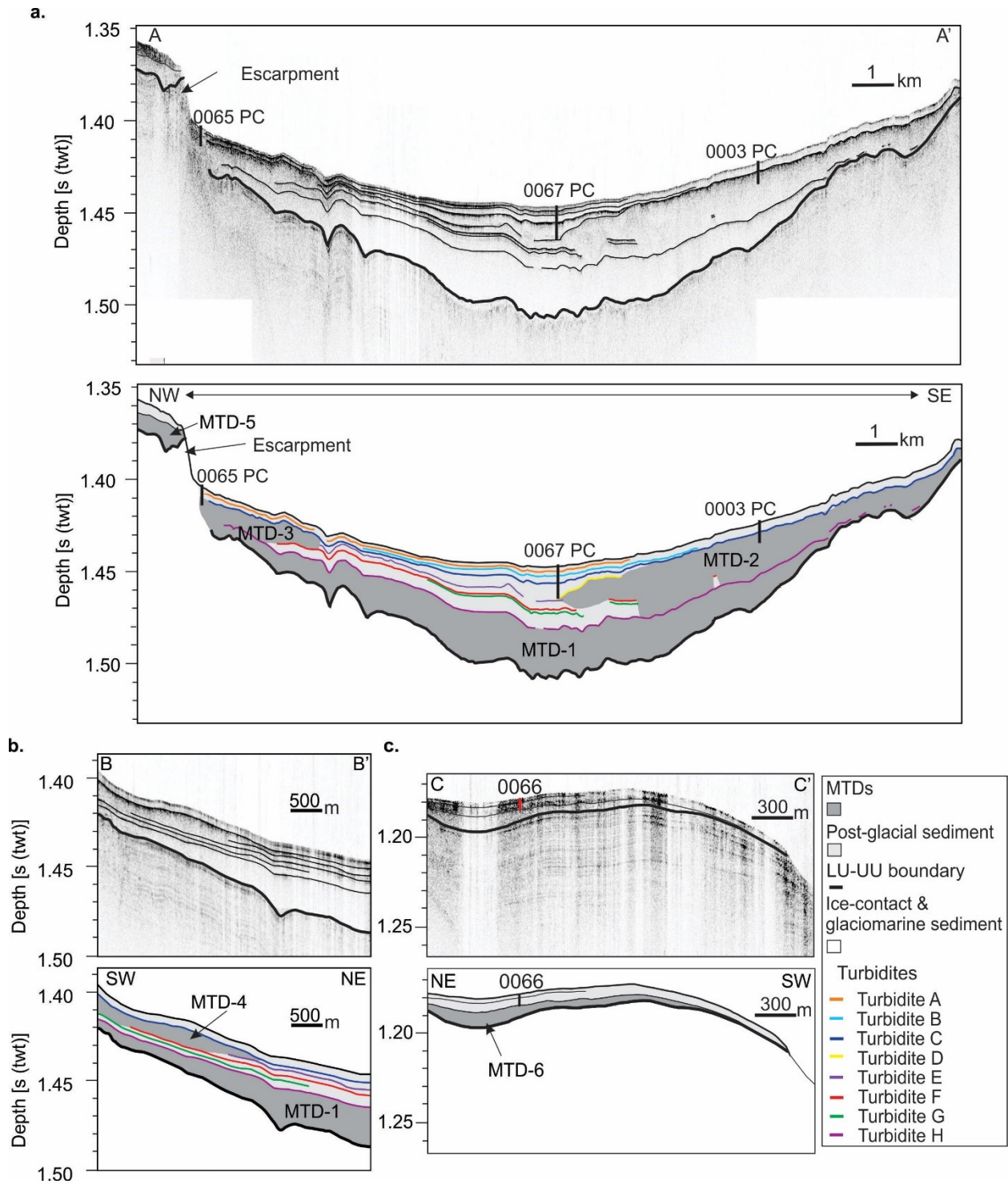


Figure 4.7: Sub-bottom profiler lines showing the extents of turbidites A through H and MTDs 1 through 6 in the subsurface. Locations of the sub-bottom profiler lines are indicated on Figure 4.3.

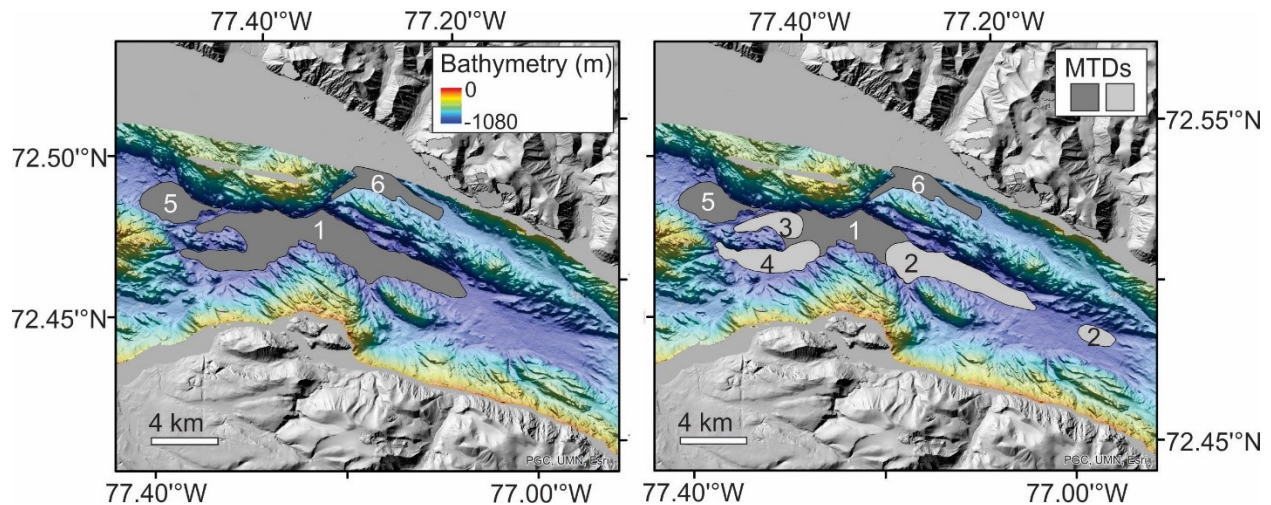


Figure 4.8: Map showing extent of MTDs extrapolated from the sub-bottom profiler data. Multibeam bathymetry collected for ArcticNet by OMG (2005-2008). DEM(s) created from DigitalGlobe, Inc. imagery.

4.5.2 Seafloor instability features in core data

The sediment cores collected from Pond Inlet are composed of postglacial sediments including hemipelagic and mass wasting deposits (Broom et al., submitted). The mass wasting deposits include a sand-silt turbidite lithofacies and three MTD lithofacies composed of: 1) inclined stratified mud, 2) folded mud, and 3) clast supported monomict mudclast conglomerate. The longest cores from the Pond Inlet and Perched Basins (cores 0067 and 0066) were examined to evaluate the occurrence of mass wasting in the subsurface at sub-centimetre scale. In core 0067, massive to laminated olive-grey hemipelagic sediments are interrupted by three MTD deposits and six turbidites over 10.6 m (Figure 4.9; Figure 4.5). The MTD lithofacies include mudclast conglomerates, and a 30 cm section of inclined stratified mud. The inclined stratified mud is interpreted as a small slump deposit (Tripsanas et al. 2008; Broom et al., submitted). The turbidites are 1 to 47 cm thick, commonly show erosive bases, are normally graded, and are composed of silt and sand. The sandy turbidites are composed of up to 92% very fine to coarse sand; silty turbidite are composed of up to 72% silt. The thickest turbidite interval (47 cm) is composed of multiple fining upwards sequences. These could correspond to multiple B through

E divisions in the Bouma sequence (Bouma, 1962) (multiple turbidites), or they could be related to hyperpycnal flows (St-Onge et al., 2004). The two lowermost turbidites directly overlie 15-37 cm thick deposits of monomict mudclast conglomerate. These are likely part of a debris flow deposit (Jenner et al. 2007; Broom et al., submitted). Core 0066, from Perched Basin, was also examined for evidence of mass wasting. The core does not penetrate MTD lithofacies, however massive to laminated olive-grey to dark-grey hemipelagic sediments are interrupted by 10 predominately silty turbidites that are 1 to 8 cm thick (Figure 4.9). These turbidites are below the resolution of the sub-bottom profiler data. Here, the sandy turbidites are up to 67% very fine to medium sand, and the silty turbidites are composed of up to 76% silt.

Using the radiocarbon dates and extrapolated ages from the age model, and the seismic imagery, several of the upper turbidites are correlated between cores 0065, 0067 and 0003 in Pond Inlet Basin (Figure 4.9). The upper two correlated turbidites (Turbidite A and Turbidite B) extend between cores 0065 and 0067, and have average ages of 1.1 ± 0.1 ka BP and 2.0 ± 0.1 ka BP respectively (Figure 4.9). The lower correlated turbidite (Turbidite C), is the most extensive and can be followed from core 0065 to 0003 for over 22 km (Figure 4.9). It has an average age of 2.9 ± 0.1 ka BP. Based on the age model for core 0066, two turbidites in Perched Basin are similar in age to those correlated in Pond Inlet Basin. They have approximate ages of 1.1 and 3.2 ka BP, similar in age to Turbidite A and Turbidite C in Pond Inlet Basin (Figure 4.9).

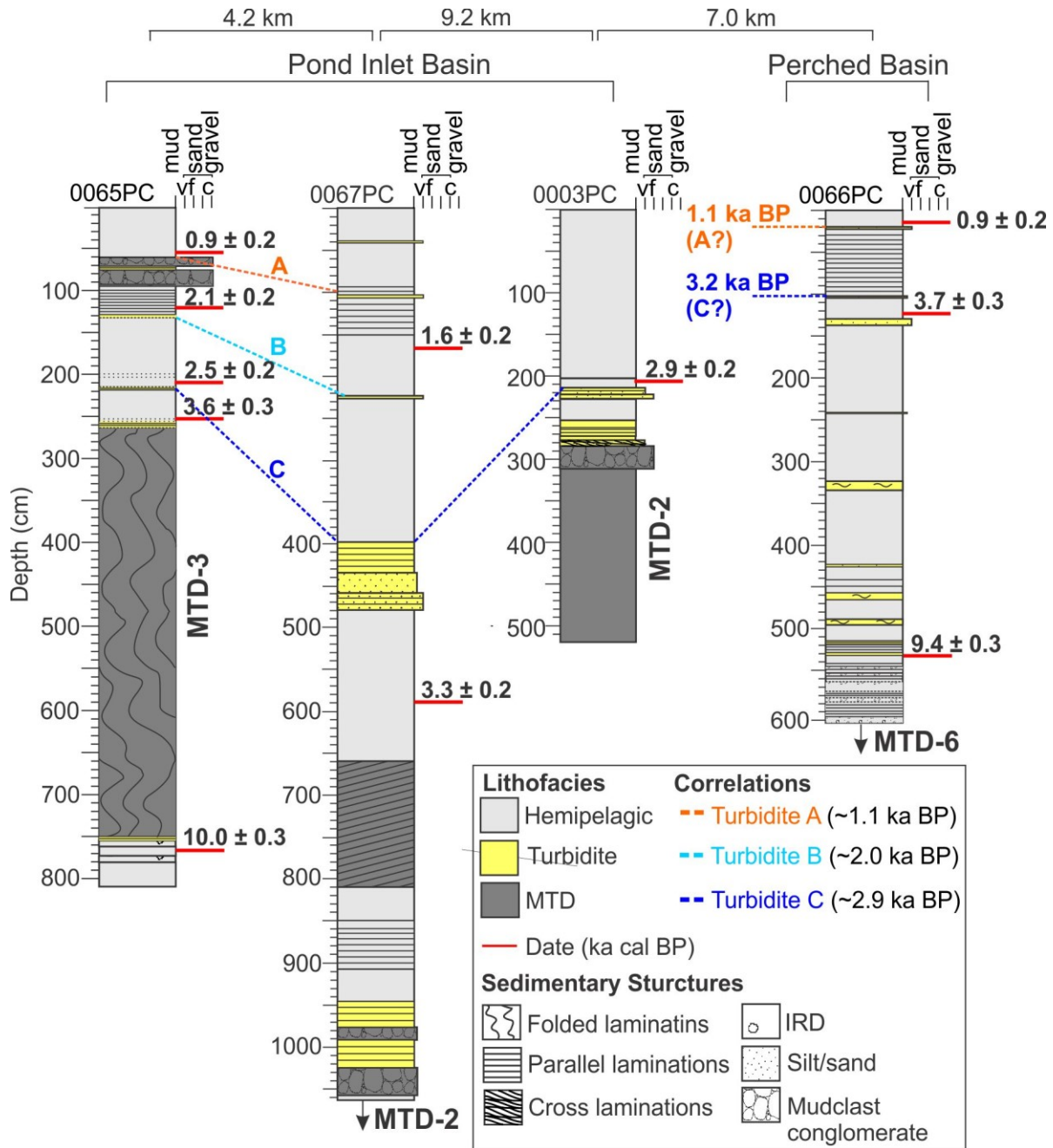


Figure 4.9 Lithofacies interpretations for cores 0065, 0067, and 0003 in the Pond Inlet Basin, and core 0066 in the Perched Basin. Calibrated radiocarbon dates are marked in red. Correlations between Turbidite A, Turbidite B, and Turbidite C are also shown.

By correlating the cores with the sub-bottom profiler data using synthetic seismograms, two cores (0065 and 0003) are shown to penetrate two of the wedge-shaped MTDs in the subsurface. Core 0003 penetrates the top of MTD-2 (Figure 4.9; Figure 4.10). The MTD sediment occurs from 311 cm to the base of the core and appears as a massive olive-grey mud deposit, similar in

colour to the hemipelagic deposits above. The upper 35 cm of the massive mud deposit contains horizontal mottling (Figure 4.10). The massive mud deposit is overlain by 27 cm of monomict mudclast conglomerate and two 12-30 cm thick turbidites. The two turbidites are 25 cm apart and are likely resolved as one reflection (Turbidite C) by the sub-bottom profiler data. The age model reveals that the upper turbidite that overlies MTD-2 is approximately 3.0 ka BP, corresponding to Turbidite C (average age of 2.9 ka BP). MTD-2 has an approximate age of 4.6 ka BP based on the extrapolated age of the overlying reflector (Turbidite D) just below core 0067. MTD-2 is assumed to be older than MTD-3 and MTD-4 because at core site 0067 there is approximately 7.5 m of sediment between MTD-2 and Turbidite C, and this turbidite directly overlies MTD-3 and MTD-4 in the sub-bottom profiler data. This is further supported by the observation of horizontal mottling at the top of the MTD-2 interval in core 0003 (Figure 4.10). This mottling, which was caused by bioturbation, does not appear to have been displaced, and could represent a period of hemipelagic sedimentation on top of the MTD, representing the time between the deposition of MTD-2 and Turbidite C.

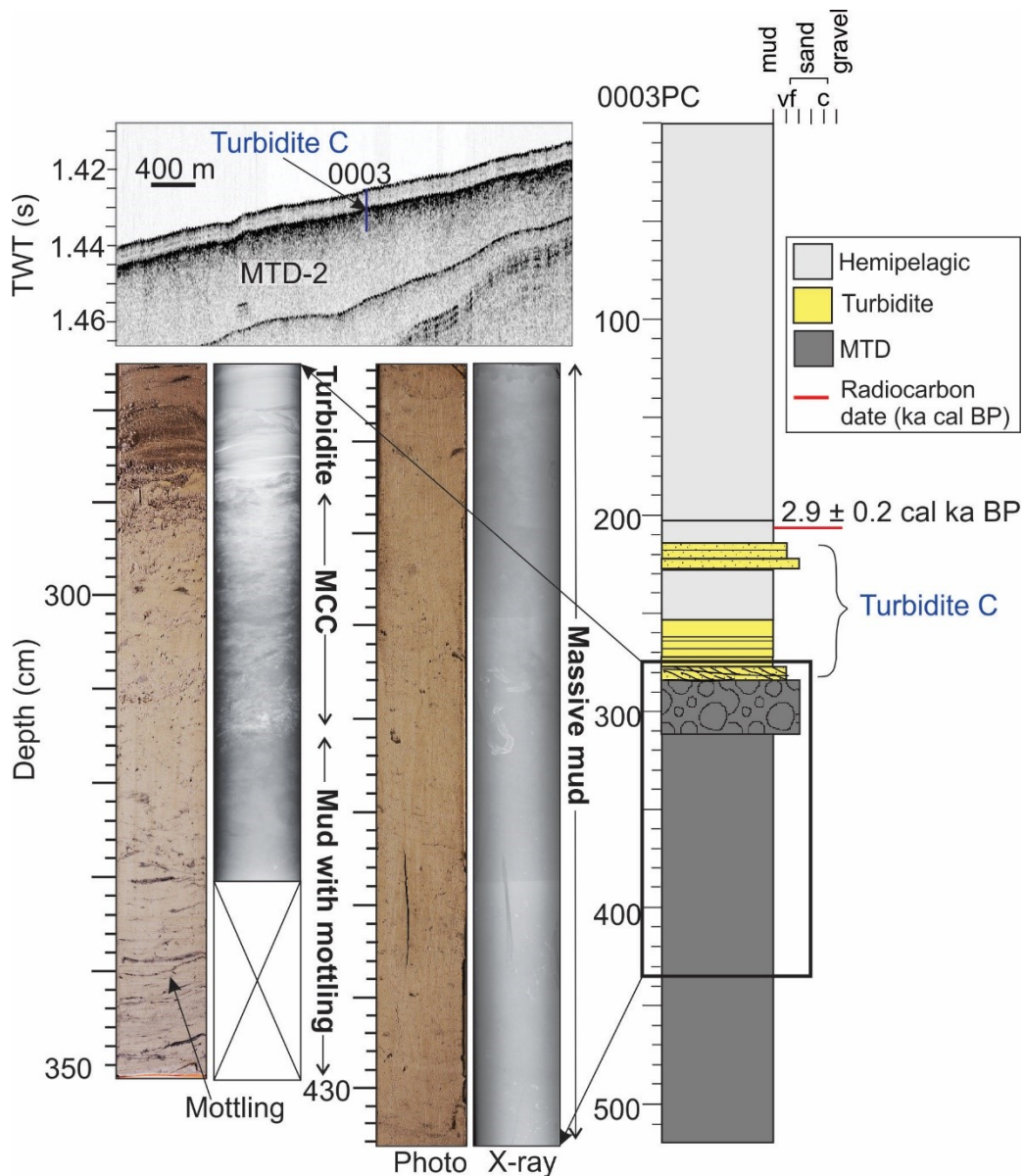


Figure 4.10: Piston core 0003 in sub-bottom and core data shows MTD-2 as a massive mud deposit overlain by normal hemipelagic sedimentation with mottling. This is overlain by a mudclast conglomerate (MCC) cut by Turbidite C, which is resolved as a single high-amplitude reflector in sub-bottom profiler data and recognized as the two separate turbidites in core 0003.

Core 0065 penetrates MTD-3 at the base of the escarpment (Figure 4.7; Figure 4.9; Figure 4.11).

The MTD deposit occurs from 262 to 750 cm in core and consists of folded olive-grey to dark grey silty-mud. This deposit shows convoluted silt-sand laminations along with sharp, angled contacts between olive-grey and dark-grey silty-mud (Figure 4.11). The MTD is overlain by two thin turbidites, which appear to be resolved as a single strong reflector above the MTD-3 in sub-

bottom profiler data (Figure 4.11). The age model reveals that the upper overlying turbidite was deposited approximately 2.7 ka BP, corresponding to Turbidite C (average age of 2.9 ka BP). MTD-3 is older than the overlying reflector and based on the age model was deposited prior to 3.6 ka BP.

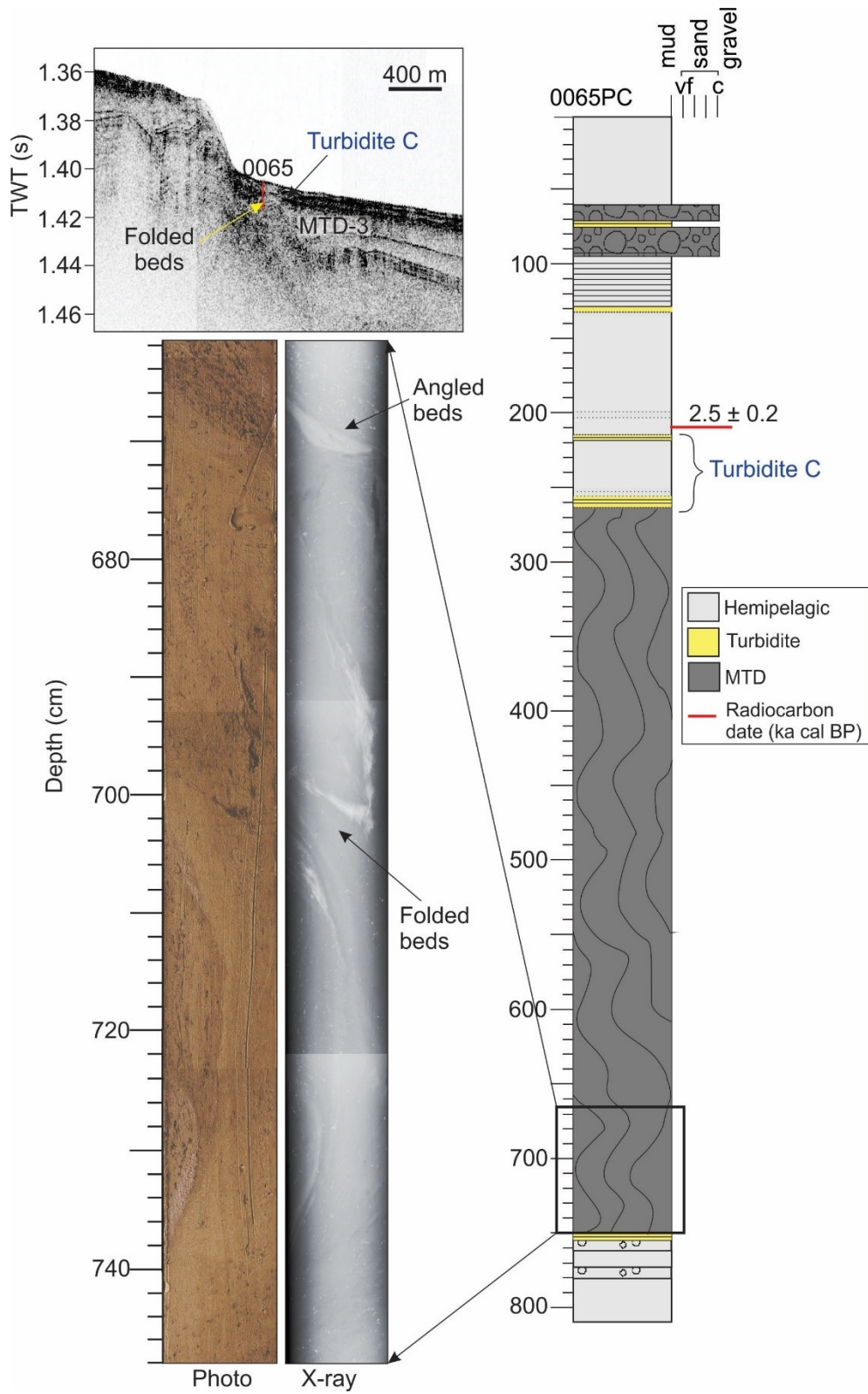


Figure 4.11: Piston core 0065 in sub-bottom and core data showing folded beds in MTD-3 at the base of the core and the overlying turbidites (Turbidite C).

4.5.3 Slope stability analysis

Slope stability analysis of the five piston cores using Equation 4.2 reveals the sediments within the five piston cores have a $FS > 1$, indicating these sediments are stable under gravitational loading alone. Core 0067 was taken from the centre of Pond Inlet, where the slope is 0.9° , and it is the only core that does not penetrate one of the large MTDs, so it was used for the following slope stability analysis. Equation 4.2 shows that sediment is stable under current conditions in core 0067, with a minimum FS of 9.72 near the base of the core (Figure 4.12a). Core 0067 is used to assess three factors that control slope instability in Pond Inlet including: slope angle, overburden height, and horizontal acceleration produced by earthquakes.

Using Equation 4.3, the minimum critical slope angle required to fail sediments in core 0067 is 8.60° (Figure 4.12b). From the multibeam bathymetric data the majority of areas that exceed a slope of 8.6° include the slopes along the bedrock highs and crag and tail features, the steep flanks along the sides of the inlet, and the delta entering Pond Inlet from northern Baffin Island (Figure 4.13). It is also noted that the critical angle is not exceeded at the escarpment (maximum of approximately 7°). From Equation 4.4, a minimum critical height of 57 m of overburden is required to produce a $FS < 1$ at a slope angle of 0.9° . In the case of an earthquake, the minimum acceleration coefficient (from Equation 4.7) required to produce a $FS < 1$ at a slope angle of 0.9° is 0.13 g.

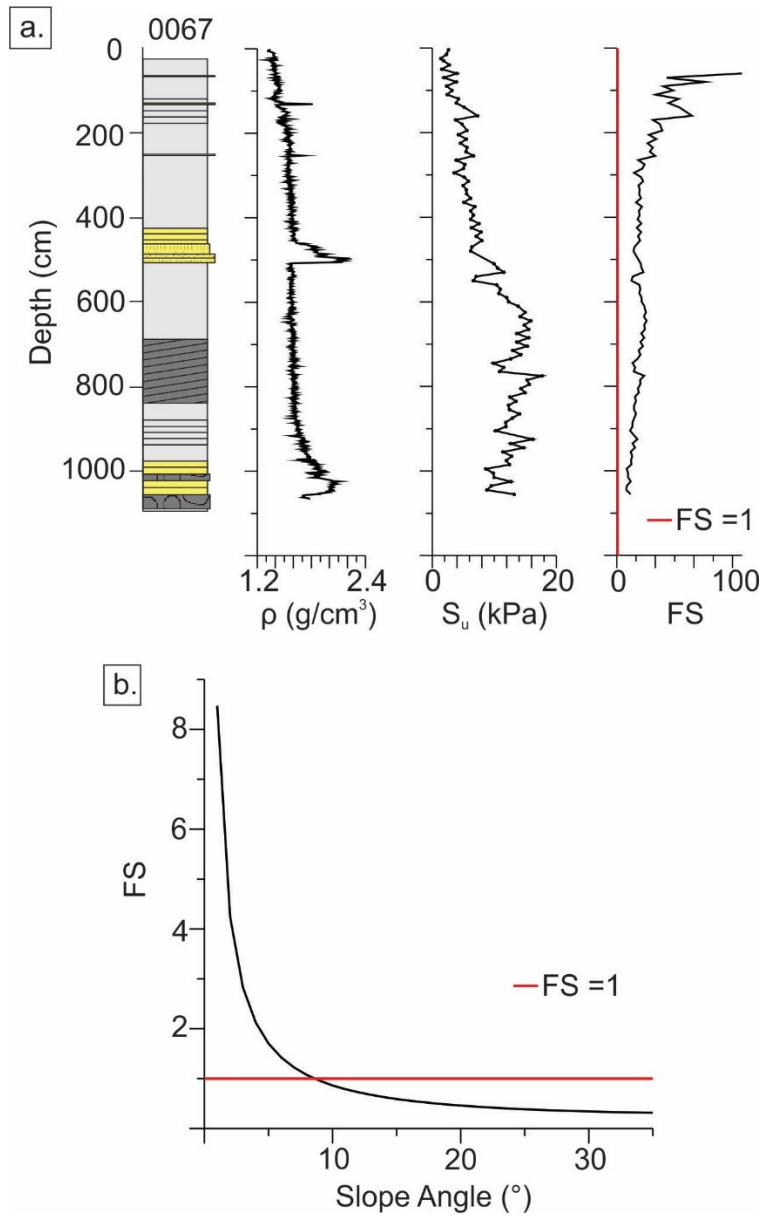


Figure 4.12: (a) Slope stability analysis of core 0067 showing from left to right: core interpretation, down core bulk density (ρ), undrained shear strength (S_u), and factor of safety (FS). (b) Graph showing factor of safety (FS) vs slope angle, with the critical angle marked where $FS=1$.

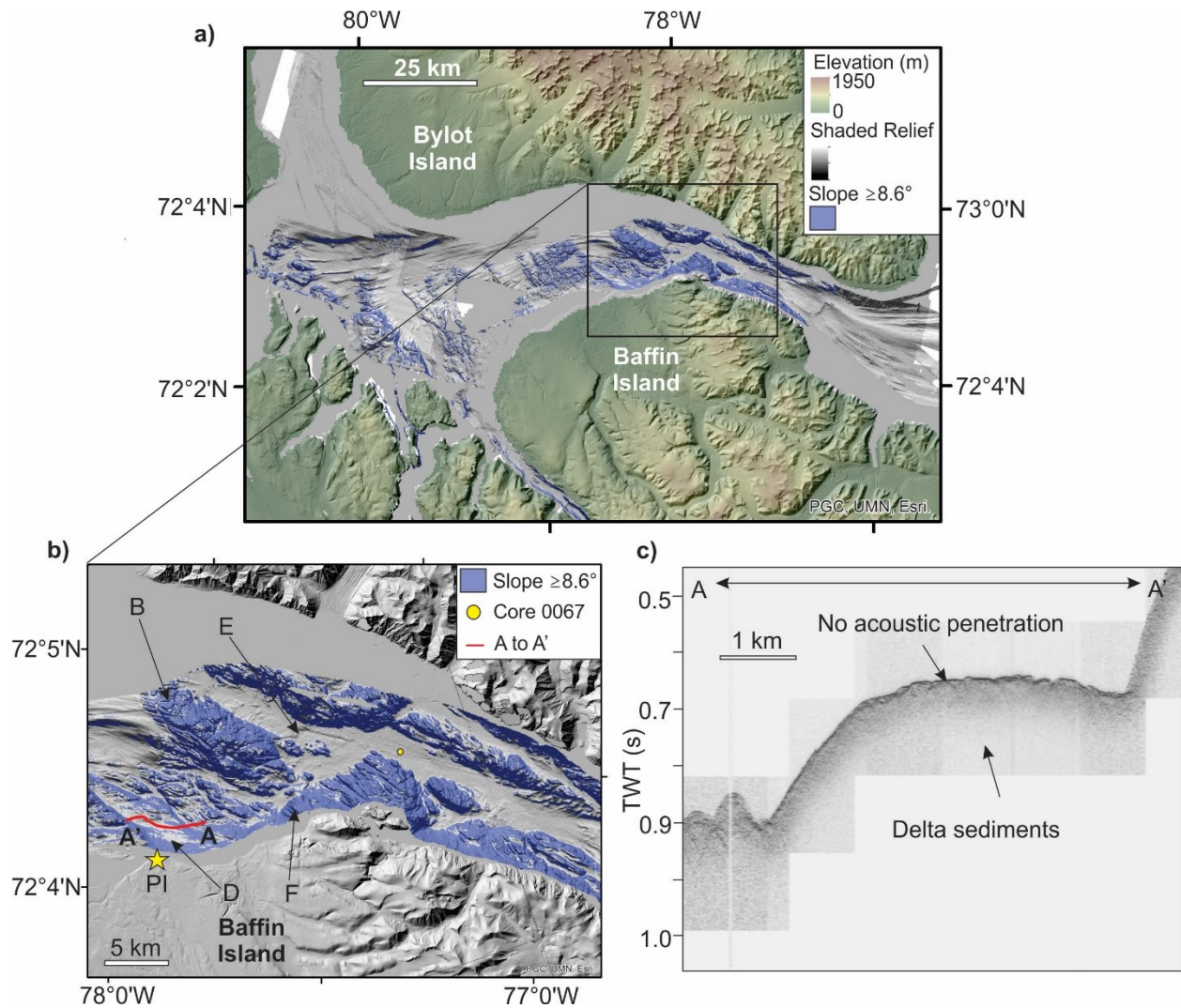


Figure 4.13 a) Map of Pond Inlet and Eclipse Sound showing areas with a slope angle of $\geq 8.6^\circ$ b) Shows bedrock highs (B), delta (D), inlet flanks (F), and the escarpment (E). c) Sub-bottom line A-A' marked on zoomed image. PI = Pond Inlet. Multibeam bathymetry collected by OMG as part of ArcticNet (2005-2008). DEM(s) created from DigitalGlobe, Inc. imagery.

4.5.4 Prediction of run-up height from subaerial landslides

Table 4.7 and Figure 4.14 show predicted run-up heights at the Hamlet of Pond Inlet from a subaerial landslide entering the inlet at Sites 1 through 7 (Figure 4.4) based on the empirically-based SPLASH model. The most and least conservative volumes estimates from the 2017 Nuugaatsiaq landslide (Bessette-Kirton et al., 2017; Chao et al., 2018) are used to predict possible run-up elevations at the Hamlet of Pond Inlet if a landslide of similar volume occurred

along the steep mountain faces of Bylot Island (Table 4.7). Results from Equation 4.8 using the conservative volume estimate (33.4 Mm³) predict a run-up of 14 m at the Hamlet from a landslide occurring at Site 1, and an 11 m run-up from a landslide at Site 7. When the largest estimated landslide volume for the Nuugaatsiaq landslide is tested (74.4 Mm³), a 22 m run-up height is predicted at the Hamlet from a landslide at Site 1 (Figure 4.14), and a 17 m run-up from Site 7.

Table 4.8 shows the volumes of landslide material required at each of the seven sites to produce a 10 and 60 m run-up height at the Hamlet of Pond Inlet. Volumes required to produce a 10 m run-up height (Figure 4.14) are on the same order of magnitude as the Nuugaatsiaq landslide, and to produce a 60 m run-up (Figure 4.14), the required volumes are greater by an order magnitude.

Table 4.7: Run-up heights (m) at the Hamlet of Pond Inlet predicted by Equation 4.8 for a landslide occurring at Sites 1-7 on Bylot Island with a volume of 33.4 Mm³ and 74.4 Mm³. See Figure 4.4 for site locations.

Site	Run-up (m) from a 33.4 Mm ³ landslide	Run-up (m) from a 74.4 Mm ³ landslide
1	14	22
2	14	22
3	14	22
4	13	21
5	12	19
6	11	18
7	11	17

Table 4.8: Volumes (Mm³) of landslide material required by Equation 4.8 at Sites 1-7 on Bylot Island to produce 10 and 60 m run-up heights at the Hamlet of Pond Inlet. See Figure 4.4 for site locations.

Site	Volume (Mm ³) for 10 m run-up	Volume (Mm ³) for 60 m run-up
1	19.3	444
2	19.1	439
3	19.4	447
4	20.2	466
5	23.5	542
6	27.2	627
7	30.7	706

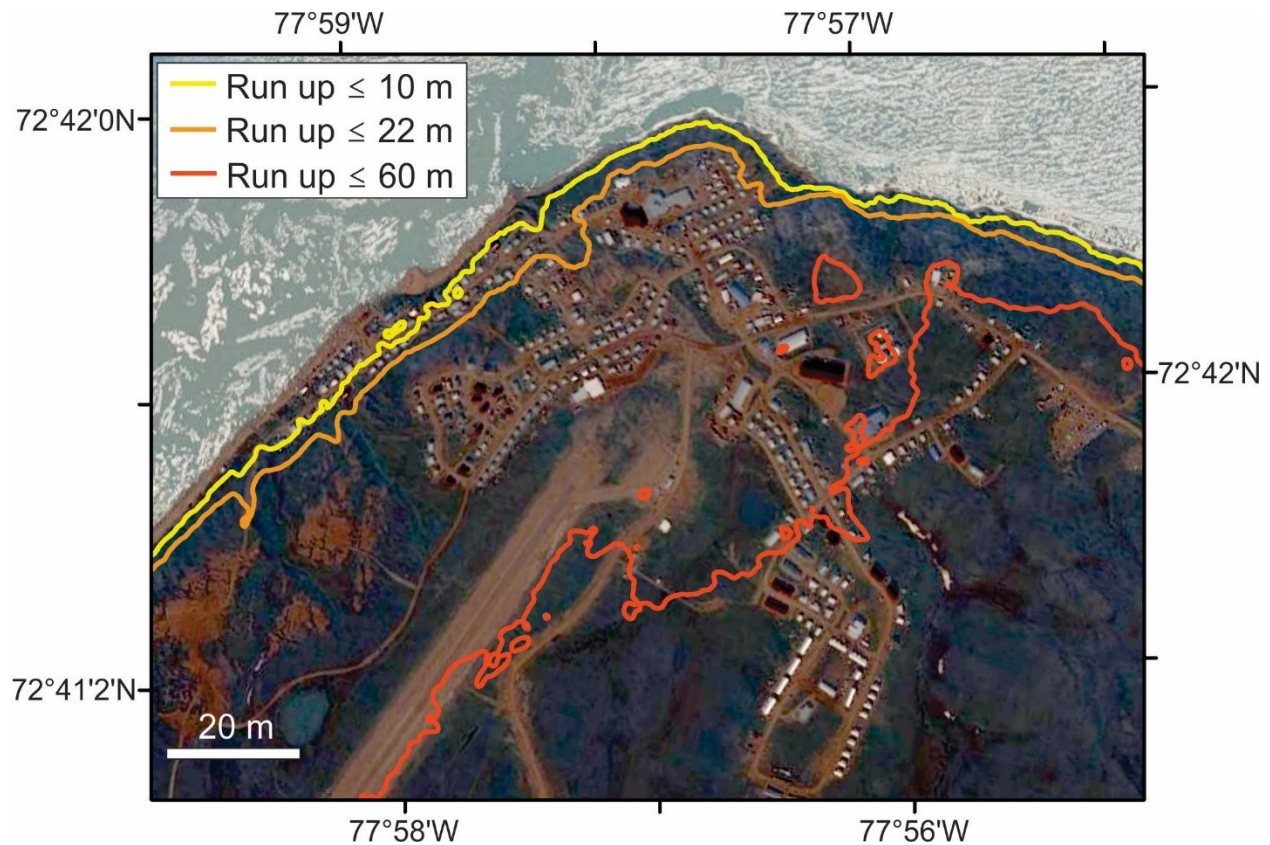


Figure 4.14: Results of SPASH analysis for the Hamlet of Pond Inlet showing run-up heights of 10 and 22 m asl. An elevation of 60 m asl is shown to display the run-up height needed to inundate the airport and the majority of the Hamlet. Base map imagery U.S. Geological Survey, Landsat/Copernicus, IBCAO. Base map data SIO, NOAA, U.S. Navy, NGA, GEOBO; ©2018 Google.

4.6 Discussion

4.6.1 Slope instability in the postglacial record

The averaged (Turbidites A-C) and extrapolated (Turbidites D-H) turbidite ages were used to constrain the frequency of mass movement events in Pond Inlet from the late Pleistocene through the Holocene. It is important note that the extrapolated ages are likely maximum ages, as they are based on assumptions that sedimentation rates did not change from the basal radiocarbon date of 3.3 ka cal BP in core 0067 to the depth of the lowermost high-amplitude reflection in the postglacial record. These reflections occur up to 20 m below the depth of the basal radiocarbon date. Sedimentation rates were likely higher during the early Holocene as the ice front was receding from Pond Inlet (Broom et al., submitted; Andrews et al., 1985; Bellwald et al., 2019),

suggesting these are maximum ages. These extrapolated ages indicate basin-wide instability in Pond Inlet Basin is recorded after 12.7 ka BP, starting with the deposition of the first MTD (MTD-1) and postglacial turbidite. Within Perched Basin, the deposition of the first MTD (MTD-6) and turbidite occurred at approximately 10.7 ka BP. Over the last 12.7 ka, there has been an average of one mass wasting event recorded in central Pond Inlet every 1.6 ka. More recently, over the last 2.9 ka, the MTD recurrence interval is 1.0 ka. When mass movement events are examined at a finer scale, at the resolution of the core data, more frequent events are observed. In core 0067, if the monomict mudclast conglomerate overlain by turbidites is included as part of the same debris flow or debris avalanche deposit, then the age model indicates that seven gravity driven flows have been recorded over the last 5.5 ka, which corresponds to one event every 800 years. At this time, the 45 cm thick turbidite interval with multiple fining upwards sequences is treated as one continuous deposit, as more work is needed to understand if these are multiple turbidites or if they are related to hyperpycnal flows (St.-Onge et al., 2004). The age model for core 0066 reveals that nine turbidites were deposited over the last 10.7 ka, which corresponds to one turbidite every 1.2 ka. Though turbidites and MTDs are common in the subsurface, the lack of preservation of mass wasting at the seabed or subaerially suggests that few modern slope failures have occurred within Pond Inlet and Eclipse Sound or that they are too small to be resolved by conventional seabed mapping methods.

More information is needed to determine the geohazard significance of the escarpment in Pond Inlet Basin. It is still unknown if this escarpment is a pre-Quaternary bedrock bathymetric feature that has not been smoothed over by the deposition of postglacial deposits, or if it is an active fault or inactive fault line scarp. The thickness of the postglacial sediments adjacent to the escarpment is similar above and below this feature, allowing for the possibility that the scarp

could be late Holocene. However, no cores have been collected above the escarpment to determine if the reflections above this feature are older than turbidites and MTDs deposited below.

4.6.2 Nature of MTD transport

In the study area, six MTDs cover areas up to 34 km². The wedge shaped MTDs (MTDs 2-5) truncate moderate to high amplitude reflections, indicating that some of these deposits have undergone transport; however, more information is needed to determine if transportation distance was significant. Only two piston cores (0065 & 0003) penetrate the large (≥ 9 m thick) MTDs observed in the subsurface. Where core 0065 was taken, adjacent to MTD-3, internal structures of the unconsolidated sediments are preserved within the folded mud deposit, indicating that the transport distance was probably not significant (Tripsanas et al., 2008). The deposits in core 0065 and 0003 have similar composition and colour to the surrounding hemipelagic sediments, suggesting transport distance could be short. The mudclasts in core 0003 are similar in composition and colour to the underlying massive mud deposit, suggesting they are locally sourced.

MTDs in core and acoustic data exhibit some degree of deformation and/or transport. We use the term autochthonous for MTDs that display evidence for having been deformed in place, and allochthonous for MTDs that show significant transport. Terms such as frontally confined and frontally emergent have also been used to describe these processes (Frey-Martínez et al., 2006). The local nature of the sediment and the preservation of internal structures in the MTDs in core 0065 and 0003 suggest that these are autochthonous MTDs. The massive mud that makes up the MTD interval in core 0003 could indicate the disturbed material is composed of homogeneous mud, or that sediment deformation processes are sufficiently vigorous to homogenize the

sediment. The turbidites that overlie these MTDs have a coarser composition than the surrounding hemipelagic mud suggesting these are allochthonous deposits that have travelled a greater distance from their source area.

To test if some of the MTDs are autochthonous, sedimentation rates from the age model (this study) were used to determine if the MTDs have maintained their original deposition thickness. Determining the rate of sedimentation prior to, during, and after an MTD was deposited reveals if (i) the sediment mostly existed prior to deformation and was mobilized in place or (ii) the package of sediment was instantaneously added. For the large folded mud MTD in core 0065, if the age model treated this MTD as an instantaneous deposit, sedimentation rates are extraordinarily low (0.03 mm/year) in the sediments deposited above and below that event (Figure 4.15). Instead, if the MTD deformed internally with little to no change in net sediment thickness, the sedimentation rate including the deposit are 0.8 mm/year (Figure 4.15), which matches closely with the average sedimentation rate in the central basin determined by Broom et al. (submitted) of 0.9 mm/year. This corroborates that the MTD in core 0065 and potentially other MTDs in Pond Inlet are autochthonous and have not been transported a significant distance.

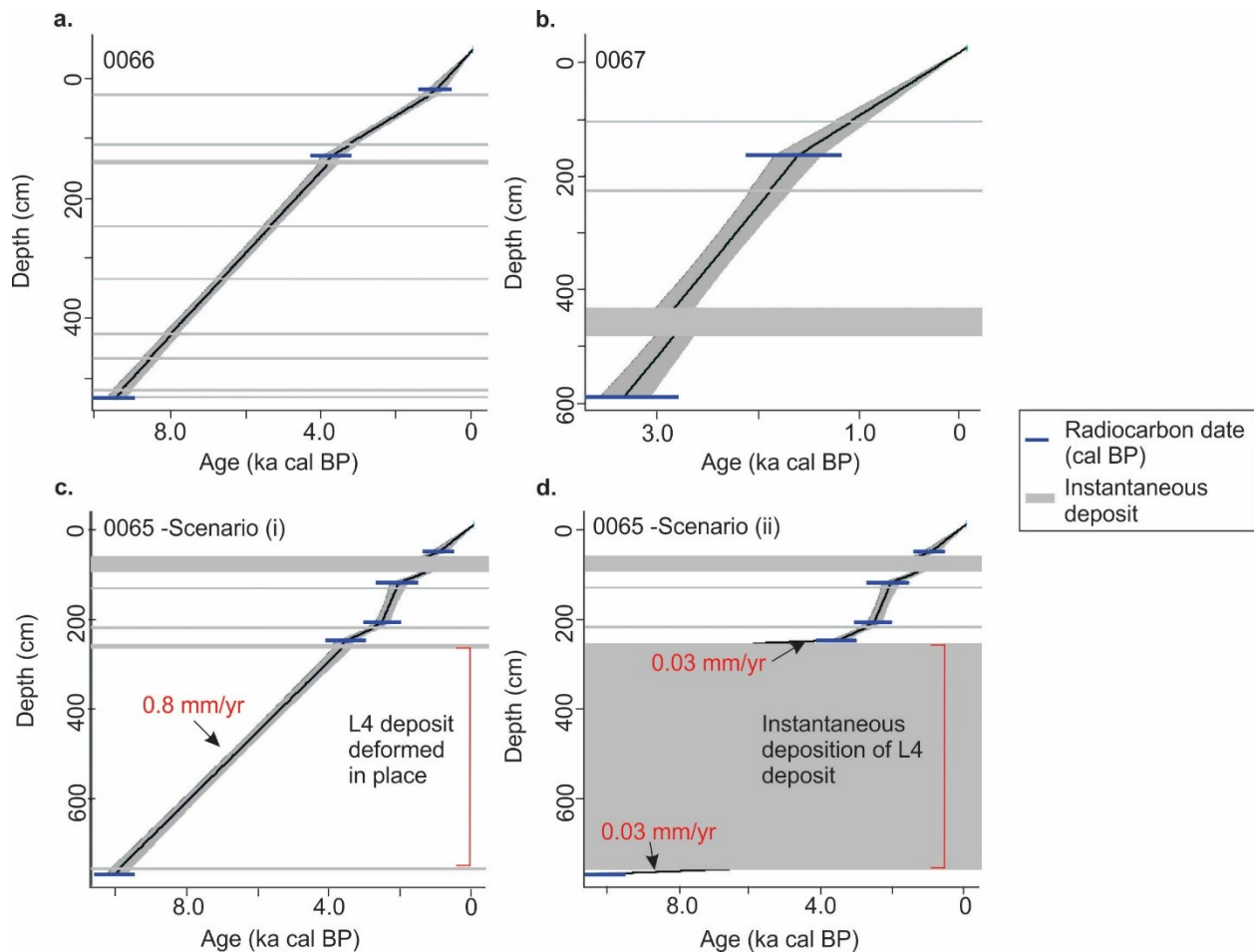


Figure 4.15: Age models (Blaauw, 2010; version 2.2) for (a) core 0066 with three radiocarbon dates and nine instantaneous deposits; (b) core 0067 with two radiocarbon dates and three instantaneous deposits; (c) core 0065 with five radiocarbon dates and treating the L4 deposit as if it was deformed in place; (d) core 0065 with five radiocarbon dates and treating the L4 deposit as if it was instantaneously deposited. Radiocarbon dates are plotted with 2-sigma error.

4.6.3 Triggering mechanisms

Although other possible triggering mechanisms are recognized for the gravity driven flows in Pond Inlet (e.g. glacial outburst flood, flood, storms, permafrost thaw, unloading of valley walls), the available data afford the opportunity to evaluate the plausibility of 1) slope angle and 2) earthquakes as potential factors triggering the mass transport deposits. The critical angle of 8.6° from core 0067 is exceeded on bedrock highs, the flanks of the inlet, and the delta just north of the Hamlet (Figure 4.13). The bedrock highs and steep fjord flanks are likely covered with a thin veneer of hemipelagic sediment not imaged by the multibeam. The critical angle calculation

accounts for overburden pressure, which includes the overburden height. The critical angle of 8.6° is calculated for sediments with 10.5 m of overburden. Sediments above bedrock highs and inlet flanks are unlikely to exceed this thickness, as no sediments are imaged by the sub-bottom profiler data. This suggests that hemipelagic sediments are stable under slope angle alone and would require an external triggering mechanism for slope failure. The mass wasting scars south of Navy Board Inlet are also in an area that exceeds the critical angle. The gullies occur to the south glacier outlets on Bylot Island and are probably related to the glacio-fluvial discharge (Figure 4.5). The delta entering the inlet just north of the Hamlet of Pond Inlet has a slope greater than 8.6° ; however, the sub-bottom profiler data shows little acoustic penetration. This suggests sediments at the seabed are composed of coarser material such as sand (Damuth, 1980), and this material would not have the same physical properties as the hemipelagic sediments from the deep basin, and therefore cannot be directly compared. The escarpment does not exceed the critical angle, so slope angle alone is not enough to result in the MTDs and turbidites below this feature. These results suggest that even in most places where the critical angle is exceeded in Pond Inlet and Eclipse Sound, an external triggering mechanism is likely required to fail the sediments.

To evaluate the critical acceleration, the minimum peak ground acceleration (PGA) (our minimum horizontal seismic coefficient) needed to trigger slope instability at core site 0067 is compared to the 2015 National Building Code interpolated seismic hazard values. In Pond Inlet, there is a 5% probability in 50 years that ground motions will exceed 0.19 PGA (Halchuk et al., 2015). This is above the critical acceleration of 0.13 g calculated for core 0067, which suggests that there is the potential for ground acceleration to exceed the minimum acceleration in the next 50 years. There is a 10% probability that in 50 years that ground motions will exceed 0.12 g,

which is just below the minimum acceleration. This comparison indicates that the high seismicity of Baffin Bay is a plausible triggering mechanism for slope failures in the inlet and should be investigated further. A hazard probability of 5 to 10% is assigned to seismogenic failures from earthquakes external to Pond Inlet and Eclipse Sound. The 1933 7.3 M_s strike slip earthquake does not appear to have produced mass wasting deposits in Pond Inlet. This earthquake was over 250 km from the center of Pond Inlet, which could have been too far to produce slope instability in this region, and the strike-slip motion of the earthquake might not have produced the vertical ground motion required to trigger slope failure. To understand if seismicity is an effective triggering mechanism in northern Baffin Bay, records of the timing of mass movement events should be extended into surrounding fjords to determine if turbidites and/or MTDs have been simultaneously triggered over the surrounding region (Goldfinger, 2011).

4.6.3 Potential for a displacement wave at the Hamlet of Pond Inlet

The results from Equation 4.8 indicate the plausibility that a subaerial landslide on Bylot Island cliffs above Pond Inlet similar in size to the 2017 Nuugaatsiaq landslide could generate a displacement wave with a large enough run-up height to impact the Hamlet of Pond Inlet. The impact would be limited to infrastructures below 22 m asl. The airport and the majority of the community resides <60 m asl. A landslide on Bylot Island would need to be an order of magnitude larger than the Nuugaatsiaq landslide (444 Mm^3 from Site 1 and 774 mM^3 from Site 2) to produce a 60 m run-up at the Hamlet (Table 4.8). These results justify the need for field and remote sensing analyses of large fractures and evidence of slope instability on the southern coastal cliffs of Bylot Island.

4.7 Conclusions

Our investigation of the marine record of Pond Inlet and Eclipse Sound, including acoustic and core data, show that the postglacial record is frequently interrupted by mass wasting deposits including MTDs and turbidites. The results reveal: 1) mass wasting is recorded in the postglacial sediments after 12.7 ka BP, 2) since 12.7 ka BP, sub-bottom profiler data record at least one mass movement event every 1.6 ka, and the recurrence interval has decreased to one event every 1.0 ka over the last 2.9 ka, and 3) some of the MTDs have likely undergone little transport and have been mobilized in place. The slope stability assessment indicates that an external triggering mechanism is required to cause slope failure, and that the high seismicity of Baffin Bay is a plausible triggering mechanism that requires further investigation. The SPLASH analysis demonstrates that there is a potential for landslide-generated displacement waves that could cause run-up heights that exceed the elevation of infrastructure (>10 m) within the Hamlet of Pond Inlet. Further investigation is needed to evaluate whether or not fractures and foliation patterns on the southern coast of Bylot Island are optimal for failure.

4.8 References cited in Chapter 4

- Aksu, A.E., 1984. Subaqueous debris flow deposits in Baffin Bay. *Geo-Marine Lett.* 4, 83–90. <https://doi.org/10.1007/BF02277077>
- Aksu, A.E., Hiscott, R.N., 1989. Slides and debris flows on the high-latitude continental slopes of Baffin Bay. *Geology* 17, 885–888. [https://doi.org/10.1130/00917613\(1989\)017<0885:SADFOT>2.3.CO;2](https://doi.org/10.1130/00917613(1989)017<0885:SADFOT>2.3.CO;2)
- Andrews, J.T., 1970. Present and postglacial rates of uplift for glaciated northern and eastern North America derived from postglacial uplift curves. *Can. J. Earth Sci.* 7, 1184–1184. <https://doi.org/10.1139/e70-112>
- Andrews, J.T., Jull, A.J.T., Donahue, D.J., Short, S.K., Osterman, L.E., 1985. Sedimentation rates in Baffin Island fjord cores from comparative radiocarbon dates. *Can. J. Earth Sci.* 22, 1827–1834. <https://doi.org/10.1139/e85-194>

- Basham, P.W., Forsyth, D.A., Wetmiller, R.J., 1977. The seismicity of northern Canada 14, 1646–1667. <https://doi.org/10.1139/e77-140>
- Bellwald, B., Hjelstuen, B.O., Sejrup, H.P., Stokowy, T., Kuvås, J., 2019. Holocene mass movements in west and mid-Norwegian fjords and lakes. *Mar. Geol.* 407, 192–212. <https://doi.org/10.1016/j.margeo.2018.11.007>
- Bent, A.L., 2002. The 1933 Ms= 7.3 Baffin Bay earthquake: Strike-slip faulting along the northeastern Canadian passive margin. *Geophys. J. Int.* 150, 724–736.
- Bessette-Kirton, E., Allstadt, K., Pursley, J., Godt, J., 2017. Preliminary Analysis of Satellite Imagery and Seismic Observations of the Nuugaatsiaq Landslide and Tsunami, Greenland [WWW Document]. URL https://www.usgs.gov/natural-hazards/landslide-hazards/science/preliminary-analysis-satellite-imagery-and-seismic?qt-science_center_objects=0#qt-science_center_objects
- Blaauw, M., 2010. Methods and code for “classical” age-modelling of radiocarbon sequences. *Quat. Geochronol.* 5, 512–518. <https://doi.org/10.1016/j.quageo.2010.01.002>
- Bouma, A.H., 1962. *Sedimentology of some Flysch deposits; a graphic approach to facies interpretation.* Elsevier Pub. Co, Amsterdam, New York.
- Brouard, E., Lajeunesse, P., 2019. Geomorphology Glacial to postglacial submarine landform assemblages in fi ords of northeastern Baf fi n Island. *Geomorphology* 330, 40–56. <https://doi.org/10.1016/j.geomorph.2019.01.007>
- Campbell, D.C., 2014. CCGS Hudson Expedition 2013-029. Geological Hazard Assessment of Baffin Bay and Biodiversity Assessment of Hatton Basin. August 14-September 16, 2013. 122.
- Chao, W., Wu, T., Ma, K., Kuo, Y., Wu, Y., Zhao, L., Chung, M., Wu, H., Tsai, Y., 2018. The Large Greenland Landslide of 2017: Was a Tsunami Warning Possible? *Seismol. Res. Lett.* 89, 1335–1344. <https://doi.org/10.1785/0220170160>
- Coulthard, R.D., Furze, M.F.A., Pieńkowski, A.J., Chantel Nixon, F., England, J.H., 2010. New marine ΔR values for Arctic Canada. *Quat. Geochronol.* 5, 419–434. <https://doi.org/10.1016/j.quageo.2010.03.002>
- Damuth, J.E., 1980. Use of high-frequency (3.5–12 kHz) echograms in the study of near-bottom sedimentation processes in the deep-sea: a review. *Mar. Geol.* 38, 51–75.
- Dyke, A.S., 2004. An outline of North American deglaciation with emphasis on central and northern Canada, in: *Developments in Quaternary Sciences.* Elsevier, pp. 373–424.
- Fine, I. V., Rabinovich, A.B., Bornhold, B.D., Thomson, R.E., Kulikov, E.A., 2005. The Grand Banks landslide-generated tsunami of November 18, 1929: Preliminary analysis and numerical modeling. *Mar. Geol.* 215, 45–57. <https://doi.org/10.1016/j.margeo.2004.11.007>

- Frey-Martínez, J., Cartwright, J., James, D., 2006. Frontally confined versus frontally emergent submarine landslides: A 3D seismic characterisation. *Mar. Pet. Geol.* 23, 585–604. <https://doi.org/10.1016/j.marpetgeo.2006.04.002>
- Fritz, H.M., Giachetti, T., Anderson, S., Gauthier, D., 2017. Field Survey of the 17 June 2017 Landslide and Tsunami in Karrat Fjord, Greenland.
- Goldfinger, C., 2011. Submarine Paleoseismology Based on Turbidite Records. *Ann. Rev. Mar. Sci.* 3, 35–66. <https://doi.org/10.1146/annurev-marine-120709-142852>
- Government of Nunavut, 2015. Community transportation initiatives program policy.
- Halchuk, S., Adams, J., Allen, T.I., 2015. Fifth generation seismic hazard maps of Canada: Maps and grid values to be used with the 2015 National Building Code of Canada. *Geol. Surv. Canada Open File 7893* 26p. <https://doi.org/10.4095/297378>
- Hampton, M.A., Lee, H.J., Locat, J., 1996. Submarine landslides. *Rev. Geophys.* 34, 33–59.
- Hermanns, R.L., Hansen, L., Sletten, K., Böhme, M., Bunkholt, H.S.S., Eilertsen, R., Fischer, L., L’Heureux, J.-S., Høgaas, F., Nordahl, B., Oppikofer, T., Rubensdotter, L., Solberg, I.-L., Stalsberg, K., Yugsi Molina, F.X., 2012. Systematic geological mapping for landslide understanding in the Norwegian context. *Landslides Eng. Slopes Prot. Soc. through Improv. Underst.* 265–271.
- Hermanns, R.L., L’Heureux, J.S., Blikra, L.H., 2013. Landslide triggered tsunami, displacement wave, in: *Encyclopedia of Natural Hazards*. Springer, Dordrecht, pp. 611–615. <https://doi.org/10.1007/978-1-4020-4399-4>
- Hermanns, R.L., Oppikofer, T., Roberts, N.J., Sandøy, G., 2014. Catalogue of Historical Displacement Waves and Landslide-Triggered Tsunamis in Norway, in: G., L., A., M., J., L., Y., H., M., C.A. (Eds.), *Engineering Geology for Society and Territory*. Springer, Cham.
- Hewitt, K., Clague, J.J., Orwin, J.F., 2008. Legacies of catastrophic rock slope failures in mountain landscapes. *Earth-Science Rev.* 87, 1–38. <https://doi.org/10.1016/j.earscirev.2007.10.002>
- Hilger, P., Hermanns, R.L., Gosse, J.C., Jacobs, B., Etzelmüller, B., Krautblatter, M., 2018. Multiple rock-slope failures from Mannen in Romsdal Valley, western Norway, revealed from Quaternary geological mapping and ^{10}Be exposure dating. <https://doi.org/10.1177/0959683618798165>
- Jenner, K.A., Piper, D.J.W., Campbell, D.C., Mosher, D.C., 2007. Lithofacies and origin of late quaternary mass transport deposits in submarine canyons, central Scotian Slope, Canada. *Sedimentology* 54, 19–38. <https://doi.org/10.1111/j.1365-3091.2006.00819.x>
- Keen, M.J., Johnson, J., Park, I., 1972. Geophysical and Geological Studies in Eastern and Northern Baffin Bay and Lancaster Sound. *Can. J. Earth Sci.* 9, 689–708.

- Klassen, R.A., 1993. Quaternary geology and glacial history of Bylot Island, Northwest Territories.
- Lochte, A. A., Repschläger, J., Kienast, M., Garbe-Schönberg, D., Andersen, N., Hamann, C., & Schneider, R. 2019. Labrador Sea freshening at 8.5 ka BP caused by Hudson Bay Ice Saddle collapse. *Nature communications*, 10.
- Lund, B., 2015. Paleoseismology of Glaciated Terrain, in: *Encyclopedia of Earthquake Engineering*. Springer, Berlin, Heidelberg, pp. 1–16. <https://doi.org/10.1007/978-3-642-35344-4>
- Moorman, B.J., Michel, F.A., 1999. The Burial of Ice in the Proglacial Environment on Bylot Island \ Arctic Canada 50–64.
- Morgenstern, N.R., 1967. Submarine slumping and the initiation of turbidity currents. *Mar. Geotech.* 189–220.
- Newmark, N.M., 1965. Effects of Earthquakes on Dams and Embankments. *Géotechnique* 15, 139–160. <https://doi.org/10.1680/geot.1965.15.2.139>
- Oakey, G.N., Chalmers, J.A., 2012. A new model for the Paleogene motion of Greenland relative to North America: Plate reconstructions of the Davis Strait and Nares Strait regions between Canada and Greenland. *J. Geophys. Res. Solid Earth* 117.
- OMG, 2005. Multibeam Sonar Data collected from the CCGS Amundsen: Ocean Mapping Group, University of New Brunswick, Fredericton, New Brunswick, Canada [WWW Document]. *Ocean Mapp. Gr.* URL <http://www.omg.unb.ca/Projects/Arctic/index.html>
- Oppikofer, T., Hermanns, R.L., Roberts, N.J., Böhme, M., 2018. SPLASH: semi-empirical prediction of landslide-generated displacement wave run-up heights. *Geol. Soc. London, Spec. Publ.* 477. <https://doi.org/10.1144/SP477.1>
- Quinlan, G., 1984. Postglacial rebound and the focal mechanisms of eastern Canadian earthquakes. *Can. J. Earth Sci.* 21, 1018–1023. <https://doi.org/10.1139/e84-106>
- Roberts, N.J., McKillop, R., Hermanns, R.L., Clague, J.J., Oppikofer, T., 2014. Preliminary Global Catalogue of Displacement Waves from Subaerial Landslides, in: K., S., P., C., Y., Y. (Eds.), *Landslide Science for a Safer Geoenvironment*. Springer, Cham, pp. 1–486. <https://doi.org/10.1007/978-3-319-04999-1>
- Statistics Canada, 2017. Pond Inlet, HAM [Census subdivision], Nunavut and Canada [Country] (table). *Census Profile. 2016 Census*. Statistics Canada Catalogue no. 98-316-X2016001. Ottawa. Released November 29, 2017. [WWW Document]. URL <https://www12.statcan.gc.ca/census-recensement/2016/dp-pd/prof/index.cfm?Lang=E> (accessed 11.8.18).
- Steffen, R., Wu, P., Steffen, H., Eaton, D.W., 2014a. The effect of earth rheology and ice-sheet size on fault slip and magnitude of postglacial earthquakes. *Earth Planet. Sci. Lett.* 388, 71–80. <https://doi.org/10.1016/j.epsl.2013.11.058>

- Steffen, R., Wu, P., Steffen, H., Eaton, D.W., 2014b. Computers & Geosciences On the implementation of faults in finite-element glacial isostatic adjustment models. *Comput. Geosci.* 62, 150–159. <https://doi.org/10.1016/j.cageo.2013.06.012>
- Stein, S., Sleep, N.H., Geller, R.J., Wang, S., Kroeger, G.C., 1979. Earthquakes along the passive margin of eastern Canada 6, 537–540.
- St-Onge, G., Mulder, T., Piper, D.J.W., Hillaire-Marcel, C., Stoner, J.S., 2004. Earthquake and flood-induced turbidites in the Saguenay Fjord (Québec): A Holocene paleoseismicity record. *Quat. Sci. Rev.* 23, 283–294. <https://doi.org/10.1016/j.quascirev.2003.03.001>
- Syvitski, J.P.M., 1989. Glacier-Influenced Fjords : Oceanographic Controls. *Mar. Geol.* 85, 301–329.
- Syvitski, J.P.M., Burrell, D.C., Skei, J.M., 1987. Subaqueous Slope Failure, in: *Fjords*. Springer, New York.
- Tripanas, E.K., Piper, D.J.W., Jenner, K.A., Bryant, W.R., 2008. Submarine mass-transport facies: New perspectives on flow processes from cores on the eastern North American margin. *Sedimentology* 55, 97–136. <https://doi.org/10.1111/j.1365-3091.2007.00894.x>

CHAPTER 5: CONCLUSIONS

5.1 Conclusions and significance

The following summarizes the main conclusions derived from Chapters 2 through 4, their significance, and how they relate to the thesis objectives. The results show that hypothesis 1: the postglacial sedimentary succession in the deep basin in Pond Inlet is dominated by mass wasting deposits related to the region's high seismicity, could not be falsified. This hypothesis is supported by the sub-bottom profiler and core data that show a significant record of mass wasting in Pond Inlet, with MTDs comprising up to 90% of the postglacial sediments in the center of the inlet. The slope stability analysis reveals that sediments are stable under current conditions and require an external triggering mechanism to generate slope instability. The results show that the surrounding seismicity is a plausible triggering mechanism, however a more regional study is needed to support or refute that seismicity is the dominant mechanism initiating slope failures. Other triggering mechanisms including storms, floods, regional deglaciation and permafrost thaw cannot be ruled out at this time.

The results reveal that hypothesis 2: there is a significant probability of displacement wave hazard to the Hamlet of Pond Inlet, was not falsified. The results from the SPLASH analysis show that a landslide on southern Bylot Island, similar in size to the 2017 Nuugaatsiaq landslide, could generate a displacement wave with run-up heights from 11-22 m at the Hamlet of Pond Inlet. This would affect infrastructure, including housing. Further research investigating the Bylot Island steep mountain faces for evidence of slope instability including fractures or slope failures is warranted to further support or falsify this hypothesis.

5.1.1 Interpretation of the bathymetric and depositional record

The seabed of Pond Inlet and Eclipse Sound is composed of glacially streamlined and plucked bedrock, glacial depositional landforms, and postglacial sediments. Glacial landforms include crag and tail features, drumlins, mega scale glacial lineations, iceberg scours and moraines. A linear escarpment with up to 20 m of relief occurs between two bedrock highs in central Pond Inlet, which could represent a pre-glacial fault-line scarp, or an active fault scarp.

The acoustic stratigraphy of Pond Inlet is separated into a Lower Unit composed of glacial till and glaciomarine sediments, and an Upper Unit composed of postglacial sediments. Glacial till is characterized by prolonged high-amplitude continuous reflection with rough morphology and little acoustic penetration. The glaciomarine sediments are characterized by moderate to high amplitude continuous reflections. These are overlain by postglacial sediments composed of hemipelagic deposits interrupted by turbidites and MTDs. The hemipelagic and turbidite deposits are characterized by the well stratified acoustic facies with moderate-high amplitude, continuous reflections. These deposits are frequently interrupted by lens and wedge shaped MTDs. The MTDs are composed of acoustically chaotic to transparent acoustic facies with chaotic to transparent internal reflections.

The core data penetrate postglacial sediments, which are composed of hemipelagic sediments interrupted by MTDs and turbidites. Hemipelagic deposits make up the majority of postglacial sediments in core and are dominated by olive-grey bioturbated to homogeneous mud. Turbidites are composed of sand/silt deposits up to 47 cm in thickness. The MTDs show varying degrees of deformation including inclined stratified mud interpreted to represent slumps, folded mud interpreted as slides, and monomict mudclast conglomerates interpreted to represent debris flows/submarine landslides. In most MTDs, bedding is somewhat preserved and the composition

is similar to surrounding hemipelagic deposits, suggesting these are autochthonous MTDs that have been disturbed in place and not undergone significant transport.

5.1.2 Extent of mass wasting

Gravity driven flows make up a significant portion of the postglacial sedimentary record (between 45-90% in Pond Inlet Basin). In central Pond Inlet, hemipelagic sediments are interrupted by five MTDs and eight turbidites. MTDs are up to 22 thick, cover areas of up to 34 km², and the largest MTD has an estimated volume of 322 Mm³. Turbidites can be traced for at least 22 km, and few mass wasting features are preserved at the seabed.

5.1.3 Chronology for depositional processes and key events

(1) Timing of deglaciation of Pond Inlet and Eclipse Sound

The sedimentary record from Pond Inlet preserves an archive from the Last Glacial Maximum (LGM) to present day. The crag and tail and drumlinoid features and the MSGs formed under fast flowing, thick, grounded glacier ice (Dowdeswell et al., 2016) during the LGM. During this time, the upper portion of ice-contact glacial till was deposited. During glacial retreat, the calving of icebergs from the receding ice-front produced the iceberg scours observed at the seabed. During the Younger Dryas (YD), the ice-front re-advanced and terminated at the moraine in eastern Pond Inlet.

Over the Holocene, background sedimentation rates (excluding turbidites and MTDs) remain relatively stable with an average of 0.9 mm/yr in Pond Inlet Basin and 0.6 mm/yr in Perched Basin. The centre of Pond Inlet was ice-free prior to the deposition of the first postglacial turbidites at approximately 10.7 ka BP. Terrestrial dates indicate the coast around Eclipse Sound and Navy Board Inlet was deglaciated between 9.8 ± 0.6 ka cal BP though 6.0 ± 0.6 ka cal BP

(Dyke and Hooper, 2001; McNeely and Atkinson, 1996). At the same time, we see the cessation of IRD deposition in Pond Inlet cores, which could agree with the deglaciation of the coast, as fewer icebergs would have been calving off the ice-front.

(2) Timing and frequency of slope failures

This thesis provides the first constraints on the timing and frequency of slope failures in the fjords and inlets offshore northern Baffin Island. The first postglacial turbidites that directly overlie the first MTDs have extrapolated ages of 10.7 ka BP in Perched Basin and <12.7 ka BP in Pond Inlet Basin. In Pond Inlet, there has been an average of one mass wasting event recorded every 1.6 ka over the Holocene. The frequency of mass wasting increased from 2.9 ka BP to present day to an average of one event every 1.0 ka. The lack of slide scars preserved at the seabed suggest that few modern slope failures have occurred in this region.

5.1.4 Potential landslide hazard for Pond Inlet and Eclipse Sound

In the marine record, postglacial mud in Pond Inlet is stable under gravitational loading alone, and an external triggering mechanism is likely required to trigger slope failure. Earthquakes, deglacial unloading of valley walls, glacial outburst floods, permafrost thawing, tributary floods, and storms are all external triggering mechanisms that could be responsible mass wasting in this region. The calculated peak ground acceleration (PGA) from an earthquake needed to trigger slope instability in Pond Inlet is 0.13 g. The seismic hazard values from the National Building Code predicts a 5% probability that in 50 years that ground motions will exceed 0.19 PGA in the Pond Inlet region (Halchuk et al., 2015), indicating the surrounding seismicity is a plausible triggering mechanism. The 1933 7.3 M_s strike-slip earthquake does not appear to have triggered a mass wasting event in Pond Inlet. Insufficient paleoseismic data for northern Baffin Bay, and the limited (<100 year) instrumental record make it difficult to fully evaluate seismic triggering,

although expanding chronologies of mass wasting into surrounding fjords could reveal that a regional triggering mechanism like seismicity is more likely.

There is the potential for a subaerial landslide occurring on the steep slopes of southern Bylot Island to generate a displacement wave at the Hamlet of Pond Inlet. If a landslide, similar in size to the 2017 Nuugaatsiaq landslide, occurred along southern Bylot Island, a displacement wave with a run-up height of 11-22 m at the Hamlet could be generated. This could have significant impact on the Hamlet of Pond Inlet as infrastructure, including housing, exists within metres of sea level. To reach the airport and flood the majority of the housing with a run-up height of 60 m asl, a landslide on Bylot Island would need to be an order of magnitude larger than the Nuugaatsiaq landslide.

5.2 Suggested future research

Further investigations should be undertaken to evaluate the geohazards of northern Baffin Island and Pond Inlet including: (1) determining if a regional triggering mechanism is responsible for slope failures in the fjords and inlets of Baffin Island, (2) the nature of the escarpment in Pond Inlet, and (3) identification of large fractures or unstable rock slopes in the vicinity of the Hamlet of Pond Inlet and other coastal communities. More research could also be conducted on the seismicity of Baffin Bay, and since the instrumental earthquake record is relatively short (<100 years), paleoseismicity and paleotsunamis research could improve our understanding of the recurrence of earthquakes in this region.

5.2.1 Triggering mechanisms

Local and regional triggering mechanisms could contribute to the record of mass wasting observed in Pond Inlet and Eclipse Sound. It is difficult to differentiate between local versus

regional triggering mechanisms without investigating additional fjords. To determine if earthquakes are responsible for slope failures observed in the fjords and inlets of Baffin Island, including Pond Inlet and Eclipse Sound, chronologies should be extended into surrounding fjords. If slope failures have been triggered synchronously within multiple fjords, this would provide stronger evidence for a regional triggering mechanism like seismicity (Goldfinger, 2011).

The slope stability analysis in this study established the minimum horizontal PGA required to trigger slope instability in the postglacial mud. To determine if earthquakes in the instrumental record have been large and close enough to trigger slope instability, future work can be done to relate PGA to earthquake magnitude. This could be done using ground motion prediction equations developed by Toro et al. (1997); Toro (2002); Atkinson and Boore (2006) and others which relate earthquake magnitude and distance from the epicentre to PGA. These models were developed using earthquakes from eastern North America and are somewhat limited by their geographical area and the limited instrumental record. No model has been made for the eastern Canadian Arctic. Other advanced geotechnical testing could be completed, including consolidation and triaxial tests to determine the stress history of the sediment cores.

5.2.2 Nature of escarpment

More information is required to determine the nature of the escarpment in central Pond Inlet. To determine if this is an active fault or a pre-Quaternary fault line scarp, one additional core would need to be collected. A core collected on the upper portion of the escarpment could be compared to the deposits in core 0065. If the MTDs and turbidites dated in core 0065 are younger than mass wasting deposits in the core above the escarpment, this would indicate that recent failure have occurred along this feature and could suggest that this is an active fault. Acquisition of

medium resolution seismic reflection data at the correct orientation would potentially image if there is fault offset in the sub-surface.

If a research vessel was returning to Pond Inlet to explore the nature of the escarpment, additional strategic coring is recommended to constrain the deglacial history. A core should be taken above the moraine in eastern Pond Inlet to determine the age of the oldest postglacial sediments deposited above it. This could confirm if the moraine was deposited during a YD re-advance.

5.2.3 Displacement wave risk at the Hamlet of Pond Inlet

A subaerial landslide on the southern coast of Bylot Island could affect the Hamlet of Pond Inlet. Future field work is needed to investigate the steep mountain faces along the coast of southern Bylot Island for fractures, evidence of slope instability or slope failures. There is no published information on subaerial landslide volumes from northern Baffin Island, which limited our ability to predict displacement wave run-up heights. Future work should also investigate if the MTDs preserved in Pond Inlet had the potential to produce displacement waves.

5.3 References cited in Chapter 5

- Atkinson, G.M., Boore, D.M., 2006. Earthquake ground-motion prediction equations for eastern North America. *Bull. Seismol. Soc. Am.* 96, 2181–2205. <https://doi.org/10.1785/0120050245>
- Dowdeswell, E.K., Todd, B.J., Dowdeswell, J.A., 2016. Crag-and-tail features: convergent ice flow through Eclipse Sound, Baffin Island, Arctic Canada. *Geol. Soc. London, Mem.* 46, 55–56. <https://doi.org/10.1144/M46.106>
- Dyke, A.S., Hooper, J.M.G., 2001. Deglaciation of Northwest Baffin Island, Nunavut.
- Goldfinger, C., 2011. Submarine Paleoseismology Based on Turbidite Records. *Ann. Rev. Mar. Sci.* 3, 35–66. <https://doi.org/10.1146/annurev-marine-120709-142852>

- Halchuk, S., Adams, J., Allen, T.I., 2015. Fifth generation seismic hazard maps of Canada: Maps and grid values to be used with the 2015 National Building Code of Canada. Geol. Surv. Canada Open File 7893 26p. <https://doi.org/10.4095/297378>
- McNeely, R., Atkinson, D.E., 1996. Geological Survey of Canada Radiocarbon dates XXXII, Geological Survey of Canada Paper 83-1A. <https://doi.org/10.1126/science.ns-6.149S.521-a>
- Toro, G.R., 2002. Modification of the Toro et al. (1997) attenuation equations for large magnitudes and short distances 1–10.
- Toro, G.R., Abrahamson, N.A., Schneider, J.F., 1997. Model of Strong Ground Motions from Earthquakes in Central and Eastern North America: Best Estimates and Uncertainties. *Seismol. Res. Lett.* 68, 41–57. <https://doi.org/10.1785/gssrl.68.1.41>

BIBLIOGRAPHY

- Aksu, A.E., 1984. Subaqueous debris flow deposits in Baffin Bay. *Geo-Marine Lett.* 4, 83–90. <https://doi.org/10.1007/BF02277077>
- Aksu, A.E., Hiscott, R.N., 1989. Slides and debris flows on the high-latitude continental slopes of Baffin Bay. *Geology* 17, 885–888. [https://doi.org/10.1130/0091-7613\(1989\)017<0885:SADFOT>2.3.CO;2](https://doi.org/10.1130/0091-7613(1989)017<0885:SADFOT>2.3.CO;2)
- Andrews, J.T., 1970. Present and postglacial rates of uplift for glaciated northern and eastern North America derived from postglacial uplift curves. *Can. J. Earth Sci.* 7, 1184–1184. <https://doi.org/10.1139/e70-112>
- Andrews, J.T., Ives, J.D., 1978. “Cockburn” Nomenclature and the Late Quaternary History of the Eastern Canadian Arctic. *Arct. Alp. Res.* 10, 617. <https://doi.org/10.2307/1550683>
- Andrews, J.T., Jull, A.J.T., Donahue, D.J., Short, S.K., Osterman, L.E., 1985. Sedimentation rates in Baffin Island fiord cores from comparative radiocarbon dates. *Can. J. Earth Sci.* 22, 1827–1834. <https://doi.org/10.1139/e85-194>
- Atkinson, G.M., Boore, D.M., 2006. Earthquake ground-motion prediction equations for eastern North America. *Bull. Seismol. Soc. Am.* 96, 2181–2205. <https://doi.org/10.1785/0120050245>
- Basham, P.W., Forsyth, D.A., Wetmiller, R.J., 1977. The seismicity of northern Canada 14, 1646–1667. <https://doi.org/10.1139/e77-140>
- Bellwald, B., Hjelstuen, B.O., Sejrup, H.P., Haflidason, H., 2016. Postglacial mass movements and depositional environments in a high-latitude fjord system – Hardangerfjorden, Western Norway. *Mar. Geol.* 379, 157–175. <https://doi.org/10.1016/j.margeo.2016.06.002>
- Bellwald, B., Hjelstuen, B.O., Sejrup, H.P., Stokowy, T., Kuvås, J., 2019. Holocene mass movements in west and mid-Norwegian fjords and lakes. *Mar. Geol.* 407, 192–212. <https://doi.org/10.1016/j.margeo.2018.11.007>
- Bent, A.L., 2002. The 1933 $M_s = 7.3$ Baffin Bay earthquake: strike-slip faulting along the northeastern Canadian passive margin. *Geophys. J. Int.* 150, 724–736.
- Bessette-Kirton, E., Allstadt, K., Pursley, J., Godt, J., 2017. Preliminary Analysis of Satellite Imagery and Seismic Observations of the Nuugaatsiaq Landslide and Tsunami, Greenland [WWW Document]. URL https://www.usgs.gov/natural-hazards/landslide-hazards/science/preliminary-analysis-satellite-imagery-and-seismic?qt-science_center_objects=0#qt-science_center_objects
- Blaauw, M., 2010. Methods and code for “classical” age-modelling of radiocarbon sequences. *Quat. Geochronol.* 5, 512–518. <https://doi.org/10.1016/j.quageo.2010.01.002>
- Bondevik, S., Mangerud, J., Dawson, S., Dawson, A., Lohne, Ø., 2003. Record-breaking Height for 8000-Year-Old Tsunami in the North Atlantic. *Eos, Trans. Am. Geophys. Union* 84, 289–293. <https://doi.org/https://doi.org/10.1029/2003EO310001>

- Bornhold, B.D., Finlayson, N.M., Monahan, D., 1976. Submerged drainage patterns in Barrow Strait, Canadian Arctic. *Can. J. Earth Sci.* 13, 305–311.
- Bouma, A.H., 1962. *Sedimentology of some Flysch deposits; a graphic approach to facies interpretation.* Elsevier Pub. Co, Amsterdam, New York.
- Briner, J.P., Davis, P.T., Miller, G.H., 2009. Latest Pleistocene and Holocene glaciation of Baffin Island, Arctic Canada: key patterns and chronologies. *Quat. Sci. Rev.* 28, 2075–2087. <https://doi.org/10.1016/j.quascirev.2008.09.017>
- Briner, J.P., Miller, G.H., Finkel, R., Hess, D.P., 2008. Glacial erosion at the fjord onset zone and implications for the organization of ice flow on Baffin Island, Arctic Canada. *Geomorphology* 97, 126–134. <https://doi.org/10.1016/j.geomorph.2007.02.039>
- Briner, J.P., Overeem, I., Miller, G.H., Finkel, R., 2007. The deglaciation of Clyde Inlet, northeastern Baffin Island, Arctic Canada. *J. Quat. Sci.* 22, 223–232.
- Brouard, E., Lajeunesse, P., 2019. Geomorphology Glacial to postglacial submarine landform assemblages in fi ords of northeastern Baf fi n Island. *Geomorphology* 330, 40–56. <https://doi.org/10.1016/j.geomorph.2019.01.007>
- Brouard, E., Lajeunesse, P., 2017. Maximum extent and decay of the Laurentide Ice Sheet in Western Baffin Bay during the Last glacial episode. *Sci. Rep.* 7, 1–8. <https://doi.org/10.1038/s41598-017-11010-9>
- Campbell, D.C., 2014. CCGS Hudson Expedition 2013-029. Geological Hazard Assessment of Baffin Bay and Biodiversity Assessment of Hatton Basin. August 14-September 16, 2013. 122.
- Chao, W., Wu, T., Ma, K., Kuo, Y., Wu, Y., Zhao, L., Chung, M., Wu, H., Tsai, Y., 2018. The Large Greenland Landslide of 2017: Was a Tsunami Warning Possible? *Seismol. Res. Lett.* 89, 1335–1344. <https://doi.org/10.1785/0220170160>
- Coulthard, R.D., Furze, M.F.A., Pieńkowski, A.J., Chantel Nixon, F., England, J.H., 2010. New marine ΔR values for Arctic Canada. *Quat. Geochronol.* 5, 419–434. <https://doi.org/10.1016/j.quageo.2010.03.002>
- Currie, L.D., Coutand, I., Brent, T.A., Issler, D.R., Wielens, H., 2012. Structural style and thermal history of the eastern Lancaster Sound and Bylot Island area, NU. *Geol. Assoc. Canada–Mineralogical Assoc. Canada, Jt. Annu. Meet. St. John’s, Newfoundland, May 27–29, 2012, Abstr. p. 31.*
- Damuth, J.E., 1980. Use of high-frequency (3.5–12 kHz) echograms in the study of near-bottom sedimentation processes in the deep-sea: a review. *Mar. Geol.* 38, 51–75.
- Di Giacomo, D., Storchak, D.A., Safronova, N., Ozgo, P., Harris, J., Verney, R., Bondar, I., 2014. A New ISC Service: The Bibliography of Seismic Events. *Seismol. Res. Lett.* 85, 354–360. <https://doi.org/10.1785/0220130143>
- Dowdeswell, E.K., Dowdeswell, J.A., Cawkwell, F., 2007. On the Glaciers of Bylot Island, Nunavut, Arctic Canada. *Arctic, Antarct. Alp. Res.* 39, 402–411. [https://doi.org/10.1657/1523-0430\(07-069\)](https://doi.org/10.1657/1523-0430(07-069))

- Dowdeswell, E.K., Todd, B.J., Dowdeswell, J.A., 2016. Crag-and-tail features: convergent ice flow through Eclipse Sound, Baffin Island, Arctic Canada. *Geol. Soc. London, Mem.* 46, 55–56. <https://doi.org/10.1144/M46.106>
- Duchesne, M.J., Pinet, N., Bédard, K., St-Onge, G., Lajeunesse, P., Campbell, D.C., Bolduc, A., 2010. Role of the bedrock topography in the Quaternary filling of a giant estuarine basin: The Lower St. Lawrence Estuary, Eastern Canada. *Basin Res.* 22, 933–951. <https://doi.org/10.1111/j.1365-2117.2009.00457.x>
- Dyke, A.S., 2008. The Steensby Inlet Ice Stream in the context of the deglaciation of Northern Baffin Island, Eastern Arctic Canada. *Earth Surf. Process. Landforms J. Br. Geomorphol. Res. Gr.* 33, 573–592.
- Dyke, A.S., 2004. An outline of North American deglaciation with emphasis on central and northern Canada. *Dev. Quat. Sci.* 2, 373–424. [https://doi.org/10.1016/S1571-0866\(04\)80209-4](https://doi.org/10.1016/S1571-0866(04)80209-4)
- Dyke, A.S., 2004. An outline of North American deglaciation with emphasis on central and northern Canada, in: *Developments in Quaternary Sciences*. Elsevier, pp. 373–424.
- Dyke, A.S., Andrews, J.T., Clark, P.U., England, J.H., Miller, G.H., Shaw, J., Veillette, J.J., 2002. The Laurentide and Innuitian ice sheets during the last glacial maximum. *Quat. Sci. Rev.* 21, 9–31.
- Dyke, A.S., Clark, J.T.A.P.U., England, J.H., 2001. GEOLOGICAL SURVEY OF CANADA OPEN FILE 4120 Radiocarbon Dates pertinent to defining the last glacial maximum for the Laurentide and Innuitian ice sheets.
- Dyke, A.S., Hooper, J., Savelle, J.M., 1996. A history of sea ice in the Canadian Arctic archipelago based on postglacial remains of the bowhead whale (*Balaena mysticetus*). *Arctic* 49, 235–255. <https://doi.org/10.14430/arctic1200>
- Dyke, A.S., Hooper, J.M.G., 2001. Deglaciation of Northwest Baffin Island, Nunavut.
- Falconer, G., Andrews, J.T., Ives, J.D., 1965. Late-Wisconsin End Moraines in Northern Canada. *Science* (80-.). 147, 608–610.
- Fine, I. V., Rabinovich, A.B., Bornhold, B.D., Thomson, R.E., Kulikov, E.A., 2005. The Grand Banks landslide-generated tsunami of November 18, 1929: Preliminary analysis and numerical modeling. *Mar. Geol.* 215, 45–57. <https://doi.org/10.1016/j.margeo.2004.11.007>
- Fischer, L., Käab, A., Huggel, C., Noetzli, J., 2006. Geology, glacier retreat and permafrost degradation as controlling factors of slope instabilities in a high-mountain rock wall: The Monte Rosa east face. *Nat. Hazards Earth Syst. Sci.* 6, 761–772. <https://doi.org/10.5194/nhess-6-761-2006>
- Fischer, L., Purves, R.S., Huggel, C., Noetzli, J., Haeblerli, W., 2012. On the influence of topographic, geological and cryospheric factors on rock avalanches and rockfalls in high-mountain areas. *Nat. Hazards Earth Syst. Sci.* 12, 241–254. <https://doi.org/10.5194/nhess-12-241-2012>

- Frey-Martínez, J., Cartwright, J., James, D., 2006. Frontally confined versus frontally emergent submarine landslides: A 3D seismic characterisation. *Mar. Pet. Geol.* 23, 585–604. <https://doi.org/10.1016/j.marpetgeo.2006.04.002>
- Fritz, H.M., Giachetti, T., Anderson, S., Gauthier, D., 2017. Field Survey of the 17 June 2017 Landslide and Tsunami in Karrat Fjord, Greenland.
- Gauthier, G., Rochefort, L., Reed, A., 1996. Exploitation of wetland ecosystems by herbivores on bylot island. *Geosci. Canada* 23.
- Gilbert, R., 1983. Sedimentary processes of Canadian Arctic fjords. *Sediment. Geol.* 36, 147–175.
- Goldfinger, C., 2011. Submarine Paleoseismology Based on Turbidite Records. *Ann. Rev. Mar. Sci.* 3, 35–66. <https://doi.org/10.1146/annurev-marine-120709-142852>
- Government of Nunavut, 2015. Community transportation initiatives program policy.
- Halchuk, S., Adams, J., Allen, T.I., 2015. Fifth generation seismic hazard maps of Canada: Maps and grid values to be used with the 2015 National Building Code of Canada. *Geol. Surv. Canada Open File 7893* 26p. <https://doi.org/10.4095/297378>
- Hampton, M.A., Lee, H.J., Locat, J., 1996. Submarine landslides. *Rev. Geophys.* 34, 33–59.
- Hermanns, R.L., Hansen, L., Sletten, K., Böhme, M., Bunkholt, H.S.S., Eilertsen, R., Fischer, L., L’Heureux, J.-S., Høgaas, F., Nordahl, B., Oppikofer, T., Rubensdotter, L., Solberg, I.-L., Stalsberg, K., Yugsi Molina, F.X., 2012. Systematic geological mapping for landslide understanding in the Norwegian context. *Landslides Eng. Slopes Prot. Soc. through Improv. Underst.* 265–271.
- Hermanns, R.L., L’Heureux, J.S., Blikra, L.H., 2013. Landslide triggered tsunami, displacement wave, in: *Encyclopedia of Natural Hazards*. Springer, Dordrecht, pp. 611–615. <https://doi.org/10.1007/978-1-4020-4399-4>
- Hermanns, R.L., Oppikofer, T., Roberts, N.J., Sandøy, G., 2014. Catalogue of Historical Displacement Waves and Landslide-Triggered Tsunamis in Norway, in: G., L., A., M., J., L., Y., H., M., C.A. (Eds.), *Engineering Geology for Society and Territory*. Springer, Cham.
- Hewitt, K., Clague, J.J., Orwin, J.F., 2008. Legacies of catastrophic rock slope failures in mountain landscapes. *Earth-Science Rev.* 87, 1–38. <https://doi.org/10.1016/j.earscirev.2007.10.002>
- Hilchey, A., 2004. Deglacial geologic history of the Ravn River valley, northern Baffin Island, Nunavut. Dalhousie University.
- Hilger, P., Hermanns, R.L., Gosse, J.C., Jacobs, B., Etzelmüller, B., Krautblatter, M., 2018. Multiple rock-slope failures from Mannen in Romsdal Valley, western Norway, revealed from Quaternary geological mapping and ^{10}Be exposure dating. <https://doi.org/10.1177/0959683618798165>

- Hjelstuen, B.O., Haflidason, H., Sejrup, H.P., Lyså, A., 2009. Sedimentary processes and depositional environments in glaciated fjord systems - Evidence from Nordfjord, Norway. *Mar. Geol.* 258, 88–99. <https://doi.org/10.1016/j.margeo.2008.11.010>
- International Seismological Centre, 2017. International Seismological Centre 2017: Bulletin of the International Seismological Centre [WWW Document]. Int. Seismol. Centre, online Bull. URL <http://www.isc.ac.uk> (accessed 7.20.10).
- Jackson, G.D., Davidson, A., 1975. Geology, Pond Inlet and Nova Zembla Island, District of Franklin.
- Jackson, G.D., Davidson, A., 1975. Bylot Island map-area, District of Franklin.
- Jenner, K.A., Piper, D.J.W., Campbell, D.C., Mosher, D.C., 2007. Lithofacies and origin of late quaternary mass transport deposits in submarine canyons, central Scotian Slope, Canada. *Sedimentology* 54, 19–38. <https://doi.org/10.1111/j.1365-3091.2006.00819.x>
- Keen, M.J., Johnson, J., Park, I., 1972. Geophysical and Geological Studies in Eastern and Northern Baffin Bay and Lancaster Sound. *Can. J. Earth Sci.* 9, 689–708.
- Klassen, R.A., 1993. Quaternary geology and glacial history of Bylot Island, Northwest Territories.
- Li, G., Piper, D.J.W., Calvin Campbell, D., 2011. The Quaternary Lancaster Sound trough-mouth fan, NW Baffin Bay. *J. Quat. Sci.* 26, 511–522. <https://doi.org/10.1002/jqs.1479>
- Lochte, A. A., Repschläger, J., Kienast, M., Garbe-Schönberg, D., Andersen, N., Hamann, C., & Schneider, R. 2019. Labrador Sea freshening at 8.5 ka BP caused by Hudson Bay Ice Saddle collapse. *Nature communications*, 10.
- Lund, B., 2015. Paleoseismology of Glaciated Terrain, in: *Encyclopedia of Earthquake Engineering*. Springer, Berlin, Heidelberg, pp. 1–16. <https://doi.org/10.1007/978-3-642-35344-4>
- MacLean, B., Williams, G.L., Srivastava, S.. (Eds.), 1990. Geology of Baffin Bay and Davis Strait, in: *Geology of the Continental Margin of Eastern Canada*. Geological Survey of Canada, Geology of Canada series no. 2, pp. 293–348.
- Margreth, A., Gosse, J.C., Dyke, A.S., 2017. Wisconsinan and early Holocene glacial dynamics of Cumberland Peninsula, Baffin Island, Arctic Canada. *Quat. Sci. Rev.* 168, 79–100. <https://doi.org/10.1016/j.quascirev.2017.04.033>
- Marko, J.R., Birch, J.R., Wilson, M.A., 1986. A Study of Long-Term Satellite-Tracked Iceberg Drifts in Baffin Bay. *Arctic* 35, 234–240.
- McNeely, R., Atkinson, D.E., 1996. Geological Survey of Canada Radiocarbon dates XXXII, Geological Survey of Canada Paper 83-1A. <https://doi.org/10.1126/science.ns-6.149S.521-a>
- Miller, G.H., Dyke, A.S., 1974. Proposed Extent of Late Wisconsin Laurentide Ice on Eastern Baffin Island. *Geology* 2, 125–130.
- Moorman, B.J., Michel, F.A., 1999. The Burial of Ice in the Proglacial Environment on Bylot Island \ Arctic Canada 50–64.

- Morgenstern, N.R., 1967. Submarine slumping and the initiation of turbidity currents. *Mar. Geotech.* 189–220.
- Newmark, N.M., 1965. Effects of Earthquakes on Dams and Embankments. *Géotechnique* 15, 139–160. <https://doi.org/10.1680/geot.1965.15.2.139>
- Oakey, G.N., Chalmers, J.A., 2012. A new model for the Paleogene motion of Greenland relative to North America: Plate reconstructions of the Davis Strait and Nares Strait regions between Canada and Greenland. *J. Geophys. Res. Solid Earth* 117.
- OMG, 2005. Multibeam Sonar Data collected from the CCGS Amundsen: Ocean Mapping Group, University of New Brunswick, Fredericton, New Brunswick, Canada [WWW Document]. *Ocean Mapp. Gr.* URL <http://www.omg.unb.ca/Projects/Arctic/index.html>
- Oppikofer, T., Hermanns, R.L., Roberts, N.J., Böhme, M., 2018. SPLASH: semi-empirical prediction of landslide-generated displacement wave run-up heights. *Geol. Soc. London, Spec. Publ.* 477. <https://doi.org/10.1144/SP477.1>
- Ottesen, D., Dowdeswell, J.A., Rise, L., 2005. Submarine landforms and the reconstruction of fast-flowing ice streams within a large Quaternary ice sheet: The 2500-km-long Norwegian-Svalbard margin (57°–80°N). *Bull. Geol. Soc. Am.* 117, 1033–1050. <https://doi.org/10.1130/B25577.1>
- Piper, D.J.W., Stow, D.A.W., 1991. Fine-grained turbidites, in: Einsele, G., Seilacher, A. (Eds.), *Cyclic and Event Stratification*. Springer Verlag, New York, pp. 360–376.
- Posamentier, H.W., Kolla, V., 2003. Seismic Geomorphology and Stratigraphy of Depositional Elements in Deep-Water Settings. *J. Sediment. Res.* 73, 367–388. <https://doi.org/10.1306/111302730367>
- Quinlan, G., 1984. Postglacial rebound and the focal mechanisms of eastern Canadian earthquakes. *Can. J. Earth Sci.* 21, 1018–1023. <https://doi.org/10.1139/e84-106>
- Roberts, N.J., McKillop, R., Hermanns, R.L., Clague, J.J., Oppikofer, T., 2014. Preliminary Global Catalogue of Displacement Waves from Subaerial Landslides, in: K., S., P., C., Y., Y. (Eds.), *Landslide Science for a Safer Geoenvironment*. Springer, Cham, pp. 1–486. <https://doi.org/10.1007/978-3-319-04999-1>
- Sangree, J.B., Widmier, J.M., 1979. Interpretation of Depositional Facies from Seismic Data. *Geophysics* 44, 131–160. <https://doi.org/10.1190/1.1440957>
- Schiermeier, Q., 2017. Huge landslide triggered rare Greenland mega-tsunami. *Nat. News.* <https://doi.org/doi:10.1038/nature.2017.22374>
- Skipton, D.R., Saumur, B.M., St-Onge, M.R., Wodicka, N., Bros, E.R., Currie, L.D., Weller, O.M., Haggart, J.W., 2018. Bedrock geology, Pond Inlet, Nunavut, part of NTS 38-B; Geological Survey of Canada, Canadian Geoscience Map 347, scale 1:100 000. <https://doi.org/https://doi.org/10.4095/306578>

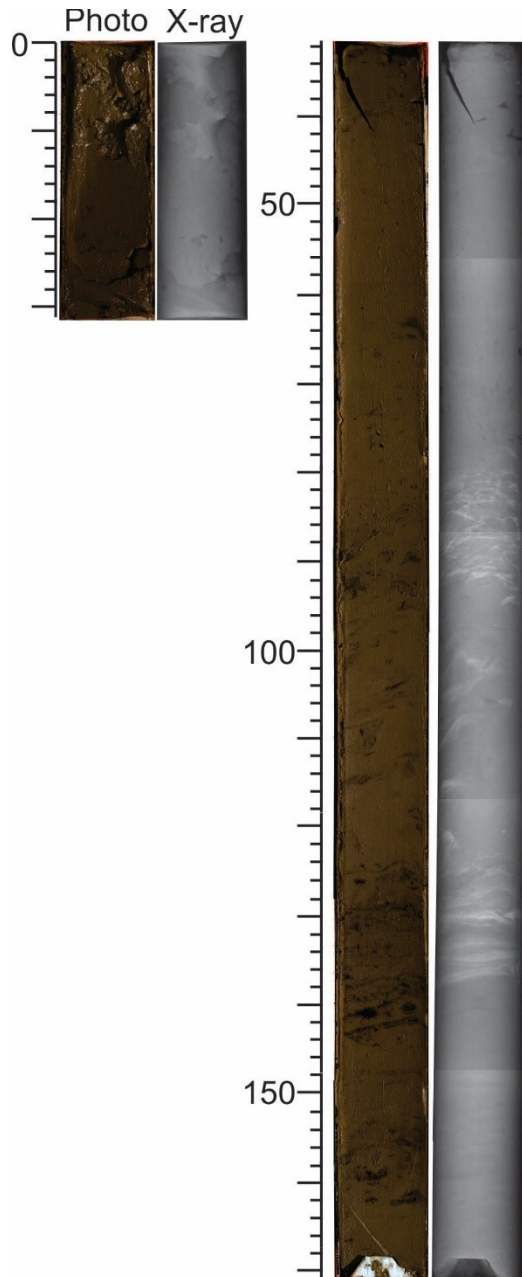
- St-Onge, G., Chapron, E., Mulsow, S., Salas, M., Viel, M., Debret, M., Foucher, A., Mulder, T., Winiarski, T., Desmet, M., Costa, P.J.M., Ghaleb, B., Jaouen, A., Locat, J., 2012. Comparison of earthquake-triggered turbidites from the Saguenay (Eastern Canada) and Reloncavi (Chilean margin) Fjords: Implications for paleoseismicity and sedimentology. *Sediment. Geol.* 243–244, 89–107. <https://doi.org/10.1016/j.sedgeo.2011.11.003>
- St-Onge, G., Mulder, T., Piper, D.J.W., Hillaire-Marcel, C., Stoner, J.S., 2004. Earthquake and flood-induced turbidites in the Saguenay Fjord (Québec): A Holocene paleoseismicity record. *Quat. Sci. Rev.* 23, 283–294. <https://doi.org/10.1016/j.quascirev.2003.03.001>
- Statistics Canada, 2017. Pond Inlet, HAM [Census subdivision], Nunavut and Canada [Country] (table). Census Profile. 2016 Census. Statistics Canada Catalogue no. 98-316-X2016001. Ottawa. Released November 29, 2017. [WWW Document]. URL <https://www12.statcan.gc.ca/census-recensement/2016/dp-pd/prof/index.cfm?Lang=E> (accessed 11.8.18).
- Steffen, R., Wu, P., Steffen, H., Eaton, D.W., 2014a. The effect of earth rheology and ice-sheet size on fault slip and magnitude of postglacial earthquakes. *Earth Planet. Sci. Lett.* 388, 71–80. <https://doi.org/10.1016/j.epsl.2013.11.058>
- Steffen, R., Wu, P., Steffen, H., Eaton, D.W., 2014b. Computers & Geosciences On the implementation of faults in finite-element glacial isostatic adjustment models. *Comput. Geosci.* 62, 150–159. <https://doi.org/10.1016/j.cageo.2013.06.012>
- Stein, S., Sleep, N.H., Geller, R.J., Wang, S., Kroeger, G.C., 1979. Earthquakes along the passive margin of eastern Canada 6, 537–540.
- Stuiver, M., Reimer, P.J., and Reimer, R., 2017. [WWW program] [WWW Document]. URL <http://calib.org>
- Syvitski, J.P.M., 1989. Glacier-Influenced Fjords : Oceanographic Controls. *Mar. Geol.* 85, 301–329.
- Syvitski, J.P.M., Burrell, D.C., Skei, J.M., 1987. Subaqueous Slope Failure, in: *Fjords*. Springer, New York.
- Syvitski, J.P.M., Praeg, D.B., 1989. Quaternary Sedimentation in the St. Lawrence Estuary and Adjoining Areas, Eastern Canada: An Overview Based on High-Resolution Seismo-Stratigraphy. *Géographie Phys. Quat.* 43, 291. <https://doi.org/10.7202/032784ar>
- Taylor, K.C., Lamoreyt, G.W., Doylet, G.A., Mayewskill, P.A., White, W.C., Barlow, L.K., 1993. The “flickering switch” of late Pleistocene climate change. *Nature* 361, 432–436.
- Toro, G.R., 2002. Modification of the Toro et al. (1997) attenuation equations for large magnitudes and short distances 1–10.
- Toro, G.R., Abrahamson, N.A., Schneider, J.F., 1997. Model of Strong Ground Motions from Earthquakes in Central and Eastern North America: Best Estimates and Uncertainties. *Seismol. Res. Lett.* 68, 41–57. <https://doi.org/10.1785/gssrl.68.1.41>

- Tripsanas, E.K., Piper, D.J.W., Jenner, K.A., Bryant, W.R., 2008. Submarine mass-transport facies: New perspectives on flow processes from cores on the eastern North American margin. *Sedimentology* 55, 97–136. <https://doi.org/10.1111/j.1365-3091.2007.00894.x>
- Valeur, H.H., Hansen, C., Hansen, K.Q., Rasmussen, L., Thingvad, N., 1996. Weather, sea and ice conditions in eastern Baffin Bay, offshore northwest Greenland: A review. *Miner. Resour. Adm. Greenl.* 96–12, 37 pp.
- Willenbring Staiger, J., Gosse, J., Little, E.C., Utting, D.J., Finkel, R., Johnson, J. V, Fastook, J., 2006. Glacial erosion and sediment dispersion from detrital cosmogenic nuclide analyses of till 1, 29–42. <https://doi.org/10.1016/j.quageo.2006.06.009>

APPENDICES

Appendix A: Core photography & x-radiographs

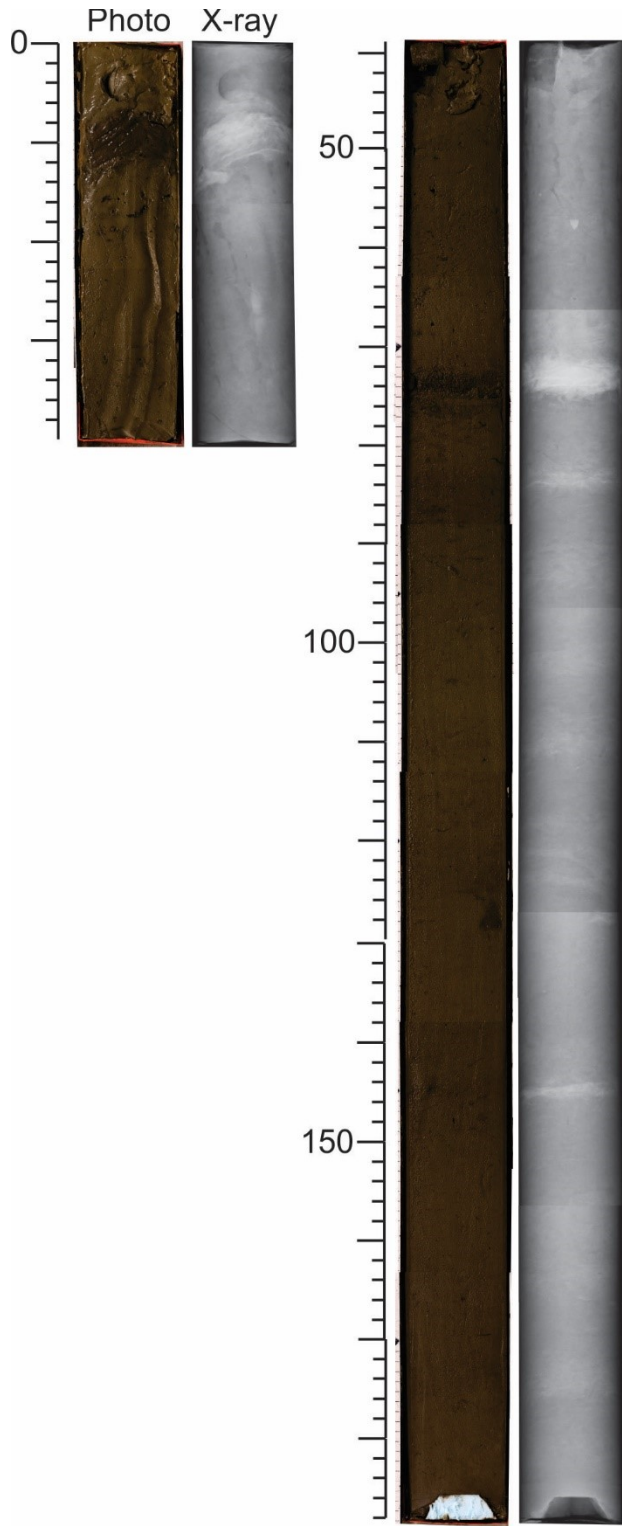
Core 0065TWC



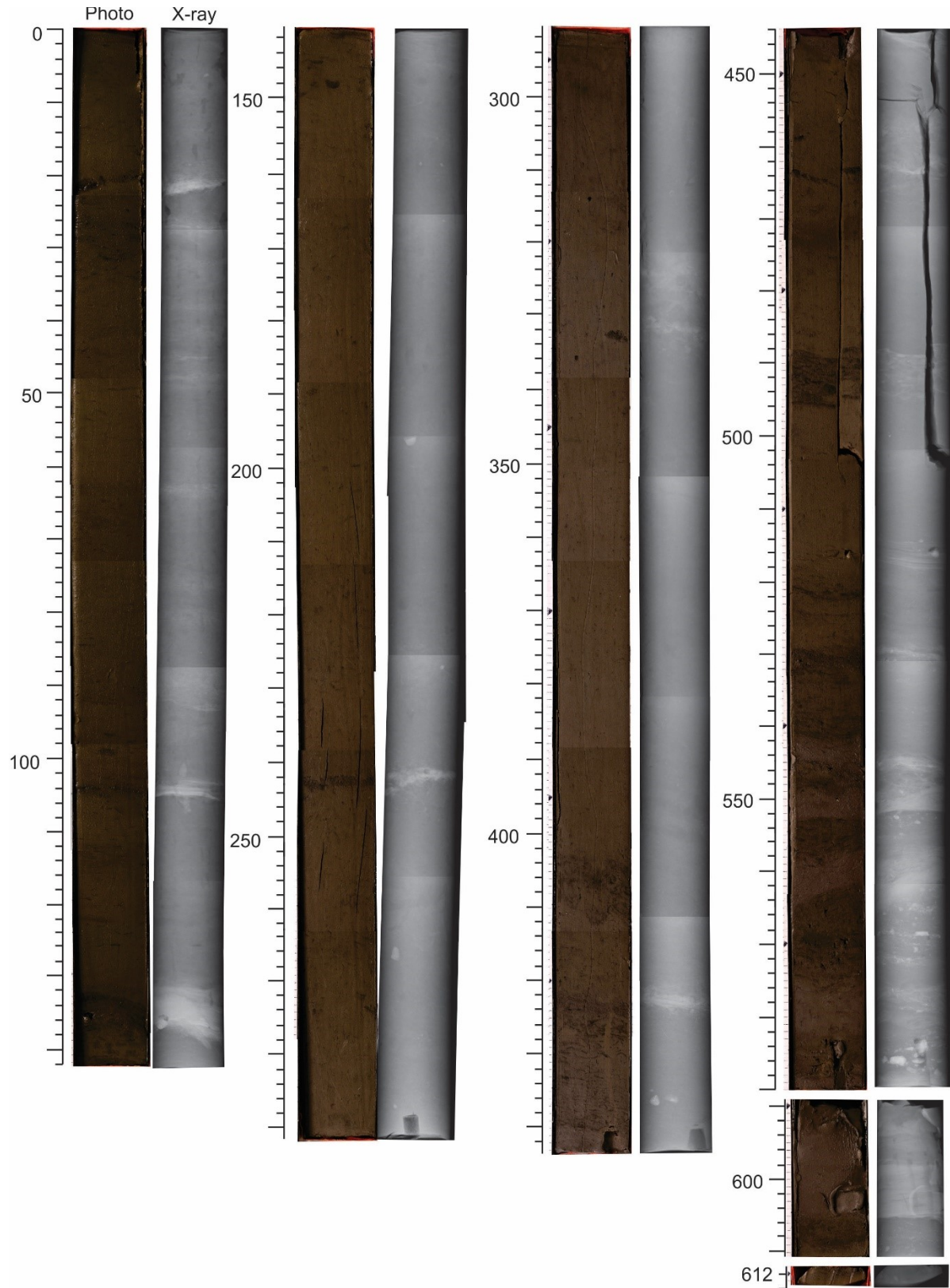
Core 0065PC



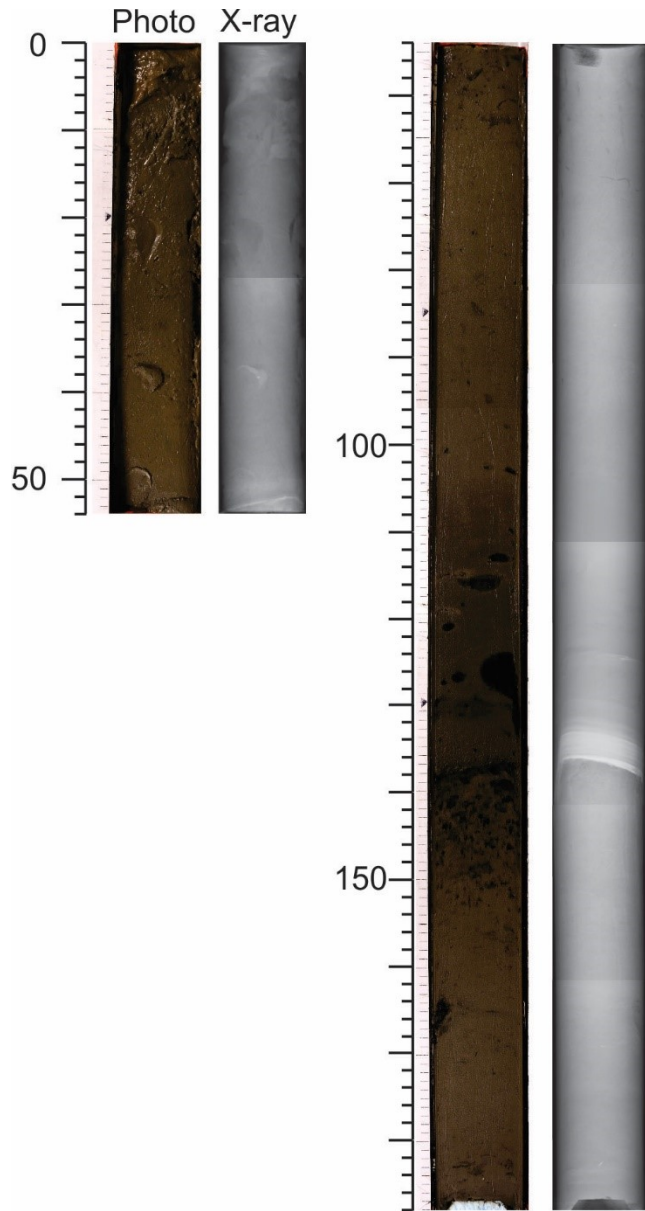
Core 0066TWC



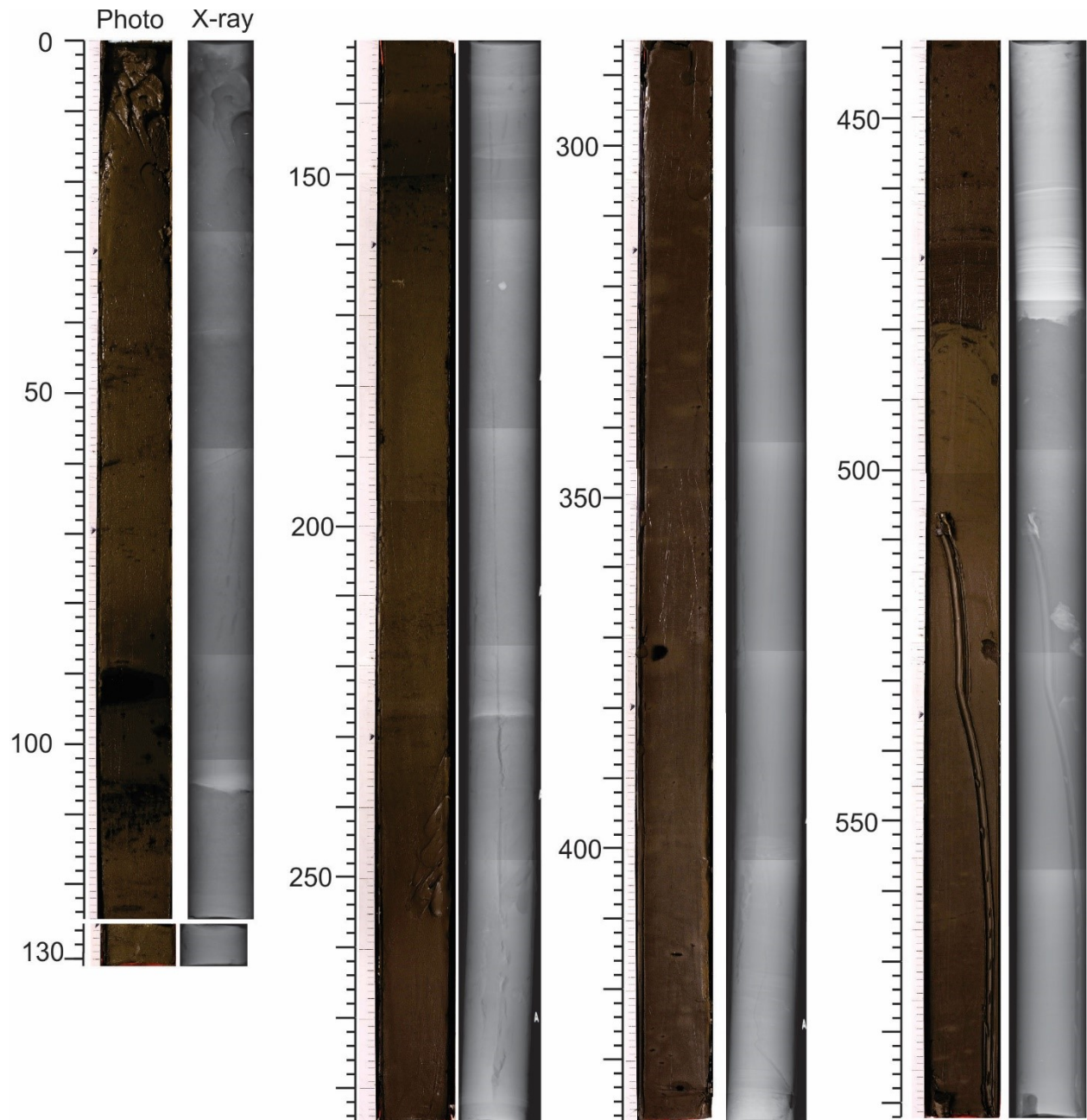
Core 0066PC

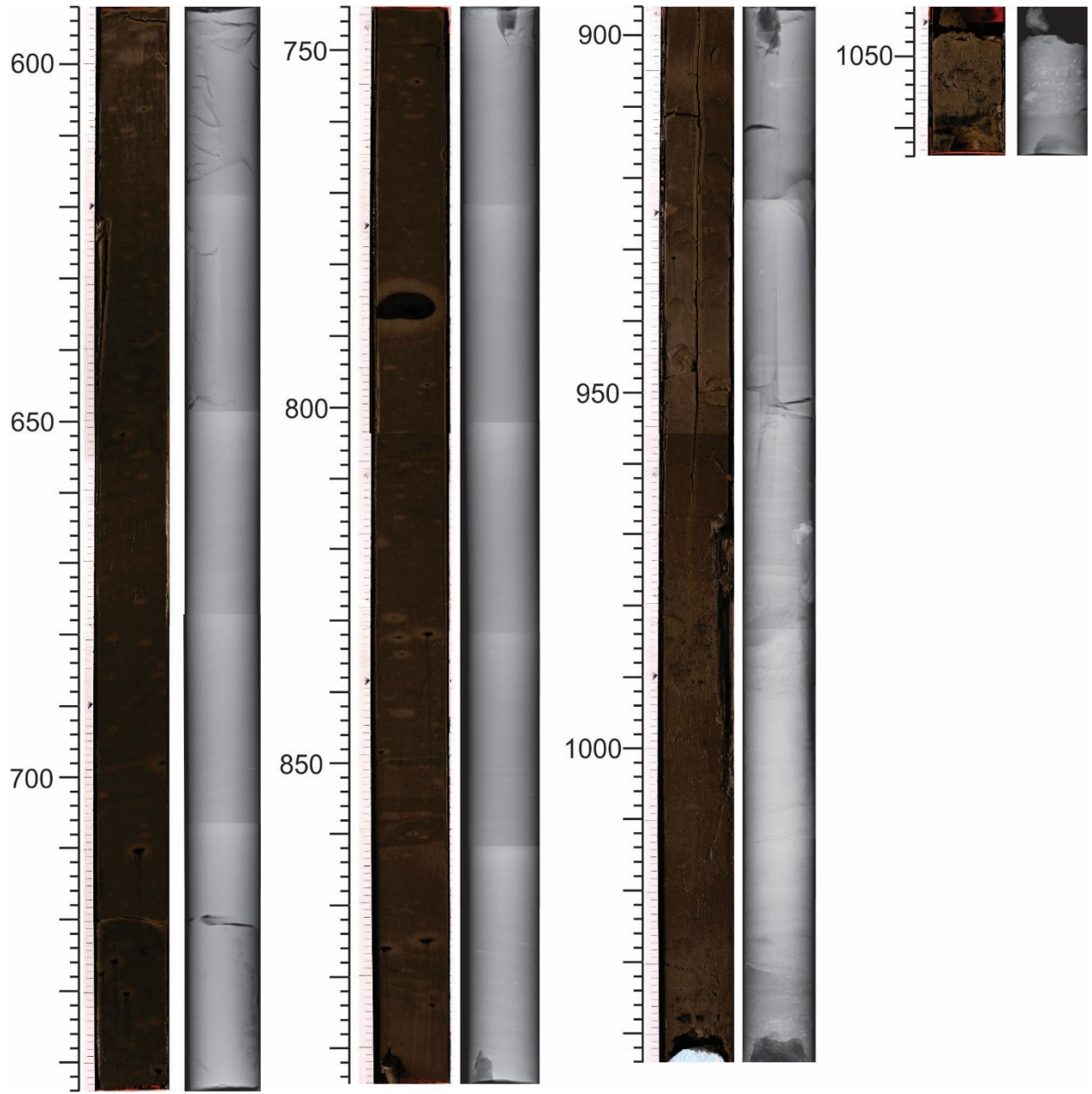


Core 0067TWC



Core 0067PC





Core 0068Bpush



Core 0068Cpush



Core 0002TWC



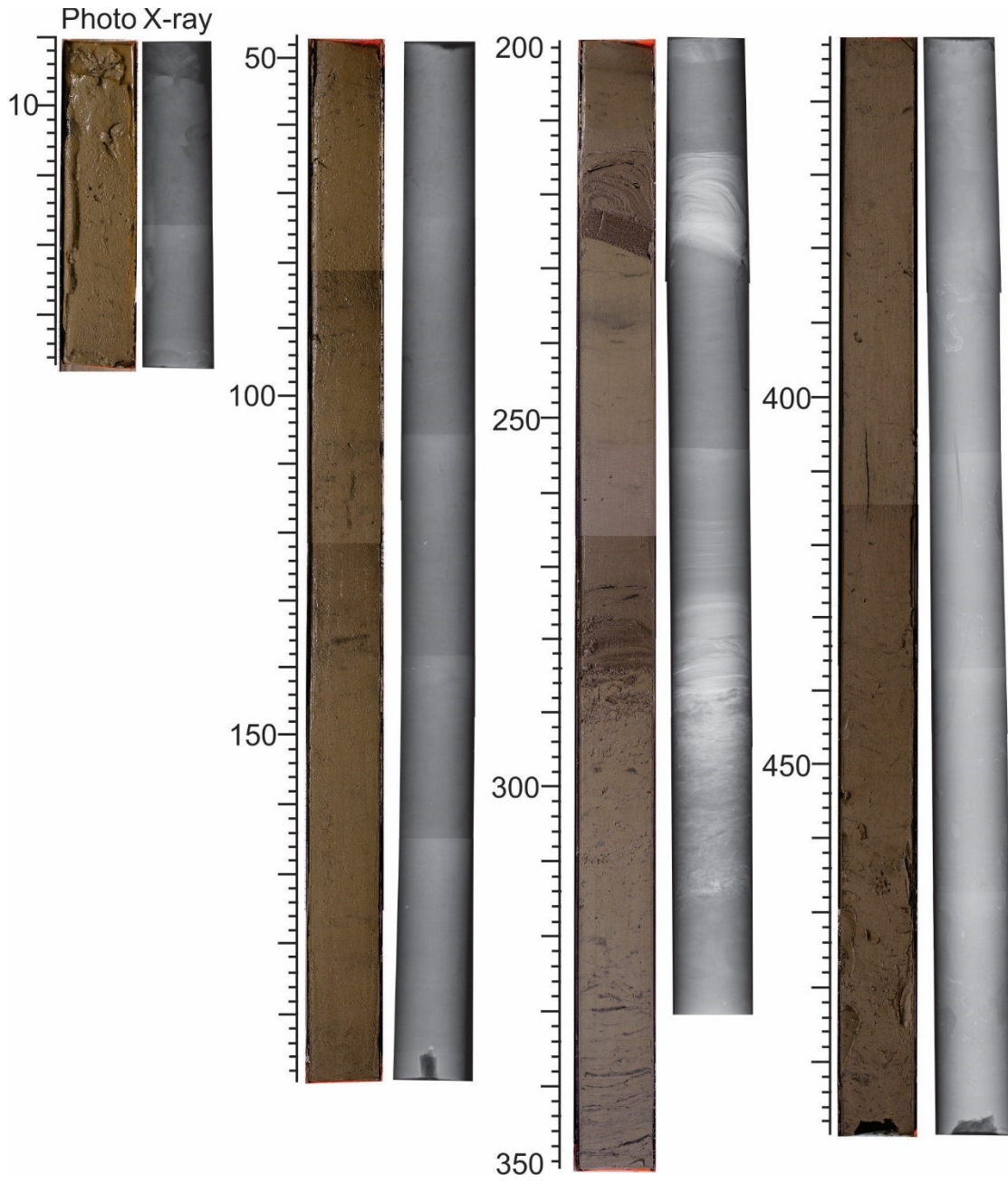
Core 0002PC



Core 0003TWC

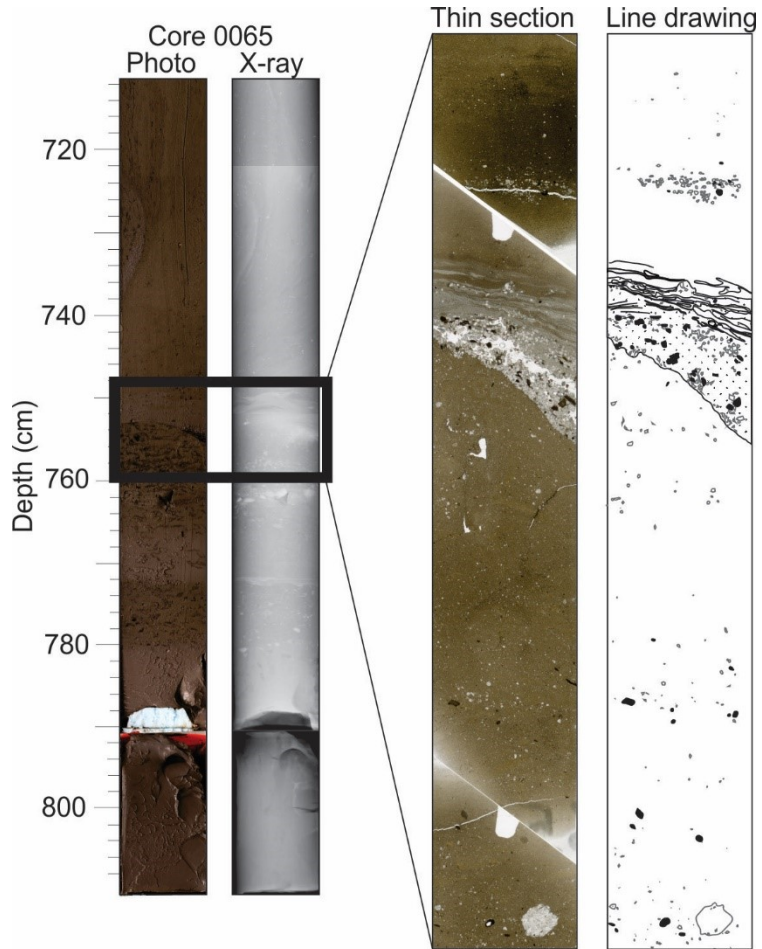


Core 0003PC

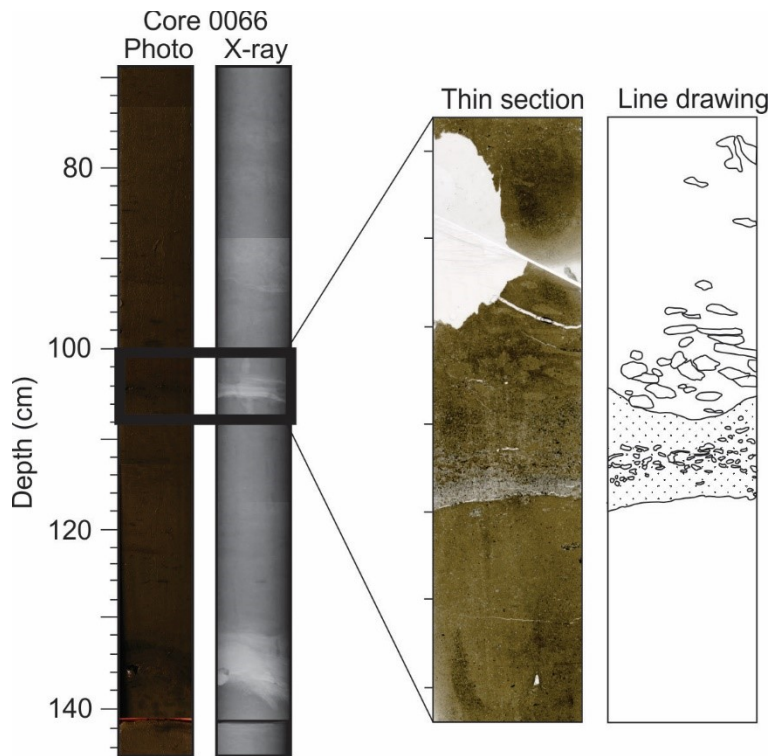


Appendix B: Thin sections

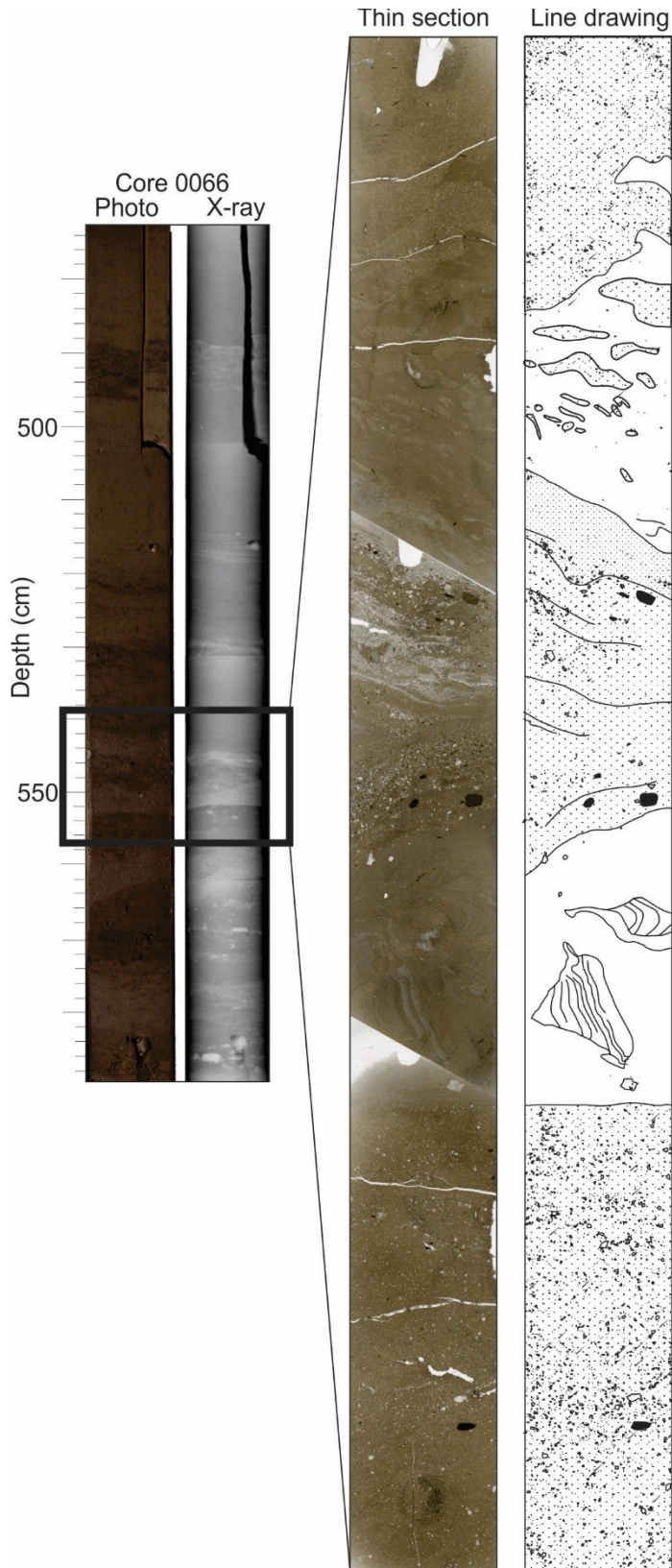
Core 0065PC thin section 749 to 760 cm



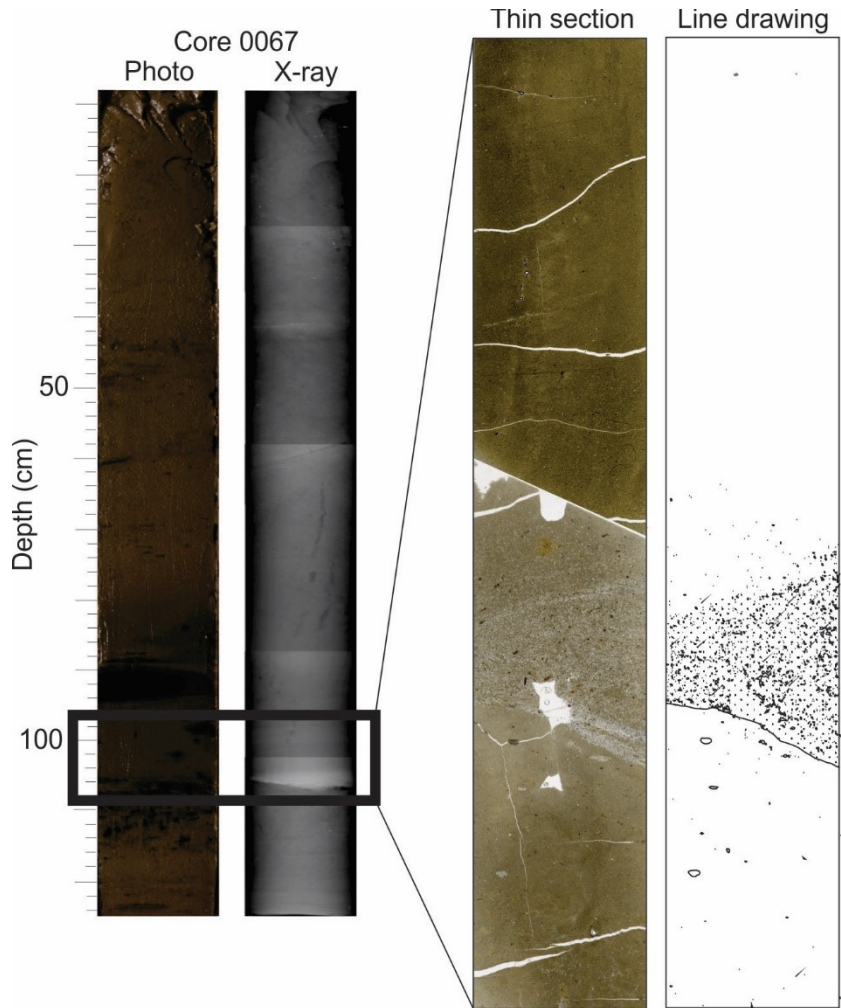
Core 0066PC thin section 100 to 106 cm



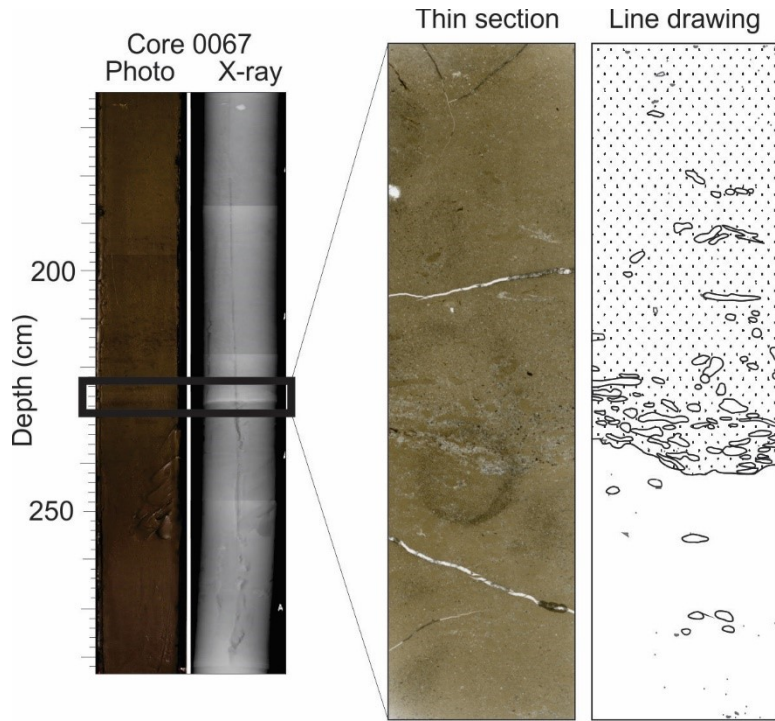
Core 0066PC thin section 549 to 567 cm



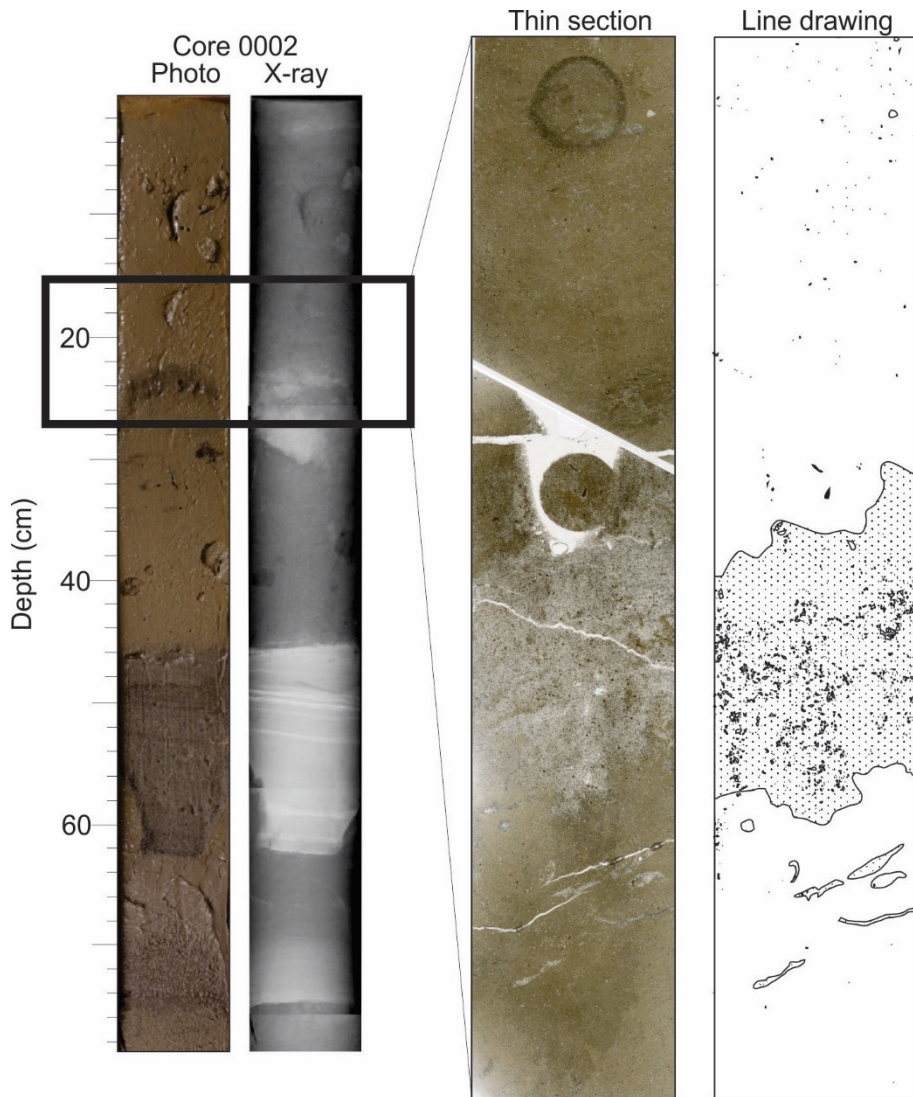
Core 0067PC thin section 96 to 104 cm



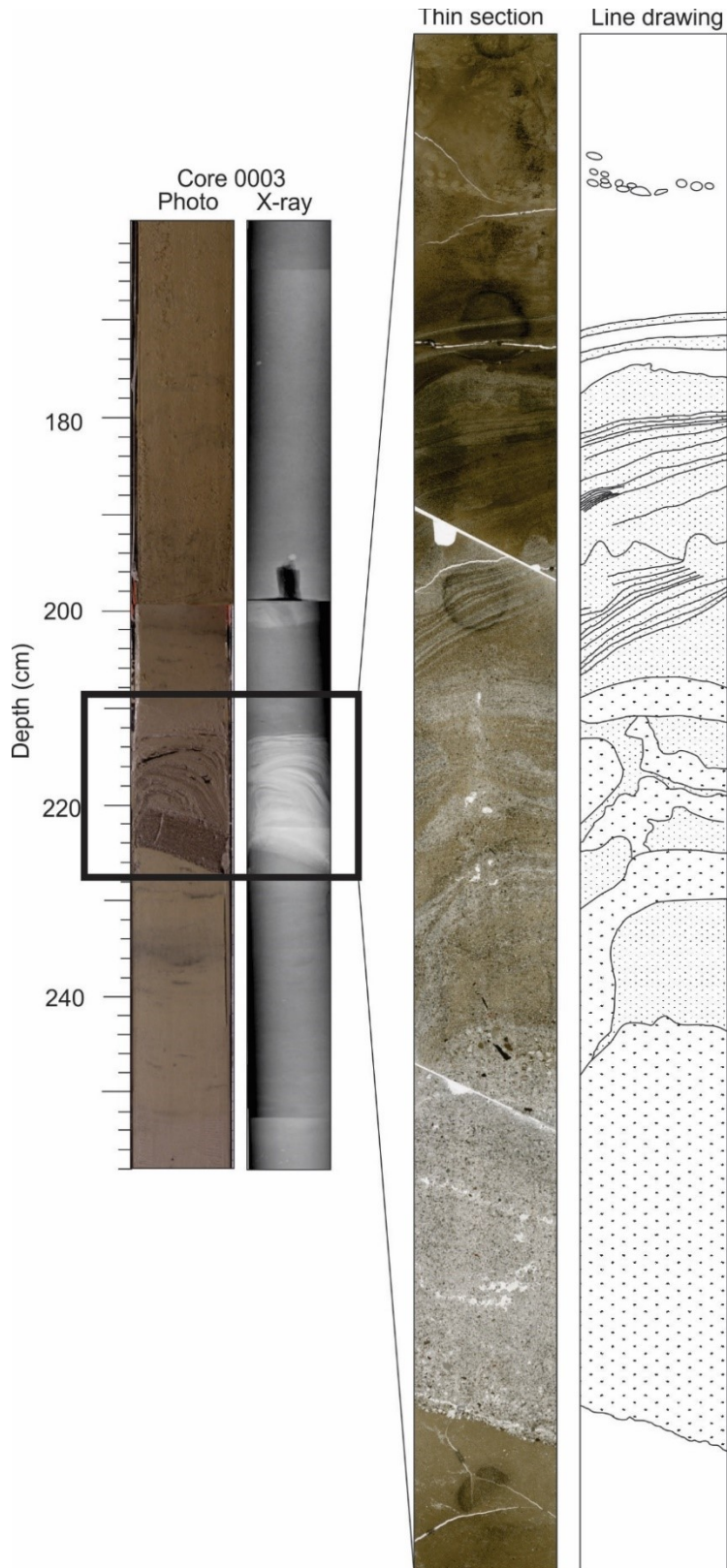
Core 0067PC thin section 223 to 229 cm



Core 0002PC thin section 15 to 27 cm

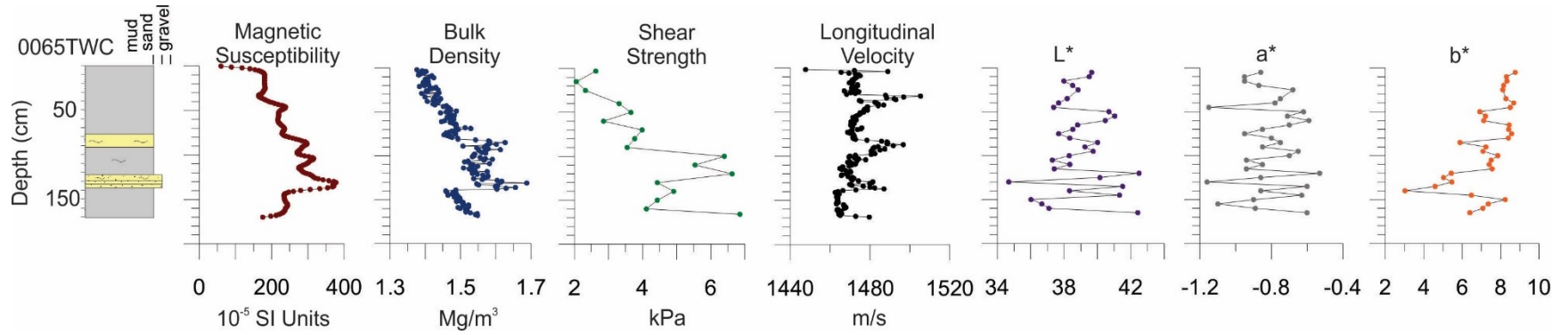


Core 0003PC thin section 208 to 224 cm

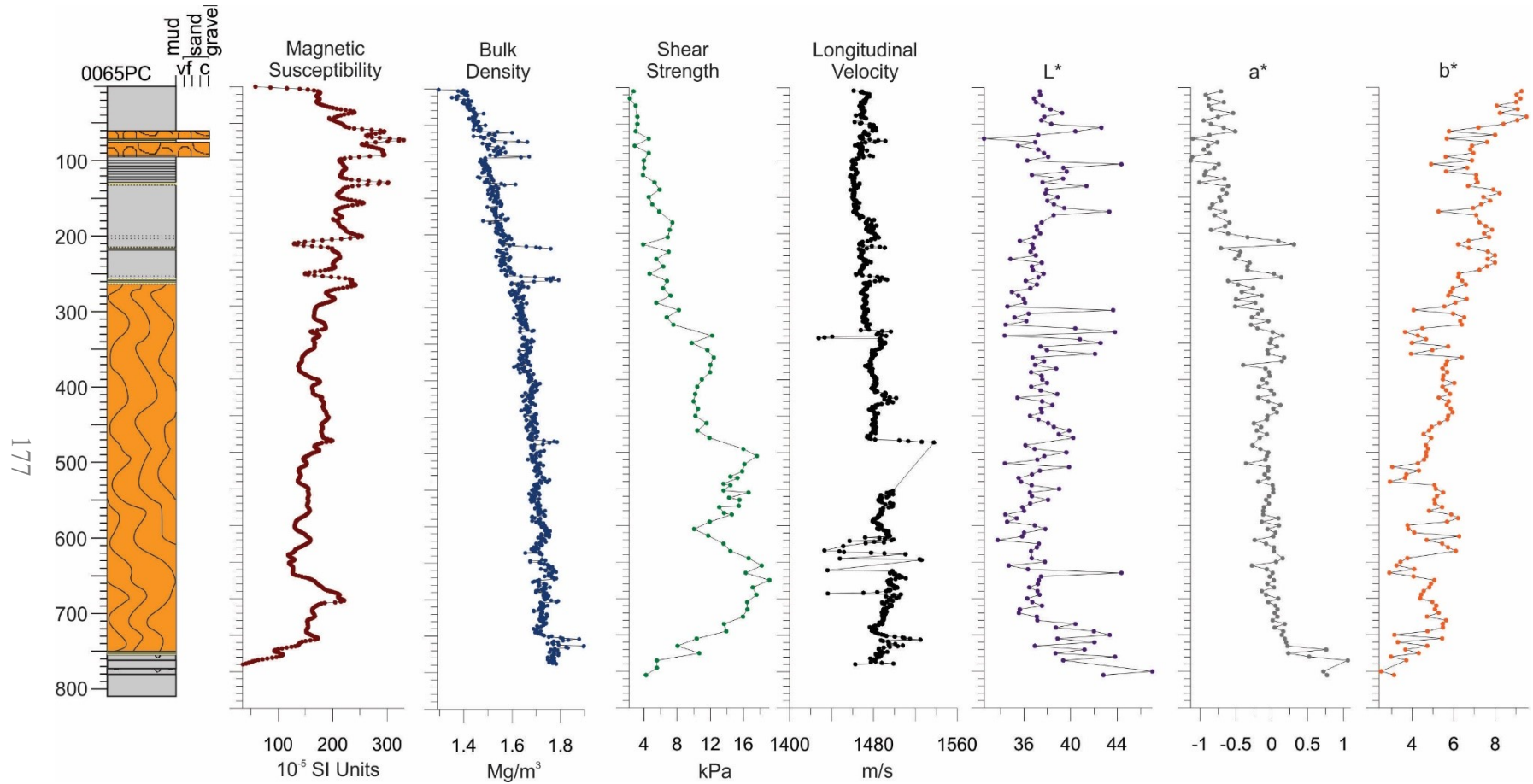


Appendix C: Physical properties

Core 0065TWC

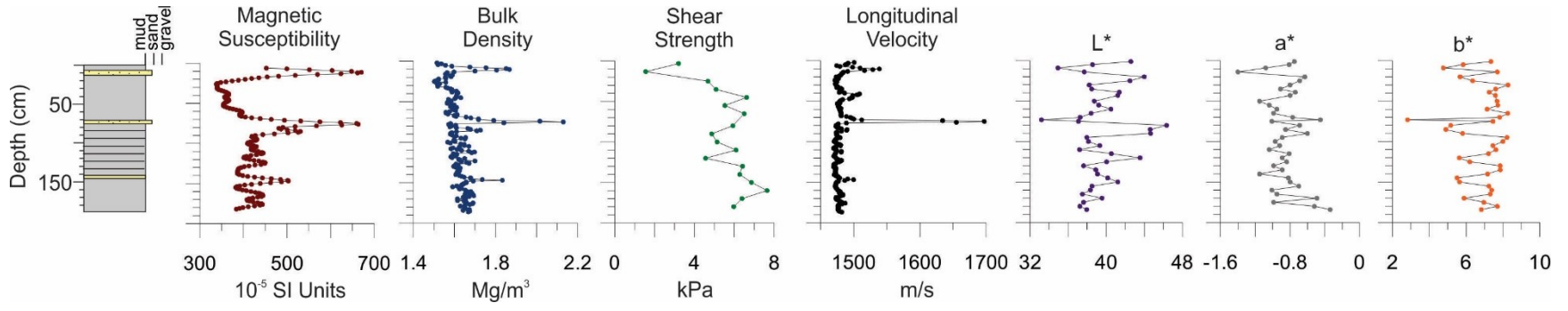


Core 0065PC

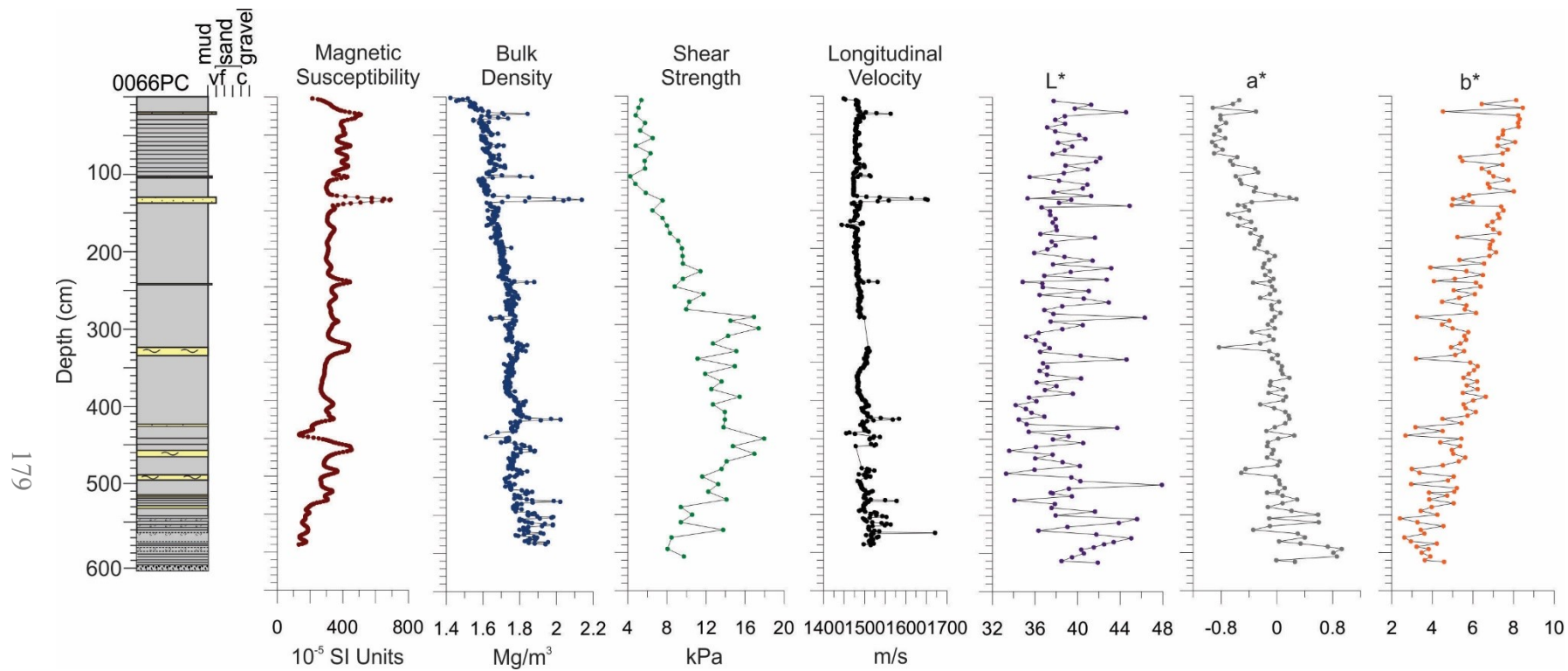


177

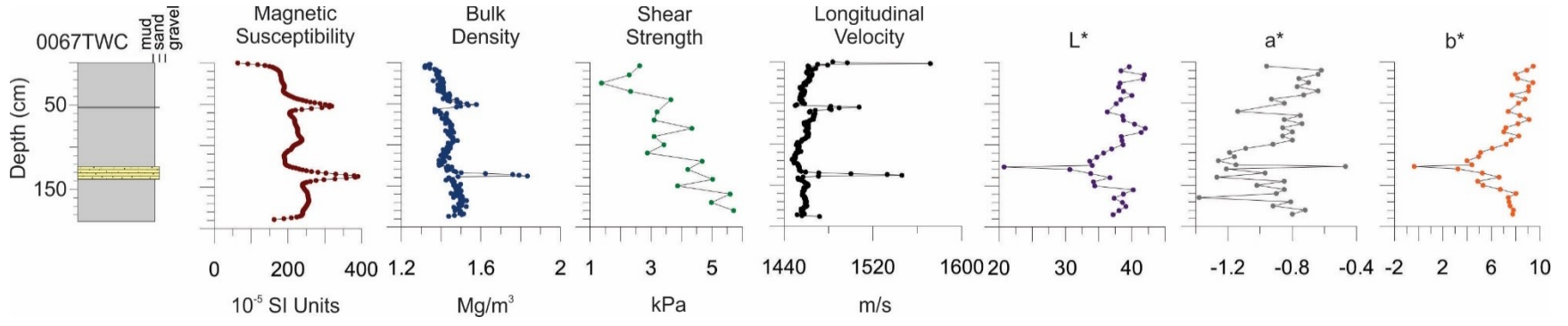
Core 0066TWC



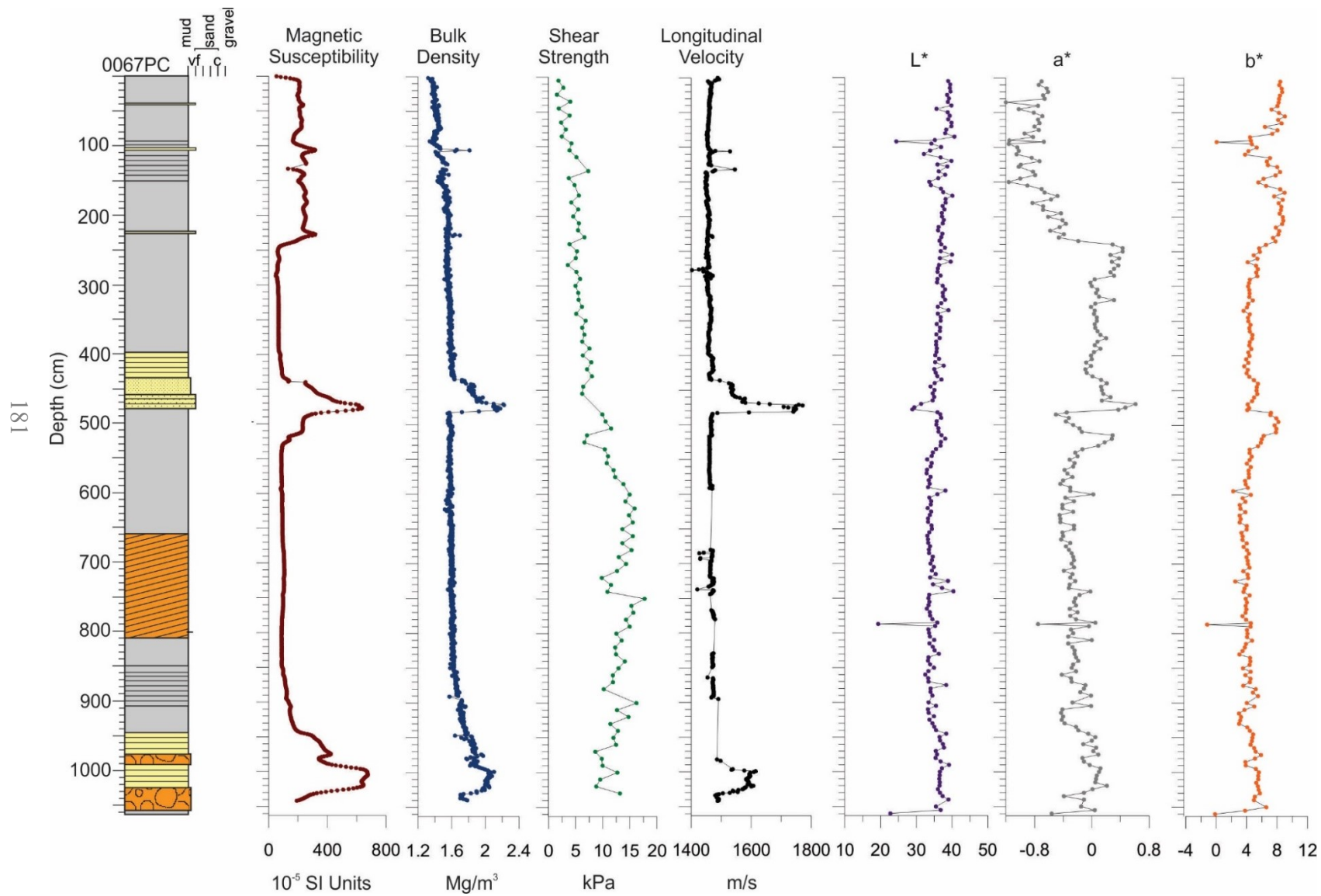
Core 0066PC



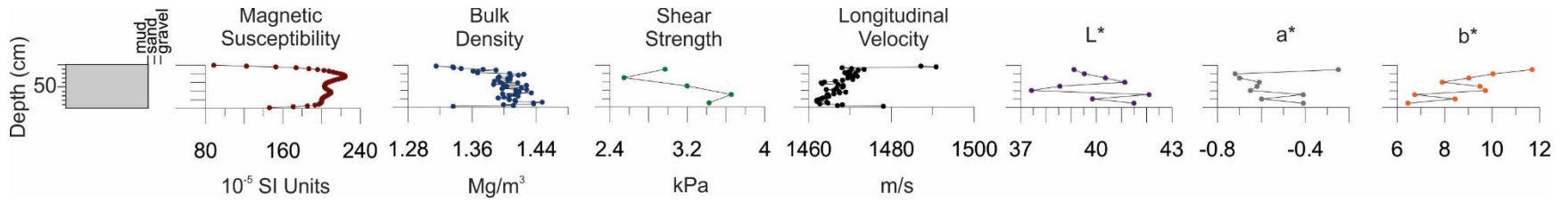
Core 0067TWC



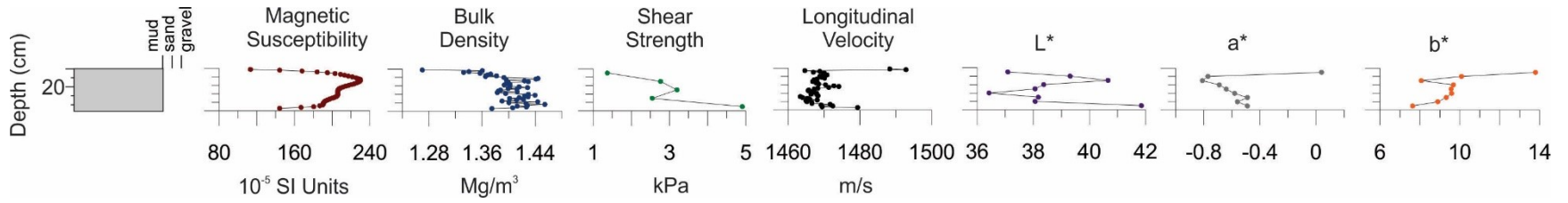
Core 0067PC



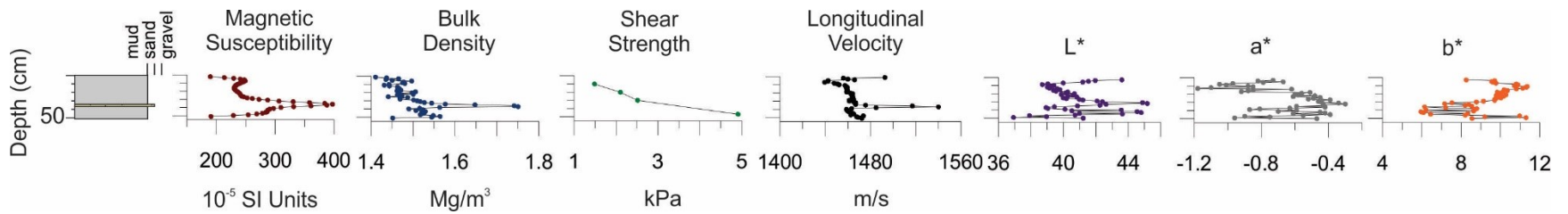
Core 0068bPush



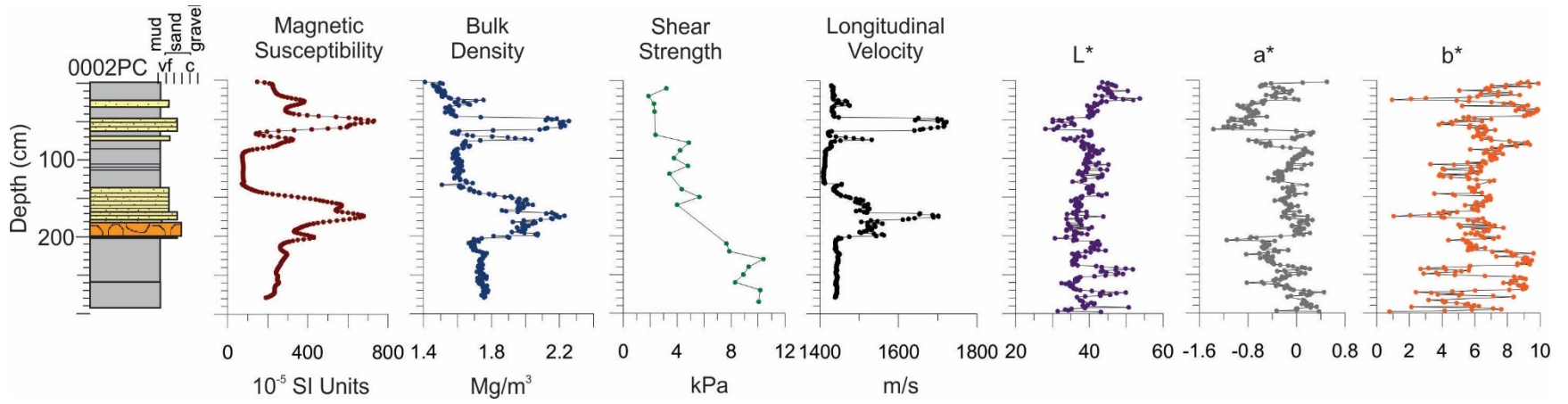
Core 0068cPush



Core 0002TWC

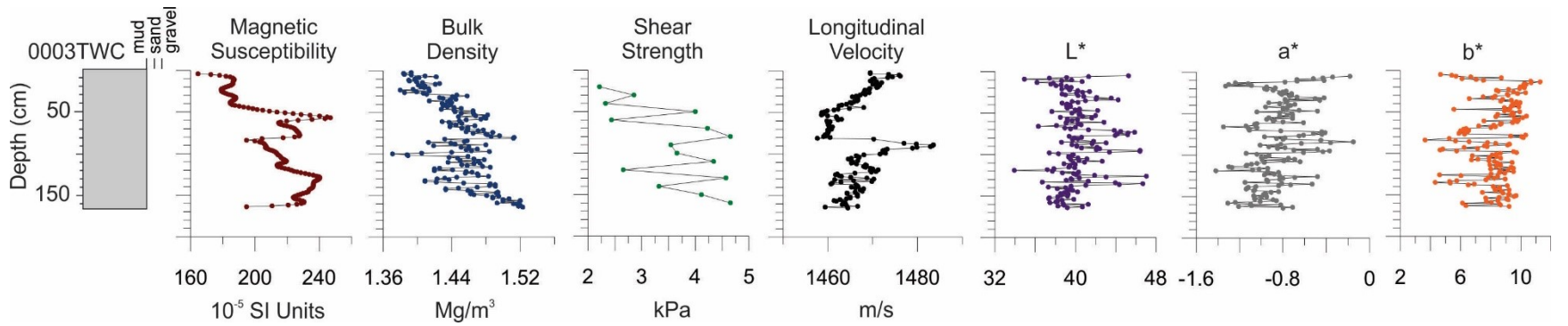


Core 0002PC

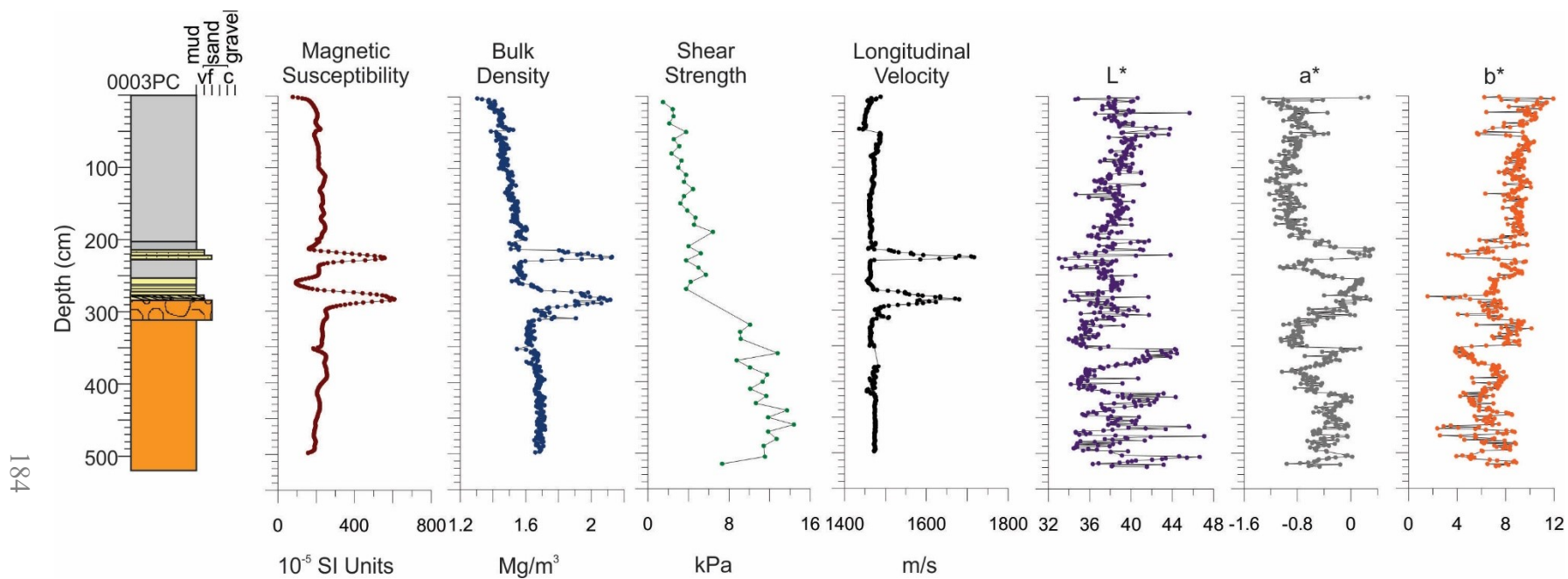


183

Core 0003TWC

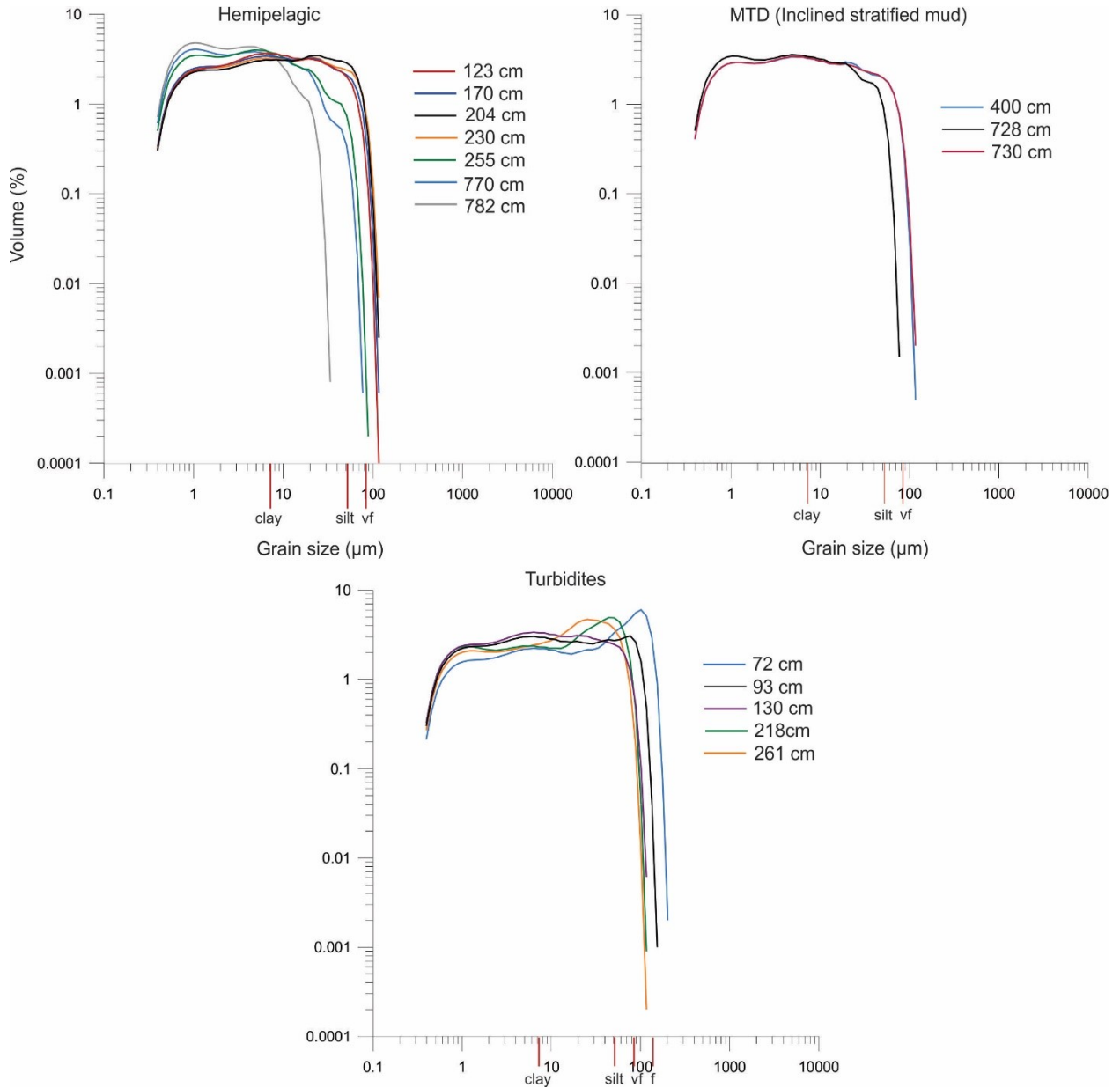


Core 0003PC

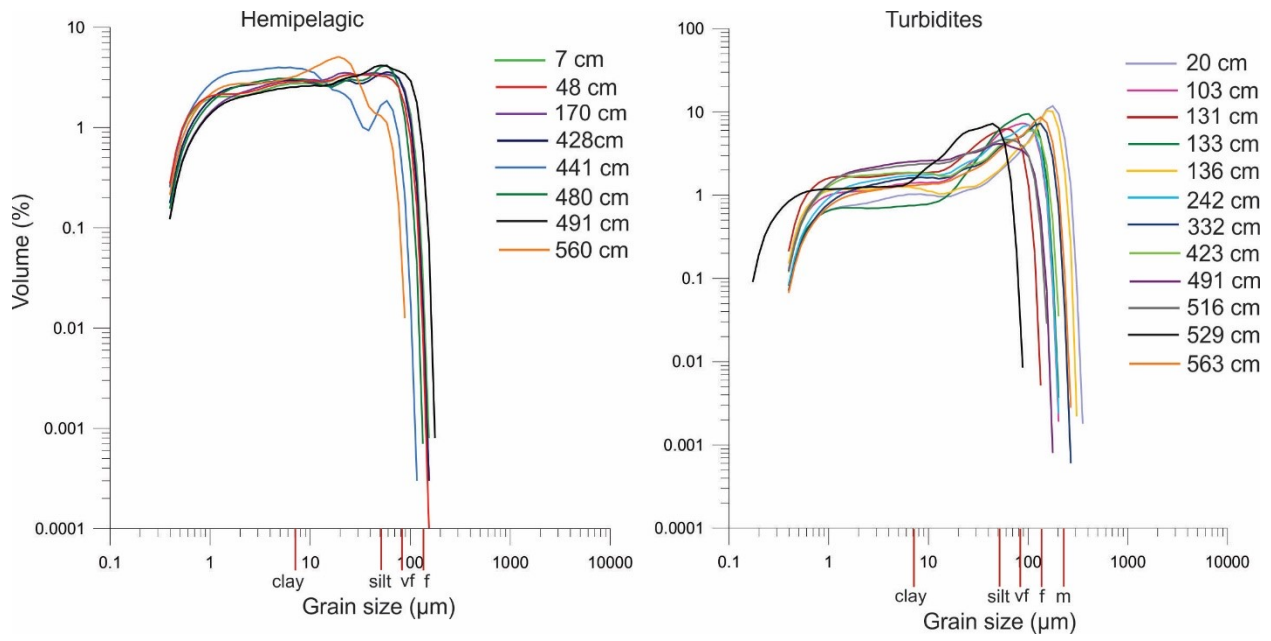


Appendix D: Grain size analysis

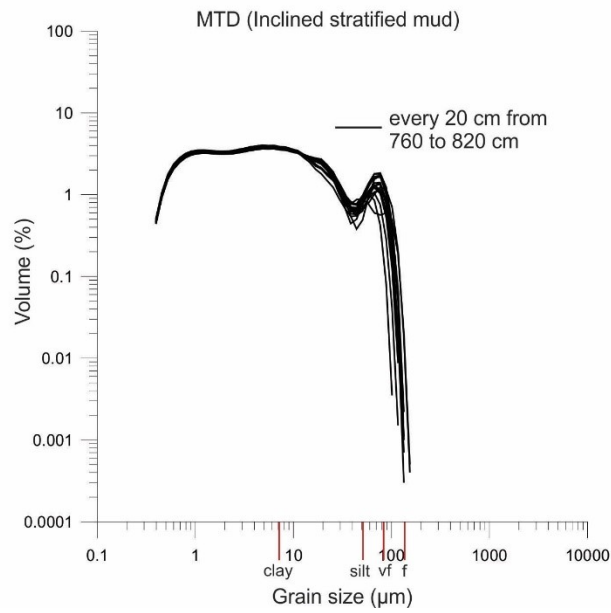
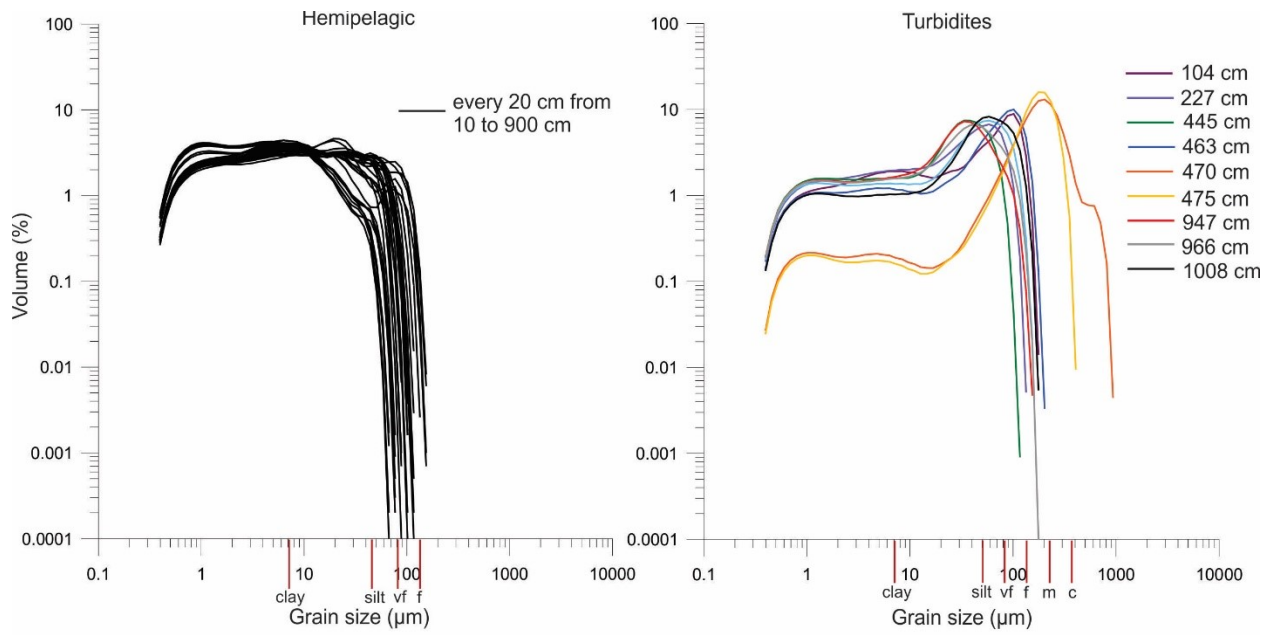
Core 0065PC grain size plots



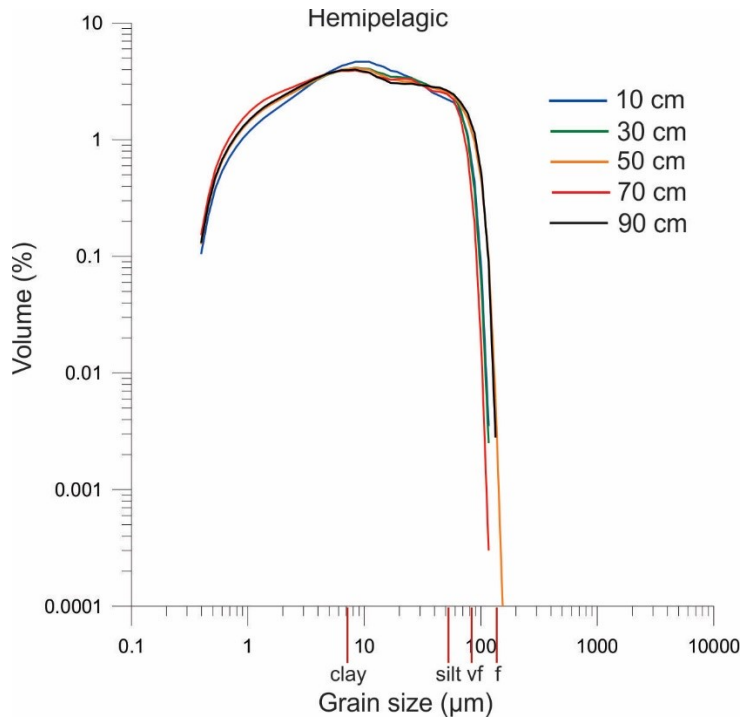
Core 0066PC grain size plots



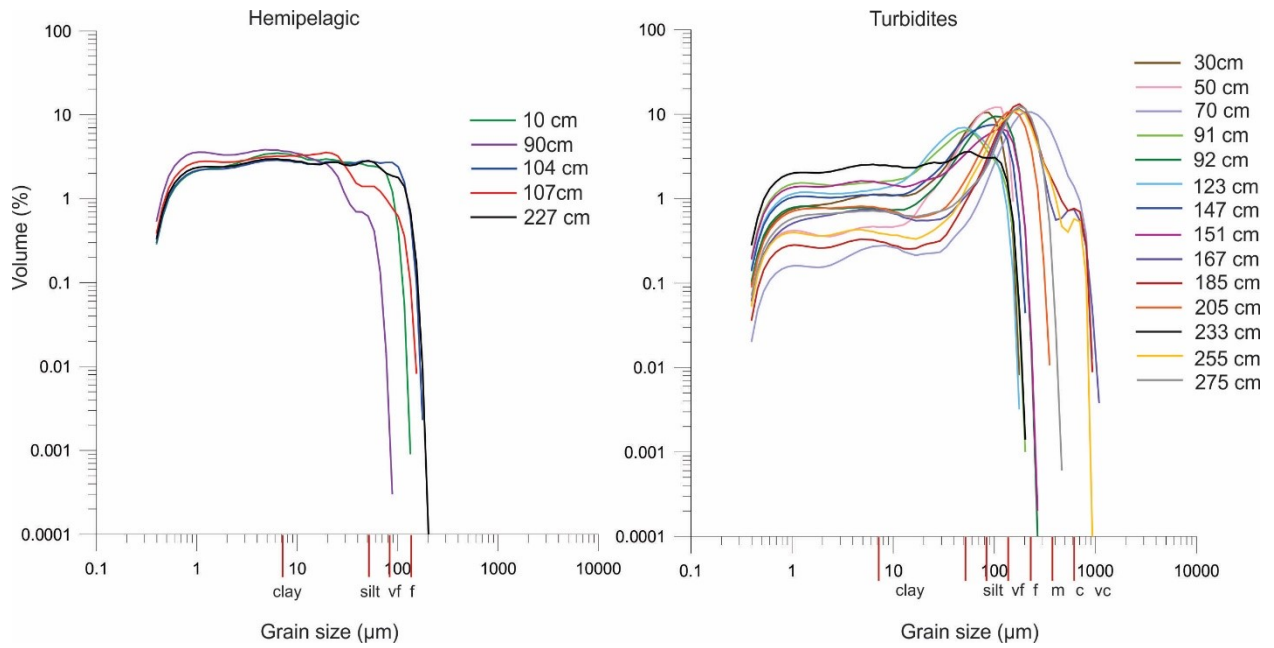
Core 0067PC grain size plots



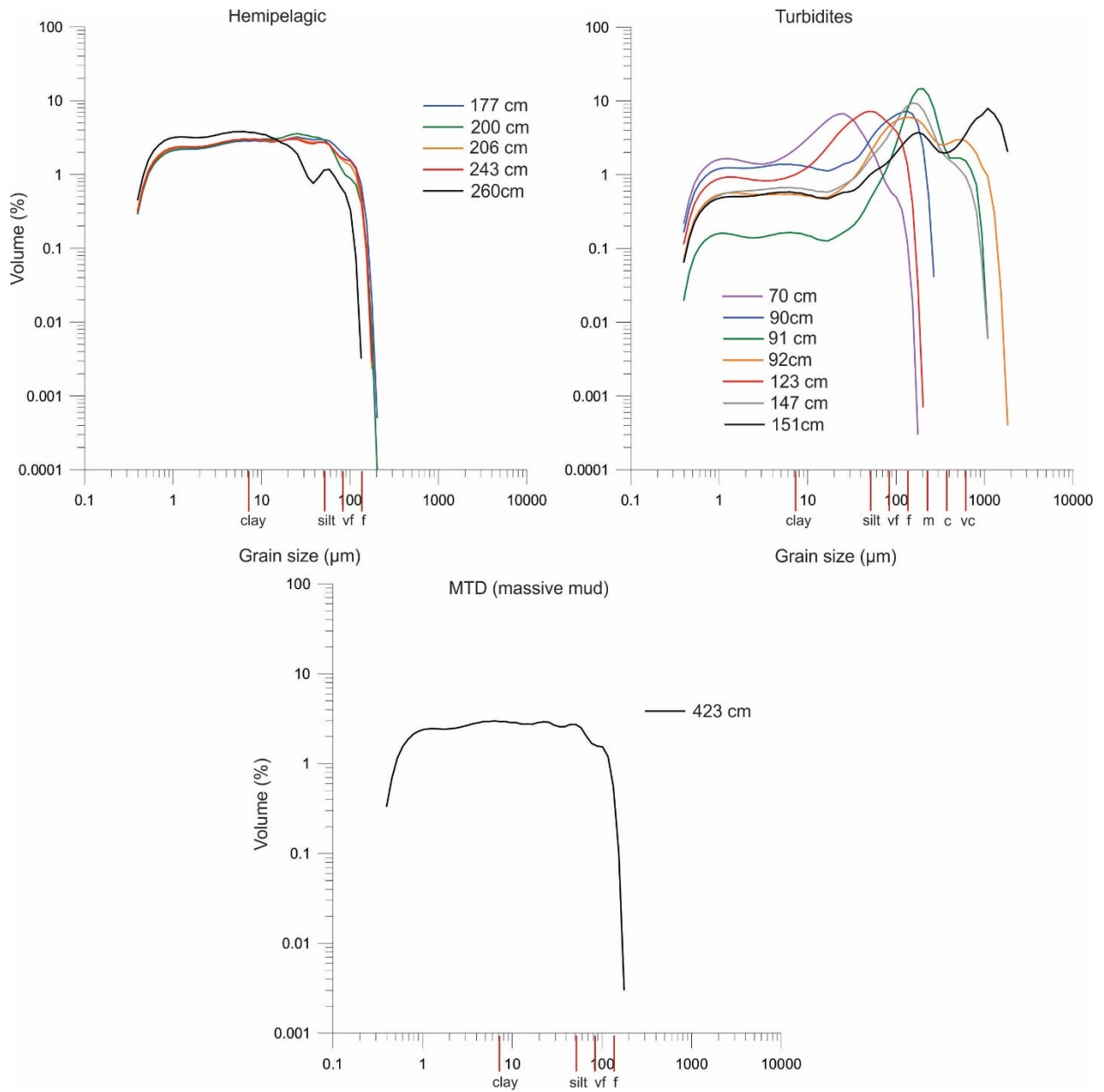
Core 0068 Push grain size plots



Core 0002PC grain size plots

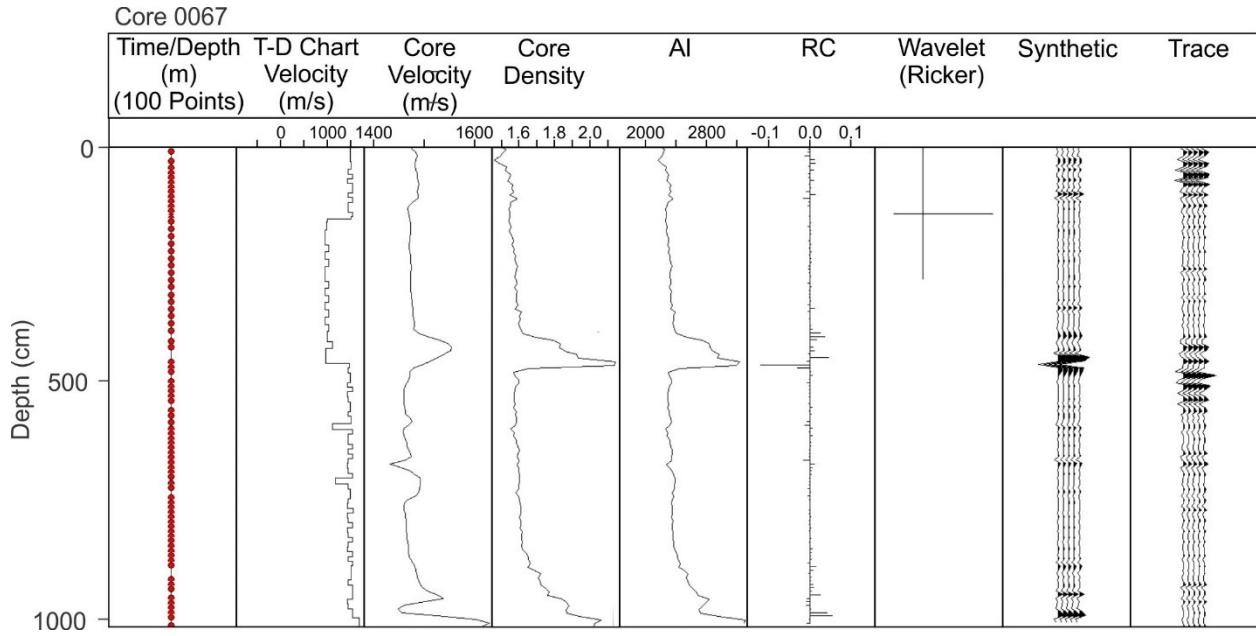


Core 0003PC grain size plots



Appendix E: Synthetic seismograms

Core 0067PC synthetic seismogram



Appendix F: SPLASH analysis

Site 1 SPLASH analysis

Location	Latitude	Latitude	Volume (Mm ³)	Distance (km)	Run up (m)
Site 1	72°54'5.00"N	78° 6'38.73"W	1.93E+01	21.7	10
Site 1	72°54'5.00"N	78° 6'38.73"W	3.34E+01	21.7	14
Site 1	72°54'5.00"N	78° 6'38.73"W	4.50E+01	21.7	16
Site 1	72°54'5.00"N	78° 6'38.73"W	7.44E+01	21.7	22
Site 1	72°54'5.00"N	78° 6'38.73"W	4.44E+02	21.7	60

Site 2 SPLASH analysis

Location	Latitude	Latitude	Volume (Mm ³)	Distance (km)	Run up (m)
Site 2	72°54'19.23"N	78° 0'9.54"W	1.91E+01	21.5	10
Site 2	72°54'19.23"N	78° 0'9.54"W	3.34E+01	21.5	14
Site 2	72°54'19.23"N	78° 0'9.54"W	4.50E+01	21.5	16
Site 2	72°54'19.23"N	78° 0'9.54"W	7.44E+01	21.5	22
Site 2	72°54'19.23"N	78° 0'9.54"W	4.39E+02	21.5	60

Site 3 SPLASH analysis

Location	Latitude	Latitude	Volume (Mm ³)	Distance (km)	Run up (m)
Site 3	72°54'25.79"N	77°54'42.46"W	1.94E+01	21.8	10
Site 3	72°54'25.79"N	77°54'42.46"W	3.34E+01	21.8	14
Site 3	72°54'25.79"N	77°54'42.46"W	4.50E+01	21.8	16
Site 3	72°54'25.79"N	77°54'42.46"W	7.44E+01	21.8	22
Site 3	72°54'25.79"N	77°54'42.46"W	4.47E+02	21.8	60

Site 4 SPLASH analysis

Location	Latitude	Latitude	Volume (Mm ³)	Distance (km)	Run up (m)
Site 4	72°54'11.92"N	77°45'51.87"W	2.02E+01	22.5	10
Site 4	72°54'11.92"N	77°45'51.87"W	3.34E+01	22.5	13
Site 4	72°54'11.92"N	77°45'51.87"W	4.50E+01	22.5	16
Site 4	72°54'11.92"N	77°45'51.87"W	7.44E+01	22.5	21
Site 4	72°54'11.92"N	77°45'51.87"W	4.66E+02	22.5	60

Site 5 SPLASH analysis

Location	Latitude	Latitude	Volume (Mm ³)	Distance (km)	Run up (m)
Site 5	72°54'31.56"N	77°31'18.14"W	2.35E+01	25.3	10
Site 5	72°54'31.56"N	77°31'18.14"W	3.34E+01	25.3	12
Site 5	72°54'31.56"N	77°31'18.14"W	4.50E+01	25.3	14
Site 5	72°54'31.56"N	77°31'18.14"W	7.44E+01	25.3	19
Site 5	72°54'31.56"N	77°31'18.14"W	5.42E+02	25.3	60

Site 6 SPLASH analysis

Location	Latitude	Latitude	Volume (Mm ³)	Distance (km)	Run up (m)
Site 6	72°52'16.00"N	77°17'37.01"W	2.72E+01	28.3	10
Site 6	72°52'16.00"N	77°17'37.01"W	3.34E+01	28.3	11
Site 6	72°52'16.00"N	77°17'37.01"W	4.50E+01	28.3	13
Site 6	72°52'16.00"N	77°17'37.01"W	7.44E+01	28.3	18
Site 6	72°52'16.00"N	77°17'37.01"W	6.27E+02	28.3	60

Site 7 SPLASH analysis

Location	Latitude	Latitude	Volume (Mm ³)	Distance (km)	Run up (m)
Site 7	72°51'52.52"N	77°10'9.63"W	3.07E+01	31.0	10
Site 7	72°51'52.52"N	77°10'9.63"W	3.34E+01	31.0	11
Site 7	72°51'52.52"N	77°10'9.63"W	4.50E+01	31.0	13
Site 7	72°51'52.52"N	77°10'9.63"W	7.44E+01	31.0	18
Site 7	72°51'52.52"N	77°10'9.63"W	7.06E+02	31.0	60

Appendix G: Slope stability analysis

Core 0065PC slope stability analysis

Core	Core Type	Depth (cm)	Bulk Density (g/cm ³)	Effective Overburden Pressure (kPa)	Shear Strength (kPa)	FS	Critical Angle	Critical Acceleration	Critical Height
0065	TWC	3	1.3917	0.035951	2.62732	1413.01		73.22486	84.66681
0065	PC	15	1.3913	0.46444	2.74155	114.1333		5.866935	34.19404
0065	PC	25	1.4181	0.821254	2.28463	53.78782		2.737503	26.85782
0065	PC	35	1.4156	1.204724	2.99064	47.99787		2.437244	33.55342
0065	PC	50	1.445	1.820081	3.19848	33.97805		1.710196	33.93245
0065	PC	60	1.4896	2.236847	3.19848	27.64731		1.381893	33.13226
0065	PC	70	1.5994	2.684001	2.99064	21.54403		1.065385	30.12117
0065	PC	80	1.5199	3.151389	4.56925	28.03422		1.401957	44.79456
0065	PC	90	1.5412	3.658463	2.87987	15.22018		0.737439	27.35956
0065	PC	100	1.5424	4.165959	4.56925	21.20682		1.047897	42.35672
0065	PC	110	1.4662	4.657268	3.98751	16.5545		0.806635	36.37103
0065	PC	120	1.4821	5.113185	3.9981	15.11846		0.732164	36.23562
0065	PC	130	1.5133	5.578582	3.87675	13.43661		0.644945	34.88829
0065	PC	140	1.5545	6.048235	5.25464	16.79809		0.819267	46.97153
0065	PC	150	1.5362	6.54843	5.87051	17.33342		0.847028	51.93047
0065	PC	160	1.5318	7.04059	4.56925	12.5482		0.598873	40.10035
0065	PC	170	1.5548	7.546553	4.98439	12.77053		0.610403	43.36153
0065	PC	180	1.5321	8.040183	5.8258	14.00991		0.674676	50.36798
0065	PC	195	1.553	8.802449	7.42504	16.30951		0.79393	63.52172
0065	PC	205	1.559	9.316488	7.08891	14.71204		0.711087	60.2384
0065	PC	215	1.5837	9.8447	6.85388	13.46107		0.646214	57.80492
0065	PC	225	1.5901	10.3832	3.88387	7.232344	24.21332	0.323201	32.50187
0065	PC	235	1.5643	10.96221	6.97815	12.30801		0.586418	57.77002
0065	PC	245	1.5863	11.49587	5.4831	9.222102	36.26988	0.426387	45.12766

Core	Core Type	Depth (cm)	Bulk Density (g/cm ³)	Effective Overburden Pressure (kPa)	Shear Strength (kPa)	FS	Critical Angle	Critical Acceleration	Critical Height
0065	PC	255	1.5867	12.0271	6.31356	10.14984		0.474498	51.6947
0065	PC	265	1.5739	12.57858	4.68349	7.199191	24.0657	0.321481	38.10451
0065	PC	275	1.6419	13.24653	6.75662	9.862181		0.45958	54.1692
0065	PC	285	1.6289	13.84023	6.28272	8.777079	32.60786	0.403308	49.96221
0065	PC	295	1.6158	14.41881	7.19968	9.65449	43.51187	0.44881	56.88505
0065	PC	305	1.6415	15.01147	5.4831	7.062338	23.46506	0.314384	43.02245
0065	PC	315	1.6294	15.60859	8.19656	10.15345		0.474685	63.88088
0065	PC	325	1.642	16.20688	6.73965	8.04051	28.13702	0.365111	52.19318
0065	PC	350	1.6494	17.74089	12.22275	13.32107		0.638953	93.12232
0065	PC	360	1.6617	18.36964	9.74726	10.25953		0.480186	73.7695
0065	PC	370	1.6747	18.99211	11.6516	11.862		0.563288	87.66098
0065	PC	380	1.6421	19.60702	12.4056	12.23353		0.582555	92.85004
0065	PC	390	1.6174	20.21967	11.99429	11.46954		0.542936	89.34235
0065	PC	400	1.6661	20.83047	11.96254	11.10375		0.523967	88.71082
0065	PC	410	1.6685	21.46883	10.96621	9.876289		0.460312	80.87689
0065	PC	420	1.684	22.12395	10.41184	9.09935	35.12941	0.420021	76.33197
0065	PC	430	1.6686	22.76608	10.16659	8.634409	31.63493	0.39591	74.15627
0065	PC	440	1.6803	23.39556	9.96878	8.238614	29.22557	0.375384	72.40251
0065	PC	450	1.6624	24.02767	10.50928	8.456815	30.50858	0.3867	76.0092
0065	PC	460	1.6801	24.66763	10.19031	7.987401	27.85563	0.362357	73.38547
0065	PC	470	1.6683	25.31538	11.53737	8.811868	32.85611	0.405113	82.7204
0065	PC	480	1.7062	25.96081	10.41184	7.754518	26.66651	0.35028	74.34347
0065	PC	490	1.6748	26.60779	11.88006	8.632873	31.62482	0.39583	84.48863
0065	PC	505	1.6866	27.62077	15.99239	11.19498		0.528697	112.9175
0065	PC	515	1.6804	28.28543	17.61152	12.0387		0.572452	123.8322
0065	PC	526	1.7287	29.0109	16.10772	10.7354		0.504865	112.7849
0065	PC	536	1.7166	29.67937	15.84084	10.31975		0.483309	110.4793

Core	Core Type	Depth (cm)	Bulk Density (g/cm ³)	Effective Overburden Pressure (kPa)	Shear Strength (kPa)	FS	Critical Angle	Critical Acceleration	Critical Height
0065	PC	543	1.7318	30.1523	14.42983	9.253081	36.58122	0.427993	100.3536
0065	PC	545	1.7311	30.29176	15.26877	9.745971		0.453554	106.0885
0065	PC	553	1.6907	30.83806	13.59089	8.52131	30.90804	0.390045	94.11921
0065	PC	555	1.7099	30.97078	14.42928	9.008201	34.35855	0.415294	99.85685
0065	PC	562	1.698	31.43273	13.59089	8.360097	29.92767	0.381684	93.84138
0065	PC	565	1.6705	31.63022	16.61108	10.15409		0.474719	114.5873
0065	PC	572	1.7114	32.08842	14.27244	8.59994	31.4096	0.394122	98.25129
0065	PC	575	1.6907	32.28371	15.52716	9.299384	37.06863	0.430394	106.7994
0065	PC	583	1.7092	32.81755	15.43656	9.094732	35.08897	0.419781	105.9023
0065	PC	585	1.6943	32.9509	13.08752	7.679547	26.29766	0.346392	89.73013
0065	PC	593	1.7085	33.49437	13.64508	7.876799	27.28224	0.356621	93.29347
0065	PC	595	1.7359	33.63182	14.58612	8.385615	30.07894	0.383008	99.65491
0065	PC	605	1.7285	34.29791	11.913	6.715821	22.00078	0.296414	81.15238
0065	PC	615	1.7354	34.99276	10.03776	5.54631	17.5045	0.235765	68.12807
0065	PC	624	1.7533	35.62565	11.74521	6.374462	20.62585	0.278712	79.44653
0065	PC	635	1.7238	36.37785	13.59089	7.223646	24.1745	0.32275	91.61719
0065	PC	645	1.7141	37.03844	14.42928	7.532472	25.59148	0.338765	97.03849
0065	PC	655	1.7233	37.71842	16.61108	8.515104	30.86915	0.389723	111.3982
0065	PC	665	1.7664	38.40702	18.19344	9.159035	35.66712	0.423116	121.6517
0065	PC	675	1.7537	39.12533	16.2755	8.043071	28.15069	0.365244	108.4358
0065	PC	685	1.692	39.83168	19.13448	9.288243	36.94873	0.429817	127.0782
0065	PC	695	1.7383	40.51885	17.11445	8.16679	28.82337	0.37166	113.366
0065	PC	705	1.7509	41.20665	17.56608	8.242389	29.24696	0.37558	116.0617
0065	PC	715	1.725	41.91515	16.44329	7.585134	25.8418	0.341496	108.3219
0065	PC	725	1.6885	42.60001	16.4682	7.474497	25.31902	0.335758	108.2348
0065	PC	735	1.7199	43.28598	15.93993	7.120077	23.7168	0.317379	104.5247
0065	PC	745	1.7285	43.97677	13.64508	5.999269	19.17847	0.259255	89.26915
0065	PC	755	1.695	44.64448	13.92646	6.031405	19.30011	0.260922	90.952

Core	Core Type	Depth (cm)	Bulk Density (g/cm ³)	Effective Overburden Pressure (kPa)	Shear Strength (kPa)	FS	Critical Angle	Critical Acceleration	Critical Height
0065	PC	765	1.8321	45.37685	10.35144	4.410745	13.57248	0.176876	67.39383
0065	PC	775	1.8227	46.14497	8.05386	3.374623	10.21515	0.123145	52.23646
0065	PC	785	1.77	46.88607	10.66512	4.398124	13.53046	0.176222	68.95788

Core 0066PC slope stability analysis

Core	Core Type	Depth (cm)	Bulk Density (g/cm ³)	Effective Overburden Pressure (kPa)	Shear Strength (kPa)	FS	Critical Angle	Critical Acceleration	Critical Height
0066	TWC	3	1.5362	0.049308	3.19848	5097.211		64.86579	305.8079
0066	TWC	13	1.5979	0.703625	1.5507	173.1764		2.191503	45.02222
0066	TWC	25	1.5018	1.32525	4.68349	277.6987		3.521887	138.8381
0066	TWC	35	1.588	1.83449	5.09516	218.2451		2.765148	152.7592
0066	TWC	45	1.6304	2.407033	6.62542	216.2885		2.740243	194.6439
0066	TWC	55	1.5176	2.928493	5.53821	148.6029		1.878725	163.4499
0066	PC	58	1.4547	3.062579	5.36887	137.7519		1.740611	159.7793
0066	PC	68	1.5903	3.575218	5.09516	111.9844		1.412635	152.2864
0066	PC	78	1.5917	4.188225	4.79772	90.01335		1.132983	140.4095
0066	PC	88	1.5864	4.765171	5.75974	94.97875		1.196184	167.1491
0066	PC	98	1.6015	5.340895	5.25464	77.30916		0.971281	151.5137
0066	PC	108	1.6154	5.929439	6.53509	86.60441		1.089593	187.0504
0066	PC	118	1.6749	6.531042	4.79772	57.72374		0.721993	136.217
0066	PC	128	1.6369	7.119144	6.31356	69.68649		0.874258	178.383
0066	PC	138	1.6339	7.739999	5.71157	57.98513		0.72532	160.026
0066	PC	148	1.6679	8.382179	5.75974	53.99431		0.674524	159.8102
0066	PC	158	1.8662	9.023434	4.22656	36.80588	34.76016	0.455746	116.2972
0066	PC	168	1.6144	9.592355	4.76286	39.01617	41.6213	0.483879	131.0837
0066	PC	180	1.6139	10.2899	5.8258	44.48835		0.55353	160.1451
0066	PC	190	1.8303	11.10524	7.53197	53.29454		0.665617	202.5028
0066	PC	203	1.6819	11.9152	6.51119	42.93989		0.533821	174.3218
0066	PC	213	1.6316	12.53768	7.53197	47.20559		0.588116	201.0795
0066	PC	223	1.6858	13.15411	7.99619	47.76654		0.595256	213.0215
0066	PC	233	1.6681	13.79446	8.30732	47.32148		0.589591	220.5002
0066	PC	243	1.701	14.43289	9.13851	49.75357		0.620547	241.7828
0066	PC	253	1.6887	15.09539	9.52573	49.58566		0.61841	250.8831
0066	PC	263	1.6982	15.76081	9.59543	47.83964		0.596186	251.6161

Core	Core Type	Depth (cm)	Bulk Density (g/cm ³)	Effective Overburden Pressure (kPa)	Shear Strength (kPa)	FS	Critical Angle	Critical Acceleration	Critical Height
0066	PC	273	1.717	16.43014	9.63649	46.08712		0.57388	251.6153
0066	PC	283	1.7069	17.11413	11.42314	52.44847		0.654848	296.8343
0066	PC	293	1.7231	17.78806	9.63649	42.5689		0.529099	249.4335
0066	PC	303	1.7332	18.51482	8.79581	37.33003	35.91516	0.462417	226.2017
0066	PC	313	1.7348	19.22669	11.74101	47.98473		0.598033	300.3601
0066	PC	323	1.7299	19.94945	10.28082	40.49475		0.502699	261.5749
0066	PC	333	1.7597	20.65975	9.96878	37.91569	37.40295	0.469872	252.498
0066	PC	343	1.6401	21.36434	16.90624	62.18128		0.77873	426.529
0066	PC	348	1.7692	21.71031	14.50738	52.50794		0.655605	365.4257
0066	PC	358	1.739	22.41946	17.38999	60.95036		0.763063	436.3693
0066	PC	368	1.7588	23.13007	14.26205	48.45148		0.603974	356.574
0066	PC	378	1.8062	23.85172	12.70405	41.8528		0.519984	316.3816
0066	PC	388	1.7882	24.6167	15.10098	48.20336		0.600816	374.0278
0066	PC	398	1.7621	25.34655	11.13564	34.5222	30.74124	0.426679	274.7744
0066	PC	408	1.7512	26.05939	14.93319	45.0288		0.560409	367.4052
0066	PC	418	1.7377	26.76943	11.91983	34.98912	31.47156	0.432622	292.4853
0066	PC	428	1.7174	27.46773	13.59089	38.88009	40.86272	0.482147	332.7866
0066	PC	438	1.7402	28.16268	12.5472	35.00861	31.50284	0.43287	306.6506
0066	PC	448	1.7737	28.87426	15.43655	42.00891		0.521971	376.3693
0066	PC	458	1.8221	29.63295	12.70405	33.68754	29.51446	0.416055	308.5529
0066	PC	468	1.7816	30.38624	13.92646	36.01353	33.21908	0.445661	337.0594
0066	PC	478	1.9144	31.20357	13.92646	35.07021	31.60214	0.433654	335.2441
0066	PC	488	1.7547	31.94501	13.80193	33.94993	29.89036	0.419395	331.3244
0066	PC	503	1.7418	32.9452	17.95339	42.82095		0.532307	430.7439
0066	PC	513	1.8556	33.68138	14.74296	34.39512	30.54835	0.425061	352.8653
0066	PC	523	1.785	34.45494	16.94666	38.64868	39.82041	0.479201	404.2324
0066	PC	533	1.7519	35.17944	14.1156	31.52916	26.68434	0.388582	336.0736
0066	PC	543	1.7832	35.8979	13.59089	29.74958	24.60885	0.365932	323.0543

Core	Core Type	Depth (cm)	Bulk Density (g/cm ³)	Effective Overburden Pressure (kPa)	Shear Strength (kPa)	FS	Critical Angle	Critical Acceleration	Critical Height
0066	PC	553	1.7386	36.64781	11.60616	24.88528	19.6503	0.304018	275.209
0066	PC	563	1.749	37.34489	13.25531	27.89078	22.61282	0.342272	314.0248
0066	PC	573	1.8466	38.08982	12.23352	25.2374	19.98368	0.308499	289.1971
0066	PC	583	1.8683	38.86432	14.09425	28.49659	23.24713	0.349983	332.2433
0066	PC	593	1.7852	39.65748	9.4104	18.64597	14.16613	0.224602	221.1233
0066	PC	603	1.8474	40.43932	10.57069	20.54005	15.75988	0.24871	247.693
0066	PC	613	1.867	41.2712	9.4104	17.9169	13.56553	0.215322	219.6435
0066	PC	623	1.8224	42.10775	13.75867	25.67535	20.40294	0.314074	319.889
0066	PC	633	1.8907	42.92585	8.46936	15.50364	11.62065	0.184606	196.2602

Core 0067PC slope stability analysis

Core	Core Type	Depth (cm)	Bulk Density (g/cm ³)	Effective Overburden Pressure (kPa)	Shear Strength (kPa)	FS	Critical Angle	Critical Acceleration	Critical Height
0067	TWC	4	1.3202	0.06	2.62732	2884.60		43.88	230.74
0067	TWC	15	1.3773	0.43	2.28463	351.18		5.33	105.34
0067	TWC	25	1.3949	0.79	1.37078	114.28		1.72	57.14
0067	PC	30	1.3582	0.95	1.8277	126.13		1.90	75.67
0067	PC	40	1.4233	1.30	2.74155	138.56		2.09	110.83
0067	PC	50	1.3637	1.66	1.5507	61.56		0.92	61.56
0067	PC	60	1.4074	2.02	3.9981	129.77		1.96	155.70
0067	PC	70	1.4042	2.40	1.88299	51.64		0.77	72.29
0067	PC	80	1.3974	2.78	3.88387	91.81		1.38	146.88
0067	PC	90	1.4441	3.18	2.32605	48.14		0.72	86.64
0067	PC	100	1.4681	3.59	3.19848	58.50		0.88	116.99
0067	PC	110	1.402	3.97	2.43681	40.30		0.60	88.64
0067	PC	120	1.3657	4.33	4.22656	64.23		0.96	154.13
0067	PC	130	1.6602	4.75	3.87675	53.63		0.80	139.42
0067	PC	140	1.4614	5.21	5.14041	64.90		0.97	181.71
0067	PC	160	1.5141	6.16	7.31081	78.02		1.17	249.63
0067	PC	170	1.461	6.61	3.76599	37.42		0.55	127.22
0067	PC	180	1.4993	7.05	4.79772	44.72		0.67	160.99
0067	PC	195	1.5458	7.79	5.59734	47.22		0.70	184.14
0067	PC	205	1.5797	8.30	4.20904	33.33		0.49	136.66
0067	PC	215	1.5046	8.81	5.4831	40.91		0.61	175.91
0067	PC	225	1.5769	9.33	4.54133	32.00	38.42	0.47	143.99
0067	PC	235	1.5589	9.86	5.59734	37.33		0.55	175.43
0067	PC	245	1.5342	10.38	5.42745	34.35		0.51	168.30
0067	PC	255	1.527	10.93	6.62542	39.84		0.59	203.15
0067	PC	265	1.5689	11.45	3.87675	22.26	21.32	0.32	117.97

200

Core	Core Type	Depth (cm)	Bulk Density (g/cm ³)	Effective Overburden Pressure (kPa)	Shear Strength (kPa)	FS	Critical Angle	Critical Acceleration	Critical Height
0067	PC	275	1.5262	11.96	5.25464	28.87	30.73	0.42	158.75
0067	PC	285	1.5508	12.47	5.02618	26.48	26.84	0.39	150.93
0067	PC	295	1.5597	12.99	3.54446	17.93	16.54	0.26	105.80
0067	PC	305	1.5328	13.50	5.14041	25.02	24.80	0.37	152.63
0067	PC	315	1.5417	14.02	5.8258	27.31	28.11	0.40	172.06
0067	PC	325	1.5556	14.54	4.98439	22.53	21.64	0.33	146.44
0067	PC	335	1.5802	15.07	5.4831	23.91	23.35	0.35	160.20
0067	PC	345	1.5771	15.61	5.53821	23.32	22.61	0.34	160.92
0067	PC	355	1.5677	16.15	6.16849	25.10	24.91	0.37	178.22
0067	PC	365	1.5727	16.70	5.09516	20.05	18.80	0.29	146.34
0067		375	1.601	17.25	6.85388	26.11	26.31	0.38	195.82
0067	PC	385	1.5833	17.80	6.2028	22.90	22.09	0.33	176.34
0067	PC	395	1.5991	18.35	6.62542	23.73	23.12	0.35	187.48
0067	PC	405	1.593	18.90	6.2028	21.57	20.51	0.31	174.71
0067	PC	415	1.6168	19.45	7.53927	25.48	25.41	0.37	211.43
0067	PC	425	1.6407	20.01	6.31356	20.74	19.57	0.30	176.28
0067	PC	435	1.6048	20.58	7.88196	25.18	25.00	0.37	219.01
0067	PC	445	1.5947	21.14	7.08891	22.04	21.06	0.32	196.10
0067	PC	455	1.6277	21.72	7.99619	24.20	23.71	0.35	220.18
0067	PC	470	1.8698	22.77	6.39696	18.47	17.10	0.27	173.58
0067	PC	480	1.8664	23.56	6.2028	17.31	15.89	0.25	166.12
0067	PC	510	1.5701	26.30	9.93813	24.83	24.54	0.36	253.26
0067	PC	520	1.5842	26.84	10.52261	25.77	25.82	0.38	267.93
0067	PC	530	1.5917	27.39	11.53737	27.68	28.70	0.41	293.41
0067	PC	540	1.6073	27.96	7.08891	16.67	15.24	0.24	179.98
0067	PC	550	1.5794	28.50	6.62542	15.28	13.85	0.22	168.04
0067	PC	560	1.5677	29.04	10.39505	23.52	22.86	0.34	263.44
0067	PC	570	1.5849	29.58	10.96621	24.36	23.92	0.36	277.71

Core	Core Type	Depth (cm)	Bulk Density (g/cm ³)	Effective Overburden Pressure (kPa)	Shear Strength (kPa)	FS	Critical Angle	Critical Acceleration	Critical Height
0067	PC	580	1.5771	30.12	10.74413	23.44	22.75	0.34	271.91
0067	PC	590	1.5698	30.66	11.99429	25.71	25.74	0.38	303.36
0067	PC	600	1.5979	31.21	12.29483	25.89	26.00	0.38	310.70
0067	PC	610	1.582	31.76	13.82199	28.61	30.26	0.42	348.96
0067	PC	625	1.5777	32.58	14.96431	30.19	33.36	0.44	377.28
0067	PC	635	1.5732	33.11	14.17783	28.14	29.46	0.41	357.40
0067	PC	645	1.5718	33.65	15.87816	31.01	35.33	0.46	399.97
0067	PC	655	1.5843	34.19	14.84241	28.53	30.12	0.42	373.71
0067	PC	665	1.5961	34.74	15.53546	29.39	31.71	0.43	390.82
0067	PC	675	1.6115	35.31	13.624	25.36	25.26	0.37	342.34
0067	PC	685	1.6095	35.87	15.53546	28.47	30.01	0.42	389.95
0067	PC	695	1.5881	36.42	13.624	24.58	24.21	0.36	341.67
0067	PC	705	1.5814	36.99	15.307	27.20	27.93	0.40	383.48
0067	PC	715	1.5907	37.55	12.95942	22.69	21.83	0.33	324.36
0067	PC	725	1.5916	38.11	14.27892	24.62	24.26	0.36	357.01
0067	PC	735	1.5861	38.68	12.62713	21.46	20.38	0.31	315.37
0067	PC	745	1.6041	39.30	9.82	16.43	15.00	0.23	244.74
0067	PC	755	1.5957	39.81	11.52	19.02	17.68	0.27	287.15
0067	PC	765	1.5953	40.36	10.85	17.67	16.27	0.25	270.35
0067	PC	775	1.5902	40.93	17.71	28.44	29.96	0.42	440.69
0067	PC	785	1.5906	41.50	15.29	24.21	23.73	0.35	380.07
0067	PC	795	1.5962	42.07	15.65	24.45	24.04	0.36	388.69
0067	PC	805	1.6196	42.65	14.29	22.02	21.04	0.32	354.48
0067	PC	815	1.6045	43.22	14.96	22.76	21.92	0.33	370.93
0067	PC	825	1.6185	43.79	12.52	18.78	17.43	0.27	309.92
0067	PC	835	1.6214	44.36	13.48	19.97	18.71	0.29	333.46
0067	PC	845	1.6213	44.95	12.29	17.98	16.58	0.26	303.81
0067	PC	855	1.6173	45.53	12.45	17.98	16.58	0.26	307.35

Core	Core Type	Depth (cm)	Bulk Density (g/cm ³)	Effective Overburden Pressure (kPa)	Shear Strength (kPa)	FS	Critical Angle	Critical Acceleration	Critical Height
0067	PC	865	1.6289	46.11	14.07	20.05	18.80	0.29	346.85
0067	PC	875	1.5803	46.69	12.91	18.17	16.78	0.26	317.96
0067	PC	885	1.6308	47.29	11.85	16.47	15.04	0.24	291.54
0067	PC	895	1.6455	47.90	11.88	16.30	14.87	0.23	291.76
0067	PC	905	1.6677	48.52	10.19	13.80	12.42	0.19	249.83
0067	PC	925	1.7153	49.79	16.22	21.41	20.33	0.31	396.10
0067	PC	935	1.6747	50.47	12.63	16.44	15.01	0.24	307.48
0067	PC	945	1.7182	51.15	14.74	18.94	17.59	0.27	357.85
0067	PC	955	1.7351	51.84	11.40872	14.47	13.06	0.20	276.26
0067	PC	965	1.7719	52.55	12.79391	16.00	14.57	0.23	308.79
0067	PC	975	1.7138	53.28	11.96254	14.76	13.34	0.21	287.71
0067	PC	985	1.829	54.07	12.45122	15.14	13.71	0.22	298.13
0067	PC	995	1.8486	54.89	8.63961	10.34	9.17	0.14	205.83
0067	PC	1005	1.7726	55.74	9.8239	11.58	10.32	0.16	232.80
0067	PC	1015	1.8186	56.56	9.96878	11.58	10.32	0.16	235.14
0067	PC	1025	2.0683	57.51	12.67968	14.49	13.08	0.21	297.05
0067	PC	1035	2.0163	58.51	9.52573	10.70	9.50	0.15	221.48
0067	PC	1045	2.0375	59.48	8.79581	9.72	8.60	0.13	203.11
0067	PC	1055	1.8279	60.38	13.18095	14.35	12.94	0.20	302.70

Core 0002PC slope stability analysis

Core	Core Type	Depth (cm)	Bulk Density (g/cm ³)	Effective Overburden Pressure (kPa)	Shear Strength (kPa)	FS	Critical Angle	Critical Acceleration	Critical Height
0002	TWC	10	1.4427	0.385955	1.485	264.637		3.833872	52.92181
0002	PC	22	1.484	0.906596	3.19848	242.6557		3.514214	106.7572
0002	PC	32	1.508	1.380345	1.88299	93.8255		1.34989	60.04197
0002	PC	42	1.662	1.962275	2.28463	80.07865		1.14998	67.25895
0002	PC	52	1.549	2.497803	2.32605	64.05036		0.916893	66.60533
0002	PC	82	1.657	5.119182	2.39886	32.23035	34.79363	0.454159	52.85218
0002	PC	92	1.636	5.882154	4.87363	56.98713		0.814178	104.8452
0002	PC	102	1.596	6.477401	4.22656	44.87939		0.638104	91.54427
0002	PC	112	1.571	7.029434	3.76599	36.84847		0.521317	82.53185
0002	PC	122	1.624	7.602019	4.79772	43.40768		0.616703	105.9035
0002	PC	132	1.609	8.170386	3.43369	28.90541	28.59758	0.405807	76.30222
0002	PC	152	1.677	9.338487	4.34079	31.97076	34.19062	0.450384	97.18082
0002	PC	162	1.877	10.07448	5.64898	38.5663		0.546298	124.9416
0002	PC	172	2.043	11.00852	3.9981	24.9796	23.29125	0.348717	85.92074
0002	PC	222	1.686	15.64328	7.6535	33.65062	39.04923	0.474813	149.3929
0002	PC	232	1.73	16.30651	7.86426	33.17093	37.34973	0.467837	153.8968
0002	PC	242	1.734	17.0207	10.39505	42.00586		0.596317	203.2869
0002	PC	252	1.721	17.7175	9.3042	36.11912		0.510711	182.0211
0002	PC	262	1.734	18.41693	8.91005	33.27542	37.68685	0.469357	174.3448
0002	PC	272	1.747	19.12264	8.30732	29.87953	30.16244	0.419973	162.5275
0002	PC	282	1.781	19.84296	10.16659	35.23948		0.497919	198.7296

Core 0003PC slope stability analysis

Core	Core Type	Depth (cm)	Bulk Density (g/cm ³)	Effective Overburden Pressure (kPa)	Shear Strength (kPa)	FS	Critical Angle	Critical Acceleration	Critical Height
0003	TWC	20	1.408	0.668699	2.21529	281.1156		3.301512	112.4384
0003	TWC	30	1.458	1.04761	2.85578	231.3183		2.714588	138.7813
0003	TWC	40	1.3712	1.415566	2.32605	139.4356		1.631637	111.5407
0003	PC	45	1.414	1.594772	1.48501	79.01607		0.919517	71.10952
0003	PC	55	1.4472	1.974263	2.43681	104.7373		1.222674	115.2031
0003	PC	65	1.4524	2.388742	2.51309	89.27369		1.040416	116.0477
0003	PC	75	1.4321	2.803009	2.10452	63.71084		0.739126	95.55962
0003	PC	85	1.4203	3.232721	3.76963	98.94987		1.154461	168.2031
0003	PC	95	1.451	3.640655	2.54758	59.37902		0.68807	112.8123
0003	PC	105	1.463	4.064651	3.08425	64.38891		0.747117	135.2073
0003	PC	125	1.4543	4.924252	2.32605	40.0833	35.43105	0.460646	100.2013
0003	PC	135	1.4371	5.355873	3.31271	52.48533		0.606819	141.7006
0003	PC	145	1.5192	5.816226	2.99064	43.63225		0.502474	126.5247
0003	PC	155	1.5173	6.288136	3.76963	50.86997		0.58778	157.686
0003	PC	165	1.4986	6.762899	3.54446	44.47357		0.51239	146.7526
0003	PC	185	1.5373	7.718383	4.45502	48.97879		0.56549	181.209
0003	PC	195	1.5542	8.218622	3.54446	36.59619	29.8017	0.419545	142.7152
0003	PC	205	1.5296	8.722385	3.19848	31.11667	23.58592	0.354963	127.5695
0003	PC	215	1.5702	9.234607	3.87675	35.6233	28.54966	0.408079	153.1695
0003	PC	225	1.5455	9.782694	4.68349	40.62523	36.61842	0.467033	182.8009
0003	PC	245	1.5583	10.82049	6.39696	50.16621		0.579485	245.7974
0003	PC	252	1.859	11.25976	3.9981	30.13071	22.62386	0.343342	151.8483
0003	PC	265	1.5966	12.41549	5.20592	35.58103	28.49719	0.407581	188.5663
0003	PC	275	1.5671	12.94301	3.76963	24.71429	17.81317	0.279503	135.9192
0003	PC	285	1.5969	13.47313	4.98439	31.39267	23.86148	0.358216	178.9258
0003	PC	295	1.5587	13.99902	5.71157	34.62123	27.34295	0.396268	204.2511

Core	Core Type	Depth (cm)	Bulk Density (g/cm ³)	Effective Overburden Pressure (kPa)	Shear Strength (kPa)	FS	Critical Angle	Critical Acceleration	Critical Height
0003	PC	305	1.6871	14.60419	4.20904	24.45628	17.59941	0.276462	149.173
0003	PC	315	1.9914	15.47124	3.76963	20.67561	14.5819	0.231902	130.2473
0003	PC	325	1.9759	16.45122	10.05236	51.8507		0.599339	337.0061
0003	PC	335	1.6742	17.18131	9.08267	44.85822		0.516924	300.5292
0003	PC	345	1.9052	17.88075	9.13851	43.36851		0.499366	299.2219
0003	PC	355	1.6485	18.49631	12.79391	58.69525		0.68001	416.7073
0003	PC	365	1.6358	19.08501	8.75038	38.90625	33.24497	0.446772	283.9959
0003	PC	375	1.6244	19.67614	10.05236	43.35237		0.499176	325.1202
0003	PC	395	1.6484	20.84404	11.3089	46.03871		0.530837	363.6806
0003	PC	415	1.6519	22.08664	10.07955	38.72544	32.94258	0.444641	321.3988
0003	PC	425	1.6781	22.71929	11.6516	43.51866		0.501135	369.8829
0003	PC	435	1.6741	23.37097	10.63337	38.60815	32.75019	0.443259	335.8676
0003	PC	445	1.6558	24.00655	13.70776	48.45308		0.559294	431.2025
0003	PC	455	1.6788	24.64576	11.85178	40.8062	37.05305	0.469166	371.3107
0003	PC	465	1.6991	25.29562	14.39315	48.28312		0.557291	449.0018
0003	PC	475	1.693	25.94846	11.85178	38.75759	32.99584	0.44502	368.1716
0003	PC	485	1.7103	26.60897	12.67968	40.43571	36.18556	0.464799	392.1991
0003	PC	495	1.7091	27.26275	11.40872	35.51011	28.40949	0.406745	351.5256
0003	PC	505	1.688	27.91785	11.53737	35.06789	27.8716	0.401533	354.1611
0003	PC	515	1.69	28.56396	7.31044	21.7175	15.39406	0.244182	223.6747

Appendix H: Age model results

Core 0065 age model results

Core	Core type	Depth (cm)	min95%	max95%	age (yr BP)	sed rate (mm/year)
0065	TWC	-10	-65	-61	-63	0.62
0065	TWC	-9	-51	-42	-47	0.62
0065	TWC	-8	-38	-23	-31	0.62
0065	TWC	-7	-25	-2	-14	0.62
0065	TWC	-6	-12	18	2	0.62
0065	TWC	-5	1	38	18	0.62
0065	TWC	-4	14	58	34	0.62
0065	TWC	-3	26	78	51	0.62
0065	TWC	-2	39	98	67	0.62
0065	TWC	-1	52	118	83	0.62
0065	TWC	0	64	138	99	0.62
0065	PC	1	77	158	115	0.62
0065	PC	2	90	178	132	0.62
0065	PC	3	103	198	148	0.62
0065	PC	4	116	218	164	0.62
0065	PC	5	128	238	180	0.62
0065	PC	6	141	259	197	0.62
0065	PC	7	154	279	213	0.62
0065	PC	8	167	299	229	0.62
0065	PC	9	180	319	245	0.62
0065	PC	10	192	339	262	0.62
0065	PC	11	205	359	278	0.62
0065	PC	12	218	379	294	0.62
0065	PC	13	230	399	310	0.62
0065	PC	14	243	419	326	0.62
0065	PC	15	256	440	343	0.62
0065	PC	16	269	460	359	0.62
0065	PC	17	281	480	375	0.62
0065	PC	18	294	500	391	0.62
0065	PC	19	307	520	408	0.62
0065	PC	20	320	540	424	0.62
0065	PC	21	333	560	440	0.62
0065	PC	22	345	580	456	0.62
0065	PC	23	358	600	472	0.62
0065	PC	24	371	621	489	0.62
0065	PC	25	384	641	505	0.62
0065	PC	26	396	661	521	0.62
0065	PC	27	409	681	537	0.62

Core	Core type	Depth (cm)	min95%	max95%	age (yr BP)	sed rate (mm/year)
0065	PC	28	422	701	554	0.62
0065	PC	29	435	721	570	0.62
0065	PC	30	447	741	586	0.62
0065	PC	31	460	761	602	0.62
0065	PC	32	473	781	618	0.62
0065	PC	33	486	801	635	0.62
0065	PC	34	499	822	651	0.62
0065	PC	35	511	842	667	0.62
0065	PC	36	524	862	683	0.62
0065	PC	37	537	882	700	0.62
0065	PC	38	550	902	716	0.62
0065	PC	39	562	922	732	0.62
0065	PC	40	575	942	748	0.62
0065	PC	41	588	962	765	0.62
0065	PC	42	601	982	781	0.62
0065	PC	43	614	1002	797	0.62
0065	PC	44	626	1022	813	0.62
0065	PC	45	639	1043	829	0.62
0065	PC	46	652	1063	846	0.62
0065	PC	47	665	1083	862	0.62
0065	PC	48	677	1103	878	0.62
0065	PC	49	690	1123	894	0.62
0065	PC	50	703	1143	911	0.32
0065	PC	51	740	1169	942	0.32
0065	PC	52	777	1193	974	0.32
0065	PC	53	814	1219	1006	0.32
0065	PC	54	850	1245	1037	0.32
0065	PC	55	886	1271	1069	0.32
0065	PC	56	922	1299	1101	0.32
0065	PC	57	958	1326	1133	0.32
0065	PC	58	992	1353	1164	0.32
0065	PC	59	1026	1379	1196	0.32
0065	PC	60	1060	1407	1228	0.32
0065	PC	61	1094	1435	1259	10.99
0065	PC	96	1128	1463	1291	0.32
0065	PC	97	1160	1493	1323	0.32
0065	PC	98	1191	1524	1355	0.32
0065	PC	99	1223	1554	1386	0.32
0065	PC	100	1254	1585	1418	0.32
0065	PC	101	1284	1617	1450	0.32
0065	PC	102	1315	1651	1482	0.32
0065	PC	103	1344	1684	1513	0.32

Core	Core type	Depth (cm)	min95%	max95%	age (yr BP)	sed rate (mm/year)
0065	PC	104	1374	1717	1545	0.32
0065	PC	105	1403	1751	1577	0.32
0065	PC	106	1431	1785	1608	0.32
0065	PC	107	1460	1820	1640	0.32
0065	PC	108	1487	1856	1672	0.32
0065	PC	109	1514	1891	1704	0.32
0065	PC	110	1541	1927	1735	0.32
0065	PC	111	1568	1961	1767	0.32
0065	PC	112	1594	1998	1799	0.32
0065	PC	113	1620	2034	1830	0.32
0065	PC	114	1648	2071	1862	0.32
0065	PC	115	1674	2108	1894	0.32
0065	PC	116	1701	2146	1926	0.32
0065	PC	117	1726	2183	1957	0.32
0065	PC	118	1752	2220	1989	0.32
0065	PC	119	1776	2260	2021	0.32
0065	PC	120	1801	2298	2052	1.83
0065	PC	121	1808	2300	2058	1.83
0065	PC	122	1817	2303	2063	1.83
0065	PC	123	1825	2305	2069	1.83
0065	PC	124	1833	2308	2074	1.83
0065	PC	125	1841	2311	2080	1.83
0065	PC	126	1850	2314	2085	1.83
0065	PC	127	1858	2317	2091	1.83
0065	PC	128	1866	2319	2096	1.83
0065	PC	129	1875	2323	2102	1.83
0065	PC	130	1882	2327	2107	5.49
0065	PC	133	1890	2330	2112	1.83
0065	PC	134	1896	2333	2118	1.83
0065	PC	135	1905	2336	2123	1.83
0065	PC	136	1912	2340	2129	1.83
0065	PC	137	1919	2343	2134	1.83
0065	PC	138	1927	2346	2140	1.83
0065	PC	139	1934	2349	2145	1.83
0065	PC	140	1941	2353	2151	1.83
0065	PC	141	1949	2356	2156	1.83
0065	PC	142	1957	2361	2162	1.83
0065	PC	143	1964	2365	2167	1.83
0065	PC	144	1972	2368	2172	1.83
0065	PC	145	1979	2372	2178	1.83
0065	PC	146	1986	2376	2183	1.83
0065	PC	147	1994	2380	2189	1.83

Core	Core type	Depth (cm)	min95%	max95%	age (yr BP)	sed rate (mm/year)
0065	PC	148	2001	2384	2194	1.83
0065	PC	149	2008	2389	2200	1.83
0065	PC	150	2016	2393	2205	1.83
0065	PC	151	2023	2397	2211	1.83
0065	PC	152	2030	2402	2216	1.83
0065	PC	153	2036	2405	2221	1.83
0065	PC	154	2042	2410	2227	1.83
0065	PC	155	2048	2414	2232	1.83
0065	PC	156	2055	2419	2238	1.83
0065	PC	157	2062	2424	2243	1.83
0065	PC	158	2069	2429	2249	1.83
0065	PC	159	2075	2434	2254	1.83
0065	PC	160	2082	2439	2260	1.83
0065	PC	161	2088	2443	2265	1.83
0065	PC	162	2093	2448	2271	1.83
0065	PC	163	2099	2452	2276	1.83
0065	PC	164	2104	2458	2281	1.83
0065	PC	165	2110	2462	2287	1.83
0065	PC	166	2116	2467	2292	1.83
0065	PC	167	2122	2472	2298	1.83
0065	PC	168	2128	2477	2303	1.83
0065	PC	169	2134	2482	2309	1.83
0065	PC	170	2138	2487	2314	1.83
0065	PC	171	2144	2492	2320	1.83
0065	PC	172	2149	2497	2325	1.83
0065	PC	173	2154	2503	2330	1.83
0065	PC	174	2159	2508	2336	1.83
0065	PC	175	2164	2513	2341	1.83
0065	PC	176	2169	2519	2347	1.83
0065	PC	177	2173	2524	2352	1.83
0065	PC	178	2178	2529	2358	1.83
0065	PC	179	2183	2535	2363	1.83
0065	PC	180	2187	2541	2369	1.83
0065	PC	181	2192	2547	2374	1.83
0065	PC	182	2196	2553	2380	1.83
0065	PC	183	2201	2559	2385	1.83
0065	PC	184	2206	2565	2390	1.83
0065	PC	185	2211	2571	2396	1.83
0065	PC	186	2216	2577	2401	1.83
0065	PC	187	2220	2583	2407	1.83
0065	PC	188	2224	2590	2412	1.83
0065	PC	189	2228	2596	2418	1.83

Core	Core type	Depth (cm)	min95%	max95%	age (yr BP)	sed rate (mm/year)
0065	PC	190	2232	2603	2423	1.83
0065	PC	191	2237	2609	2429	1.83
0065	PC	192	2241	2617	2434	1.83
0065	PC	193	2245	2623	2440	1.83
0065	PC	194	2249	2630	2445	1.83
0065	PC	195	2253	2636	2450	1.83
0065	PC	196	2257	2643	2456	1.83
0065	PC	197	2261	2650	2461	1.83
0065	PC	198	2265	2657	2467	1.83
0065	PC	199	2269	2665	2472	1.83
0065	PC	200	2273	2672	2478	1.83
0065	PC	201	2276	2679	2483	1.83
0065	PC	202	2279	2687	2489	1.83
0065	PC	203	2282	2694	2494	1.83
0065	PC	204	2285	2701	2499	1.83
0065	PC	205	2289	2708	2505	1.83
0065	PC	206	2292	2716	2510	1.83
0065	PC	207	2295	2725	2516	1.83
0065	PC	208	2298	2732	2521	0.37
0065	PC	209	2331	2755	2549	0.37
0065	PC	210	2363	2776	2576	0.37
0065	PC	211	2396	2798	2603	0.37
0065	PC	212	2427	2823	2631	0.37
0065	PC	213	2458	2846	2658	0.37
0065	PC	214	2491	2870	2685	0.37
0065	PC	215	2522	2893	2712	0.37
0065	PC	216	2553	2918	2740	1.46
0065	PC	220	2584	2944	2767	0.37
0065	PC	221	2613	2969	2794	0.37
0065	PC	222	2643	2994	2822	0.37
0065	PC	223	2671	3020	2849	0.37
0065	PC	224	2700	3046	2876	0.37
0065	PC	225	2729	3074	2904	0.37
0065	PC	226	2757	3100	2931	0.37
0065	PC	227	2785	3128	2958	0.37
0065	PC	228	2812	3157	2986	0.37
0065	PC	229	2840	3184	3013	0.37
0065	PC	230	2867	3214	3040	0.37
0065	PC	231	2893	3243	3068	0.37
0065	PC	232	2920	3274	3095	0.37
0065	PC	233	2946	3303	3122	0.37
0065	PC	234	2972	3333	3149	0.37

Core	Core type	Depth (cm)	min95%	max95%	age (yr BP)	sed rate (mm/year)
0065	PC	235	2996	3364	3177	0.37
0065	PC	236	3019	3395	3204	0.37
0065	PC	237	3043	3427	3231	0.37
0065	PC	238	3066	3459	3259	0.37
0065	PC	239	3088	3491	3286	0.37
0065	PC	240	3111	3523	3313	0.37
0065	PC	241	3134	3556	3341	0.37
0065	PC	242	3156	3590	3368	0.37
0065	PC	243	3176	3624	3395	0.37
0065	PC	244	3198	3658	3423	0.37
0065	PC	245	3220	3693	3450	0.37
0065	PC	246	3241	3726	3477	0.37
0065	PC	247	3261	3761	3505	0.37
0065	PC	248	3282	3795	3532	0.78
0065	PC	249	3295	3807	3545	0.78
0065	PC	250	3309	3819	3557	0.78
0065	PC	251	3322	3832	3570	0.78
0065	PC	252	3336	3844	3583	0.78
0065	PC	253	3349	3856	3596	0.78
0065	PC	254	3363	3868	3609	0.78
0065	PC	255	3376	3881	3621	7.04
0065	PC	264	3389	3893	3634	0.78
0065	PC	265	3402	3906	3647	0.78
0065	PC	266	3416	3918	3660	0.78
0065	PC	267	3429	3930	3673	0.78
0065	PC	268	3442	3942	3685	0.78
0065	PC	269	3455	3955	3698	0.78
0065	PC	270	3468	3967	3711	0.78
0065	PC	271	3481	3980	3724	0.78
0065	PC	272	3495	3992	3736	0.78
0065	PC	273	3507	4004	3749	0.78
0065	PC	274	3520	4016	3762	0.78
0065	PC	275	3533	4028	3775	0.78
0065	PC	276	3547	4040	3788	0.78
0065	PC	277	3561	4052	3800	0.78
0065	PC	278	3574	4064	3813	0.78
0065	PC	279	3587	4076	3826	0.78
0065	PC	280	3600	4089	3839	0.78
0065	PC	281	3613	4101	3852	0.78
0065	PC	282	3627	4113	3864	0.78
0065	PC	283	3640	4126	3877	0.78
0065	PC	284	3653	4138	3890	0.78

Core	Core type	Depth (cm)	min95%	max95%	age (yr BP)	sed rate (mm/year)
0065	PC	285	3667	4150	3903	0.78
0065	PC	286	3680	4162	3916	0.78
0065	PC	287	3693	4174	3928	0.78
0065	PC	288	3707	4187	3941	0.78
0065	PC	289	3720	4199	3954	0.78
0065	PC	290	3733	4211	3967	0.78
0065	PC	291	3746	4223	3979	0.78
0065	PC	292	3759	4235	3992	0.78
0065	PC	293	3773	4247	4005	0.78
0065	PC	294	3786	4260	4018	0.78
0065	PC	295	3799	4272	4031	0.78
0065	PC	296	3812	4284	4043	0.78
0065	PC	297	3826	4297	4056	0.78
0065	PC	298	3839	4309	4069	0.78
0065	PC	299	3852	4321	4082	0.78
0065	PC	300	3866	4333	4095	0.78
0065	PC	301	3879	4346	4107	0.78
0065	PC	302	3892	4358	4120	0.78
0065	PC	303	3905	4370	4133	0.78
0065	PC	304	3918	4383	4146	0.78
0065	PC	305	3932	4395	4158	0.78
0065	PC	306	3945	4407	4171	0.78
0065	PC	307	3958	4420	4184	0.78
0065	PC	308	3972	4432	4197	0.78
0065	PC	309	3985	4444	4210	0.78
0065	PC	310	3999	4457	4222	0.78
0065	PC	311	4012	4469	4235	0.78
0065	PC	312	4025	4482	4248	0.78
0065	PC	313	4038	4494	4261	0.78
0065	PC	314	4052	4506	4274	0.78
0065	PC	315	4065	4519	4286	0.78
0065	PC	316	4078	4531	4299	0.78
0065	PC	317	4092	4543	4312	0.78
0065	PC	318	4105	4556	4325	0.78
0065	PC	319	4118	4568	4338	0.78
0065	PC	320	4131	4580	4350	0.78
0065	PC	321	4145	4592	4363	0.78
0065	PC	322	4158	4604	4376	0.78
0065	PC	323	4172	4616	4389	0.78
0065	PC	324	4185	4629	4401	0.78
0065	PC	325	4198	4641	4414	0.78
0065	PC	326	4211	4654	4427	0.78

Core	Core type	Depth (cm)	min95%	max95%	age (yr BP)	sed rate (mm/year)
0065	PC	327	4225	4666	4440	0.78
0065	PC	328	4238	4679	4453	0.78
0065	PC	329	4251	4691	4465	0.78
0065	PC	330	4265	4704	4478	0.78
0065	PC	331	4278	4716	4491	0.78
0065	PC	332	4291	4729	4504	0.78
0065	PC	333	4304	4741	4517	0.78
0065	PC	334	4318	4754	4529	0.78
0065	PC	335	4331	4766	4542	0.78
0065	PC	336	4344	4778	4555	0.78
0065	PC	337	4357	4791	4568	0.78
0065	PC	338	4371	4803	4581	0.78
0065	PC	339	4384	4815	4593	0.78
0065	PC	340	4397	4828	4606	0.78
0065	PC	341	4411	4840	4619	0.78
0065	PC	342	4424	4852	4632	0.78
0065	PC	343	4437	4864	4644	0.78
0065	PC	344	4450	4877	4657	0.78
0065	PC	345	4463	4889	4670	0.78
0065	PC	346	4476	4902	4683	0.78
0065	PC	347	4489	4915	4696	0.78
0065	PC	348	4502	4927	4708	0.78
0065	PC	349	4515	4939	4721	0.78
0065	PC	350	4528	4952	4734	0.78
0065	PC	351	4541	4965	4747	0.78
0065	PC	352	4555	4977	4760	0.78
0065	PC	353	4568	4990	4772	0.78
0065	PC	354	4581	5003	4785	0.78
0065	PC	355	4594	5015	4798	0.78
0065	PC	356	4607	5028	4811	0.78
0065	PC	357	4620	5040	4824	0.78
0065	PC	358	4632	5052	4836	0.78
0065	PC	359	4645	5065	4849	0.78
0065	PC	360	4658	5077	4862	0.78
0065	PC	361	4671	5089	4875	0.78
0065	PC	362	4684	5102	4887	0.78
0065	PC	363	4698	5114	4900	0.78
0065	PC	364	4711	5127	4913	0.78
0065	PC	365	4724	5139	4926	0.78
0065	PC	366	4737	5152	4939	0.78
0065	PC	367	4749	5164	4951	0.78
0065	PC	368	4762	5176	4964	0.78

Core	Core type	Depth (cm)	min95%	max95%	age (yr BP)	sed rate (mm/year)
0065	PC	369	4775	5189	4977	0.78
0065	PC	370	4789	5202	4990	0.78
0065	PC	371	4802	5214	5003	0.78
0065	PC	372	4814	5227	5015	0.78
0065	PC	373	4827	5239	5028	0.78
0065	PC	374	4840	5251	5041	0.78
0065	PC	375	4853	5264	5054	0.78
0065	PC	376	4866	5276	5066	0.78
0065	PC	377	4879	5288	5079	0.78
0065	PC	378	4892	5301	5092	0.78
0065	PC	379	4906	5314	5105	0.78
0065	PC	380	4918	5326	5118	0.78
0065	PC	381	4931	5339	5130	0.78
0065	PC	382	4944	5351	5143	0.78
0065	PC	383	4958	5364	5156	0.78
0065	PC	384	4971	5376	5169	0.78
0065	PC	385	4984	5389	5182	0.78
0065	PC	386	4997	5402	5194	0.78
0065	PC	387	5010	5414	5207	0.78
0065	PC	388	5022	5427	5220	0.78
0065	PC	389	5035	5439	5233	0.78
0065	PC	390	5048	5452	5246	0.78
0065	PC	391	5061	5465	5258	0.78
0065	PC	392	5074	5477	5271	0.78
0065	PC	393	5086	5490	5284	0.78
0065	PC	394	5100	5502	5297	0.78
0065	PC	395	5113	5515	5309	0.78
0065	PC	396	5126	5527	5322	0.78
0065	PC	397	5139	5540	5335	0.78
0065	PC	398	5152	5552	5348	0.78
0065	PC	399	5165	5564	5361	0.78
0065	PC	400	5178	5577	5373	0.78
0065	PC	401	5190	5590	5386	0.78
0065	PC	402	5203	5602	5399	0.78
0065	PC	403	5216	5615	5412	0.78
0065	PC	404	5229	5627	5425	0.78
0065	PC	405	5242	5640	5437	0.78
0065	PC	406	5255	5653	5450	0.78
0065	PC	407	5268	5665	5463	0.78
0065	PC	408	5281	5677	5476	0.78
0065	PC	409	5294	5690	5489	0.78
0065	PC	410	5307	5702	5501	0.78

Core	Core type	Depth (cm)	min95%	max95%	age (yr BP)	sed rate (mm/year)
0065	PC	411	5320	5715	5514	0.78
0065	PC	412	5333	5728	5527	0.78
0065	PC	413	5346	5740	5540	0.78
0065	PC	414	5359	5753	5552	0.78
0065	PC	415	5372	5765	5565	0.78
0065	PC	416	5385	5778	5578	0.78
0065	PC	417	5398	5790	5591	0.78
0065	PC	418	5411	5803	5604	0.78
0065	PC	419	5424	5815	5616	0.78
0065	PC	420	5437	5828	5629	0.78
0065	PC	421	5450	5840	5642	0.78
0065	PC	422	5463	5853	5655	0.78
0065	PC	423	5476	5865	5668	0.78
0065	PC	424	5489	5878	5680	0.78
0065	PC	425	5502	5890	5693	0.78
0065	PC	426	5515	5903	5706	0.78
0065	PC	427	5527	5916	5719	0.78
0065	PC	428	5540	5928	5732	0.78
0065	PC	429	5553	5941	5744	0.78
0065	PC	430	5565	5953	5757	0.78
0065	PC	431	5578	5966	5770	0.78
0065	PC	432	5591	5978	5783	0.78
0065	PC	433	5604	5991	5795	0.78
0065	PC	434	5617	6004	5808	0.78
0065	PC	435	5630	6016	5821	0.78
0065	PC	436	5643	6029	5834	0.78
0065	PC	437	5656	6042	5847	0.78
0065	PC	438	5669	6054	5859	0.78
0065	PC	439	5681	6067	5872	0.78
0065	PC	440	5694	6079	5885	0.78
0065	PC	441	5707	6092	5898	0.78
0065	PC	442	5720	6104	5911	0.78
0065	PC	443	5733	6117	5923	0.78
0065	PC	444	5745	6129	5936	0.78
0065	PC	445	5758	6142	5949	0.78
0065	PC	446	5771	6155	5962	0.78
0065	PC	447	5783	6167	5974	0.78
0065	PC	448	5796	6180	5987	0.78
0065	PC	449	5809	6192	6000	0.78
0065	PC	450	5822	6205	6013	0.78
0065	PC	451	5834	6217	6026	0.78
0065	PC	452	5848	6229	6038	0.78

Core	Core type	Depth (cm)	min95%	max95%	age (yr BP)	sed rate (mm/year)
0065	PC	453	5861	6242	6051	0.78
0065	PC	454	5873	6255	6064	0.78
0065	PC	455	5886	6267	6077	0.78
0065	PC	456	5899	6280	6090	0.78
0065	PC	457	5911	6292	6102	0.78
0065	PC	458	5924	6305	6115	0.78
0065	PC	459	5936	6318	6128	0.78
0065	PC	460	5949	6330	6141	0.78
0065	PC	461	5962	6343	6154	0.78
0065	PC	462	5975	6356	6166	0.78
0065	PC	463	5988	6369	6179	0.78
0065	PC	464	6000	6381	6192	0.78
0065	PC	465	6013	6394	6205	0.78
0065	PC	466	6026	6406	6217	0.78
0065	PC	467	6039	6419	6230	0.78
0065	PC	468	6052	6431	6243	0.78
0065	PC	469	6064	6444	6256	0.78
0065	PC	470	6078	6457	6269	0.78
0065	PC	471	6090	6470	6281	0.78
0065	PC	472	6103	6483	6294	0.78
0065	PC	473	6116	6495	6307	0.78
0065	PC	474	6129	6508	6320	0.78
0065	PC	475	6141	6521	6333	0.78
0065	PC	476	6154	6534	6345	0.78
0065	PC	477	6167	6547	6358	0.78
0065	PC	478	6180	6559	6371	0.78
0065	PC	479	6193	6572	6384	0.78
0065	PC	480	6205	6585	6397	0.78
0065	PC	481	6218	6597	6409	0.78
0065	PC	482	6231	6610	6422	0.78
0065	PC	483	6244	6623	6435	0.78
0065	PC	484	6256	6636	6448	0.78
0065	PC	485	6269	6648	6460	0.78
0065	PC	486	6282	6662	6473	0.78
0065	PC	487	6294	6675	6486	0.78
0065	PC	488	6307	6687	6499	0.78
0065	PC	489	6320	6700	6512	0.78
0065	PC	490	6333	6713	6524	0.78
0065	PC	491	6345	6725	6537	0.78
0065	PC	492	6358	6738	6550	0.78
0065	PC	493	6370	6751	6563	0.78
0065	PC	494	6383	6763	6576	0.78

Core	Core type	Depth (cm)	min95%	max95%	age (yr BP)	sed rate (mm/year)
0065	PC	495	6395	6776	6588	0.78
0065	PC	496	6408	6789	6601	0.78
0065	PC	497	6421	6801	6614	0.78
0065	PC	498	6434	6814	6627	0.78
0065	PC	499	6446	6827	6640	0.78
0065	PC	500	6459	6840	6652	0.78
0065	PC	501	6471	6853	6665	0.78
0065	PC	502	6484	6866	6678	0.78
0065	PC	503	6497	6879	6691	0.78
0065	PC	504	6509	6891	6703	0.78
0065	PC	505	6522	6904	6716	0.78
0065	PC	506	6534	6917	6729	0.78
0065	PC	507	6547	6930	6742	0.78
0065	PC	508	6559	6942	6755	0.78
0065	PC	509	6572	6956	6767	0.78
0065	PC	510	6585	6968	6780	0.78
0065	PC	511	6597	6981	6793	0.78
0065	PC	512	6610	6994	6806	0.78
0065	PC	513	6622	7007	6819	0.78
0065	PC	514	6635	7020	6831	0.78
0065	PC	515	6647	7033	6844	0.78
0065	PC	516	6660	7045	6857	0.78
0065	PC	517	6672	7058	6870	0.78
0065	PC	518	6685	7071	6883	0.78
0065	PC	519	6698	7084	6895	0.78
0065	PC	520	6710	7097	6908	0.78
0065	PC	521	6722	7109	6921	0.78
0065	PC	522	6735	7123	6934	0.78
0065	PC	523	6747	7135	6946	0.78
0065	PC	524	6760	7148	6959	0.78
0065	PC	525	6772	7161	6972	0.78
0065	PC	526	6785	7174	6985	0.78
0065	PC	527	6797	7186	6998	0.78
0065	PC	528	6810	7199	7010	0.78
0065	PC	529	6822	7212	7023	0.78
0065	PC	530	6835	7225	7036	0.78
0065	PC	531	6847	7237	7049	0.78
0065	PC	532	6860	7250	7062	0.78
0065	PC	533	6873	7263	7074	0.78
0065	PC	534	6885	7275	7087	0.78
0065	PC	535	6898	7288	7100	0.78
0065	PC	536	6911	7300	7113	0.78

Core	Core type	Depth (cm)	min95%	max95%	age (yr BP)	sed rate (mm/year)
0065	PC	537	6923	7313	7125	0.78
0065	PC	538	6937	7326	7138	0.78
0065	PC	539	6949	7339	7151	0.78
0065	PC	540	6961	7352	7164	0.78
0065	PC	541	6974	7365	7177	0.78
0065	PC	542	6986	7378	7189	0.78
0065	PC	543	6999	7391	7202	0.78
0065	PC	544	7011	7403	7215	0.78
0065	PC	545	7024	7416	7228	0.78
0065	PC	546	7036	7429	7241	0.78
0065	PC	547	7048	7442	7253	0.78
0065	PC	548	7061	7455	7266	0.78
0065	PC	549	7073	7468	7279	0.78
0065	PC	550	7086	7481	7292	0.78
0065	PC	551	7098	7493	7305	0.78
0065	PC	552	7110	7506	7317	0.78
0065	PC	553	7123	7519	7330	0.78
0065	PC	554	7135	7531	7343	0.78
0065	PC	555	7148	7544	7356	0.78
0065	PC	556	7160	7557	7368	0.78
0065	PC	557	7173	7570	7381	0.78
0065	PC	558	7185	7583	7394	0.78
0065	PC	559	7197	7595	7407	0.78
0065	PC	560	7209	7608	7420	0.78
0065	PC	561	7222	7621	7432	0.78
0065	PC	562	7234	7634	7445	0.78
0065	PC	563	7247	7647	7458	0.78
0065	PC	564	7259	7660	7471	0.78
0065	PC	565	7272	7673	7484	0.78
0065	PC	566	7284	7686	7496	0.78
0065	PC	567	7296	7699	7509	0.78
0065	PC	568	7309	7712	7522	0.78
0065	PC	569	7321	7725	7535	0.78
0065	PC	570	7333	7738	7548	0.78
0065	PC	571	7345	7751	7560	0.78
0065	PC	572	7358	7764	7573	0.78
0065	PC	573	7370	7777	7586	0.78
0065	PC	574	7383	7790	7599	0.78
0065	PC	575	7395	7803	7611	0.78
0065	PC	576	7407	7815	7624	0.78
0065	PC	577	7420	7828	7637	0.78
0065	PC	578	7432	7841	7650	0.78

Core	Core type	Depth (cm)	min95%	max95%	age (yr BP)	sed rate (mm/year)
0065	PC	579	7445	7854	7663	0.78
0065	PC	580	7458	7867	7675	0.78
0065	PC	581	7470	7880	7688	0.78
0065	PC	582	7482	7893	7701	0.78
0065	PC	583	7495	7906	7714	0.78
0065	PC	584	7507	7919	7727	0.78
0065	PC	585	7519	7933	7739	0.78
0065	PC	586	7532	7945	7752	0.78
0065	PC	587	7544	7959	7765	0.78
0065	PC	588	7556	7972	7778	0.78
0065	PC	589	7568	7985	7791	0.78
0065	PC	590	7580	7998	7803	0.78
0065	PC	591	7593	8011	7816	0.78
0065	PC	592	7606	8024	7829	0.78
0065	PC	593	7618	8037	7842	0.78
0065	PC	594	7630	8050	7854	0.78
0065	PC	595	7642	8063	7867	0.78
0065	PC	596	7655	8076	7880	0.78
0065	PC	597	7667	8089	7893	0.78
0065	PC	598	7680	8102	7906	0.78
0065	PC	599	7692	8115	7918	0.78
0065	PC	600	7704	8128	7931	0.78
0065	PC	601	7716	8142	7944	0.78
0065	PC	602	7729	8155	7957	0.78
0065	PC	603	7741	8168	7970	0.78
0065	PC	604	7754	8181	7982	0.78
0065	PC	605	7766	8194	7995	0.78
0065	PC	606	7779	8207	8008	0.78
0065	PC	607	7791	8220	8021	0.78
0065	PC	608	7803	8233	8033	0.78
0065	PC	609	7815	8246	8046	0.78
0065	PC	610	7828	8258	8059	0.78
0065	PC	611	7840	8271	8072	0.78
0065	PC	612	7852	8284	8085	0.78
0065	PC	613	7864	8297	8097	0.78
0065	PC	614	7877	8311	8110	0.78
0065	PC	615	7889	8324	8123	0.78
0065	PC	616	7901	8336	8136	0.78
0065	PC	617	7914	8349	8149	0.78
0065	PC	618	7926	8362	8161	0.78
0065	PC	619	7938	8375	8174	0.78
0065	PC	620	7950	8388	8187	0.78

Core	Core type	Depth (cm)	min95%	max95%	age (yr BP)	sed rate (mm/year)
0065	PC	621	7963	8401	8200	0.78
0065	PC	622	7975	8414	8213	0.78
0065	PC	623	7987	8427	8225	0.78
0065	PC	624	8000	8440	8238	0.78
0065	PC	625	8012	8453	8251	0.78
0065	PC	626	8024	8466	8264	0.78
0065	PC	627	8036	8479	8276	0.78
0065	PC	628	8049	8492	8289	0.78
0065	PC	629	8061	8505	8302	0.78
0065	PC	630	8074	8518	8315	0.78
0065	PC	631	8086	8530	8328	0.78
0065	PC	632	8099	8543	8340	0.78
0065	PC	633	8111	8556	8353	0.78
0065	PC	634	8123	8569	8366	0.78
0065	PC	635	8136	8582	8379	0.78
0065	PC	636	8148	8595	8392	0.78
0065	PC	637	8160	8608	8404	0.78
0065	PC	638	8173	8621	8417	0.78
0065	PC	639	8185	8634	8430	0.78
0065	PC	640	8197	8647	8443	0.78
0065	PC	641	8209	8659	8456	0.78
0065	PC	642	8221	8672	8468	0.78
0065	PC	643	8234	8685	8481	0.78
0065	PC	644	8246	8698	8494	0.78
0065	PC	645	8258	8711	8507	0.78
0065	PC	646	8271	8725	8519	0.78
0065	PC	647	8283	8738	8532	0.78
0065	PC	648	8295	8751	8545	0.78
0065	PC	649	8307	8764	8558	0.78
0065	PC	650	8320	8777	8571	0.78
0065	PC	651	8333	8790	8583	0.78
0065	PC	652	8345	8803	8596	0.78
0065	PC	653	8357	8816	8609	0.78
0065	PC	654	8369	8829	8622	0.78
0065	PC	655	8381	8842	8635	0.78
0065	PC	656	8394	8856	8647	0.78
0065	PC	657	8406	8869	8660	0.78
0065	PC	658	8418	8882	8673	0.78
0065	PC	659	8430	8895	8686	0.78
0065	PC	660	8442	8908	8699	0.78
0065	PC	661	8455	8921	8711	0.78
0065	PC	662	8467	8934	8724	0.78

Core	Core type	Depth (cm)	min95%	max95%	age (yr BP)	sed rate (mm/year)
0065	PC	663	8479	8947	8737	0.78
0065	PC	664	8492	8961	8750	0.78
0065	PC	665	8504	8974	8762	0.78
0065	PC	666	8516	8987	8775	0.78
0065	PC	667	8529	9000	8788	0.78
0065	PC	668	8541	9013	8801	0.78
0065	PC	669	8553	9026	8814	0.78
0065	PC	670	8565	9039	8826	0.78
0065	PC	671	8577	9052	8839	0.78
0065	PC	672	8590	9065	8852	0.78
0065	PC	673	8602	9078	8865	0.78
0065	PC	674	8614	9091	8878	0.78
0065	PC	675	8626	9104	8890	0.78
0065	PC	676	8638	9117	8903	0.78
0065	PC	677	8651	9130	8916	0.78
0065	PC	678	8663	9142	8929	0.78
0065	PC	679	8675	9156	8941	0.78
0065	PC	680	8687	9168	8954	0.78
0065	PC	681	8699	9181	8967	0.78
0065	PC	682	8712	9194	8980	0.78
0065	PC	683	8724	9207	8993	0.78
0065	PC	684	8737	9220	9005	0.78
0065	PC	685	8749	9234	9018	0.78
0065	PC	686	8761	9247	9031	0.78
0065	PC	687	8774	9260	9044	0.78
0065	PC	688	8786	9273	9057	0.78
0065	PC	689	8798	9286	9069	0.78
0065	PC	690	8810	9300	9082	0.78
0065	PC	691	8823	9313	9095	0.78
0065	PC	692	8834	9326	9108	0.78
0065	PC	693	8846	9339	9121	0.78
0065	PC	694	8858	9353	9133	0.78
0065	PC	695	8870	9366	9146	0.78
0065	PC	696	8882	9379	9159	0.78
0065	PC	697	8894	9392	9172	0.78
0065	PC	698	8906	9405	9184	0.78
0065	PC	699	8918	9419	9197	0.78
0065	PC	700	8930	9432	9210	0.78
0065	PC	701	8943	9446	9223	0.78
0065	PC	702	8955	9459	9236	0.78
0065	PC	703	8967	9472	9248	0.78
0065	PC	704	8979	9485	9261	0.78

Core	Core type	Depth (cm)	min95%	max95%	age (yr BP)	sed rate (mm/year)
0065	PC	705	8991	9498	9274	0.78
0065	PC	706	9004	9512	9287	0.78
0065	PC	707	9016	9525	9300	0.78
0065	PC	708	9028	9538	9312	0.78
0065	PC	709	9040	9551	9325	0.78
0065	PC	710	9053	9564	9338	0.78
0065	PC	711	9065	9577	9351	0.78
0065	PC	712	9077	9591	9364	0.78
0065	PC	713	9090	9604	9376	0.78
0065	PC	714	9102	9617	9389	0.78
0065	PC	715	9114	9630	9402	0.78
0065	PC	716	9126	9644	9415	0.78
0065	PC	717	9138	9657	9427	0.78
0065	PC	718	9150	9670	9440	0.78
0065	PC	719	9162	9684	9453	0.78
0065	PC	720	9174	9697	9466	0.78
0065	PC	721	9186	9710	9479	0.78
0065	PC	722	9199	9723	9491	0.78
0065	PC	723	9211	9737	9504	0.78
0065	PC	724	9223	9750	9517	0.78
0065	PC	725	9235	9763	9530	0.78
0065	PC	726	9248	9777	9543	0.78
0065	PC	727	9260	9790	9555	0.78
0065	PC	728	9272	9803	9568	0.78
0065	PC	729	9285	9816	9581	0.78
0065	PC	730	9297	9830	9594	0.78
0065	PC	731	9309	9843	9607	0.78
0065	PC	732	9321	9856	9619	0.78
0065	PC	733	9333	9870	9632	0.78
0065	PC	734	9345	9883	9645	0.78
0065	PC	735	9358	9896	9658	0.78
0065	PC	736	9370	9910	9670	0.78
0065	PC	737	9382	9923	9683	0.78
0065	PC	738	9394	9937	9696	0.78
0065	PC	739	9407	9950	9709	0.78
0065	PC	740	9419	9963	9722	0.78
0065	PC	741	9431	9976	9734	0.78
0065	PC	742	9443	9989	9747	0.78
0065	PC	743	9456	10003	9760	0.78
0065	PC	744	9468	10016	9773	0.78
0065	PC	745	9480	10029	9786	0.78
0065	PC	746	9492	10043	9798	0.78

Core	Core type	Depth (cm)	min95%	max95%	age (yr BP)	sed rate (mm/year)
0065	PC	747	9505	10056	9811	0.78
0065	PC	748	9517	10070	9824	0.78
0065	PC	749	9529	10083	9837	0.78
0065	PC	750	9541	10097	9849	3.91
0065	PC	755	9553	10110	9862	0.78
0065	PC	756	9566	10123	9875	0.78
0065	PC	757	9578	10137	9888	0.78
0065	PC	758	9590	10150	9901	0.78
0065	PC	759	9602	10163	9913	0.78
0065	PC	760	9614	10177	9926	0.78
0065	PC	761	9627	10190	9939	0.78
0065	PC	762	9639	10203	9952	0.78
0065	PC	763	9651	10217	9965	0.78
0065	PC	764	9663	10230	9977	0.78
0065	PC	765	9676	10243	9990	0.78
0065	PC	766	9688	10256	10003	0.78

Core 0066 age model results

Core	Core type	Depth (cm)	min95%	max95%	age (yr BP)	sed rate (mm/year)
0066	TWC	-53	-65	-61	-63	0.69
0066	TWC	-52	-52	-44	-48	0.69
0066	TWC	-51	-41	-26	-34	0.69
0066	TWC	-50	-29	-8	-19	0.69
0066	TWC	-49	-18	10	-5	0.69
0066	TWC	-48	-6	28	10	0.69
0066	TWC	-47	5	46	24	0.69
0066	TWC	-46	16	64	39	0.69
0066	TWC	-45	28	82	53	0.69
0066	TWC	-44	39	101	68	0.69
0066	TWC	-43	51	119	83	0.69
0066	TWC	-42	62	137	97	0.69
0066	TWC	-41	73	155	112	0.69
0066	TWC	-40	85	173	126	0.69
0066	TWC	-39	96	191	141	0.69
0066	TWC	-38	107	210	155	0.69
0066	TWC	-37	119	228	170	0.69
0066	TWC	-36	130	246	184	0.69
0066	TWC	-35	141	264	199	0.69
0066	TWC	-34	153	282	214	0.69
0066	TWC	-33	164	300	228	0.69
0066	TWC	-32	176	319	243	0.69
0066	TWC	-31	187	337	257	0.69
0066	TWC	-30	198	355	272	0.69
0066	TWC	-29	210	373	286	0.69
0066	TWC	-28	221	391	301	0.69
0066	TWC	-27	232	409	315	0.69
0066	TWC	-26	244	428	330	0.69
0066	TWC	-25	255	446	345	0.69
0066	TWC	-24	266	464	359	0.69
0066	TWC	-23	278	482	374	0.69
0066	TWC	-22	289	500	388	0.69
0066	TWC	-21	300	518	403	0.69
0066	TWC	-20	312	536	417	0.69
0066	TWC	-19	323	555	432	0.69
0066	TWC	-18	335	573	446	0.69
0066	TWC	-17	346	591	461	0.69
0066	TWC	-16	357	609	476	0.69
0066	TWC	-15	369	627	490	0.69
0066	TWC	-14	380	646	505	0.69

Core	Core type	Depth (cm)	min95%	max95%	age (yr BP)	sed rate (mm/year)
0066	TWC	-13	392	664	519	0.69
0066	TWC	-12	403	682	534	0.69
0066	TWC	-11	414	700	548	0.69
0066	TWC	-10	426	718	563	0.69
0066	TWC	-9	437	737	577	0.69
0066	TWC	-8	448	755	592	0.69
0066	TWC	-7	460	773	606	0.69
0066	TWC	-6	471	791	621	0.69
0066	TWC	-5	482	809	636	0.69
0066	TWC	-4	494	827	650	0.69
0066	TWC	-3	505	845	665	0.69
0066	TWC	-2	517	864	679	0.69
0066	TWC	-1	528	882	694	0.69
0066	TWC	0	539	900	708	0.69
0066	PC	1	551	918	723	0.69
0066	PC	2	562	936	737	0.69
0066	PC	3	573	954	752	0.69
0066	PC	4	585	973	767	0.69
0066	PC	5	596	991	781	0.69
0066	PC	6	607	1009	796	0.69
0066	PC	7	619	1027	810	0.69
0066	PC	8	630	1045	825	0.69
0066	PC	9	641	1063	839	0.69
0066	PC	10	653	1081	854	0.69
0066	PC	11	664	1100	868	0.69
0066	PC	12	675	1118	883	0.69
0066	PC	13	687	1136	898	0.69
0066	PC	14	698	1154	912	0.38
0066	PC	15	726	1179	939	0.38
0066	PC	16	755	1202	965	0.38
0066	PC	17	783	1226	991	0.38
0066	PC	18	811	1250	1018	0.38
0066	PC	19	839	1275	1044	0.38
0066	PC	20	868	1299	1071	0.38
0066	PC	21	896	1322	1097	1.52
0066	PC	25	925	1346	1123	0.38
0066	PC	26	953	1371	1150	0.38
0066	PC	27	981	1394	1176	0.38
0066	PC	28	1008	1420	1203	0.38
0066	PC	29	1036	1444	1229	0.38
0066	PC	30	1065	1468	1256	0.38
0066	PC	31	1093	1493	1282	0.38

Core	Core type	Depth (cm)	min95%	max95%	age (yr BP)	sed rate (mm/year)
0066	PC	32	1121	1518	1308	0.38
0066	PC	33	1150	1542	1335	0.38
0066	PC	34	1178	1567	1361	0.38
0066	PC	35	1205	1591	1388	0.38
0066	PC	36	1233	1615	1414	0.38
0066	PC	37	1261	1640	1440	0.38
0066	PC	38	1288	1666	1467	0.38
0066	PC	39	1315	1691	1493	0.38
0066	PC	40	1342	1716	1520	0.38
0066	PC	41	1370	1740	1546	0.38
0066	PC	42	1398	1765	1572	0.38
0066	PC	43	1425	1790	1599	0.38
0066	PC	44	1452	1816	1625	0.38
0066	PC	45	1479	1840	1652	0.38
0066	PC	46	1506	1865	1678	0.38
0066	PC	47	1533	1890	1705	0.38
0066	PC	48	1561	1916	1731	0.38
0066	PC	49	1588	1941	1757	0.38
0066	PC	50	1615	1966	1784	0.38
0066	PC	51	1642	1992	1810	0.38
0066	PC	52	1669	2018	1837	0.38
0066	PC	53	1696	2044	1863	0.38
0066	PC	54	1723	2070	1889	0.38
0066	PC	55	1750	2096	1916	0.38
0066	PC	56	1777	2121	1942	0.38
0066	PC	57	1803	2146	1969	0.38
0066	PC	58	1829	2172	1995	0.38
0066	PC	59	1856	2199	2022	0.38
0066	PC	60	1882	2225	2048	0.38
0066	PC	61	1909	2251	2074	0.38
0066	PC	62	1935	2277	2101	0.38
0066	PC	63	1962	2303	2127	0.38
0066	PC	64	1989	2329	2154	0.38
0066	PC	65	2015	2356	2180	0.38
0066	PC	66	2042	2383	2206	0.38
0066	PC	67	2068	2410	2233	0.38
0066	PC	68	2094	2437	2259	0.38
0066	PC	69	2120	2464	2286	0.38
0066	PC	70	2146	2491	2312	0.38
0066	PC	71	2172	2518	2338	0.38
0066	PC	72	2198	2545	2365	0.38
0066	PC	73	2224	2572	2391	0.38

Core	Core type	Depth (cm)	min95%	max95%	age (yr BP)	sed rate (mm/year)
0066	PC	74	2250	2598	2418	0.38
0066	PC	75	2275	2625	2444	0.38
0066	PC	76	2301	2653	2471	0.38
0066	PC	77	2327	2679	2497	0.38
0066	PC	78	2352	2707	2523	0.38
0066	PC	79	2377	2734	2550	0.38
0066	PC	80	2403	2761	2576	0.38
0066	PC	81	2428	2789	2603	0.38
0066	PC	82	2453	2816	2629	0.38
0066	PC	83	2478	2844	2655	0.38
0066	PC	84	2503	2872	2682	0.38
0066	PC	85	2529	2900	2708	0.38
0066	PC	86	2555	2928	2735	0.38
0066	PC	87	2580	2957	2761	0.38
0066	PC	88	2604	2984	2788	0.38
0066	PC	89	2629	3011	2814	0.38
0066	PC	90	2655	3039	2840	0.38
0066	PC	91	2679	3066	2867	0.38
0066	PC	92	2704	3095	2893	0.38
0066	PC	93	2728	3123	2920	0.38
0066	PC	94	2753	3151	2946	0.38
0066	PC	95	2778	3179	2972	0.38
0066	PC	96	2803	3207	2999	0.38
0066	PC	97	2828	3236	3025	0.38
0066	PC	98	2854	3264	3052	0.38
0066	PC	99	2878	3292	3078	0.38
0066	PC	100	2904	3320	3105	0.38
0066	PC	101	2929	3348	3131	0.38
0066	PC	102	2954	3376	3157	0.38
0066	PC	103	2978	3404	3184	0.38
0066	PC	104	3002	3434	3210	1.52
0066	PC	108	3027	3463	3237	0.38
0066	PC	109	3051	3492	3263	0.38
0066	PC	110	3075	3520	3289	0.38
0066	PC	111	3099	3550	3316	0.38
0066	PC	112	3123	3579	3342	0.38
0066	PC	113	3148	3608	3369	0.38
0066	PC	114	3173	3637	3395	0.38
0066	PC	115	3196	3665	3421	0.38
0066	PC	116	3221	3694	3448	0.38
0066	PC	117	3245	3723	3474	0.38
0066	PC	118	3269	3752	3501	0.38

Core	Core type	Depth (cm)	min95%	max95%	age (yr BP)	sed rate (mm/year)
0066	PC	119	3294	3780	3527	0.38
0066	PC	120	3318	3809	3554	0.38
0066	PC	121	3342	3837	3580	0.38
0066	PC	122	3366	3866	3606	0.38
0066	PC	123	3390	3895	3633	0.38
0066	PC	124	3413	3923	3659	0.38
0066	PC	125	3437	3952	3686	0.67
0066	PC	126	3453	3967	3700	0.67
0066	PC	127	3468	3981	3715	0.67
0066	PC	128	3484	3995	3730	0.67
0066	PC	129	3500	4010	3745	0.67
0066	PC	130	3515	4024	3760	0.67
0066	PC	131	3530	4038	3775	0.67
0066	PC	132	3545	4053	3790	5.38
0066	PC	140	3561	4067	3805	0.67
0066	PC	141	3576	4082	3819	0.67
0066	PC	142	3591	4095	3834	0.67
0066	PC	143	3607	4110	3849	0.67
0066	PC	144	3622	4124	3864	0.67
0066	PC	145	3638	4138	3879	0.67
0066	PC	146	3654	4152	3894	0.67
0066	PC	147	3669	4166	3909	0.67
0066	PC	148	3685	4180	3923	0.67
0066	PC	149	3700	4195	3938	0.67
0066	PC	150	3716	4209	3953	0.67
0066	PC	151	3731	4223	3968	0.67
0066	PC	152	3747	4237	3983	0.67
0066	PC	153	3763	4251	3998	0.67
0066	PC	154	3778	4265	4013	0.67
0066	PC	155	3793	4279	4027	0.67
0066	PC	156	3809	4292	4042	0.67
0066	PC	157	3824	4306	4057	0.67
0066	PC	158	3840	4320	4072	0.67
0066	PC	159	3855	4335	4087	0.67
0066	PC	160	3870	4348	4102	0.67
0066	PC	161	3886	4363	4117	0.67
0066	PC	162	3901	4378	4131	0.67
0066	PC	163	3916	4392	4146	0.67
0066	PC	164	3932	4406	4161	0.67
0066	PC	165	3947	4420	4176	0.67
0066	PC	166	3963	4434	4191	0.67
0066	PC	167	3979	4448	4206	0.67

Core	Core type	Depth (cm)	min95%	max95%	age (yr BP)	sed rate (mm/year)
0066	PC	168	3994	4462	4221	0.67
0066	PC	169	4010	4476	4236	0.67
0066	PC	170	4025	4490	4250	0.67
0066	PC	171	4040	4504	4265	0.67
0066	PC	172	4056	4518	4280	0.67
0066	PC	173	4071	4532	4295	0.67
0066	PC	174	4087	4546	4310	0.67
0066	PC	175	4103	4561	4325	0.67
0066	PC	176	4118	4575	4340	0.67
0066	PC	177	4134	4589	4354	0.67
0066	PC	178	4150	4604	4369	0.67
0066	PC	179	4165	4618	4384	0.67
0066	PC	180	4180	4632	4399	0.67
0066	PC	181	4196	4646	4414	0.67
0066	PC	182	4212	4660	4429	0.67
0066	PC	183	4227	4674	4444	0.67
0066	PC	184	4242	4689	4458	0.67
0066	PC	185	4257	4703	4473	0.67
0066	PC	186	4273	4717	4488	0.67
0066	PC	187	4288	4731	4503	0.67
0066	PC	188	4304	4746	4518	0.67
0066	PC	189	4319	4760	4533	0.67
0066	PC	190	4335	4774	4548	0.67
0066	PC	191	4350	4788	4563	0.67
0066	PC	192	4365	4803	4577	0.67
0066	PC	193	4381	4817	4592	0.67
0066	PC	194	4396	4831	4607	0.67
0066	PC	195	4412	4845	4622	0.67
0066	PC	196	4427	4860	4637	0.67
0066	PC	197	4442	4875	4652	0.67
0066	PC	198	4457	4889	4667	0.67
0066	PC	199	4473	4904	4681	0.67
0066	PC	200	4488	4918	4696	0.67
0066	PC	201	4503	4932	4711	0.67
0066	PC	202	4518	4947	4726	0.67
0066	PC	203	4534	4961	4741	0.67
0066	PC	204	4550	4975	4756	0.67
0066	PC	205	4565	4990	4771	0.67
0066	PC	206	4581	5004	4785	0.67
0066	PC	207	4596	5018	4800	0.67
0066	PC	208	4611	5033	4815	0.67
0066	PC	209	4627	5047	4830	0.67

Core	Core type	Depth (cm)	min95%	max95%	age (yr BP)	sed rate (mm/year)
0066	PC	210	4642	5061	4845	0.67
0066	PC	211	4657	5075	4860	0.67
0066	PC	212	4673	5090	4875	0.67
0066	PC	213	4688	5104	4890	0.67
0066	PC	214	4703	5118	4904	0.67
0066	PC	215	4718	5133	4919	0.67
0066	PC	216	4733	5147	4934	0.67
0066	PC	217	4749	5162	4949	0.67
0066	PC	218	4764	5176	4964	0.67
0066	PC	219	4779	5190	4979	0.67
0066	PC	220	4795	5205	4994	0.67
0066	PC	221	4810	5219	5008	0.67
0066	PC	222	4825	5233	5023	0.67
0066	PC	223	4840	5248	5038	0.67
0066	PC	224	4856	5262	5053	0.67
0066	PC	225	4871	5277	5068	0.67
0066	PC	226	4887	5291	5083	0.67
0066	PC	227	4902	5305	5098	0.67
0066	PC	228	4917	5320	5112	0.67
0066	PC	229	4933	5334	5127	0.67
0066	PC	230	4948	5349	5142	0.67
0066	PC	231	4963	5363	5157	0.67
0066	PC	232	4979	5378	5172	0.67
0066	PC	233	4994	5392	5187	0.67
0066	PC	234	5009	5407	5202	0.67
0066	PC	235	5024	5421	5216	0.67
0066	PC	236	5039	5436	5231	0.67
0066	PC	237	5055	5451	5246	0.67
0066	PC	238	5069	5465	5261	0.67
0066	PC	239	5085	5479	5276	0.67
0066	PC	240	5100	5493	5291	0.67
0066	PC	241	5115	5508	5306	0.67
0066	PC	242	5130	5523	5321	2.02
0066	PC	245	5146	5537	5335	0.67
0066	PC	246	5161	5552	5350	0.67
0066	PC	247	5176	5566	5365	0.67
0066	PC	248	5192	5581	5380	0.67
0066	PC	249	5207	5595	5395	0.67
0066	PC	250	5222	5609	5410	0.67
0066	PC	251	5238	5624	5425	0.67
0066	PC	252	5254	5638	5439	0.67
0066	PC	253	5269	5653	5454	0.67

Core	Core type	Depth (cm)	min95%	max95%	age (yr BP)	sed rate (mm/year)
0066	PC	254	5284	5667	5469	0.67
0066	PC	255	5299	5681	5484	0.67
0066	PC	256	5314	5696	5499	0.67
0066	PC	257	5330	5710	5514	0.67
0066	PC	258	5345	5725	5529	0.67
0066	PC	259	5360	5739	5543	0.67
0066	PC	260	5375	5753	5558	0.67
0066	PC	261	5390	5767	5573	0.67
0066	PC	262	5406	5782	5588	0.67
0066	PC	263	5421	5796	5603	0.67
0066	PC	264	5436	5811	5618	0.67
0066	PC	265	5451	5825	5633	0.67
0066	PC	266	5466	5839	5648	0.67
0066	PC	267	5481	5854	5662	0.67
0066	PC	268	5496	5868	5677	0.67
0066	PC	269	5512	5882	5692	0.67
0066	PC	270	5526	5897	5707	0.67
0066	PC	271	5542	5911	5722	0.67
0066	PC	272	5557	5926	5737	0.67
0066	PC	273	5571	5940	5752	0.67
0066	PC	274	5587	5955	5766	0.67
0066	PC	275	5602	5969	5781	0.67
0066	PC	276	5617	5983	5796	0.67
0066	PC	277	5632	5998	5811	0.67
0066	PC	278	5647	6012	5826	0.67
0066	PC	279	5663	6027	5841	0.67
0066	PC	280	5678	6041	5856	0.67
0066	PC	281	5693	6056	5870	0.67
0066	PC	282	5709	6070	5885	0.67
0066	PC	283	5724	6085	5900	0.67
0066	PC	284	5739	6099	5915	0.67
0066	PC	285	5754	6114	5930	0.67
0066	PC	286	5769	6129	5945	0.67
0066	PC	287	5784	6143	5960	0.67
0066	PC	288	5799	6158	5974	0.67
0066	PC	289	5814	6172	5989	0.67
0066	PC	290	5829	6187	6004	0.67
0066	PC	291	5844	6201	6019	0.67
0066	PC	292	5859	6216	6034	0.67
0066	PC	293	5874	6231	6049	0.67
0066	PC	294	5889	6245	6064	0.67
0066	PC	295	5903	6260	6079	0.67

Core	Core type	Depth (cm)	min95%	max95%	age (yr BP)	sed rate (mm/year)
0066	PC	296	5919	6274	6093	0.67
0066	PC	297	5934	6289	6108	0.67
0066	PC	298	5949	6304	6123	0.67
0066	PC	299	5964	6318	6138	0.67
0066	PC	300	5978	6333	6153	0.67
0066	PC	301	5993	6347	6168	0.67
0066	PC	302	6009	6362	6183	0.67
0066	PC	303	6024	6377	6197	0.67
0066	PC	304	6038	6392	6212	0.67
0066	PC	305	6054	6407	6227	0.67
0066	PC	306	6069	6421	6242	0.67
0066	PC	307	6083	6436	6257	0.67
0066	PC	308	6098	6450	6272	0.67
0066	PC	309	6113	6464	6287	0.67
0066	PC	310	6128	6479	6301	0.67
0066	PC	311	6143	6494	6316	0.67
0066	PC	312	6158	6508	6331	0.67
0066	PC	313	6173	6523	6346	0.67
0066	PC	314	6188	6537	6361	0.67
0066	PC	315	6203	6552	6376	0.67
0066	PC	316	6218	6567	6391	0.67
0066	PC	317	6233	6582	6406	0.67
0066	PC	318	6248	6596	6420	0.67
0066	PC	319	6263	6611	6435	0.67
0066	PC	320	6278	6627	6450	0.67
0066	PC	321	6293	6641	6465	0.67
0066	PC	322	6308	6656	6480	0.67
0066	PC	323	6323	6671	6495	0.67
0066	PC	324	6337	6686	6510	0.67
0066	PC	325	6353	6701	6524	0.67
0066	PC	326	6368	6716	6539	0.67
0066	PC	327	6383	6731	6554	0.67
0066	PC	328	6398	6746	6569	0.67
0066	PC	329	6412	6760	6584	0.67
0066	PC	330	6427	6775	6599	0.67
0066	PC	331	6442	6790	6614	0.67
0066	PC	332	6457	6805	6628	1.35
0066	PC	334	6472	6819	6643	0.67
0066	PC	335	6487	6834	6658	0.67
0066	PC	336	6502	6849	6673	0.67
0066	PC	337	6517	6864	6688	0.67
0066	PC	338	6531	6879	6703	0.67

Core	Core type	Depth (cm)	min95%	max95%	age (yr BP)	sed rate (mm/year)
0066	PC	339	6546	6894	6718	0.67
0066	PC	340	6561	6908	6732	0.67
0066	PC	341	6576	6923	6747	0.67
0066	PC	342	6590	6938	6762	0.67
0066	PC	343	6604	6952	6777	0.67
0066	PC	344	6619	6967	6792	0.67
0066	PC	345	6634	6982	6807	0.67
0066	PC	346	6649	6997	6822	0.67
0066	PC	347	6664	7012	6837	0.67
0066	PC	348	6679	7027	6851	0.67
0066	PC	349	6693	7042	6866	0.67
0066	PC	350	6708	7057	6881	0.67
0066	PC	351	6723	7072	6896	0.67
0066	PC	352	6738	7087	6911	0.67
0066	PC	353	6752	7102	6926	0.67
0066	PC	354	6767	7117	6941	0.67
0066	PC	355	6782	7132	6955	0.67
0066	PC	356	6797	7147	6970	0.67
0066	PC	357	6812	7162	6985	0.67
0066	PC	358	6826	7177	7000	0.67
0066	PC	359	6841	7192	7015	0.67
0066	PC	360	6856	7207	7030	0.67
0066	PC	361	6870	7221	7045	0.67
0066	PC	362	6885	7236	7059	0.67
0066	PC	363	6899	7251	7074	0.67
0066	PC	364	6914	7266	7089	0.67
0066	PC	365	6928	7281	7104	0.67
0066	PC	366	6943	7296	7119	0.67
0066	PC	367	6958	7311	7134	0.67
0066	PC	368	6972	7326	7149	0.67
0066	PC	369	6986	7341	7164	0.67
0066	PC	370	7001	7357	7178	0.67
0066	PC	371	7015	7372	7193	0.67
0066	PC	372	7030	7387	7208	0.67
0066	PC	373	7044	7401	7223	0.67
0066	PC	374	7059	7416	7238	0.67
0066	PC	375	7073	7432	7253	0.67
0066	PC	376	7088	7446	7268	0.67
0066	PC	377	7102	7462	7282	0.67
0066	PC	378	7117	7477	7297	0.67
0066	PC	379	7131	7492	7312	0.67
0066	PC	380	7146	7507	7327	0.67

Core	Core type	Depth (cm)	min95%	max95%	age (yr BP)	sed rate (mm/year)
0066	PC	381	7160	7522	7342	0.67
0066	PC	382	7175	7537	7357	0.67
0066	PC	383	7189	7553	7372	0.67
0066	PC	384	7204	7568	7386	0.67
0066	PC	385	7219	7583	7401	0.67
0066	PC	386	7233	7598	7416	0.67
0066	PC	387	7248	7613	7431	0.67
0066	PC	388	7262	7628	7446	0.67
0066	PC	389	7276	7643	7461	0.67
0066	PC	390	7291	7658	7476	0.67
0066	PC	391	7305	7674	7491	0.67
0066	PC	392	7320	7689	7505	0.67
0066	PC	393	7334	7704	7520	0.67
0066	PC	394	7349	7720	7535	0.67
0066	PC	395	7363	7736	7550	0.67
0066	PC	396	7378	7751	7565	0.67
0066	PC	397	7392	7767	7580	0.67
0066	PC	398	7407	7781	7595	0.67
0066	PC	399	7421	7796	7609	0.67
0066	PC	400	7435	7810	7624	0.67
0066	PC	401	7450	7826	7639	0.67
0066	PC	402	7464	7841	7654	0.67
0066	PC	403	7479	7856	7669	0.67
0066	PC	404	7493	7871	7684	0.67
0066	PC	405	7508	7887	7699	0.67
0066	PC	406	7522	7902	7713	0.67
0066	PC	407	7537	7917	7728	0.67
0066	PC	408	7551	7933	7743	0.67
0066	PC	409	7565	7948	7758	0.67
0066	PC	410	7580	7964	7773	0.67
0066	PC	411	7595	7979	7788	0.67
0066	PC	412	7610	7994	7803	0.67
0066	PC	413	7624	8010	7817	0.67
0066	PC	414	7639	8026	7832	0.67
0066	PC	415	7654	8041	7847	0.67
0066	PC	416	7668	8056	7862	0.67
0066	PC	417	7682	8072	7877	0.67
0066	PC	418	7697	8087	7892	0.67
0066	PC	419	7712	8102	7907	0.67
0066	PC	420	7726	8118	7922	0.67
0066	PC	421	7741	8133	7936	0.67
0066	PC	422	7755	8149	7951	2.69

Core	Core type	Depth (cm)	min95%	max95%	age (yr BP)	sed rate (mm/year)
0066	PC	426	7769	8164	7966	0.67
0066	PC	427	7784	8179	7981	0.67
0066	PC	428	7798	8195	7996	0.67
0066	PC	429	7812	8211	8011	0.67
0066	PC	430	7827	8226	8026	0.67
0066	PC	431	7841	8241	8040	0.67
0066	PC	432	7855	8256	8055	0.67
0066	PC	433	7870	8272	8070	0.67
0066	PC	434	7885	8287	8085	0.67
0066	PC	435	7899	8303	8100	0.67
0066	PC	436	7914	8318	8115	0.67
0066	PC	437	7928	8333	8130	0.67
0066	PC	438	7943	8348	8144	0.67
0066	PC	439	7957	8363	8159	0.67
0066	PC	440	7971	8379	8174	0.67
0066	PC	441	7986	8394	8189	0.67
0066	PC	442	8000	8409	8204	0.67
0066	PC	443	8014	8424	8219	0.67
0066	PC	444	8028	8440	8234	0.67
0066	PC	445	8043	8455	8249	0.67
0066	PC	446	8057	8470	8263	0.67
0066	PC	447	8071	8486	8278	0.67
0066	PC	448	8086	8502	8293	0.67
0066	PC	449	8100	8517	8308	0.67
0066	PC	450	8114	8532	8323	0.67
0066	PC	451	8129	8548	8338	0.67
0066	PC	452	8143	8564	8353	0.67
0066	PC	453	8157	8579	8367	0.67
0066	PC	454	8171	8594	8382	0.67
0066	PC	455	8186	8609	8397	0.67
0066	PC	456	8200	8625	8412	0.67
0066	PC	457	8214	8641	8427	0.67
0066	PC	458	8229	8656	8442	0.67
0066	PC	459	8243	8671	8457	0.67
0066	PC	460	8257	8687	8471	0.67
0066	PC	461	8272	8701	8486	0.67
0066	PC	462	8286	8716	8501	0.67
0066	PC	463	8300	8731	8516	2.69
0066	PC	467	8314	8746	8531	0.67
0066	PC	468	8328	8761	8546	0.67
0066	PC	469	8343	8777	8561	0.67
0066	PC	470	8357	8792	8575	0.67

Core	Core type	Depth (cm)	min95%	max95%	age (yr BP)	sed rate (mm/year)
0066	PC	471	8371	8808	8590	0.67
0066	PC	472	8385	8823	8605	0.67
0066	PC	473	8399	8839	8620	0.67
0066	PC	474	8413	8854	8635	0.67
0066	PC	475	8427	8870	8650	0.67
0066	PC	476	8441	8886	8665	0.67
0066	PC	477	8455	8901	8680	0.67
0066	PC	478	8469	8916	8694	0.67
0066	PC	479	8484	8932	8709	0.67
0066	PC	480	8498	8947	8724	0.67
0066	PC	481	8513	8963	8739	0.67
0066	PC	482	8527	8978	8754	0.67
0066	PC	483	8542	8993	8769	0.67
0066	PC	484	8556	9009	8784	0.67
0066	PC	485	8571	9025	8798	0.67
0066	PC	486	8585	9040	8813	0.67
0066	PC	487	8600	9055	8828	0.67
0066	PC	488	8614	9070	8843	0.67
0066	PC	489	8628	9086	8858	0.67
0066	PC	490	8642	9102	8873	0.67
0066	PC	491	8656	9117	8888	0.67
0066	PC	492	8670	9132	8902	0.67
0066	PC	493	8685	9148	8917	0.67
0066	PC	494	8699	9164	8932	0.67
0066	PC	495	8713	9179	8947	0.67
0066	PC	496	8727	9194	8962	0.67
0066	PC	497	8741	9210	8977	0.67
0066	PC	498	8755	9225	8992	0.67
0066	PC	499	8770	9240	9007	0.67
0066	PC	500	8784	9256	9021	0.67
0066	PC	501	8798	9271	9036	0.67
0066	PC	502	8812	9286	9051	0.67
0066	PC	503	8826	9302	9066	0.67
0066	PC	504	8841	9318	9081	0.67
0066	PC	505	8855	9333	9096	0.67
0066	PC	506	8869	9348	9111	0.67
0066	PC	507	8883	9364	9125	0.67
0066	PC	508	8897	9379	9140	0.67
0066	PC	509	8912	9395	9155	0.67
0066	PC	510	8926	9410	9170	0.67
0066	PC	511	8941	9426	9185	0.67
0066	PC	512	8955	9441	9200	0.67

Core	Core type	Depth (cm)	min95%	max95%	age (yr BP)	sed rate (mm/year)
0066	PC	513	8969	9457	9215	0.67
0066	PC	514	8984	9472	9229	0.67
0066	PC	515	8998	9488	9244	0.67
0066	PC	516	9012	9503	9259	2.69
0066	PC	520	9026	9519	9274	0.67
0066	PC	521	9041	9534	9289	0.67
0066	PC	522	9055	9549	9304	0.67
0066	PC	523	9068	9564	9319	0.67
0066	PC	524	9083	9580	9333	0.67
0066	PC	525	9097	9596	9348	0.67
0066	PC	526	9111	9611	9363	0.67
0066	PC	527	9125	9627	9378	0.67
0066	PC	528	9139	9642	9393	0.67
0066	PC	529	9154	9658	9408	1.35
0066	PC	531	9168	9673	9423	1.35

Core 0067 age model results

Core	Core type	Depth (cm)	min95%	max95%	age (yr BP)	sed rate (mm/year)
0067	TWC	-25	-65	-61	-63	1.12
0067	TWC	-24	-56	-52	-54	1.12
0067	TWC	-23	-48	-42	-45	1.12
0067	TWC	-22	-40	-32	-36	1.12
0067	TWC	-21	-33	-22	-27	1.12
0067	TWC	-20	-25	-12	-18	1.12
0067	TWC	-19	-17	-2	-10	1.12
0067	TWC	-18	-9	8	-1	1.12
0067	TWC	-17	-2	18	8	1.12
0067	TWC	-16	6	28	17	1.12
0067	TWC	-15	14	39	26	1.12
0067	TWC	-14	22	49	35	1.12
0067	TWC	-13	29	59	44	1.12
0067	TWC	-12	37	69	53	1.12
0067	TWC	-11	45	79	62	1.12
0067	TWC	-10	52	89	71	1.12
0067	TWC	-9	60	100	79	1.12
0067	TWC	-8	68	110	88	1.12
0067	TWC	-7	76	120	97	1.12
0067	TWC	-6	83	130	106	1.12
0067	TWC	-5	91	140	115	1.12
0067	TWC	-4	99	150	124	1.12
0067	TWC	-3	106	160	133	1.12
0067	TWC	-2	114	171	142	1.12
0067	TWC	-1	122	181	151	1.12
0067	TWC	0	130	191	160	1.12
0067	PC	1	137	201	168	1.12
0067	PC	2	145	211	177	1.12
0067	PC	3	153	221	186	1.12
0067	PC	4	160	232	195	1.12
0067	PC	5	168	242	204	1.12
0067	PC	6	176	252	213	1.12
0067	PC	7	183	262	222	1.12
0067	PC	8	191	272	231	1.12
0067	PC	9	199	282	240	1.12
0067	PC	10	206	293	249	1.12
0067	PC	11	214	303	258	1.12
0067	PC	12	222	313	266	1.12
0067	PC	13	229	323	275	1.12
0067	PC	14	237	333	284	1.12

Core	Core type	Depth (cm)	min95%	max95%	age (yr BP)	sed rate (mm/year)
0067	PC	15	245	343	293	1.12
0067	PC	16	252	354	302	1.12
0067	PC	17	260	364	311	1.12
0067	PC	18	268	374	320	1.12
0067	PC	19	276	384	329	1.12
0067	PC	20	283	394	338	1.12
0067	PC	21	291	404	347	1.12
0067	PC	22	299	415	355	1.12
0067	PC	23	306	425	364	1.12
0067	PC	24	314	435	373	1.12
0067	PC	25	322	445	382	1.12
0067	PC	26	329	455	391	1.12
0067	PC	27	337	465	400	1.12
0067	PC	28	345	476	409	1.12
0067	PC	29	353	486	418	1.12
0067	PC	30	360	496	427	1.12
0067	PC	31	368	506	436	1.12
0067	PC	32	376	516	444	1.12
0067	PC	33	383	526	453	1.12
0067	PC	34	391	536	462	1.12
0067	PC	35	399	547	471	1.12
0067	PC	36	406	557	480	1.12
0067	PC	37	414	567	489	1.12
0067	PC	38	422	577	498	1.12
0067	PC	39	429	587	507	1.12
0067	PC	40	437	598	516	1.12
0067	PC	41	445	608	525	1.12
0067	PC	42	453	618	534	1.12
0067	PC	43	460	628	542	1.12
0067	PC	44	468	638	551	1.12
0067	PC	45	476	648	560	1.12
0067	PC	46	483	659	569	1.12
0067	PC	47	491	669	578	1.12
0067	PC	48	499	679	587	1.12
0067	PC	49	506	689	596	1.12
0067	PC	50	514	699	605	1.12
0067	PC	51	522	709	614	1.12
0067	PC	52	529	720	623	1.12
0067	PC	53	537	730	631	1.12
0067	PC	54	545	740	640	1.12
0067	PC	55	552	750	649	1.12
0067	PC	56	560	760	658	1.12

Core	Core type	Depth (cm)	min95%	max95%	age (yr BP)	sed rate (mm/year)
0067	PC	57	568	770	667	1.12
0067	PC	58	575	780	676	1.12
0067	PC	59	583	791	685	1.12
0067	PC	60	591	801	694	1.12
0067	PC	61	598	811	703	1.12
0067	PC	62	606	821	712	1.12
0067	PC	63	614	831	720	1.12
0067	PC	64	621	841	729	1.12
0067	PC	65	629	851	738	1.12
0067	PC	66	637	862	747	1.12
0067	PC	67	644	872	756	1.12
0067	PC	68	652	882	765	1.12
0067	PC	69	660	892	774	1.12
0067	PC	70	668	902	783	1.12
0067	PC	71	675	912	792	1.12
0067	PC	72	683	923	801	1.12
0067	PC	73	691	933	810	1.12
0067	PC	74	698	943	818	1.12
0067	PC	75	706	953	827	1.12
0067	PC	76	714	963	836	1.12
0067	PC	77	721	973	845	1.12
0067	PC	78	729	984	854	1.12
0067	PC	79	737	994	863	1.12
0067	PC	80	744	1004	872	1.12
0067	PC	81	752	1014	881	1.12
0067	PC	82	760	1024	890	1.12
0067	PC	83	767	1034	899	1.12
0067	PC	84	775	1044	907	1.12
0067	PC	85	783	1055	916	1.12
0067	PC	86	790	1065	925	1.12
0067	PC	87	798	1075	934	1.12
0067	PC	88	806	1085	943	1.12
0067	PC	89	813	1095	952	1.12
0067	PC	90	821	1105	961	1.12
0067	PC	91	829	1116	970	1.12
0067	PC	92	836	1126	979	1.12
0067	PC	93	844	1136	988	1.12
0067	PC	94	852	1146	996	1.12
0067	PC	95	859	1156	1005	1.12
0067	PC	96	867	1166	1014	1.12
0067	PC	97	875	1177	1023	1.12
0067	PC	98	883	1187	1032	1.12

Core	Core type	Depth (cm)	min95%	max95%	age (yr BP)	sed rate (mm/year)
0067	PC	99	890	1197	1041	1.12
0067	PC	100	898	1207	1050	1.12
0067	PC	101	906	1217	1059	1.12
0067	PC	102	913	1227	1068	1.12
0067	PC	103	921	1238	1077	1.12
0067	PC	104	929	1248	1086	3.37
0067	PC	107	936	1258	1094	1.12
0067	PC	108	944	1268	1103	1.12
0067	PC	109	952	1278	1112	1.12
0067	PC	110	959	1288	1121	1.12
0067	PC	111	967	1299	1130	1.12
0067	PC	112	975	1309	1139	1.12
0067	PC	113	982	1319	1148	1.12
0067	PC	114	990	1329	1157	1.12
0067	PC	115	998	1339	1166	1.12
0067	PC	116	1005	1350	1175	1.12
0067	PC	117	1013	1360	1183	1.12
0067	PC	118	1021	1370	1192	1.12
0067	PC	119	1028	1380	1201	1.12
0067	PC	120	1036	1390	1210	1.12
0067	PC	121	1044	1400	1219	1.12
0067	PC	122	1052	1411	1228	1.12
0067	PC	123	1059	1421	1237	1.12
0067	PC	124	1067	1431	1246	1.12
0067	PC	125	1075	1441	1255	1.12
0067	PC	126	1082	1451	1264	1.12
0067	PC	127	1090	1461	1272	1.12
0067	PC	128	1098	1472	1281	1.12
0067	PC	129	1105	1482	1290	1.12
0067	PC	130	1113	1492	1299	1.12
0067	PC	131	1121	1502	1308	1.12
0067	PC	132	1129	1512	1317	1.12
0067	PC	133	1136	1523	1326	1.12
0067	PC	134	1144	1533	1335	1.12
0067	PC	135	1152	1543	1344	1.12
0067	PC	136	1159	1553	1353	1.12
0067	PC	137	1167	1563	1362	1.12
0067	PC	138	1175	1573	1370	1.12
0067	PC	139	1182	1584	1379	1.12
0067	PC	140	1190	1594	1388	1.12
0067	PC	141	1198	1604	1397	1.12
0067	PC	142	1206	1614	1406	1.12

Core	Core type	Depth (cm)	min95%	max95%	age (yr BP)	sed rate (mm/year)
0067	PC	143	1213	1624	1415	1.12
0067	PC	144	1221	1634	1424	1.12
0067	PC	145	1229	1645	1433	1.12
0067	PC	146	1236	1655	1442	1.12
0067	PC	147	1244	1665	1451	1.12
0067	PC	148	1252	1675	1459	1.12
0067	PC	149	1259	1685	1468	1.12
0067	PC	150	1267	1696	1477	1.12
0067	PC	151	1275	1706	1486	1.12
0067	PC	152	1283	1716	1495	1.12
0067	PC	153	1290	1726	1504	1.12
0067	PC	154	1298	1736	1513	1.12
0067	PC	155	1306	1746	1522	1.12
0067	PC	156	1313	1757	1531	1.12
0067	PC	157	1321	1767	1540	1.12
0067	PC	158	1329	1777	1548	1.12
0067	PC	159	1336	1787	1557	1.12
0067	PC	160	1344	1797	1566	1.12
0067	PC	161	1352	1807	1575	1.12
0067	PC	162	1360	1818	1584	1.12
0067	PC	163	1367	1828	1593	1.12
0067	PC	164	1375	1838	1602	2.17
0067	PC	165	1380	1841	1607	2.17
0067	PC	166	1385	1845	1611	2.17
0067	PC	167	1391	1850	1616	2.17
0067	PC	168	1396	1854	1620	2.17
0067	PC	169	1401	1858	1625	2.17
0067	PC	170	1406	1862	1630	2.17
0067	PC	171	1411	1866	1634	2.17
0067	PC	172	1416	1870	1639	2.17
0067	PC	173	1422	1874	1643	2.17
0067	PC	174	1427	1878	1648	2.17
0067	PC	175	1432	1882	1653	2.17
0067	PC	176	1437	1886	1657	2.17
0067	PC	177	1443	1890	1662	2.17
0067	PC	178	1448	1894	1666	2.17
0067	PC	179	1454	1898	1671	2.17
0067	PC	180	1459	1902	1676	2.17
0067	PC	181	1464	1906	1680	2.17
0067	PC	182	1469	1910	1685	2.17
0067	PC	183	1475	1914	1689	2.17
0067	PC	184	1480	1918	1694	2.17

Core	Core type	Depth (cm)	min95%	max95%	age (yr BP)	sed rate (mm/year)
0067	PC	185	1485	1922	1699	2.17
0067	PC	186	1491	1926	1703	2.17
0067	PC	187	1496	1930	1708	2.17
0067	PC	188	1501	1934	1713	2.17
0067	PC	189	1506	1938	1717	2.17
0067	PC	190	1511	1942	1722	2.17
0067	PC	191	1516	1946	1726	2.17
0067	PC	192	1521	1950	1731	2.17
0067	PC	193	1526	1954	1736	2.17
0067	PC	194	1531	1958	1740	2.17
0067	PC	195	1537	1962	1745	2.17
0067	PC	196	1542	1966	1749	2.17
0067	PC	197	1547	1970	1754	2.17
0067	PC	198	1552	1974	1759	2.17
0067	PC	199	1557	1978	1763	2.17
0067	PC	200	1562	1982	1768	2.17
0067	PC	201	1568	1986	1772	2.17
0067	PC	202	1573	1989	1777	2.17
0067	PC	203	1577	1993	1782	2.17
0067	PC	204	1583	1997	1786	2.17
0067	PC	205	1588	2002	1791	2.17
0067	PC	206	1593	2006	1795	2.17
0067	PC	207	1598	2010	1800	2.17
0067	PC	208	1603	2014	1805	2.17
0067	PC	209	1608	2018	1809	2.17
0067	PC	210	1613	2022	1814	2.17
0067	PC	211	1618	2027	1818	2.17
0067	PC	212	1623	2031	1823	2.17
0067	PC	213	1628	2035	1828	2.17
0067	PC	214	1633	2039	1832	2.17
0067	PC	215	1638	2043	1837	2.17
0067	PC	216	1643	2048	1842	2.17
0067	PC	217	1648	2052	1846	2.17
0067	PC	218	1653	2056	1851	2.17
0067	PC	219	1658	2060	1855	2.17
0067	PC	220	1664	2065	1860	2.17
0067	PC	221	1668	2069	1865	2.17
0067	PC	222	1673	2073	1869	2.17
0067	PC	223	1678	2077	1874	2.17
0067	PC	224	1683	2081	1878	2.17
0067	PC	225	1689	2085	1883	8.70
0067	PC	229	1694	2089	1888	2.17

Core	Core type	Depth (cm)	min95%	max95%	age (yr BP)	sed rate (mm/year)
0067	PC	230	1699	2093	1892	2.17
0067	PC	231	1703	2097	1897	2.17
0067	PC	232	1708	2101	1901	2.17
0067	PC	233	1713	2105	1906	2.17
0067	PC	234	1718	2109	1911	2.17
0067	PC	235	1723	2113	1915	2.17
0067	PC	236	1728	2117	1920	2.17
0067	PC	237	1733	2121	1924	2.17
0067	PC	238	1738	2125	1929	2.17
0067	PC	239	1743	2129	1934	2.17
0067	PC	240	1748	2133	1938	2.17
0067	PC	241	1753	2138	1943	2.17
0067	PC	242	1758	2142	1948	2.17
0067	PC	243	1763	2146	1952	2.17
0067	PC	244	1768	2151	1957	2.17
0067	PC	245	1773	2155	1961	2.17
0067	PC	246	1779	2159	1966	2.17
0067	PC	247	1784	2164	1971	2.17
0067	PC	248	1789	2168	1975	2.17
0067	PC	249	1794	2172	1980	2.17
0067	PC	250	1798	2176	1984	2.17
0067	PC	251	1803	2180	1989	2.17
0067	PC	252	1808	2185	1994	2.17
0067	PC	253	1813	2189	1998	2.17
0067	PC	254	1818	2192	2003	2.17
0067	PC	255	1824	2197	2007	2.17
0067	PC	256	1828	2201	2012	2.17
0067	PC	257	1833	2205	2017	2.17
0067	PC	258	1838	2209	2021	2.17
0067	PC	259	1843	2213	2026	2.17
0067	PC	260	1848	2217	2030	2.17
0067	PC	261	1853	2221	2035	2.17
0067	PC	262	1858	2226	2040	2.17
0067	PC	263	1863	2230	2044	2.17
0067	PC	264	1867	2234	2049	2.17
0067	PC	265	1872	2239	2054	2.17
0067	PC	266	1877	2243	2058	2.17
0067	PC	267	1882	2248	2063	2.17
0067	PC	268	1887	2252	2067	2.17
0067	PC	269	1892	2256	2072	2.17
0067	PC	270	1897	2260	2077	2.17
0067	PC	271	1902	2265	2081	2.17

Core	Core type	Depth (cm)	min95%	max95%	age (yr BP)	sed rate (mm/year)
0067	PC	272	1907	2269	2086	2.17
0067	PC	273	1912	2274	2090	2.17
0067	PC	274	1917	2278	2095	2.17
0067	PC	275	1922	2282	2100	2.17
0067	PC	276	1927	2286	2104	2.17
0067	PC	277	1932	2290	2109	2.17
0067	PC	278	1936	2295	2113	2.17
0067	PC	279	1941	2299	2118	2.17
0067	PC	280	1946	2304	2123	2.17
0067	PC	281	1951	2308	2127	2.17
0067	PC	282	1956	2313	2132	2.17
0067	PC	283	1960	2317	2136	2.17
0067	PC	284	1965	2321	2141	2.17
0067	PC	285	1970	2326	2146	2.17
0067	PC	286	1975	2331	2150	2.17
0067	PC	287	1980	2335	2155	2.17
0067	PC	288	1985	2339	2160	2.17
0067	PC	289	1989	2344	2164	2.17
0067	PC	290	1994	2348	2169	2.17
0067	PC	291	1999	2352	2173	2.17
0067	PC	292	2004	2357	2178	2.17
0067	PC	293	2008	2361	2183	2.17
0067	PC	294	2013	2365	2187	2.17
0067	PC	295	2018	2370	2192	2.17
0067	PC	296	2023	2374	2196	2.17
0067	PC	297	2028	2378	2201	2.17
0067	PC	298	2032	2382	2206	2.17
0067	PC	299	2037	2386	2210	2.17
0067	PC	300	2042	2391	2215	2.17
0067	PC	301	2047	2395	2219	2.17
0067	PC	302	2051	2400	2224	2.17
0067	PC	303	2056	2404	2229	2.17
0067	PC	304	2061	2408	2233	2.17
0067	PC	305	2066	2413	2238	2.17
0067	PC	306	2070	2418	2242	2.17
0067	PC	307	2075	2422	2247	2.17
0067	PC	308	2080	2427	2252	2.17
0067	PC	309	2084	2431	2256	2.17
0067	PC	310	2089	2435	2261	2.17
0067	PC	311	2094	2440	2265	2.17
0067	PC	312	2098	2445	2270	2.17
0067	PC	313	2103	2449	2275	2.17

Core	Core type	Depth (cm)	min95%	max95%	age (yr BP)	sed rate (mm/year)
0067	PC	314	2108	2454	2279	2.17
0067	PC	315	2113	2458	2284	2.17
0067	PC	316	2117	2462	2289	2.17
0067	PC	317	2122	2467	2293	2.17
0067	PC	318	2127	2472	2298	2.17
0067	PC	319	2131	2476	2302	2.17
0067	PC	320	2136	2480	2307	2.17
0067	PC	321	2141	2485	2312	2.17
0067	PC	322	2145	2489	2316	2.17
0067	PC	323	2151	2494	2321	2.17
0067	PC	324	2156	2498	2325	2.17
0067	PC	325	2160	2502	2330	2.17
0067	PC	326	2165	2507	2335	2.17
0067	PC	327	2169	2512	2339	2.17
0067	PC	328	2174	2516	2344	2.17
0067	PC	329	2179	2521	2348	2.17
0067	PC	330	2184	2525	2353	2.17
0067	PC	331	2189	2530	2358	2.17
0067	PC	332	2193	2535	2362	2.17
0067	PC	333	2198	2539	2367	2.17
0067	PC	334	2203	2544	2371	2.17
0067	PC	335	2208	2548	2376	2.17
0067	PC	336	2213	2553	2381	2.17
0067	PC	337	2217	2557	2385	2.17
0067	PC	338	2222	2561	2390	2.17
0067	PC	339	2226	2566	2395	2.17
0067	PC	340	2230	2570	2399	2.17
0067	PC	341	2235	2575	2404	2.17
0067	PC	342	2240	2581	2408	2.17
0067	PC	343	2244	2585	2413	2.17
0067	PC	344	2249	2590	2418	2.17
0067	PC	345	2253	2594	2422	2.17
0067	PC	346	2258	2599	2427	2.17
0067	PC	347	2262	2603	2431	2.17
0067	PC	348	2267	2608	2436	2.17
0067	PC	349	2271	2613	2441	2.17
0067	PC	350	2276	2618	2445	2.17
0067	PC	351	2280	2622	2450	2.17
0067	PC	352	2285	2626	2454	2.17
0067	PC	353	2289	2631	2459	2.17
0067	PC	354	2294	2636	2464	2.17
0067	PC	355	2298	2640	2468	2.17

Core	Core type	Depth (cm)	min95%	max95%	age (yr BP)	sed rate (mm/year)
0067	PC	356	2302	2645	2473	2.17
0067	PC	357	2307	2649	2477	2.17
0067	PC	358	2311	2654	2482	2.17
0067	PC	359	2315	2658	2487	2.17
0067	PC	360	2320	2663	2491	2.17
0067	PC	361	2324	2668	2496	2.17
0067	PC	362	2328	2673	2501	2.17
0067	PC	363	2333	2677	2505	2.17
0067	PC	364	2337	2682	2510	2.17
0067	PC	365	2342	2686	2514	2.17
0067	PC	366	2346	2691	2519	2.17
0067	PC	367	2351	2696	2524	2.17
0067	PC	368	2355	2701	2528	2.17
0067	PC	369	2360	2705	2533	2.17
0067	PC	370	2365	2710	2537	2.17
0067	PC	371	2369	2715	2542	2.17
0067	PC	372	2373	2720	2547	2.17
0067	PC	373	2378	2724	2551	2.17
0067	PC	374	2382	2729	2556	2.17
0067	PC	375	2387	2734	2560	2.17
0067	PC	376	2391	2738	2565	2.17
0067	PC	377	2396	2743	2570	2.17
0067	PC	378	2400	2748	2574	2.17
0067	PC	379	2404	2753	2579	2.17
0067	PC	380	2409	2757	2583	2.17
0067	PC	381	2413	2762	2588	2.17
0067	PC	382	2418	2767	2593	2.17
0067	PC	383	2422	2772	2597	2.17
0067	PC	384	2426	2777	2602	2.17
0067	PC	385	2430	2782	2606	2.17
0067	PC	386	2434	2787	2611	2.17
0067	PC	387	2439	2792	2616	2.17
0067	PC	388	2443	2797	2620	2.17
0067	PC	389	2448	2802	2625	2.17
0067	PC	390	2452	2806	2630	2.17
0067	PC	391	2456	2811	2634	2.17
0067	PC	392	2461	2816	2639	2.17
0067	PC	393	2465	2821	2643	2.17
0067	PC	394	2469	2826	2648	2.17
0067	PC	395	2474	2831	2653	2.17
0067	PC	396	2478	2835	2657	2.17
0067	PC	397	2483	2840	2662	2.17

Core	Core type	Depth (cm)	min95%	max95%	age (yr BP)	sed rate (mm/year)
0067	PC	398	2486	2845	2666	2.17
0067	PC	399	2491	2850	2671	2.17
0067	PC	400	2495	2855	2676	2.17
0067	PC	401	2500	2860	2680	2.17
0067	PC	402	2504	2865	2685	2.17
0067	PC	403	2508	2870	2689	2.17
0067	PC	404	2513	2875	2694	2.17
0067	PC	405	2517	2880	2699	2.17
0067	PC	406	2521	2885	2703	2.17
0067	PC	407	2525	2890	2708	2.17
0067	PC	408	2529	2895	2712	2.17
0067	PC	409	2533	2900	2717	2.17
0067	PC	410	2538	2905	2722	2.17
0067	PC	411	2542	2909	2726	2.17
0067	PC	412	2546	2915	2731	2.17
0067	PC	413	2551	2920	2736	2.17
0067	PC	414	2555	2925	2740	2.17
0067	PC	415	2559	2930	2745	2.17
0067	PC	416	2563	2935	2749	2.17
0067	PC	417	2567	2940	2754	2.17
0067	PC	418	2572	2944	2759	2.17
0067	PC	419	2576	2949	2763	2.17
0067	PC	420	2580	2954	2768	2.17
0067	PC	421	2584	2958	2772	2.17
0067	PC	422	2588	2963	2777	2.17
0067	PC	423	2593	2969	2782	2.17
0067	PC	424	2597	2974	2786	2.17
0067	PC	425	2601	2978	2791	2.17
0067	PC	426	2605	2983	2795	2.17
0067	PC	427	2610	2988	2800	2.17
0067	PC	428	2614	2993	2805	2.17
0067	PC	429	2619	2998	2809	2.17
0067	PC	430	2623	3002	2814	2.17
0067	PC	431	2627	3007	2818	2.17
0067	PC	432	2631	3012	2823	2.17
0067	PC	433	2636	3017	2828	111.11
0067	PC	482	2640	3022	2832	2.17
0067	PC	483	2643	3027	2837	2.17
0067	PC	484	2647	3032	2842	2.17
0067	PC	485	2652	3037	2846	2.17
0067	PC	486	2655	3043	2851	2.17
0067	PC	487	2659	3047	2855	2.17

Core	Core type	Depth (cm)	min95%	max95%	age (yr BP)	sed rate (mm/year)
0067	PC	488	2663	3052	2860	2.17
0067	PC	489	2668	3057	2865	2.17
0067	PC	490	2672	3062	2869	2.17
0067	PC	491	2676	3067	2874	2.17
0067	PC	492	2680	3073	2878	2.17
0067	PC	493	2684	3077	2883	2.17
0067	PC	494	2688	3082	2888	2.17
0067	PC	495	2692	3088	2892	2.17
0067	PC	496	2696	3093	2897	2.17
0067	PC	497	2700	3098	2901	2.17
0067	PC	498	2704	3103	2906	2.17
0067	PC	499	2709	3108	2911	2.17
0067	PC	500	2713	3113	2915	2.17
0067	PC	501	2717	3118	2920	2.17
0067	PC	502	2721	3122	2924	2.17
0067	PC	503	2725	3127	2929	2.17
0067	PC	504	2729	3132	2934	2.17
0067	PC	505	2732	3137	2938	2.17
0067	PC	506	2736	3142	2943	2.17
0067	PC	507	2741	3147	2948	2.17
0067	PC	508	2745	3152	2952	2.17
0067	PC	509	2749	3157	2957	2.17
0067	PC	510	2753	3161	2961	2.17
0067	PC	511	2758	3166	2966	2.17
0067	PC	512	2761	3171	2971	2.17
0067	PC	513	2765	3176	2975	2.17
0067	PC	514	2770	3181	2980	2.17
0067	PC	515	2774	3186	2984	2.17
0067	PC	516	2777	3191	2989	2.17
0067	PC	517	2782	3197	2994	2.17
0067	PC	518	2786	3202	2998	2.17
0067	PC	519	2790	3207	3003	2.17
0067	PC	520	2794	3212	3007	2.17
0067	PC	521	2798	3217	3012	2.17
0067	PC	522	2802	3222	3017	2.17
0067	PC	523	2806	3227	3021	2.17
0067	PC	524	2810	3232	3026	2.17
0067	PC	525	2815	3237	3030	2.17
0067	PC	526	2818	3242	3035	2.17
0067	PC	527	2822	3247	3040	2.17
0067	PC	528	2826	3252	3044	2.17
0067	PC	529	2830	3256	3049	2.17

Core	Core type	Depth (cm)	min95%	max95%	age (yr BP)	sed rate (mm/year)
0067	PC	530	2834	3261	3053	2.17
0067	PC	531	2838	3267	3058	2.17
0067	PC	532	2842	3272	3063	2.17
0067	PC	533	2846	3277	3067	2.17
0067	PC	534	2850	3282	3072	2.17
0067	PC	535	2855	3288	3077	2.17
0067	PC	536	2859	3292	3081	2.17
0067	PC	537	2863	3297	3086	2.17
0067	PC	538	2867	3302	3090	2.17
0067	PC	539	2871	3307	3095	2.17
0067	PC	540	2875	3312	3100	2.17
0067	PC	541	2879	3317	3104	2.17
0067	PC	542	2883	3322	3109	2.17
0067	PC	543	2887	3327	3113	2.17
0067	PC	544	2891	3332	3118	2.17
0067	PC	545	2895	3337	3123	2.17
0067	PC	546	2899	3342	3127	2.17
0067	PC	547	2903	3348	3132	2.17
0067	PC	548	2907	3352	3136	2.17
0067	PC	549	2911	3357	3141	2.17
0067	PC	550	2915	3363	3146	2.17
0067	PC	551	2920	3368	3150	2.17
0067	PC	552	2924	3373	3155	2.17
0067	PC	553	2928	3379	3159	2.17
0067	PC	554	2932	3384	3164	2.17
0067	PC	555	2936	3389	3169	2.17
0067	PC	556	2940	3394	3173	2.17
0067	PC	557	2944	3400	3178	2.17
0067	PC	558	2948	3405	3183	2.17
0067	PC	559	2952	3410	3187	2.17
0067	PC	560	2956	3415	3192	2.17
0067	PC	561	2960	3421	3196	2.17
0067	PC	562	2964	3425	3201	2.17
0067	PC	563	2968	3431	3206	2.17
0067	PC	564	2972	3436	3210	2.17
0067	PC	565	2976	3441	3215	2.17
0067	PC	566	2980	3447	3219	2.17
0067	PC	567	2984	3452	3224	2.17
0067	PC	568	2988	3457	3229	2.17
0067	PC	569	2992	3463	3233	2.17
0067	PC	570	2996	3468	3238	2.17
0067	PC	571	3000	3473	3242	2.17

Core	Core type	Depth (cm)	min95%	max95%	age (yr BP)	sed rate (mm/year)
0067	PC	572	3004	3478	3247	2.17
0067	PC	573	3008	3484	3252	2.17
0067	PC	574	3012	3489	3256	2.17
0067	PC	575	3016	3494	3261	2.17
0067	PC	576	3019	3499	3265	2.17
0067	PC	577	3023	3505	3270	2.17
0067	PC	578	3028	3510	3275	2.17
0067	PC	579	3032	3515	3279	2.17
0067	PC	580	3036	3520	3284	2.17
0067	PC	581	3040	3525	3289	2.17
0067	PC	582	3044	3531	3293	2.17
0067	PC	583	3048	3536	3298	2.17
0067	PC	584	3052	3541	3302	2.17
0067	PC	585	3056	3546	3307	2.17
0067	PC	586	3060	3552	3312	2.17
0067	PC	587	3063	3557	3316	2.17
0067	PC	588	3067	3562	3321	2.17
0067	PC	589	3071	3567	3325	2.17

Core 0002 age model results

Core	Core type	Depth (cm)	min95%	max95%	age (yr BP)	sed rate (mm/year)
0002	TWC	-12	-67	-63	-65	0.48
0002	TWC	-11	-49	-38	-44	0.48
0002	TWC	-10	-33	-12	-23	0.48
0002	TWC	-9	-17	14	-3	0.48
0002	TWC	-8	-1	40	18	0.48
0002	TWC	-7	14	66	39	0.48
0002	TWC	-6	30	92	60	0.48
0002	TWC	-5	46	119	80	0.48
0002	TWC	-4	62	145	101	0.48
0002	TWC	-3	78	171	122	0.48
0002	TWC	-2	94	197	143	0.48
0002	TWC	-1	110	224	164	0.48
0002	TWC	0	126	250	184	0.48
0002	PC	1	142	276	205	0.48
0002	PC	2	158	303	226	0.48
0002	PC	3	174	329	247	0.48
0002	PC	4	190	355	267	0.48
0002	PC	5	206	381	288	0.48
0002	PC	6	222	407	309	0.48
0002	PC	7	238	434	330	0.48
0002	PC	8	254	460	351	0.48
0002	PC	9	270	486	371	0.48
0002	PC	10	286	513	392	0.48
0002	PC	11	302	539	413	0.48
0002	PC	12	318	565	434	0.48
0002	PC	13	334	591	454	0.48
0002	PC	14	350	617	475	0.48
0002	PC	15	366	644	496	0.48
0002	PC	16	382	670	517	0.48
0002	PC	17	398	696	538	0.48
0002	PC	18	414	722	558	0.48
0002	PC	19	430	749	579	0.48
0002	PC	20	446	775	600	0.48
0002	PC	21	462	801	621	0.48
0002	PC	22	478	827	641	0.48
0002	PC	23	494	854	662	4.81
0002	PC	33	510	880	683	0.48
0002	PC	34	526	906	704	0.48

Core 0003 age model results

Core	Core type	Depth (cm)	min95%	max95%	age (yr BP)	sed rate (mm/year)
0003	PC	0	-67	-63	-65	0.69
0003	PC	1	-53	-48	-50	0.69
0003	PC	2	-39	-33	-36	0.69
0003	PC	3	-25	-17	-21	0.69
0003	PC	4	-11	-1	-7	0.69
0003	PC	5	2	14	8	0.69
0003	PC	6	16	30	22	0.69
0003	PC	7	30	46	37	0.69
0003	PC	8	43	62	51	0.69
0003	PC	9	57	77	66	0.69
0003	PC	10	70	93	81	0.69
0003	PC	11	84	109	95	0.69
0003	PC	12	98	125	110	0.69
0003	PC	13	111	141	124	0.69
0003	PC	14	125	156	139	0.69
0003	PC	15	138	172	153	0.69
0003	PC	16	152	188	168	0.69
0003	PC	17	165	204	182	0.69
0003	PC	18	179	220	197	0.69
0003	PC	19	193	235	212	0.69
0003	PC	20	206	251	226	0.69
0003	PC	21	220	267	241	0.69
0003	PC	22	233	283	255	0.69
0003	PC	23	247	299	270	0.69
0003	PC	24	261	315	284	0.69
0003	PC	25	274	330	299	0.69
0003	PC	26	288	346	314	0.69
0003	PC	27	301	362	328	0.69
0003	PC	28	315	378	343	0.69
0003	PC	29	329	394	357	0.69
0003	PC	30	342	409	372	0.69
0003	PC	31	356	425	386	0.69
0003	PC	32	369	441	401	0.69
0003	PC	33	383	457	415	0.69
0003	PC	34	396	473	430	0.69
0003	PC	35	410	489	445	0.69
0003	PC	36	424	504	459	0.69
0003	PC	37	437	520	474	0.69
0003	PC	38	451	536	488	0.69
0003	PC	39	464	552	503	0.69

Core	Core type	Depth (cm)	min95%	max95%	age (yr BP)	sed rate (mm/year)
0003	PC	40	478	568	517	0.69
0003	PC	41	491	583	532	0.69
0003	PC	42	505	599	546	0.69
0003	PC	43	519	615	561	0.69
0003	PC	44	532	631	576	0.69
0003	PC	45	546	647	590	0.69
0003	PC	46	559	663	605	0.69
0003	PC	47	573	678	619	0.69
0003	PC	48	586	694	634	0.69
0003	PC	49	600	710	648	0.69
0003	PC	50	614	726	663	0.69
0003	PC	51	627	742	677	0.69
0003	PC	52	641	758	692	0.69
0003	PC	53	654	773	707	0.69
0003	PC	54	668	789	721	0.69
0003	PC	55	682	805	736	0.69
0003	PC	56	695	821	750	0.69
0003	PC	57	709	837	765	0.69
0003	PC	58	722	853	779	0.69
0003	PC	59	736	868	794	0.69
0003	PC	60	749	884	809	0.69
0003	PC	61	763	900	823	0.69
0003	PC	62	777	916	838	0.69
0003	PC	63	790	932	852	0.69
0003	PC	64	804	948	867	0.69
0003	PC	65	817	963	881	0.69
0003	PC	66	831	979	896	0.69
0003	PC	67	844	995	910	0.69
0003	PC	68	858	1011	925	0.69
0003	PC	69	872	1027	940	0.69
0003	PC	70	885	1042	954	0.69
0003	PC	71	899	1058	969	0.69
0003	PC	72	912	1074	983	0.69
0003	PC	73	926	1090	998	0.69
0003	PC	74	939	1106	1012	0.69
0003	PC	75	953	1122	1027	0.69
0003	PC	76	967	1137	1041	0.69
0003	PC	77	980	1153	1056	0.69
0003	PC	78	994	1169	1071	0.69
0003	PC	79	1007	1185	1085	0.69
0003	PC	80	1021	1201	1100	0.69
0003	PC	81	1034	1216	1114	0.69

Core	Core type	Depth (cm)	min95%	max95%	age (yr BP)	sed rate (mm/year)
0003	PC	82	1048	1232	1129	0.69
0003	PC	83	1062	1248	1143	0.69
0003	PC	84	1075	1264	1158	0.69
0003	PC	85	1089	1280	1172	0.69
0003	PC	86	1102	1296	1187	0.69
0003	PC	87	1116	1311	1202	0.69
0003	PC	88	1129	1327	1216	0.69
0003	PC	89	1143	1343	1231	0.69
0003	PC	90	1157	1359	1245	0.69
0003	PC	91	1170	1375	1260	0.69
0003	PC	92	1184	1390	1274	0.69
0003	PC	93	1197	1406	1289	0.69
0003	PC	94	1211	1422	1303	0.69
0003	PC	95	1224	1438	1318	0.69
0003	PC	96	1238	1454	1333	0.69
0003	PC	97	1252	1470	1347	0.69
0003	PC	98	1265	1485	1362	0.69
0003	PC	99	1279	1501	1376	0.69
0003	PC	100	1292	1517	1391	0.69
0003	PC	101	1306	1533	1405	0.69
0003	PC	102	1319	1549	1420	0.69
0003	PC	103	1333	1565	1435	0.69
0003	PC	104	1347	1580	1449	0.69
0003	PC	105	1360	1596	1464	0.69
0003	PC	106	1374	1612	1478	0.69
0003	PC	107	1387	1628	1493	0.69
0003	PC	108	1401	1644	1507	0.69
0003	PC	109	1414	1660	1522	0.69
0003	PC	110	1428	1675	1536	0.69
0003	PC	111	1442	1691	1551	0.69
0003	PC	112	1455	1707	1566	0.69
0003	PC	113	1469	1723	1580	0.69
0003	PC	114	1482	1739	1595	0.69
0003	PC	115	1496	1754	1609	0.69
0003	PC	116	1510	1770	1624	0.69
0003	PC	117	1523	1786	1638	0.69
0003	PC	118	1537	1802	1653	0.69
0003	PC	119	1550	1818	1667	0.69
0003	PC	120	1564	1834	1682	0.69
0003	PC	121	1577	1849	1697	0.69
0003	PC	122	1591	1865	1711	0.69
0003	PC	123	1605	1881	1726	0.69

Core	Core type	Depth (cm)	min95%	max95%	age (yr BP)	sed rate (mm/year)
0003	PC	124	1618	1897	1740	0.69
0003	PC	125	1632	1913	1755	0.69
0003	PC	126	1645	1929	1769	0.69
0003	PC	127	1659	1944	1784	0.69
0003	PC	128	1672	1960	1798	0.69
0003	PC	129	1686	1976	1813	0.69
0003	PC	130	1700	1992	1828	0.69
0003	PC	131	1713	2008	1842	0.69
0003	PC	132	1727	2024	1857	0.69
0003	PC	133	1740	2039	1871	0.69
0003	PC	134	1754	2055	1886	0.69
0003	PC	135	1768	2071	1900	0.69
0003	PC	136	1781	2087	1915	0.69
0003	PC	137	1795	2103	1930	0.69
0003	PC	138	1808	2119	1944	0.69
0003	PC	139	1822	2134	1959	0.69
0003	PC	140	1836	2150	1973	0.69
0003	PC	141	1849	2166	1988	0.69
0003	PC	142	1863	2182	2002	0.69
0003	PC	143	1876	2198	2017	0.69
0003	PC	144	1890	2214	2031	0.69
0003	PC	145	1903	2229	2046	0.69
0003	PC	146	1917	2245	2061	0.69
0003	PC	147	1930	2261	2075	0.69
0003	PC	148	1944	2277	2090	0.69
0003	PC	149	1958	2293	2104	0.69
0003	PC	150	1971	2309	2119	0.69
0003	PC	151	1985	2324	2133	0.69
0003	PC	152	1998	2340	2148	0.69
0003	PC	153	2012	2356	2162	0.69
0003	PC	154	2025	2372	2177	0.69
0003	PC	155	2039	2388	2192	0.69
0003	PC	156	2053	2404	2206	0.69
0003	PC	157	2066	2419	2221	0.69
0003	PC	158	2080	2435	2235	0.69
0003	PC	159	2093	2451	2250	0.69
0003	PC	160	2107	2467	2264	0.69
0003	PC	161	2120	2483	2279	0.69
0003	PC	162	2134	2498	2293	0.69
0003	PC	163	2148	2514	2308	0.69
0003	PC	164	2161	2530	2323	0.69
0003	PC	165	2175	2546	2337	0.69

Core	Core type	Depth (cm)	min95%	max95%	age (yr BP)	sed rate (mm/year)
0003	PC	166	2188	2562	2352	0.69
0003	PC	167	2202	2578	2366	0.69
0003	PC	168	2215	2593	2381	0.69
0003	PC	169	2229	2609	2395	0.69
0003	PC	170	2243	2625	2410	0.69
0003	PC	171	2256	2641	2424	0.69
0003	PC	172	2270	2657	2439	0.69
0003	PC	173	2283	2673	2454	0.69
0003	PC	174	2297	2688	2468	0.69
0003	PC	175	2310	2704	2483	0.69
0003	PC	176	2324	2720	2497	0.69
0003	PC	177	2338	2736	2512	0.69
0003	PC	178	2351	2752	2526	0.69
0003	PC	179	2365	2768	2541	0.69
0003	PC	180	2378	2783	2556	0.69
0003	PC	181	2392	2799	2570	0.69
0003	PC	182	2405	2815	2585	0.69
0003	PC	183	2419	2831	2599	0.69
0003	PC	184	2433	2847	2614	0.69
0003	PC	185	2446	2863	2628	0.69
0003	PC	186	2460	2878	2643	0.69
0003	PC	187	2473	2894	2657	0.69
0003	PC	188	2487	2910	2672	0.69
0003	PC	189	2500	2926	2687	0.69
0003	PC	190	2514	2942	2701	0.69
0003	PC	191	2527	2958	2716	0.69
0003	PC	192	2541	2973	2730	0.69
0003	PC	193	2555	2989	2745	0.69
0003	PC	194	2568	3005	2759	0.69
0003	PC	195	2582	3021	2774	0.69
0003	PC	196	2595	3037	2788	0.69
0003	PC	197	2609	3053	2803	0.69
0003	PC	198	2622	3068	2818	0.69
0003	PC	199	2636	3084	2832	0.69
0003	PC	200	2650	3100	2847	0.69
0003	PC	201	2663	3116	2861	0.69
0003	PC	202	2677	3132	2876	0.69
0003	PC	203	2690	3148	2890	0.69
0003	PC	204	2704	3163	2905	0.69
0003	PC	205	2717	3179	2919	0.69
0003	PC	206	2731	3195	2934	0.69